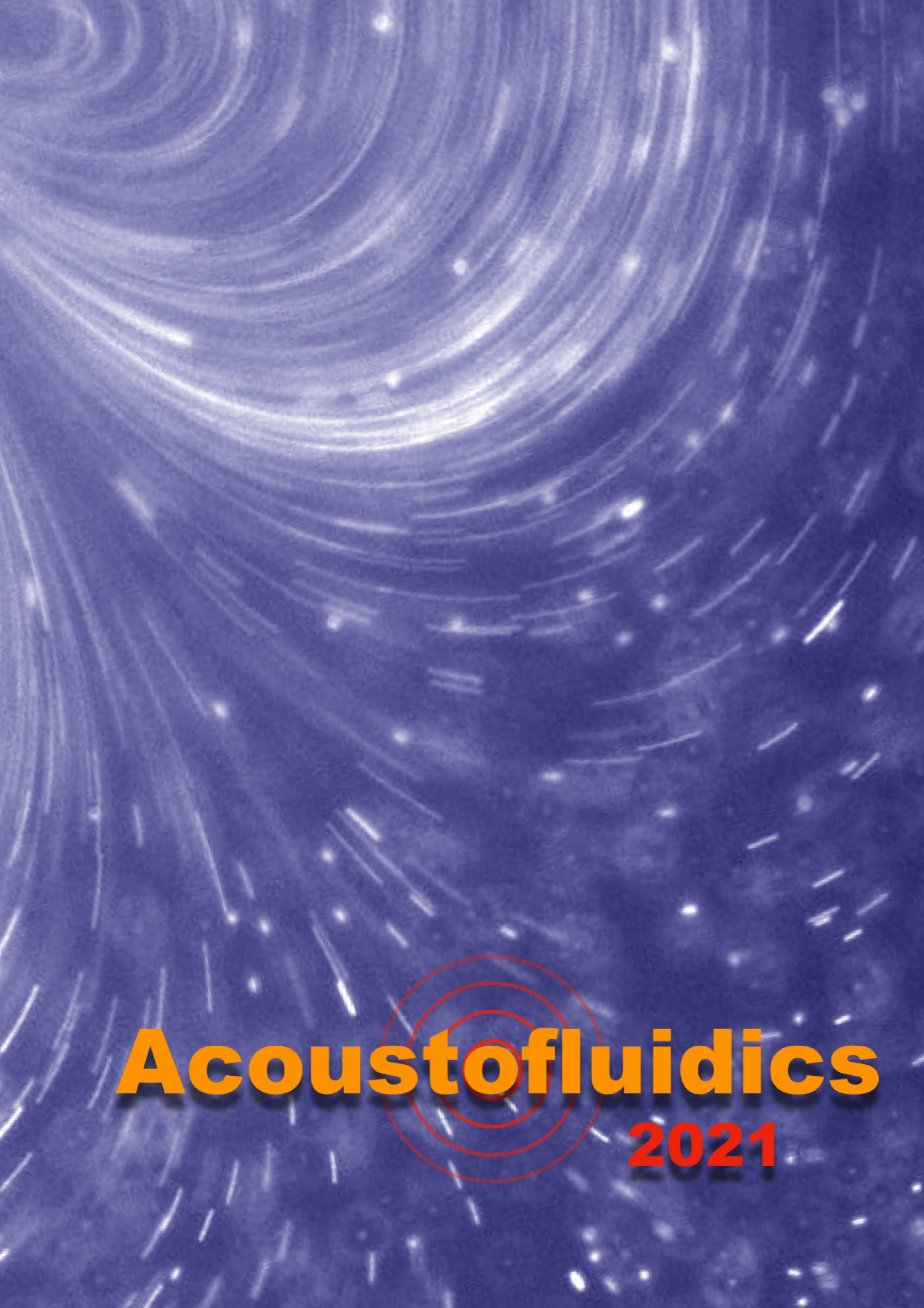

Acoustofluidics

2021

Table of Contents

Acoustofluidics 2021
26-27 August 2021
Virtual Conference

Welcome


Henrik Bruus


Thomas Franke

It is a great pleasure and honor to welcome you to Acoustofluidics 2021. After running this annual conference regularly for 18 years, first as the USWNet Annual Meeting from 2003 to 2012, and since 2013 as the Acoustofluidics Conference, we are for the second consecutive year facing the challenges imposed by the COVID-19 pandemic.

In April 2021, the USWNet Board in charge of running the Acoustofluidics Conference, decided to follow the format from 2020 and run the Acoustofluidics 2021 Conference as a virtual online conference and not as a regular conference in Glasgow as originally planned. We feel that in the current pandemic situation, it is important to offer a platform for our growing acoustofluidics community to present and discuss the most recent progress in the field and to allow especially students, postdocs, and young researchers, to connect online and exchange research news without suffering from a year-long gap in the conference cycle.

We very much appreciate the broad support and helpful feedback from so many colleagues of the acoustofluidics community that eventually rendered this year's virtual conference possible. In line with the many previous conferences, it was not difficult to engage our senior colleagues in the Organizing Committee and the Scientific Committee, and to have them volunteer as abstract reviewers and session chairs. We are very grateful for their help. Moreover, we got rapid positive feedback and acceptances from the invited speakers to present at our virtual conference. Finally, we appreciate support from our sponsors at CBMS and USWNet, as well as the good and very constructive collaboration we have had with Sara Stearns and Shirley Galloway from PMMI Global, who once more have helped setting up the conference website and dealing with the abstract submission and registration of the participants under these unusual circumstances.

It has been very gratifying for us to see the positive response in the whole acoustofluidics community to our call for papers in the beginning of June 2021 under the four topical sessions decided by the Organizing Committee: Acoustic Devices, Bio-Acoustic Systems, Physical Acoustics, and Acoustic Manipulation. We have received a total of 78 abstracts from five continents and 19 different countries (among the presenting authors). Given the strong manning of the Organizing Committee and the Scientific Committee, each abstract was reviewed by five leading experts in their respective fields. Because of the large number of submissions, and to give particularly young researchers the chance to present their work, we decided as in 2020 to allow as many speakers as possible. We eventually selected 24 abstracts for contributed talks and 28 abstracts for flash talks. Since the scientific quality of the abstracts were very high this year, the selection was not easy.

Taking a look at the final Acoustofluidics 2021 Abstract Book, we are convinced that this year's conference will again reflect the state-of-the-art in acoustofluidics research, including the newest scientific discoveries, cutting-edge acoustofluidics technologies, and innovative industrial applications as has been the case for the preceding annual Acoustofluidics Conferences.

We wish you all an inspiring, stimulating, and fruitful virtual conference on 26 - 27 August 2021!

Henrik Bruus
Chair Acoustofluidics 2021
President of USWNet

Thomas Franke
Chair Acoustofluidics 2021

Conference Officials

Conference Chairs

Thomas Franke	*University of Glasgow, UK*
Henrik Bruus	*Technical University of Denmark, DENMARK*

Organizing Committee

Anne Bernassau	*Heriot Watt University, UK*
Feiyan Cai	*Shenzhen Institute of Advanced Technology, CHINA*
Richard Fu	*Northumbria University, UK*
Ashis Kumar Sen	*Indian Institute of Technology, Madras, INDIA*
Jikui (Jack) Luo	*Zhejiang University, CHINA*
Mark Meacham	*Washington University, St. Louis, USA*
Glauber T. Silva	*Universidade Federal de Alagoas, BRAZIL*
Maria Tenje	*Uppsala University, SWEDEN*

Scientific Committee

Per Augustsson	*Lund University, SWEDEN*
Rune Barnkob	*Technical University München, GERMANY*
Michaël Baudoin	*Université de Lille, FRANCE*
Philippe Brunet	*Université Paris Diderot, FRANCE*
Bruce Drinkwater	*University of Bristol, UK*
Jürg Dual	*ETH Zürich, SWITZERLAND*
Xuexin Duan	*Tianjin University, CHINA*
James Friend	*University of California, San Diego, USA*
Peter Glynne-Jones	*University of Southampton, UK*
Xiasheng Guo	*Nanjing University, CHINA*
Tony Jun Huang	*Duke University, USA*
Thomas Laurell	*Lund University, SWEDEN*
Andreas Lenshof	*Lund University, SWEDEN*
Kian-Meng Lim	*National University of Singapore, SINGAPORE*
Mohamed El Malki	*Mohammed First University, MOROCCO*
Philippe Marmottant	*Université Grenoble Alpes, FRANCE*
Adrian Neild	*Monash University, AUSTRALIA*
Hyung Jin Sung	*Korea Advanced Institute of Science and Technology (KAIST), KOREA*
Hagen Schmidt	*Leibniz Institute (IFW Dreseden), GERMANY*
Karthick Subramani	*Indian Institute of Information Technology, Design and Mfg., INDIA*
Stefan Radel	*Technical University of Vienna, AUSTRIA*
Michel Versluis	*University of Twente, NETHERLANDS*
Martin Wiklund	*KTH Stockholm, SWEDEN*

Conference Sponsors

Chemical and Biological Microsystems Society (CBMS)
www.cbmsociety.org

Ultrasonic Standing Wave Network (USWNet)
www.uswnet.org

BelektroniG GmbH
www.belektronig.de

Invited Speakers

Session 1: Acoustic Devices

PRECISE PARTICLE AND CELL SORTING USING HIGH-FREQUENCY SURFACE ACOUSTIC WAVES
Ye Ai
Singapore University of Technology and Design, SINGAPORE

Session 2 - Bio-Acoustic Systems

ACOUSTOFLUIDIC TECHNOLOGIES FOR TISSUE ENGINEERING
Diane Dalecki
University of Rochester, USA

Session 3: Physical Acoustics

EXPLOITING PHASE SINGULARITIES TO STABLY TRAP INDIVIDUAL MICROBUBBLES WITH ACOUSTIC RADIATION FORCES
Diego Baresch
Université de Bordeaux, FRANCE

Session 4: Acoustic Manipulation

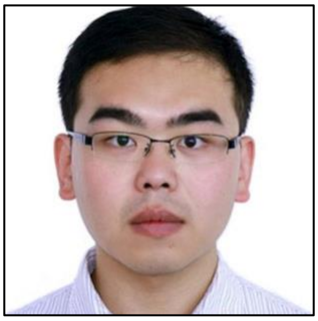

INTELLIGENT ACOUSTOFLUIDICS
Feng Guo
Indiana University, USA

Thursday 26 August

All times are US Eastern Daylight Time (EDT) - UTC/GMT -4 hours

08:00 - 08:05 **Opening Remarks**
Thomas Franke, *University of Glasgow, UK*
Henrik Bruus, *Technical University of Denmark, DENMARK*

Session 1 - Acoustic Devices

08:05 - 08:10 **Session Introduction by Session Chairs**
Peter Glynne-Jones, *University of Southampton, UK*
Richard Fu, *Northumbria University, UK*

Invited Speaker

08:10 - 08:40 **PRECISE PARTICLE AND CELL SORTING USING HIGH-FREQUENCY SURFACE ACOUSTIC WAVES**
Ye Ai, Peixian Li, Jianwei Zhong, and Zhichao Ma
Singapore University of Technology and Design, SINGAPORE

Contributed Talks

08:40 - 08:50 **NUMERICAL INVESTIGATION OF THIN-FILM TRANSDUCERS FOR EXCITING WHOLE-SYSTEM RESONANCES IN BULK ACOUSTOFLUIDICS DEVICES**
André G. Steckel and Henrik Bruus
Technical University of Denmark, DENMARK

08:50 - 09:00 **IMPROVING ACOUSTIC ENERGY CONVERSION EFFICIENCY IN BULK WAVE ACOUSTOPHORESIS DEVICES BY SIDE ACTUATION**
Wei Qiu, Thierry Baasch, Lei Jiang, and Thomas Laurell
Lund University, SWEDEN

09:00 - 09:10 **HIGH THROUGHPUT MULTINODAL ACOUSTIC TRAPPING OF EXTRACELLULAR VESICLES FOR DOWNSTREAM MASS SPECTROMETRY ANALYSIS**
Axel Broman, Lotta Happonen, Frida Palm, Oonagh Shannon, Andreas Lenshof, Johan Malmström, and Thomas Laurell
Lund University, SWEDEN

09:10 - 09:20 **SURFACE ACOUSTIC WAVE MANIPULATION OF 100 FEMTOLITER DROPLETS IN NANOCHANNELS**
Naiqing Zhang, Amihai Horesh, and James Friend
University of California, San Diego, USA

09:20 - 09:30 **PHASE CONTRAST MICROSCOPY CHARACTERIZATION OF STANDING SURFACE ACOUSTIC WAVES FOR MICROFLUIDIC APPLICATIONS**
Pierre Thibault, Ianis Bernard, and Philippe Marmottant
Université Grenoble Alpes, FRANCE

09:30 - 09:40 **WIRELESS HIGH-FREQUENCY ACOUSTOFLUIDIC MICROPUMP FOR PORTABLE DRUG DELIVERY SYSTEMS**
Rui You and Xuexin Duan
Tianjin University, CHINA

Flash Talks

09:40 - 09:44 **RAPID MICROMIXING DRIVEN BY SHARP-EDGE ACOUSTIC STREAMING IN A MICROCHANNEL**
Chuanyu Zhang[1], Geyu Zhong[1], Philippe Brunet[1], Laurent Royon[1], and Xiaofeng Guo[1,2]
[1]Université de Paris, FRANCE and
[2]Université Gustave Eiffel, ESIEE Paris, FRANCE

09:44 - 09:48 **SELECTIVE EVAPORATION-INDUCED CHANGES IN THE RESONANCE BEHAVIOR OF A PIEZOACOUSTIC INKCHANNEL**
Maaike Rump[1], Uddalok Sen[1], Roger Jeurissen[1], Christian Diddens[1], Hans Reinten[2], Detlef Lohse[1], Michel Versluis[1], and Tim Segers[1]
[1]University of Twente, NETHERLANDS and
[2]Canon Production Printing, NETHERLANDS

09:48 - 09:52 **THE ELASTIC, DIELECTRIC, AND PIEZOELECTRIC CONSTANTS OF PZT TRANSDUCERS FOR ACOUSTOFLUIDICS DETERMINED BY ELECTRICAL IMPEDANCE SPECTROSCOPY**
William N. Bodé, Fabian Lickert, and Henrik Bruus
Technical University of Denmark, DENMARK

09:52 - 09:56 **A PIEZOELECTRIC SMART PATCH OPERATED WITH MACHINE LEARNING ALGORITHMS FOR EFFECTIVE DETECTION AND ELIMINATION OF CONDENSATION**
Qian Zhang[1,2], Yong Wang[1,2,3], Tao Wang[1], Dongsheng Li[1], Jin Xie[1], Hamdi Torun[2], and Yongqing Fu[1,2]
[1]Zhejiang University, CHINA, [2]University of Northumbria, UK, and
[3]Westlake University, Hangzhou, CHINA

09:56 - 10:00 **HEAT TRANSFER MECHANISM DUE TO ACOUSTIC BODY FORCE UNDER ACOUSTIC FIELDS**
Varun Kumar Rajendran, Mohammed Azharudeen, and Karthick Subramani
Indian Institute of Information Technology, Design and Manufacturing, Kancheepuram, INDIA

10:00 - 10:04 **AXIAL DISPLACEMENT OF TYPICAL CELLS WITH 3D TRAPPING IN A HIGH-FREQUENCY SINGLE BEAM ACOUSTICAL TWEEZERS**
Zhixiong Gong[1] and Michael Baudoin[1,2]
[1]University of Lille, CNRS, FRANCE and
[2]Institut Universitaire de France, FRANCE

10:04 - 10:08 **A NUMERICAL SIMULATION OF PUMPLESS-CHAOTIC MICROMIXER UTILIZING THE VIBRATION-INDUCED FLOW**
Kanji Kaneko[1], Naoto Ujikawa[1], Yosuke Hasegawa[2],
Takeshi Hayakawa[1], and Hiroaki Suzuki[1]
[1]Chuo University, JAPAN and [2]University of Tokyo, JAPAN

10:08 – 10:25 **Break (offline)**

Session 2 - Bio-Acoustic Systems

10:25 - 10:30 **Session Introduction by Session Chairs**
Maria Tenje, *Uppsala University, SWEDEN*
Mark Meacham, *Washington University, St. Louis, USA*

Invited Speaker

10:30 - 11:00 **ACOUSTOFLUIDIC TECHNOLOGIES FOR TISSUE ENGINEERING**
Diane Dalecki, Emma G. Norris, and Denise C. Hocking
University of Rochester, USA

Contributed Talks

11:00 - 11:10 **ENABLING OFF-CHIP ANALYSIS FOR IN-DROPLET ENZYME REACTIONS USING ACOUSTOPHORESIS**
Zhenhua Liu[1], Anna Fornell[1,2], and Maria Tenje[1]
[1]Uppsala University, SWEDEN and [2]Lund University, SWEDEN

11:10 - 11:20 **BACTERIA PRECONCENTRATION USING AN ULTRASONIC NANOSIEVE WITHIN A MICROFLUIDIC DEVICE WITH FLUORESCENCE QUANTIFICATION**
Bryan Ang, Ruhollah Habibi, Kellie Tuck, Victor Cadarso,
and Adrian Neild
Monash University, AUSTRALIA

11:20 - 11:30 **ACOUSTIC DEFORMATION OF RED BLOOD CELLS**
Andreas Link, Raymond Sparrow, Esther Richter,
Mustafa Zaimagaoglu, and Thomas Franke
University of Glasgow, UK

11:30 - 11:40

NON-INVASIVE NEUROMODULATION USING ULTRASOUND: MECHANISMS OF ACTION
Aditya Vasan and James Friend
University of California, San Diego, USA

11:40 - 11:50

ENDOTHELIAL CELL BRANCH FORMATION IN HYDROGEL USING TWO DIFFERENT FREQUENCY ULTRASOUNDS FOR MICROVASCULAR NETWORKS
Le Thi Huong[1], Andreas Lenshof[2], Van Thuy Duong[1], Huu Lam Phan[1], Thomas Laurell[2], Kyo-in Koo[1]
[1]University of Ulsan, KOREA (ROK) and [2]Lund University, SWEDEN

11:50 - 12:00

USING ACOUSTOFLUIDICS TO ENGINEER SKELETAL MUSCLES
Dhananjay V. Deshmukh, Peter Reichert, Joel Zvick,
Oksana Dudaryeva, Ori Bar-Nur, Mark W. Tibbitt, and Jurg Dual
ETH Zürich, SWITZERLAND

Flash Talks

12:00 - 12:04

ACOUSTOMICROFLUIDIC TRI-SEPARATION OF PROTEINS USING APTAMER-COATED MICROPARTICLES
Muhammad Afzal[1], Jinsoo Park[2], Jessie S. Jeon[1],
and Hyung Jin Sung[1]
[1]Korea Advanced Institute of Science and Technology (KAIST), KOREA (ROK) and [2]Chonnam National University, KOREA

12:04 - 12:08

A BUBBLE-BASED ACOUSTOFLUIDIC DEVICE FOR THE STUDY OF ULTRASOUND THROMBOLYSIS
Yuan Gao[1], Mengren Wu[1], Bruce Gaynes[2,3], and Jie Xu[1]
[1]University of Illinois, Chicago, USA, [2]Loyola University Medical Center, USA, and [3]Edward Hines Jr VA Medical Center, USA

12:08 - 12:12

A SOUND IDEA TO STIMULATE CELLS: A NOVEL METHOD TO ACOUSTO-MECHANICALLY STIMULATE CELLS
Christopher Markwell[1], Luying Feng[1], Ran Tao[1,2], Steven O'Reilly[3], Richard Fu[1], and Hamdi Torun[1]
[1]Northumbria University, UK, [2]Shenzhen University, CHINA, and [3]Durham University, UK

12:12 - 12:16

NEURAL DIFFERENTIATION OF HUMAN EMBRYONIC STEM CELLS MEDIATED BY SURFACE ACOUSTIC WAVES
Chao Sun[1], Jun Wei[3], Meng Cai[3], and Xin Yang[2]
[1]Northwestern Polytechnical University, CHINA,
[2]Cardiff University, UK, and [3]iRegene Therapeutics Co., Ltd., CHINA

12:16 - 12:20 **SELF-ORGANIZATION OF HUMAN MESENCHYMAL STEM CELLS INTO SPHEROIDS TRAPPED IN ACOUSTIC LEVITATION**

Nathan Jeger-Madiot[1], Lousineh Arakelian[2], Niclas Setterblad[3], Patrick Bruneval[4], Mauricio Hoyos[1], Jérôme Larghero[2], and Jean-Luc Aider[1]
[1]Université de Paris-1, FRANCE, [2]Université de Paris, FRANCE, [3]Université de Paris Diderot, FRANCE, and [4]INSERM, FRANCE

12:20 - 12:24 **ACOUSTIC TRAPPING OF SUB-WAVELENGTH MICROPARTICLES AND CELLS IN RESONANT CYLINDRICAL SHELLS**

Qin Lin, Feiyan Cai, and Hairong Zheng
Chinese Academy of Sciences (CAS), CHINA

12:24 - 12:28 **ANALYSIS OF ACOUSTOPHORETIC FOCUSING USING THE OPEN-SOURCE 3D PARTICLE TRACKING TOOLBOX *DefocusTracker***

Massimiliano Rossi[1], Rune Barnkob[2], and Henrik Bruus[1]
[1]Technical University of Denmark, DENMARK and
[2]Technical University of Munich, GERMANY

12:28 **Adjourn for the Day**

Friday 27 August

All times are US Eastern Daylight Time (EDT) - UTC/GMT -4 hours

08:00 - 08:05 **Opening Remarks**
Thomas Franke, *University of Glasgow, UK*
Henrik Bruus, *Technical University of Denmark, DENMARK*

Session 3 - Physical Acoustics

08:05 - 08:10 **Session Introduction by Session Chairs**
Glauber T. Silva, *Universidade Federal de Alagoas, BRAZIL*
Feiyan Cai, *Shenzhen Institute of Advanced Technology, CHINA*

Invited Speaker

08:10 - 08:40 **EXPLOITING PHASE SINGULARITIES TO STABLY TRAP INDIVIDUAL MICROBUBBLES**
Diego Baresch
Université de Bordeaux, FRANCE

Contributed Talks

08:40 - 08:50 **SELF-ORGANIZATION BY ACOUSTIC CONTRAST FACTOR IN ACOUSTICALLY PACKED BEDS OF WHOLE BLOOD AND IN-LINE REMOVAL OF RED BLOOD CELLS**
Richard Soller, Ola Jakobsson, and Per Augustsson
Lund University, SWEDEN

08:50 - 09:00 **MEAN ACOUSTIC FIELDS IN ACOUSTOFLUIDICS: RADIATION FORCE AND TORQUE ON SUBWAVELENGTH AXISYMMETRIC PARTICLES**
Everton B. Lima, Giclênio C. Silva, Marcos Sales, Ana Leite, Ueslen Rocha, and Glauber T. Silva
Federal University of Alagoas, BRAZIL

09:00 - 09:10 **SUPPRESSION OF ACOUSTIC STREAMING BY AC ELECTROOSMOSIS: THEORY AND SIMULATION**
Bjørn G. Winckelmann and Henrik Bruus
Technical University of Denmark, DENMARK

09:10 - 09:20 **EFFECTS OF A LASER-INDUCED THERMAL GRADIENT ON THE ACOUSTIC STREAMING FIELD**
Franziska Martens, Wei Qiu, Andreas Ehn, and Per Augustsson
Lund University, SWEDEN

09:20 - 09:30 **QUALITATIVE CHANGES IN THE STREAMING PATTERN AT HIGH ACOUSTIC ENERGY DUE TO FRICTION-INDUCED HEATING IN THE VISCOUS BOUNDARY LAYERS**
Jonas H. Joergensen[1], Wei Qiu[2], and Henrik Bruus[1]
[1]Technical University of Denmark, DENMARK and
[2]Lund University, SWEDEN

09:30 - 09:40 **MEASURING THE TEMPORAL DIFFERENCE IN BUILD UP BETWEEN THE ACOUSTIC RADIATION FORCE AND ACOUSTIC STREAMING WITH AN OPTICAL TWEEZER**
Christoph Goering and Jürg Dual
ETH Zürich, SWITZERLAND

Flash Talks

09:40 - 09:44 **EFFECTS OF SHAPE AND WILLIS COUPLING ON ACOUSTIC RADIATION FORCE AND TORQUE**
Shahrokh Sepehrirahnama[1], Sebastian Oberst[1,2], Yan Kei Chiang[1,2], and David A. Powell[1,2]
[1]University of Technology Sydney, AUSTRALIA and
[2]University of New South Wales, AUSTRALIA

09:44 - 09:48 **EFFECT OF AXIAL PRIMARY RADIATION FORCE ON THE DYNAMICAL MOTION OF A PAIR OF MICROPARTICLES ALONG THE PRESSURE NODAL PLANE**
Sazid Z. Hoque, Amal Nath, and Ashis K. Sen
Indian Institute of Technology (IIT), Madras, INDIA

09:48 - 09:52 **GENERALIZED POTENTIAL FOR ACOUSTIC INTERACTION FORCE**
Shahrokh Sepehrirhnama[1], and Kian-Meng Lim[2]
[1]University of Technology Sydney, AUSTRALIA and
[2]National University of Singapore, SINGAPORE

09:52 - 09:56 **MICROSTREAMING AND ACOUSTIC INTERACTION FORCES BETWEEN TWO PARTICLES IN A STANDING WAVE WITHIN A VISCOUS FLUID**
Alen Pavlic, Lorenzo Ermanni, and Jürg Dual
ETH Zürich, SWITZERLAND

09:56 - 10:00 **3D3C FLOW MEASUREMENTS OF THE ACOUSTICALLY INDUCED VORTEX STRUCTURES IN A STANDING SURFACE ACOUSTIC WAVE FIELD**
Sebastian Sachs, Christian Cierpka, and Jörg König
Technische Universität Ilmenau, GERMANY

10:00 - 10:04 **BURGERS-RICCATI PHYSICS OF FAST BULK ACOUSTIC STREAMING**
Jeremy Orosco and James Friend
University of California, San Diego, USA

10:04 - 10:08 **SPECULAR-REFLECTION CONTRIBUTIONS TO DYNAMIC RADIATION FORCES ON HIGHLY REFLECTING SPHERES AND CYLINDERS: SIMPLIFIED ANALYSIS**
Philip L. Marston[1], Timothy D. Daniel[1,2], and Auberry R. Fortuner[1]
[1]Washington State University, USA and
[2]Naval Surface Warfare Center Panama City Division, USA

10:08 – 10:25 **Break (offline)**

Session 4 - Acoustic Manipulation

10:25 - 10:30 **Session Introduction by Session Chairs**
Jikui (Jack) Luo, *Zhejiang University, USA*
Ashis Kumar Sen, *Indian Institute of Technology, Madras, INDIA*

Invited Speaker

10:30 - 11:00 **INTELLIGENT ACOUSTOFLUIDICS FOR ENGINEERING HUMAN BRAIN ORGANOIDS**
Hongwei Cai, Zheng Ao, and Feng Guo
Indiana University, USA

Contributed Talks

11:00 - 11:10 **ACOUSTICALLY EXCITED CHANNEL WALLS FOR MICROBIOLOGICAL APPLICATIONS**
Michael Gerlt, Nino Läubli, Peter Ruppen, Moritz Leuthner,
Michel Manser, Alexander Wüthrich, Bradley Nelson,
Sven Panke, and Jürg Dual
ETH Zürich, SWITZERLAND

11:10 - 11:20 **SELECTING THE OPTIMAL BUFFER FOR ACOUSTIC PARTICLE SEPARATION**
Thierry Baasch and Thomas Laurell
Lund University, SWEDEN

11:20 - 11:30 **ACOUSTIC RADIATION FORCE ON ELASTIC MICROBEADS EXPERIENCING RESONANT SPHEROIDAL VIBRATIONS IN A VISCOUS FLUID**
Amir Tahmasebipour, Matthew R. Begley, and Carl D. Meinhart
University of California, Santa Barbara, USA

11:30 - 11:40

CONTACTLESS ADDITIVE MANUFACTURING USING ACOUSTIC LEVITATION
Iñigo Ezcurdia[1], Rafael Morales[2], Marco A.B. Andrade[3],
and Asier Marzo[1]
[1]Public University of Navarre, SPAIN, [2]UltraLeap Ltd., UK, and
[3]University of São Paulo, BRAZIL

11:40 - 11:50

ON-DEMAND DROPLET GENERATION USING BULK ACOUSTIC WAVE
E. Hemachandran[1], Thomas Laurell[2], and Ashis Kumar Sen[1]
[1]Indian Institute of Technology, Madras, INDIA and
[2]Lund University, SWEDEN

11:50 - 12:00

SWARMING BEHAVIORS OF MICROMOTORS POWERED BY BUBBLE OSCILLATION
Xiaolong Lu[1], Ying Wei[1], Hui Shen[1], and Wenjuan Liu[2]
[1]Nanjing University of Aeronautics and Astronautics, CHINA and
[2]Nanjing Tech University, CHINA

Flash Talks

12:00 - 12:04

CONTROLLED TRANSPORT AND MERGING OF INDIVIDUAL DROPS IN CLOSED CHANNEL ACOUSTOFLUIDIC DEVICES
Kyriacos Yiannacou and Veikko Sariola
Tampere University, FINLAND

12:04 - 12:08

PARTICLE TRAPPING IN MICROFLUIDIC SHAPED TRAPS EXPOSED TO BULK ACOUSTIC STANDING WAVES
Lokesh Malik, Amal Nath, and Ashis Kumar Sen
Indian Institute of Technology, Madras, INDIA

12:08 - 12:12

PARTICLE FOCUSING IN POLYMER-BASED ACOUSTOFLUIDIC DEVICES: AN EXPERIMENTAL AND NUMERICAL STUDY
Fabian Lickert[1], Mathias Ohlin[2], Henrik Bruus[1], and Pelle Ohlsson[2]
[1]Technical University of Denmark, DENMARK and
[2]AcouSort AB, SWEDEN

12:12 - 12:16

CELL-BASED MICROROBOT MANIPULATION BY MULTIELEMENT FOCUSED ULTRASOUND PHASED ARRAY
Hiep Xuan Cao, Van Du Nguyen, Daewon Jung, Han-Sol Lee,
Byungjeon Kang, Jong-Oh Park, and Chang-Sei Kim
Chonnam National University, KOREA (ROK)

12:16 - 12:20

FOURIER ACOUSTICAL TWEEZERS: SYNTHESIZING ARBITRARY RADIATION FORCE USING NON-MONOCHROMATIC WAVES ON DISCRETE-FREQUENCY BASIS
Yu Zhang and Xiasheng Guo
Nanjing University, CHINA

12:20 - 12:24 **GENERATION AND TRANSFER OF POLYDISPERSE DROPLETS USING LOW POWER SURFACE ACOUSTIC WAVES**
Krishnadas N. Nampoothiri, Niladri S. Satpathi, and Ashis K. Sen
Indian Institute of Technology, Madras, INDIA

12:24 - 12:28 **DROPLET IMPACT DYNAMICS ON HYDROPHOBIC AND SLIPPERY LIQUID-INFUSED POROUS SURFACES CONTROLLED BY PROPAGATING SURFACE ACOUSTIC WAVES**
Luke Haworth[1], Mehdi H. Biroun[1,2], Prashant Agrawal[1],
Bethany Orme[1], Glen McHale[3], Mohammad Rahmati[1], Hamdi Torun[1],
and Richard YongQing Fu[1]
[1]Northumbria University, UK, [2]University College London, UK, and
[3]University of Edinburgh, UK

Closing Remarks and Announcement of Acoustofluidics 2022

12:28 -12:40 Thomas Franke, University of Glasgow, UK
Henrik Bruus, Technical University of Denmark, DENMARK
Rune Barnkob, TU Munich, DE, Head of the Coakley Award 2021

12:40 **Conference Adjourns**

Abstract-Only Presentations

Acoustic Devices

AN EASY AND ACCESSIBLE MANUFACTURING METHOD FOR RECONFIGURABLE SAW DEVICES

Roman Mikhaylov[1], Mercedes S. Martin[1], Povilas Dumcius[1], Hanlin Wang[1], Fangda Wu[1],
Xiaoyan Zhang[2], Fahad Alghamdi[1], Victory Akhimien[1], Chao Sun[3], Aled Clayton[1],
Yongqing Fu[4], Lin Ye[5], Zhiqiang Dong[6], and Xin Yang[1]
[1]Cardiff University, UK, [2]Huazhong Agricultural University, CHINA,
[3]Northwestern Polytechnical University, CHINA,
[4]Northumbria University, UK, [5]Cardiff University School of Medicine, and
[6]Huazhong Agricultural University, CHINA

LAMB WAVE COUPLED RESONANCE FOR SAW ACOUSTOFLUIDICS

Junjie Huang and Xiasheng Guo
Nanjing University, CHINA

A NUMERICAL INVESTIGATION OF THE MIXING ENHANCEMENT IN A Y-JUNCTION MICROCHANNEL INDUCED BY ACOUSTIC STREAMING

Sintayehu Assefa Endaylalu, and Wei-Hsin Tien
National Taiwan Science and Technology University, TAIWAN

Bio-Acoustic Systems

ACOUSTIC DROPLET PRINTING TUMOR ORGANOIDS FOR MODELING BLADDER TUMOR IMMUNE MICROENVIRONMENT
Zhiyi Gong, Yongchang Wei, Fubing Wang, and Shishang Guo
Wuhan University, CHINA

ACOUSTIC FIBROBLAST CELL PATTERNING IN HYDROGEL FOR THREE-DIMENSIONAL CELL NETWORK FORMATION
Le Thi Huong[1], Andreas Lenshof[2], Thomas Laurell[2], and Kyo-in Koo[1]
[1]University of Ulsan, KOREA (ROK) and [2]Lund University, SWEDEN

STUDY OF THE RAYLEIGH LIMIT BY ACOUSTIC FORCE IN MICROGRAVITY
Chloé Dupuis, Xavier Mousset, Lucile Rabiet, Xavier Benoit-Gonin, Mauricio Hoyos, and Jean-Luc Aider
ESPCI, Université de Paris, FRANCE

ACOUSTO-PI: AN INTEGRATED OPTO-ACOUSTOFLUIDIC SYSTEM WITH OPEN-SOURCE ELECTRONICS FOR IN-FIELD DIAGNOSTICS
Jethro Vernon[1], Pep Canyelles-Pericas[2], Hamdi Torun[1], and Richard Yong-Qing[1]
[1]University of Northumbria, UK and [2]University of Twente, NETHERLANDS

Physical Acoustics

PARTICLE CHAIN FORMATION IN ACOUSTOPHORESIS
Thierry Baasch, Wei Qiu, and Thomas Laurell
Lund University, SWEDEN

NUMERICAL SIMULATIONS OF RELOCATION MECHANISM OF COFLOWING IMMISCIBLE FLUIDS EXPOSED TO BULK ACOUSTIC WAVE
Sazid Z. Hoque and Ashis K. Sen
Indian Institute of Technology (IIT), Madras, INDIA

TRAPPING AND “BOUNCING” OF WATER DROPLETS IN OIL-FILLED MICROWELLS UNDER SAW-INDUCED STREAMING
Amal Nath and Ashis K. Sen
Indian Institute of Technology, Madras, INDIA

MODULATED ACOUSTIC RADIATION FORCE IN A CARRIER STANDING WAVE
Mehdi Akbarzadeh, Sebastian Oberst, Shahrokh Sepehrirahnama, and Ben Halkon
University of Technology Sydney, AUSTRALIA

EFFECT OF VIBRATION VELOCITY ON LOW-FREQUENCY SHARP-EDGE ACOUSTIC STREAMING PATTERN
Geyu Zhong[1,2], Chuanyu Zhang[1], Philippe Brunet[1], Laurent Royon[1], YingWen Liu[3], and Xiaofeng Guo[1,2]
[1]Université de Paris, FRANCE, [2]Université Gustave Eiffel, FRANCE, and [3]Xi'an Jiaotong University, CHINA

3D MODEL OF THE PARTICLE ACOUSTOPHORETIC MOTION IN A RECTANGULAR DEVICE

Abelino Vargas[1,2], Marcela Camacho[1,2], J.D. Muñoz[1], and Itziar González[3]
[1]National University of Colombia, COLOMBIA, [2]International Physics Center (CIF), Biophysics Laboratory, COLOMBIA, and [3]CSIC Spanish National Research Council, SPAIN

MULTIPHYSIC MODEL BASED ON SAW-LIQUID INTERACTION FOR THE PREDICTION OF PHYSICAL STRESSES EXERTED ON CELLS AND TISSUES: SIMULATION VERSUS EXPERIMENT

D.S. Bidouba Sanvany, Francis Kosior, Denis Beyssen, Aude Gigodot, Elisabeth Gaudion, and Frederic Sarry
Université de Lorraine, FRANCE

Acoustic Manipulation

BINARY ACOUSTIC PARTICLE TRAPPING IN GLASS CAPILLARIES

Thierry Baasch[1], Anna Fornell[1,2], Carl Johannesson[1], Johan Nilsson[1], and Maria Tenje[2]
[1]Lund University, SWEDEN and [2]Uppsala University, SWEDEN

SINGLE CELL ENCAPSULATION USING SAW

Andreas Link, Raymond Sparrow, Esther Richter, Mustafa Zaimagaoglu, John McGrath, and Thomas Franke
University of Glasgow, UK

SPIRALING WAVEFRONTS AND DETECTION OF PHASE SINGULARITIES IN OBJECTS IMMERSED IN INHOMOGENEOUS ACOUSTIC FIELDS

Ludovic Alhaïtz, Diego Baresch, Thomas Brunet, Christophe Aristégui, and Olivier Poncelet
University of Bordeaux, FRANCE

CELL PHENOTYPING VIA ACOUSTIC CONTRAST FACTOR BY USING A FILLED TILTED-ANGLE ACOUSTOFLUIDIC DEVICE

Hanlin Wang[1], Joe Boardman[1], Xiaoyan Zhang[1], Chao Sun[2], Meng Cai[3], Jun Wei[3], Zhenlin Wu[4], Yongqing Fu[5], and Xin Yang[1]
[1]Cardiff University, UK, [2]Northwestern Polytechnical University, CHINA, [3]iRegene Pharmaceutical Technology Co., Ltd., CHINA, [4]Dalian University of Technology, CHINA, and [5]Northumbria University, UK

KINETIC AND THERMAL CHARACTERISTICS OF MICRO-DROPLET DRIVEN BY RAYLEIGH SURFACE ACOUSTIC WAVE

Mubbashar Mehmood, Baixin Chen, and Richard Yongqing Fu
Heriot-Watt University, UK

LYOPHILISED MONODISPERSE MICROBUBBLES AS ULTRASOUND CONTRAST AGENT

Ugur Soysal[1], Pedro N. Azevedo[1,2,3], Flavien Bureau[2], Alexandre Aubry[2], Marcio S. Carvalho[3], Amanda C.S.N. Pessoa[4], Lucimara G. de la Torre[4], Olivier Couture[5], Arnaud Tourin[2], Mathias Fink[2], and Patrick Tabeling[1]
[1]ESPCI Paris, FRANCE, [2]Université PSL, CNRS, FRANCE, [3]Pontifical Catholic University of Rio de Janeiro, BRAZIL, [4]University of Campinas, BRAZIL, and [5]Sorbonne Université, CNRS, INSERM, FRANCE

MICROPARTICLE PATTERNING INSIDE CAPILLARY TUBES ON BENDABLE THIN FILM SAW DEVICES

Sadaf MaramiZonouz[1], Mohammad Rahmati[1], Changfeng Jia[2], Tengfei Zheng[2],
and Richard Yongqing Fu[1]
[1]Northumbria University, UK and [2]Xian Jiaotong University, CHINA

THREE-DIMENSIONAL STANDING SURFACE ACOUSTIC WAVE SIMULATION MODEL FOR EFFICIENT PARTICLE SEPARATION

Lizhu Liu, Jian Zhou, Dinghong Zhang, and Zhengjia Zhan
Hunan University, CHINA

Abstracts

Acoustofluidics
2021

Session 1 - Acoustic Devices

Invited Speaker

08:10 - 08:40 **PRECISE PARTICLE AND CELL SORTING USING HIGH-FREQUENCY SURFACE ACOUSTIC WAVES**
Ye Ai, Peixian Li, Jianwei Zhong, and Zhichao Ma
Singapore University of Technology and Design, SINGAPORE

Contributed Talks

08:40 - 08:50 **NUMERICAL INVESTIGATION OF THIN-FILM TRANSDUCERS FOR EXCITING WHOLE-SYSTEM RESONANCES IN BULK ACOUSTOFLUIDICS DEVICES**
André G. Steckel and Henrik Bruus
Technical University of Denmark, DENMARK

08:50 - 09:00 **IMPROVING ACOUSTIC ENERGY CONVERSION EFFICIENCY IN BULK WAVE ACOUSTOPHORESIS DEVICES BY SIDE ACTUATION**
Wei Qiu, Thierry Baasch, Lei Jiang, and Thomas Laurell
Lund University, SWEDEN

09:00 - 09:10 **HIGH THROUGHPUT MULTINODAL ACOUSTIC TRAPPING OF EXTRACELLULAR VESICLES FOR DOWNSTREAM MASS SPECTROMETRY ANALYSIS**
Axel Broman, Lotta Happonen, Frida Palm, Oonagh Shannon, Andreas Lenshof, Johan Malmström, and Thomas Laurell
Lund University, SWEDEN

09:10 - 09:20 **SURFACE ACOUSTIC WAVE MANIPULATION OF 100 FEMTOLITER DROPLETS IN NANOCHANNELS**
Naiqing Zhang, Amihai Horesh, and James Friend
University of California, San Diego, USA

09:20 - 09:30 **PHASE CONTRAST MICROSCOPY CHARACTERIZATION OF STANDING SURFACE ACOUSTIC WAVES FOR MICROFLUIDIC APPLICATIONS**
Pierre Thibault, Ianis Bernard, and Philippe Marmottant
Université Grenoble Alpes, FRANCE

09:30 - 09:40 **WIRELESS HIGH-FREQUENCY ACOUSTOFLUIDIC MICROPUMP FOR PORTABLE DRUG DELIVERY SYSTEMS**
Rui You and Xuexin Duan
Tianjin University, CHINA

Flash Talks

09:40 - 09:44

RAPID MICROMIXING DRIVEN BY SHARP-EDGE ACOUSTIC STREAMING IN A MICROCHANNEL

Chuanyu Zhang[1], Geyu Zhong[1], Philippe Brunet[1], Laurent Royon[1], and Xiaofeng Guo[1,2]
[1]Université de Paris, FRANCE and
[2]Université Gustave Eiffel, ESIEE Paris, FRANCE

09:44 - 09:48

SELECTIVE EVAPORATION-INDUCED CHANGES IN THE RESONANCE BEHAVIOR OF A PIEZOACOUSTIC INKCHANNEL

Maaike Rump[1], Uddalok Sen[1], Roger Jeurissen[1], Christian Diddens[1], Hans Reinten[2], Detlef Lohse[1], Michel Versluis[1], and Tim Segers[1]
[1]University of Twente, NETHERLANDS and
[2]Canon Production Printing, NETHERLANDS

09:48 - 09:52

THE ELASTIC, DIELECTRIC, AND PIEZOELECTRIC CONSTANTS OF PZT TRANSDUCERS FOR ACOUSTOFLUIDICS DETERMINED BY ELECTRICAL IMPEDANCE SPECTROSCOPY

William N. Bodé, Fabian Lickert, and Henrik Bruus
Technical University of Denmark, DENMARK

09:52 - 09:56

A PIEZOELECTRIC SMART PATCH OPERATED WITH MACHINE LEARNING ALGORITHMS FOR EFFECTIVE DETECTION AND ELIMINATION OF CONDENSATION

Qian Zhang[1,2], Yong Wang[1,2,3], Tao Wang[1], Dongsheng Li[1], Jin Xie[1], Hamdi Torun[2], and Yongqing Fu[1,2]
[1]Zhejiang University, CHINA, [2]University of Northumbria, UK, and
[3]Westlake University, Hangzhou, CHINA

09:56 - 10:00

HEAT TRANSFER MECHANISM DUE TO ACOUSTIC BODY FORCE UNDER ACOUSTIC FIELDS

Varun Kumar Rajendran, Mohammed Azharudeen, and Karthick Subramani
Indian Institute of Information Technology, Design and Manufacturing, Kancheepuram, INDIA

10:00 - 10:04

AXIAL DISPLACEMENT OF TYPICAL CELLS WITH 3D TRAPPING IN A HIGH-FREQUENCY SINGLE BEAM ACOUSTICAL TWEEZERS

Zhixiong Gong[1] and Michael Baudoin[1,2]
[1]University of Lille, CNRS, FRANCE and
[2]Institut Universitaire de France, FRANCE

10:04 - 10:08

A NUMERICAL SIMULATION OF PUMPLESS-CHAOTIC MICROMIXER UTILIZING THE VIBRATION-INDUCED FLOW

Kanji Kaneko[1], Naoto Ujikawa[1], Yosuke Hasegawa[2], Takeshi Hayakawa[1], and Hiroaki Suzuki[1]
[1]Chuo University, JAPAN and [2]University of Tokyo, JAPAN

Acoustofluidics
2021
26-27 August 2021
Virtual Conference

Precise particle and cell sorting using high-frequency surface acoustic waves

Ye Ai[1], Peixian Li[1], Jianwei Zhong[1] and Zhichao Ma[1]

[1]Pillar of Engineering Product Development, Singapore University of Technology and Design, Singapore
E-mail: aiye@sutd.edu.sg, URL: https://people.sutd.edu.sg/~ye_ai/

Introduction

Biological samples are heterogeneous in nature. It is essential to identify and sort specific cell populations from highly heterogeneous biological samples for a variety of applications in biology, diagnostics, and medicine. As acoustic waves can easily propagate through solids and fluids, acoustic technique readily enables non-contact cell manipulation in relatively long operating distances. It has been found that acoustic technique has no or minor negative impact on the viability and functionality of biological cells [1], which is a significant advantage compared to existing cell sorting technologies. This abstract presents a few representative particle and cell sorting capabilities using high-frequency surface acoustic waves (SAW) that my team has developed in the past few years. We have further integrated single cell analysis with acoustic manipulation, which has enabled precise and on-demand cell sorting for diverse cell-related applications.

Label-free particle sorting with submicron resolution

We recently demonstrate a tunable acoustofluidic device for continuous particle sorting based on multi-physical properties such as size, density, and speed of sound [2]. Figure 1a shows that a slanted interdigitated transducer (SIDT) propagates a travelling wave along the channel cross-section in the sorting region. Particles exposed to the travelling wave are subjected to a non-linear acoustic radiation force (ARF) that is dependent on the particle size and material properties (e.g., density and speed of sound) [3]. Different from acoustic manipulation using standing waves, the ARF resulted from a travelling wave become non-trivial only when the particle size is larger or comparable to the acoustic wavelength ($\kappa = \pi d/\lambda \geq 1$, in which d is the particle diameter and λ is the acoustic wavelength). As a result, label-free particle sorting based on these intrinsic particle properties can be achieved. Especially when $\kappa \sim 1$, a small change in the particle size down to submicron difference could give rise to a substantial difference in the resultant ARF. Taking advantage of this unique ARF behavior at $\kappa \sim 1$, we have demonstrated the sorting of 5.0 and 5.26 μm polystyrene particles with a size difference down to 260 nm (Figure 1b-1d).

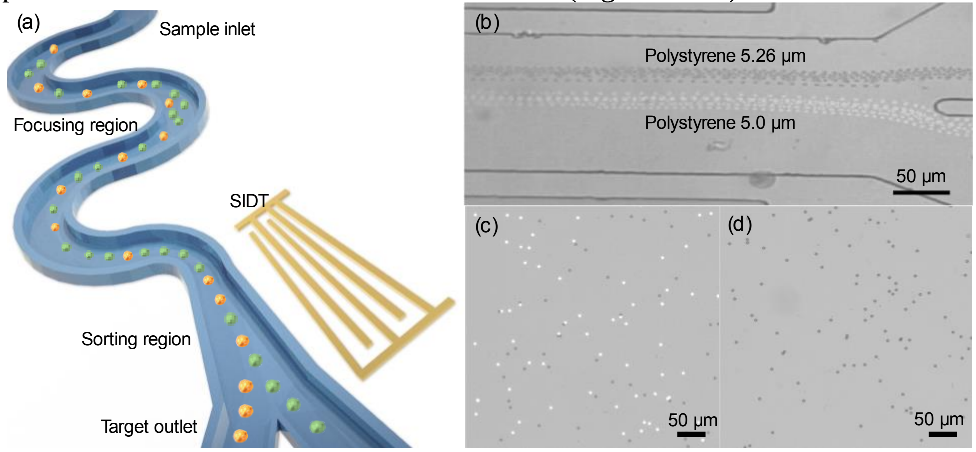

Figure 1: Label-free particle sorting with submicron resolution in a tunable acoustofluidic device. (a) Schematic of the device with a wavy channel for sheathless inertial focusing and a tunable SAW transducer. (b) Separation of 5.0 and 5.26 μm polystyrene particles in a continuous flow. Microscope images of the mixed sample input before sorting (c) and sample from target outlet (d).

Fluorescence activated cell sorting

We have integrated single-cell level fluorescence detection with our acoustic cell manipulation to build up a microfluidic fluorescence activated cell sorting (μFACS) system [4]. Once the fluorescent dye prelabeled on target cells are excited by a laser, the emission light will be detected by a photomultiplier tube (Figure 2a). The single-cell level fluorescence detection will then trigger a focused IDT (FIDT) to generate a highly focused SAW (FSAW) with a beam width comparable to the size of individual cells (i.e., ~25 μm shown in Figure 2b), which laterally displaces the detected single cell for collection. Figure 2c shows the detection and sorting process of a single cancer cell mixed in a diluted whole blood sample. Figure 2d and 2e show that a single sorting process can increase the purity of target cells from about 10% to over 90%. A direct comparison with a commercial aerosol-based FACS reveals that the cell viability drops by 35−45% using a commercial FACS machine, while the cell viability only drops by 3−4% using our μFACS system [5].

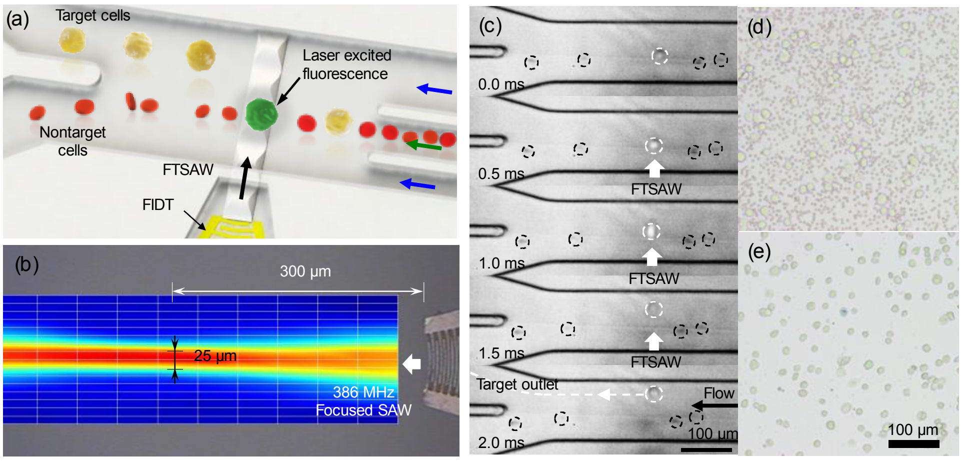

Figure 2: Fluorescence activated cell sorting (FACS) at the single cell level using a highly focused SAW. (a) Working principle of single cell level sorting. (b) A LDV measurement of the focused SAW beam. (c) Sorting of fluorescently prelabeled MCF-7 cells from diluted whole blood sample using our μFACS system. Representative images of input sample (d) and sorted sample collected from target outlet (e).

Biophysical properties activated cell sorting

Biophysical markers of cells such as cellular electrical and mechanical properties have been proven as promising label-free biomarkers for studying, characterizing, and classifying different cell types and their developmental stages. We further integrate biophysical phenotyping with our acoustic single cell manipulation to implement biophysical properties activated cell sorting (Figure 3a). Electrical phenotyping is implemented by single-cell electrical impedance characterization with two pairs of differential sensing electrodes, while mechanical phenotyping is performed by extracting the transit time for the single cell to pass through micro-constriction from the impedance signals. A real-time impedance signal processing and triggering algorithm has been developed to identify the target sample population and activate a pulsed highly focused surface acoustic wave for single-cell level sorting. We have demonstrated highly effective sorting of live MCF-7 cells from fixed cells without any labelling with a purity increase from 37.5% to 91.8% [6].

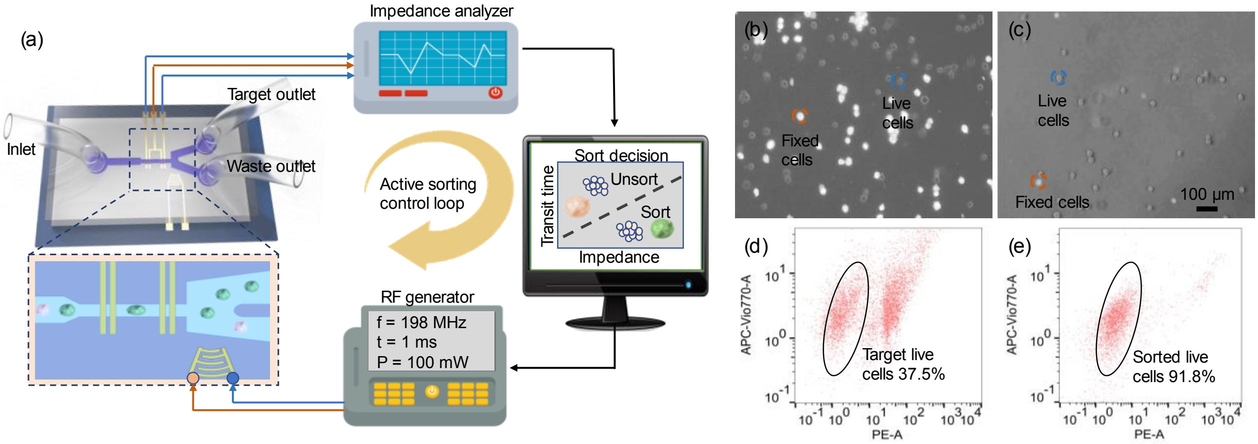

Figure 3: Biophysical properties activated cell sorting. (a) Schematic setup of the acoustofluidic cell sorting system. A mixture of live and fixed MCF-7 cells before (b: microscopic image and d: flow cytometric analysis) and after (c: microscopic image and e: flow cytometric analysis) sorting.

Conclusion

We have demonstrated precise particle and cell manipulation capabilities of our acoustofluidic systems with the use of high-frequency surface acoustic waves. Integration with single-cell analysis further broadens the application of acoustofluidic cell sorting technologies in diverse areas of biology, diagnostics, and medicine.

References

[1] M. Wiklund, A.E. Christakou, M. Ohlin, I. Iranmanesh, T. Frisk, B. Vanherberghen and B. Önfelt. Micromachines **5**, 27–49 (2014).

[2] P.X. Li, J.W. Zhong, N. Liu, X.G. Lu, M.H. Liang and Y. Ai. Sensors and Actuators B: Chemical **344**, 130203 (2021).

[3] F.G. Mitri. Wave Motion **43**, 12–19 (2005).

[4] Z.C. Ma, Y.N. Zhou, D.J. Collins and Y. Ai. Lab on a Chip **17**, 3176–3185 (2017).

[5] P.X. Li, M.H. Liang, X.G. Lu, J.M. Chow, C.J.A. Ramachandra and Y. Ai. Analytical Chemistry **92**, 15425–15435 (2019).

[6] P.X. Li and Y. Ai. Analytical Chemistry **93**, 4108–4117 (2021).

Acoustofluidics
2021
26-27 August 2021
Virtual Conference

Numerical investigation of thin-film transducers for exciting whole-system resonances in bulk acoustofluidics devices

André G. Steckel and Henrik Bruus

Department of Physics, Technical University of Denmark, Kongens Lyngby, Denmark
E-mail: angust@fysik.dtu.dk, URL: https://www.fysik.dtu.dk/microfluidics

Introduction

In bulk acoustofluidic devices, acoustic handling of microparticles and fluids has often been enabled by bulky piezoelectric (PZE) lead-zirconate-titanate (PZT) transducers [1]. We present 3D numerical simulations showing that integrated PZE thin-film transducers, constituting less than 0.1% volume-per-volume (v/v) of the acoustofluidic device, can work equally well in terms of acoustic pressure and particle focusing, when compared to a traditional device driven by a 57% v/v PZT transducer excited at its resonance. Bulk acoustic waves driven by thin-film actuation have been demonstrated in silicon-membrane devices, where the thin-film transducer constitutes 15% v/v of the membrane [2], and hence the acoustofluidics are governed by the membrane modes. The principles for the thin-film-actuated devices presented here, with the 0.1% v/v, differs from bulk-PZT-driven and membrane-driven devices by relying on the following three physical aspects: (1) The accumulation of in-plane expansion of the thin-film transducer along the device surface due to an applied orthogonal electric field, (2) the whole-system acoustic resonances of the entire device, and (3) a high acoustic Q-factor of the material that constitutes the bulk part of the device. Since the PZE thin-film constitutes only a minute part of the system, the device is insensitive to the Q-factor and resonance modes of the thin-film. Further details and animations can be found in our recent paper [3].

Modeling and results

The simulations are performed using a well-tested and experimentally validated numerical model, with thin-film transducers actuating bulk resonances in glass blocks [4], and a conventional bulk-PZT acoustofluidic device [5]. The proof-of-concept system is sketched in Fig. 1: a 1-µm thick thin-film transducer made of $\mathrm{Al_{0.6}Sc_{0.4}N}$ is attached beneath a mm-sized bulk glass chip containing a water-filled straight channel. The resulting acoustic energy density, radiation force, and microparticle focusing time are shown in Fig. 2. The response of the thin-film device is comparable to that of a conventional bulk-PZT-actuated silicon-glass bulk device. Quantitative results are summarized in Table 1.

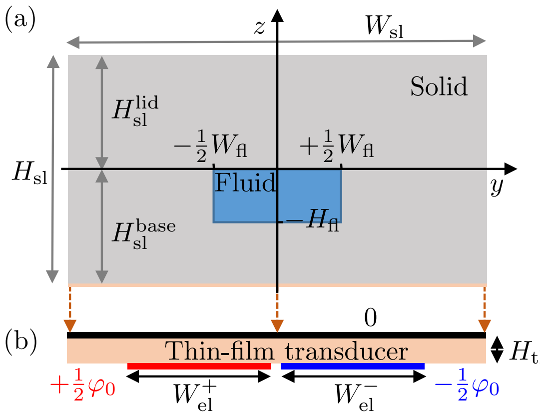

Figure 1: (a) Sketch of the yz-plane cross section of the long, straight thin-film driven device consisting of Schott D263 glass (gray) of width $W_\mathrm{sl} = 3.02$ mm and height $H_\mathrm{sl} = 1.4$ mm, an embedded water-filled microchannel (blue) of width $W_\mathrm{fl} = 0.377$ mm and height $H_\mathrm{fl} = 0.157$ mm, and an attached $\mathrm{Al_{0.6}Sc_{0.4}N}$ thin-film transducer (beige) of width W_sl and small height $H_\mathrm{thf} = 1$ µm $\approx 0.0007\ H_\mathrm{sl}$. (b) A zoom-in on the thin-film transducer (beige) showing its grounded top electrode (black, width W_sl, and potential 0) and split bottom electrode (red "+" and blue "−", width $W_\mathrm{el}^{\pm} = 1$ mm, and potential $\pm\frac{1}{2}\varphi_0 = 0.5$ V), with a 40-µm-wide gap, made to excite the anti-symmetric half-wave-like resonance mode. Adapted from Ref. [3]

Conclusion

Thin-film piezoelectric transducers can actuate bulk acoustofluidic devices through the mechanism of whole-body resonances, cumulative in-plane expansion, and high Q-factor bulk resonators. They are shown to be qualitatively and quantitatively comparable to a traditional bulk-PZT driven device.

Acknowledgments. This work was supported by the BioWings project funded by the European Union's Horizon 2020 Future and Emerging Technologies (FET) program, grant no. 801267.

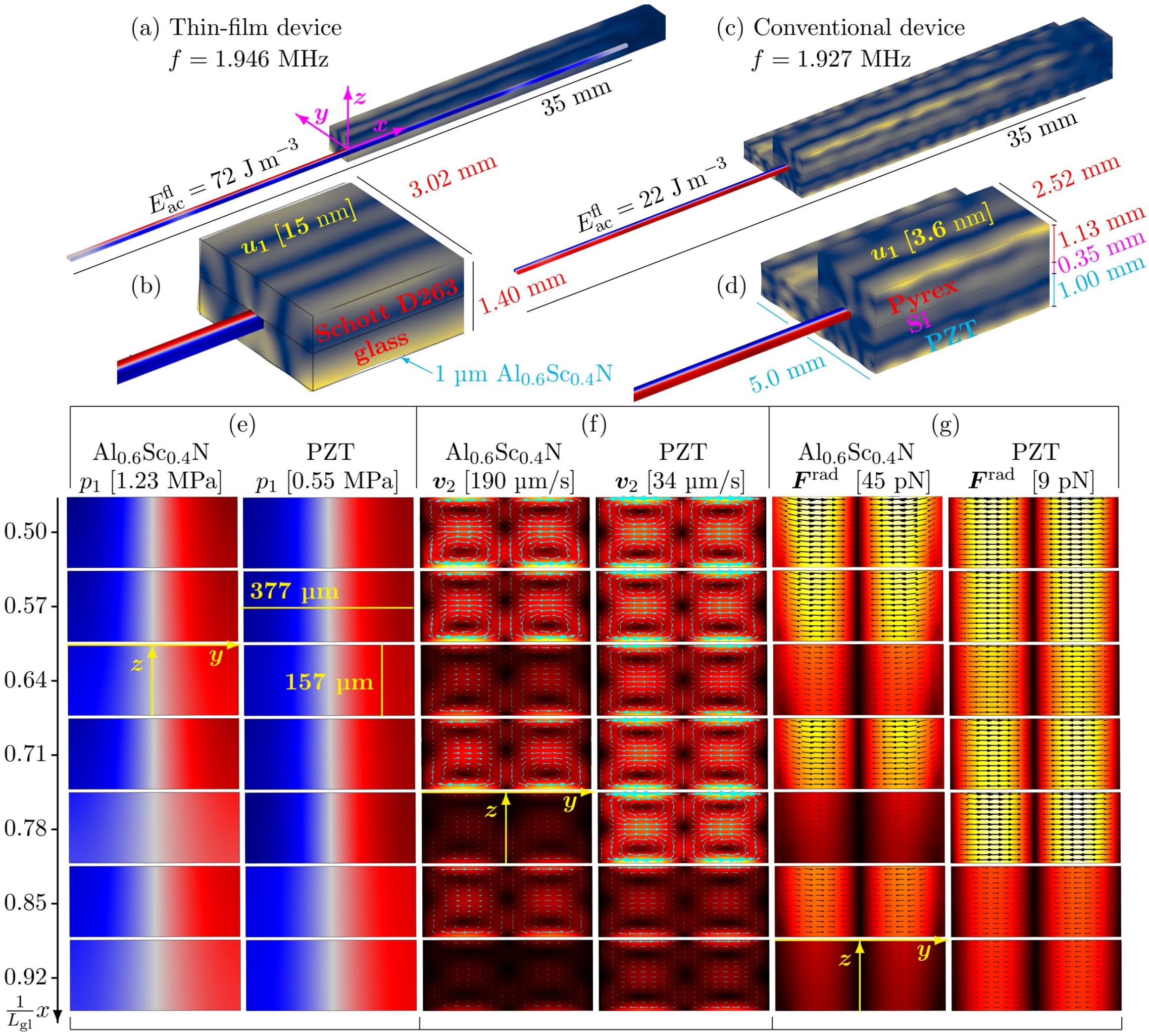

Figure 2: (a,b) A bulk glass chip driven by a 1-µm-thick $\mathrm{Al_{0.6}Sc_{0.4}N}$-thin-film transducer (not visible) actuated at resonance $f = 1.946$ MHz with 1 $\mathrm{V_{pp}}$. The 3D color plots are u_1 from 0 (blue) to 15 nm (yellow) and p_1 from -1.23 MPa (blue) to $+1.23$ MPa (red). (c,d) A conventional Si-glass chip driven by a bulk PZT actuated at resonance $f = 1.927$ MHz with 1 $\mathrm{V_{pp}}$. The color plots are u_1 from 0 (blue) to 3.6 nm (yellow) and p_1 from -0.55 MPa (blue) to $+0.55$ MPa (red). (e) Color plots of p_1 from $-p_{\mathrm{max}}$ (blue, value in the square bracket) to $+p_{\mathrm{max}}$ (red) of the $\mathrm{Al_{0.6}Sc_{0.4}N}$-driven device on the left and the PZT-driven device on the right in seven cross sections from $x/L_{\mathrm{gl}} = 0.5$ to 0.92 in steps of 0.07. (f) Color plots as in panel (e), but for the streaming velocity magnitude v_2 from 0 (black) to v_2^{max} (white, value in the square bracket) and with vectors showing $\boldsymbol{v}_2$. (g) Color and vector plot as in panel (f), but for the magnitude of the radiation force F^{rad} from 0 (black) to $F^{\mathrm{rad}}_{\mathrm{max}}$ (white, value in the square bracket) for suspended 5-µm-diameter polystyrene particles. Adapted from Ref. [3].

Table 1: Quantitative comparison of resonance modes for $\mathrm{Al_{0.6}Sc_{0.4}N}$ thin-film (thf) and Pz26 (bulk) of Fig. 2, as well as for AlN (thf) and Pz26 (thf): the resonance frequency f_{res}, the figure of merit, $R = \int_{V_{\mathrm{fl}}} -\mathrm{sign}(y) F_y^{\mathrm{rad}} \mathrm{d}V / \int_{V_{\mathrm{fl}}} |F_z^{\mathrm{rad}}| \mathrm{d}V$, the average acoustic energy density, $E_{\mathrm{ac}} = \frac{1}{V_{\mathrm{fl}}} \int_{V_{\mathrm{fl}}} \frac{1}{4}\big[\kappa_{\mathrm{fl}}|p_1|^2 + \rho_{\mathrm{fl}}|\boldsymbol{v}_1^{\mathrm{fl}}|^2\big] \mathrm{d}V$, and average time t_{foc} to focus 5-µm-diameter polystyrene particles to $|y| < 20$ µm.

Response	AlN thf	$\mathrm{Al_{0.6}Sc_{0.4}N}$ thf	Pz26 thf	Pz26 bulk
f_{res} [MHz]	1.948	1.946	1.942	1.927
R [-]	6.7	7.1	8.5	22.7
$E_{\mathrm{ac}}^{\mathrm{fl}}$ [$\mathrm{J\,m^{-3}}$]	7.3	72	2.1×10^3	22
t_{foc} [s]	5.4	0.52	0.016	1.73
$E_{\mathrm{ac}}^{\mathrm{fl}} t_{\mathrm{foc}}$ [$\mathrm{J\,s\,m^{-3}}$]	39.4	37.4	34.2	38.1
$E_{\mathrm{ac}}^{\mathrm{fl}}/e_{31,f}^2$ [$\mathrm{m\,F^{-1}}$]	7.0	10.3	9.9	–

References

[1] P. B. Muller *et al.*, Phys. Rev. E **88**, 023006 (2013). [pdf]

[2] P. Reichert, D. Deshmukh, L. Lebovitz, and J. Dual, Lab Chip **18**, 3655 (2018). [doi]

[3] A. G. Steckel, H. Bruus, J. Acoust. Soc. Am. **150**, 634 (2021). [pdf]

[4] A. G. Steckel, H. Bruus, P. Muralt, and R. Matloub, Phys. Rev. Appl. **16**, 1014014 (2021). [pdf]

[5] N. R. Skov, J. S. Bach, B. G. Winckelmann, and H Bruus. AIMS Mathematics, **4**, 99 (2019). [pdf]

Acoustofluidics 2021
26-27 August 2021
Virtual Conference

Improving acoustic energy conversion efficiency in bulk wave acoustophoresis devices by side actuation

Wei Qiu[1], Thierry Baasch[1], Lei Jiang[1], and Thomas Laurell[1]

[1]Department of Biomedical Engineering, Lund University, Lund, Sweden
E-mail: wei.qiu@bme.lth.se, http://bme.lth.se/research-pages/nanobiotechnology-and-lab-on-a-chip/

Introduction

The acoustic energy density is an essential parameter for acoustophoresis devices, which determines the magnitude of the acoustic radiation force and hence the device throughput. To date, the most typical way to achieve high energy density in the microchannel is to apply high electric power to the piezoelectric transducer, which is far from ideal in terms of energy conversion efficiency and heat generation. Recent studies have demonstrated that the energy density can be improved by breaking the actuation symmetry [1,2]. In this work we show, experimentally and numerically, that the energy density of acoustophoresis devices can be enhanced by a factor of four under the same input power by mounting the piezoelectric transducer to the side of the chip, leading to higher acoustic energy conversion efficiency compared to conventional bottom actuation devices.

Materials and methods

Nine glass chips with the same outer and channel dimensions were used to compare the chip performance under different actuation modes. Lead zirconate titanate (PZT) transducers with a length of 25 mm and a thickness of 1 mm were glued either underneath or to the side of the chip, which led to a total of three configurations under test, see Fig. 1. Two configurations, one actuated from the bottom and one actuated from the side, used the PZT with the same width (5 mm). In the third configuration, a PZT transducer with a smaller width (2 mm) was used, providing a similar ratio of the contact area between the transducer and the chip in bottom and side actuation modes. Three chips were tested for each configuration to improve the statistics.

The resonance frequency of each chip was found by flowing 4.9 µm-diameter polystyrene particles in milli-Q through the channel while the sound field was turned on and the normalized particle focusing bandwidth $\tilde{B} = \mathrm{FWHM}/W$ was measured, where FWHM and W are the full width at half maxima of the particle intensity profile and the channel width, respectively. The chip performance was first qualitatively compared by measuring $\tilde{B}$ under four different combinations of flow rate Q and input power P_in. The energy density E_ac was quantitatively investigated within the whole actuation zone for bottom actuation and side actuation with a small PZT transducer at $P_\mathrm{in} = 25\,\mathrm{mW}$ under the stop-flow condition by measuring the amplitude of particle focusing velocity using confocal micro-particle image velocimetry (PIV) [3]. Finally, the impact of the chip aspect ratio $\alpha = H_\mathrm{chip}/W_\mathrm{chip}$ on E_ac was investigated numerically by a 2D finite-element parametric study for both bottom and side actuations.

Results and discussion

The chip performance using different actuation modes is compared qualitatively by free-flow focusing measurements, shown in Fig. 2. It is found that the $\tilde{B}$ is smaller under side actuation compared to the

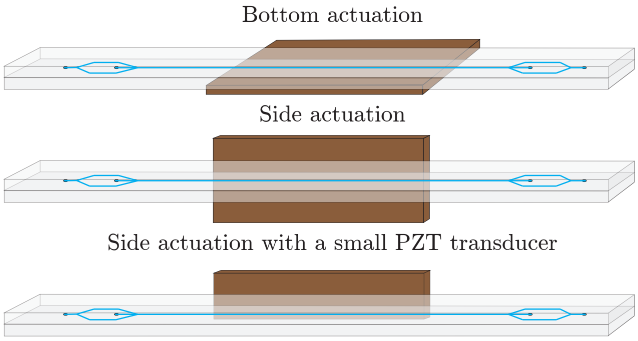

Figure 1: Sketch of the acoustophoresis glass chips (light gray) with a dimension of 70 × 3 × 1.1 mm^3. The long-straight microchannel (light blue) has a dimension of 45 × 0.375 × 0.15 mm^3. The PZT transducer (brown) was mounted either to the bottom or to the side of the chip. The PZT transducers in the top two configurations have a dimension of 25 × 5 × 1 mm^3, while the PZT transducer in the lower configuration has a dimension of 25 × 2 × 1 mm^3.

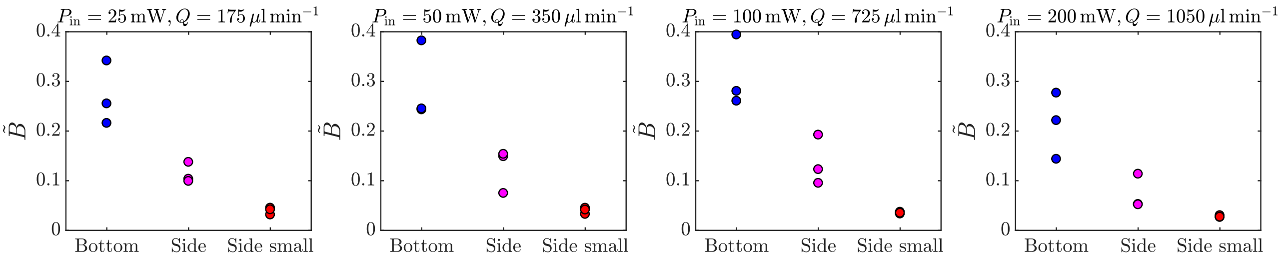

Figure 2: Qualitative comparison of chip performance using bottom (blue) and side (pink) actuations, and side actuation with a small PZT transducer (red) under four different conditions, indicated by the normalized particle focusing bandwidth $\tilde{B}$. Three chips were tested under each actuation mode.

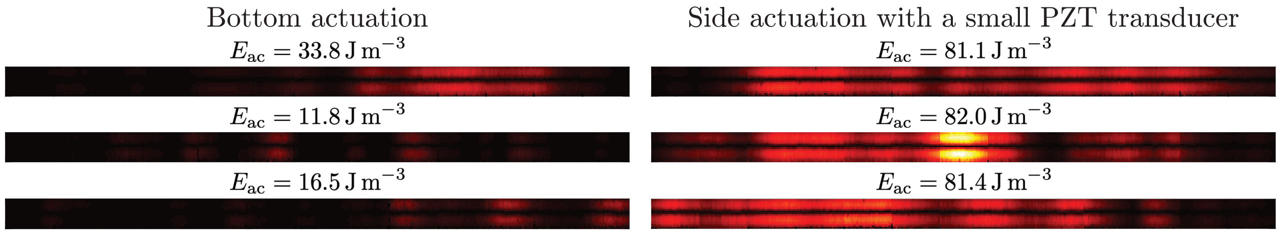

Figure 3: Confocal micro-PIV measurements of averaged energy density $E_{\rm ac}$ under bottom actuation and side actuation using small PZT transducers with 25 mW input power $P_{\rm in}$ along the 25 mm-long region where the PZT transducer locates. The color plot shows the particle focusing velocity from 0 (black) to 2.1 mm s^{-1} (white). The width dimension is expanded by a factor of three for better visibility.

bottom actuation, which indicates a higher $E_{\rm ac}$ is achieved using side actuation. Comparing the two side actuation setups, the chips with the smaller PZT transducers outperform those with the larger transducers. The side actuation with the small PZT transducers led to a four-fold increase in averaged $E_{\rm ac}$ with respect to the traditional bottom actuation devices, measured using confocal micro-PIV as shown in Fig. 3. One distinct difference between the two actuation modes is that with side actuation the hotspots (the regions with relatively high local $E_{\rm ac}$) appear in an extended region matching the transducer mounting, while the hotspots are confined in small local regions with bottom actuation.

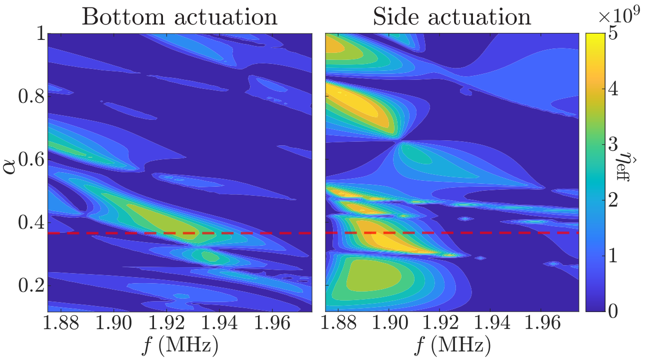

Figure 4: Parametric study of the efficiency parameter $\hat{\eta}_{\rm eff}$ at a wide range of chip aspect ratio α ($0.12 < \alpha < 1$) under bottom and side actuations. The red dashed lines indicate the α used in experiments.

We define a dimensionless efficiency parameter $\hat{\eta}_{\rm eff} = \omega E_{\rm ac} V_{\rm I}/P_{\rm in}$, which indicates the energy conversion efficiency from electric power to the acoustic power in the channel, where ω and $V_{\rm I}$ are the angular frequency and unit volume. It is found from numerical simulation that for most of the α within the range under investigation ($0.12 < \alpha < 1$), including the α used in the experiments ($\alpha = 0.37$), the $\hat{\eta}_{\rm eff}$ is higher with side actuation, see Fig. 4. Furthermore, it is easier to obtain high $\hat{\eta}_{\rm eff}$ using side actuation compared to bottom actuation, indicated by the larger area of high $\hat{\eta}_{\rm eff}$ under side actuation shown in Fig. 4. The results clearly show that side actuation in general leads to a higher energy conversion efficiency compared to bottom actuation at the α with experimental relevance.

Conclusion

In this work, we experimentally and numerically demonstrated that side actuation is able to enhance the acoustic energy density and the energy conversion efficiency of acoustophoresis devices. More details regarding the chip vibration modes under different actuation methods as well as the submicrometer particle focusing using side actuation will be provided in the conference.

References

[1] M. Bora and M. Shusteff. Lab Chip **15**, 3192-3202 (2015).
[2] A. Tahmasebipour, L. Friedrich, M. Begley, H. Bruus, and C. Meinhart. J. Acoust. Soc. Am. **148**, 359-373 (2020).
[3] P. Augustsson, R. Barnkob, S. T. Wereley, H. Bruus, and T. Laurell. Lab Chip **11**, 4152-4164 (2011).

Acoustofluidics 2021
26-27 August 2021
Virtual Conference

High throughput multinodal acoustic trapping of extracellular vesicles for downstream mass spectrometry analysis

Axel Broman[1], Lotta Happonen[2], Frida Palm[2], Oonagh Shannon[2], Andreas Lenshof[1], Johan Malmström[2] and Thomas Laurell[1]

[1]Lund University, Faculty of Engineering, Department of Biomedical Engineering, Sweden
E-mail: axel.broman@bme.lth.se
[2]Lund University, Faculty of Medicine, Department of Clinical Sciences, Infection Medicine, Sweden

Introduction

We report the use of a multinodal acoustic trap for high throughput isolation of extracellular vesicles (EVs) and subsequent quantitative mass spectrometry analysis. The multinode acoustic trap, operated at 500 µl/min, was able to isolate sufficient amounts of EVs from dilute biological samples (cell culture supernatant and urine) within minutes, enabling proteome profiling by means of mass spectrometry. This was demonstrated by differential protein expression analysis of the isolated urinary EVs and the original urine sample. Additionally, differential protein profiling of EVs from stimulated and non-stimulated platelets demonstrated an easy access to differential expression in the EV proteome.

Background

In acoustic trapping, a transducer generates a standing ultrasonic wave inside a fluidic channel. Particles that are denser and less compressible than their surrounding medium can be captured in the pressure nodes of the wave and be retained against a flow. This allows for isolation, enrichment and washing of the particles. Hammarström [1] showed that it if the trap was pre-loaded with large seed-particles, it was possible to capture nanoparticles by scattered sound particle interaction. Our device (Figure 1) is actuated at a multinode resonance, creating nine pressure nodes where particles can be retained and allowing higher throughput. Polystyrene particles (12 µm) were used as seed particles.

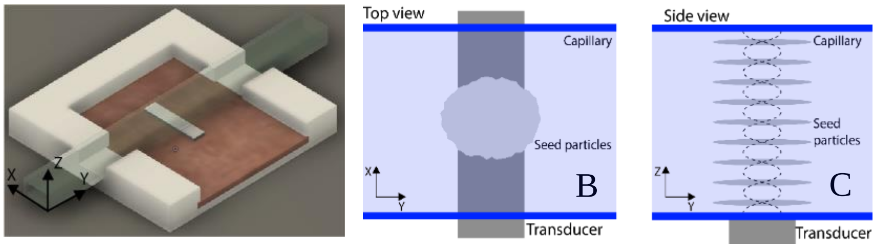

Figure 1: A) Schematic rendering of the acoustic trapping device. A glass capillary is mounted to a transducer which generates an ultrasonic standing wave. B) Illustration of a trapped seed particle cluster, viewed from above. C) Illustration of the standing wave inside the channel, viewed from the side. Nine pressure nodes can be seen stacked vertically above the transducer.

Experimental

A urine sample collected from a healthy donor was centrifuged at 2000 g for 10 minutes to remove cells and cellular debris. EVs from varying volumes of urine (1, 2 or 3 ml) were then trapped at 500 µl/min. Following a wash, the trapped clusters were released in a volume of 250 µl. The EVs in the trapped samples, along with non-trapped urine controls were lysed in a Bioruptor Plus (Diagenode). In addition to urine, EVs from human platelets were also trapped. The proteins in the samples were prepared for quantitative data independent acquisition mass spectrometry (DIA-MS) using trypsin digestion. The peptide concentration was measured and 0.5 µg was injected for urine and 1 µg for platelet vesicles per sample. The samples were analyzed on a Q Exactive HF-X (Thermo). The platelets were exposed to a non-stimulant (hepes-buffer) and 2 stimulants (human thrombin and the M1 protein, a bacterial virulence factor). The subsequently released EVs were then collected by centrifugating the platelets and collecting the supernatant. The samples, along with non-trapped controls, were then processed using the same protocol as for urine.

Results and discussion

The MS analysis generated in total 413 proteins from urine, quantified using label-free quantification. Clustering based on signal intensities of the identified proteins revealed a clear difference in the samples as shown in the protein heatmap in Figure 2. There are two main clusters (I & II) where a clear difference between trapped and non-trapped samples can be seen. In contrast, there are only minor differences when trapping different volumes of urine, which is expected since the same amount of peptide was injected throughout the sample series.

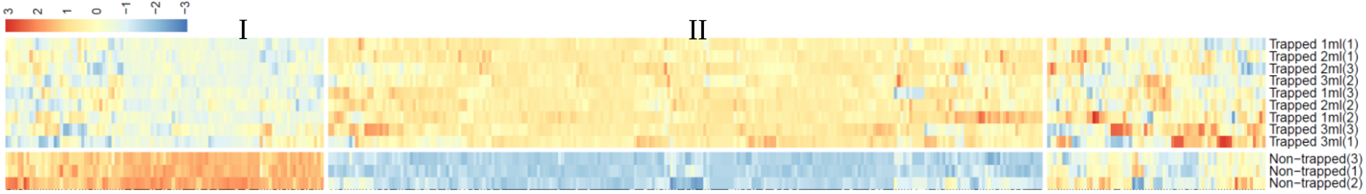

Figure 2: Protein heatmap from the urine samples. Each row corresponds to a different sample and each column represents an identified protein. The heatmap is column-normalized and the legend gives the z-score of each sample. Cluster I shows weaker protein signal in the trapped fraction, suggesting that these proteins were washed away during the washing step. Cluster II shows stronger protein signal in the trapped fraction, suggesting that these proteins are associated with EVs and are being enriched during the trapping step.

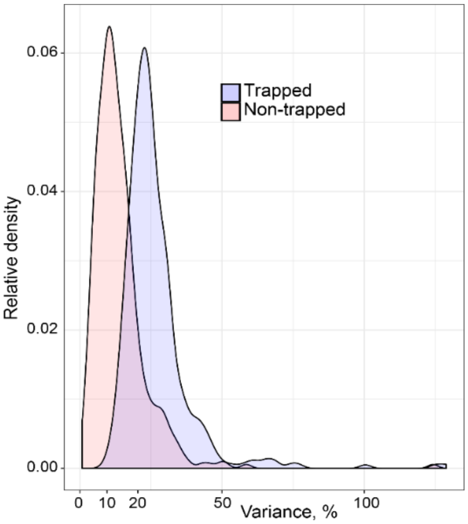

Figure 3: Variance of the trapped and non-trapped samples.

The trapping procedure did not cause large variations in the sample as can be seen by the relative protein intensity variance in trapped vs non-trapped samples, Figure 3. The trapped samples had an average variance of around 20%, compared to around 10% for non-trapped samples.

For the platelet vesicle samples, the MS analysis generated 366 proteins. The clustered proteins can be seen in Figure 4. Similar to the urine samples, there are protein clusters where the signal is stronger in the trapped samples and protein clusters where it is weaker. This can be explained by proteins that are associated with EVs being enriched in the trap, generating a stronger signal, while proteins that are not associated with EVs would be washed away during the washing step, generating a weaker signal.

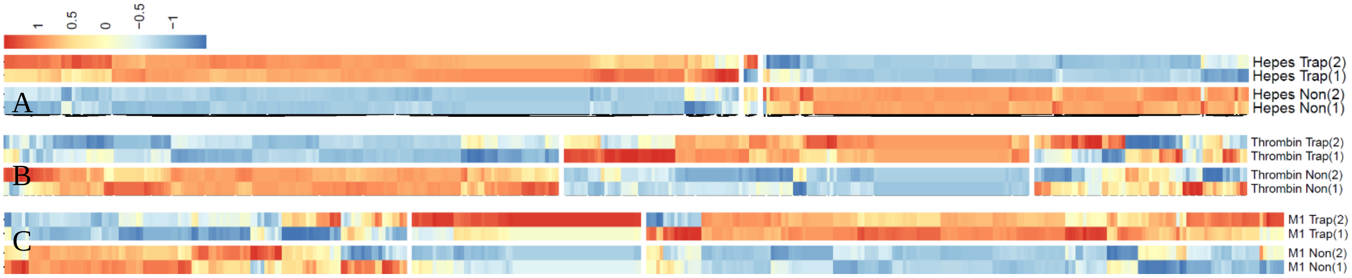

Figure 4: Protein heatmaps of EVs from human platelets stimulated by A) hepes-buffer, B) human thrombin or C) the M1 protein. For each individual stimulant, there are protein clusters which show clear differences between the trapped and non-trapped fractions. This indicates that certain proteins are washed away while other proteins are being enriched in the trap.

Conclusion

The multinodal acoustic trapping unit was able to rapidly capture EVs from milliliter volumes of dilute samples and provide sufficient material for downstream proteomic DIA-MS analyses.

References

1. B. Hammarström et al. *Lab chip*, 2012, **12**, 4296-43

Acoustofluidics 2021
26-27 August 2021
Virtual Conference

Surface acoustic wave manipulation of 100 femtoliter droplets in nanochannels

Naiqing Zhang[1], Amihai Horesh[1], and James Friend[1]

[1]Medically Advanced Devices Lab, Center for Medical Devices, Department of Mechanical and Aerospace Engineering, Jacobs School of Engineering and Department of Surgery, School of Medicine, 9500 Gilman Dr. MC0411, University of California San Diego, La Jolla, CA 92093, USA
E-mail: jfriend@ucsd.edu, URL: http://friend.ucsd.edu

Introduction

The use of MHz-order vibration has dramatically expanded in microfluidics [1], enabling fluid manipulation, atomization, and particle/cell separation. However, so far there has been few works reporting similar phenomena at the nanoscale, even though nanofluidics is potentially useful for biological analysis and sensing [2], medical diagnosis [3], and material processing [4]. The analytical devices devised to work at such small scales employ nanoliter to picoliter fluid volumes, surface area-to-volume ratios of ~ 10^7/m and more, and, ideally, the fluid volumes would be made even smaller to improve these devices' performance.

Controllable manipulation and effective mixing of fluids and colloids at the nanoscale is made exceptionally difficult by the dominance of surface and viscous forces. A variety of methods that employ carbon nanotubes have been proposed, using temperature gradients [5], Coulomb drag [6], surface waves (in theory) [7], or static electric fields [8]. Passive fL-scale fluid handling has also been devised using surface modification or geometric channel design [9, 10]. However, despite all these attempts, no effective active manipulation method has been experimentally demonstrated in a nanoscale enclosed fluidic channel system to date to our knowledge, save for two examples. Surface acoustic waves (SAW) have ben used to manipulate channel-confined fluids and suspended nanoparticles and molecules [11], and it turns out that a new mechanism of acoustic wave-fluid motion interaction [12]—*acoustogeometric streaming*—is responsible and is in fact much more powerful than classic acoustic streaming.

Concept and Method

Here, we present active 200-fL fluid droplet manipulation using MHz-order SAW within high-aspect ratio, 100-nm tall, 20–130-μm wide, 5-mm long nanoslit channels, fabricated via a direct, room-temperature bonding method [13] for lithium niobate (LN) as illustrated in Fig. 1. The undulating shape of wide traps connected by narrow necks was intentionally chosen to trap droplets in discrete locations and facilitate their manipulation among these traps. Contrary to the results seen in the past[11], a droplet will locate at a point where its surface energy is lower, the wider region of the trap in our system. The dimensions of the traps were chosen to entrap 200-fL droplets, which are 50 μm in diameter in a 100-nm tall channel. The radius of curvature of each of the four walls that form the trap was 60 μm, slightly larger than the trapped droplet, to ensure its central location while maintaining separation between the wall and fluid. The curvature of this shape was chosen to eliminate corners that could capture and trap droplets. These walls naturally lead to another trap via extension of one of the vertices of the trap to form a "neck" between them. The width of the neck was chosen to be 20 μm, less than half the diameter of the 200-fL droplets but large enough to reliably fabricate in our process. Feature sizes of 2 μm may be fabricated, but the yield is better when choosing feature sizes greater than about 10 μm.

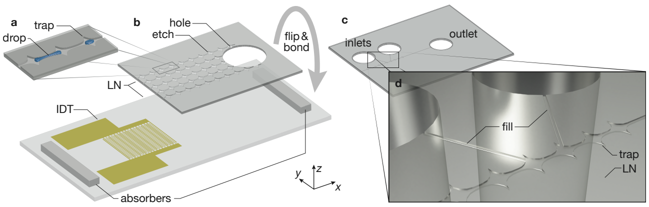

Figure 1: SAW-integrated nanofluidic femtoliter droplet devices. (a) A nonuniform nanoslit channel produces fluid droplet traps. (b,c) By etching several of these channels into a LN layer, cutting a 1 mm hole at the end distant from the SAW interdigital transducer (IDT), and then flipping the result and bonding it with room-temperature LN-LN bonding [13], machined-side down, onto the LN substrate that has the SAW IDT, it is possible to form and transport drops in these channels with heights to less than 10 nm (figures not to scale for clarity). However, ~ 100 nm height was chosen to obtain the best possible performance of the acoustic wave propagation in the nanoslit using acoustogeometric streaming [12].

Results

It is possible to induce ~200-fL droplet splitting and transport, phenomena that are governed by the time and power of the SAW actuation for a given fluid. We provide a closed-form analytical model that accurately describes the boundaries between these handling phenomena. We also report the ability to induce merging and mixing in a ~200-fL droplet, operations desirable in fluid handling whatever the scale. As an exploratory work, we set aside the issue of evaporation, actually exploiting it in forming droplets for this study. Evaporation is nonetheless an important constraint in droplet nanofluidics, more so than in droplet-based digital microfluidics, and the methods to overcome it at the microscale [14, 15] may prove beneficial at the nanoscale. Altogether, our results indicate MHz-order SAW is a powerful tool for discrete fluid droplet manipulation at the nanoscale.

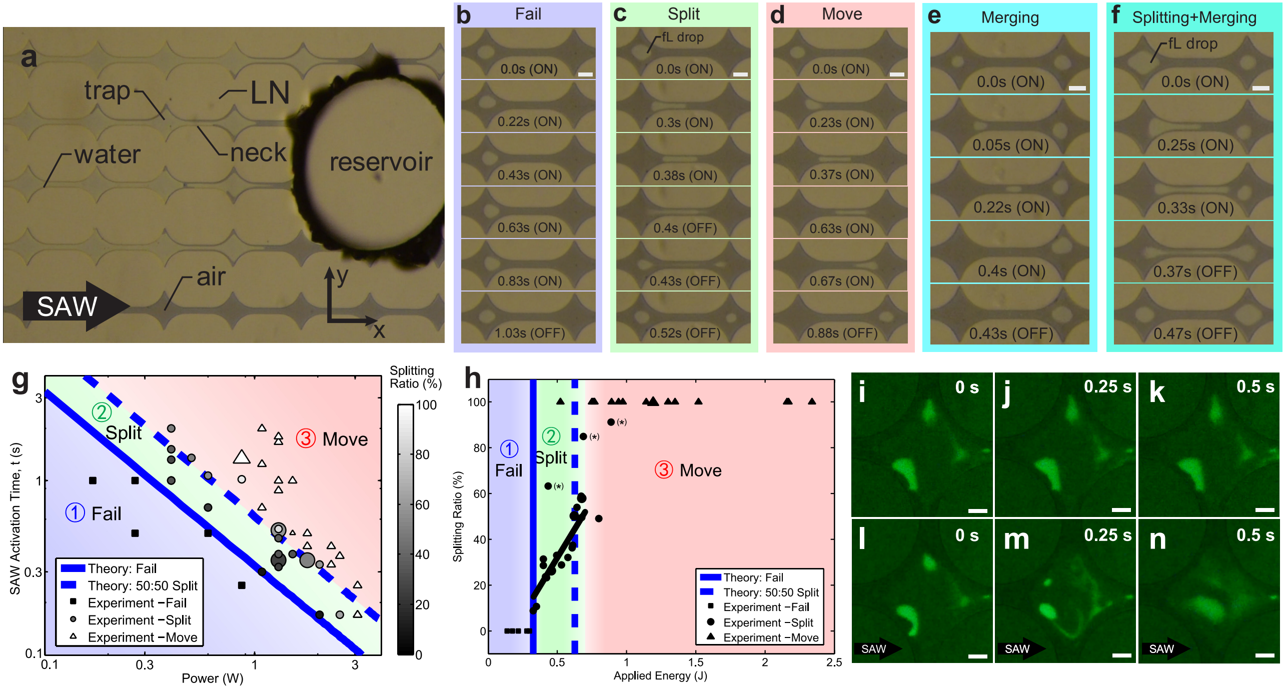

Figure 2: (a) The 100 nm height nanochannel matrix, with traps as shown separated by narrow regions, or *necks*. The channels are filled with DI water from the reservoir at right. SAW-driven evaporation slowly eliminates the water from the nanochannels over a period of about one minute. The experiment begins when the droplet diameter is 50 μm, corresponding to a volume of 200 fL. For scale, the narrowest width of the neck halfway between the traps is 20 μm and the trap is 130 μm at its widest in *all* figures in this study. The dark areas indicate trapped air and light areas are entrapped water. The direction of the SAW is from left to right. With judicious filling and evaporation, it is possible to form (b) a single droplet within a trap. After applying SAW, the (b-d) image sequences indicate three possible outcomes. Application of 270 mW SAW at 40 MHz for an activation time of 1.03 s (b) fails to propel a 200 fL droplet from one trap to the next. Capillary force overcomes the propulsive acoustic force. If, however, the SAW power is greater at 1.3 W for only 0.38 s, the droplet will (c) split. The droplet becomes trapped in the neck and a portion escapes to the next trap and the remainder returns to the original trap. With a longer SAW activation time of 0.67 s at the same power of 1.3 W, the SAW (d) completely moves the droplet to the next trap. (e) Merging of droplets using 1.78 W for 0.42 s is made possible, as is (f) splitting and merging using SAW for 0.35 s at the same power. Scale bars: 40 μm. Generally, there are three regimes (g,h) for a single droplet, and theory based upon an energy balance corresponds closely with the experimental results. Remarkably, by introducing 50 nm fluorescent polystyrene particles into the system, mixing is very slow (i–k) without SAW, but (l–n) completes in less than one second with SAW.

Conclusion

We have developed a simple technique for femtoliter droplet manipulation and mixing in a nanofluidic system using 40 MHz SAW. For the presentation, we will explain the details of the theoretical model that predicts the droplet manipulation phenomena, and will show our latest results on very high speed femtoliter droplet manipulation and fluid pumping due to acoustogeometric streaming. We are grateful to the Office of Naval Research (via grant 12368098) and the W.M. Keck Foundation for funding provided to J. Friend in support of this work.

References

1. Connacher, W. et al. *Lab Chip* **18,** 1952–1996 (14 2018). 2. Wang, C. et al. *Analytical and Bioanalytical Chemistry,* 1–10 (2019). 3. Jackson, T. C. et al. *Advances in Nanoparticles* **6,** 93 (2017). 4. Gao, J. et al. *Chemical Society Reviews* **46,** 5400–5424 (2017). 5. Liu, Z. et al. *The Journal of Physical Chemistry C* **125,** 898–907 (2020). 6. Wang, B. et al. *Journal of the American Chemical Society* **128,** 15984–15985 (2006). 7. Insepov, Z. et al. *Nano Letters* **6,** 1893–1895 (2006). 8. Zhang, Y. et al. *Nature Communications* **7,** 1–7 (2016). 9. Nakao, T. et al. *Analyst* **145,** 2669–2675 (2020). 10. Mawatari, K. et al. *Analytical Chemistry* **84,** 10812–10816 (2012). 11. Miansari, M. et al. *Advanced Functional Materials* **26,** 7861–7872 (2016). 12. Zhang, N. et al. *Physical Review Letters,* (in revision). 13. Zhang, N. et al. *JoVE (Journal of Visualized Experiments),* e60648 (2020). 14. Chatterjee, D. et al. *Lab on a Chip* **6,** 199–206 (2006). 15. Jebrail, M. J. et al. 20200324290A1 (2016).

Acoustofluidics 2021
26-27 August 2021
Virtual Conference

Phase contrast microscopy characterization of standing surface acoustic waves for microfluidic applications

Pierre Thibault, Ianis Bernard, and Philippe Marmottant

Université Grenoble-Alpes, CNRS, LIPhy, F-38000, France
E-mail: pierre.thibault@univ-grenoble-alpes.fr

Introduction

The development of microfluidic systems utilizing standing surface acoustic waves (SSAW) to manipulate fluids and particles requires an advanced control of acoustic fields. In practice, these fields depend both on the precise mechanism of the leakage of the waves into the liquid and on the fluid volume itself, regarding its dimensions and constitutive materials. Many numerical works have recently addressed this issue, either to predict acoustophoretic motions [1], or to account for heating effects associated [2] to acoustic energy dissipation. We show in the following that a standard phase contrast microscopy can be of valuable help for the *in-situ* characterization of such complex geometries.

Principle

In a paper of 1934, soon after its first phase contrast photomicrograph of a diatom of 1932, F. Zernike [3] explained how his method could advantageously help visualizing, with an optimal contrast, small phase changes induced by density variations, as compared to the knife-edge based Schlieren techniques dating back from Foucault in 1856. At the same period, Raman and Nath [4] have shown that the an acoustic wave leading to a periodic variation of a fluid refractive index $n - n_0$ also constitutes a phase-object provided the phase change is large enough along the path of light, while staying small to limit its deviation. Under such conditions, the optical images of bulk acoustic waves [5] were experimentally d found to be roughly proportional to the square of the pressure field. As a consequence, one may expect to access a quantity directly related to Gorkov's acoustic potential, and not indirectly as inferred from acoustophoretic techniques.

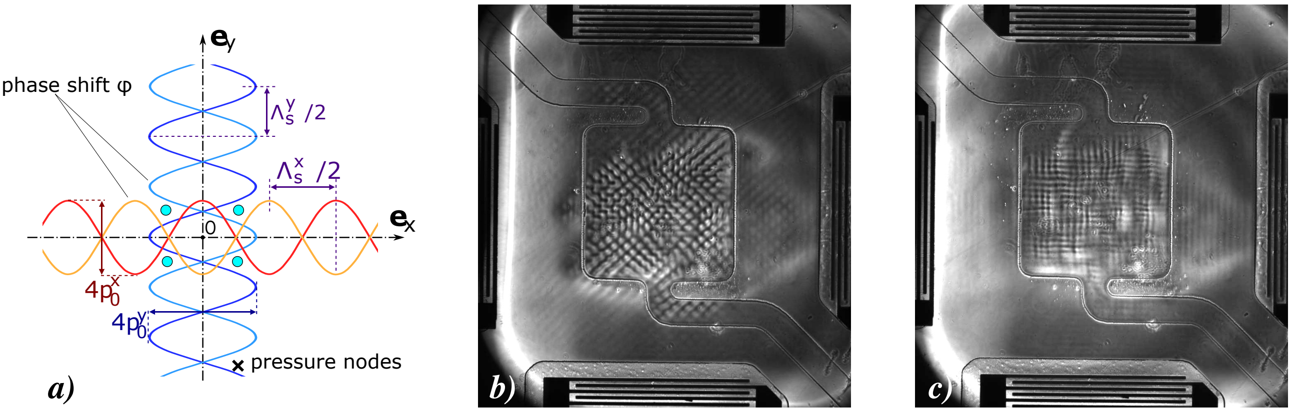

Figure 1: (a) 2D scheme of the superposition of two orthogonal SSAWs with a phase shift ϕ generated from a $LiNbO_3$ substrate. Circles correspond to pressure nodes. (b),(c) Phase contrast microscope images of a microchannel filled with water when the two perp. SAWs are emitted, with ϕ=0 (b) or ϕ=π/2 (c).

Materials and methods

The principle was tested on a previous device [6] used to study the acoustic torque that exists when two orthogonal SSAW with a time phase lag (phase shift ϕ) are simultaneously emitted [7,8]. It consists in a X-cut $LiNbO_3$ wafer assembled to a PDMS cavity (1 mm×1 mm× 150 µm) into which the fluid is introduced. SSAWs are generated from four interdigitated structures arranged in a cross geometry and excited at a same frequency of about 37 MHz (see Fig. 1a). Due to the sound velocity anisotropy of the $LiNbO_3$, the pitches of the IDTs pairs along $\mathbf{e_x}$ (crystal Y-axis) and $\mathbf{e_y}$ (crystal Z-axis) were made to be 100.0 µm and 94.5 µm. The top part of the acoustic cavity was made of a glass coverslip to create a high acoustic impedance interface. Images are obtained using a commercial Olympus IX70 Phase contrast Microscope with the microfluidic setup resting on a transparent PMMA plate.

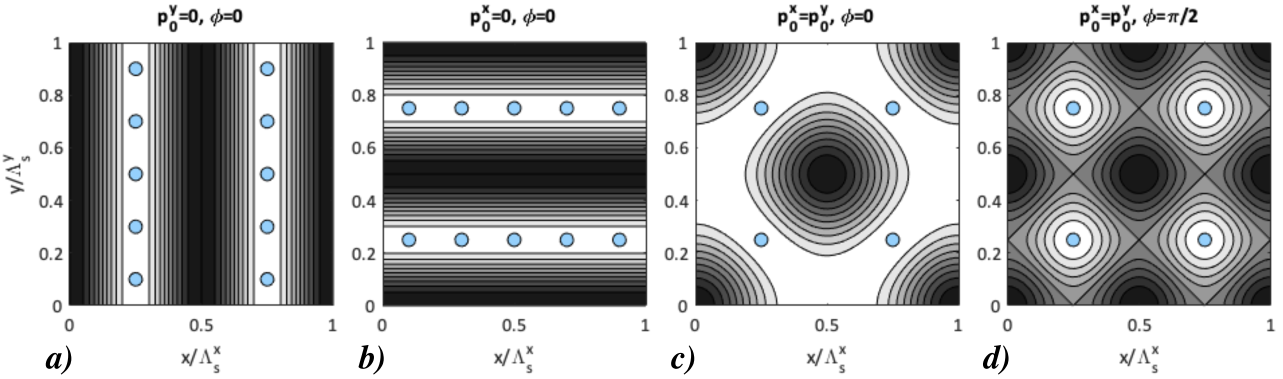

Figure 2: 2D computed time average of squared pressure field in a unit cell of dimension $\Lambda_s^x \times \Lambda_s^x$. Circles show pressure nodes of Gor'kov potential for neutrally buoyant hard particles ($f_1 >> f_2$). 1D standing wave along x (a) or y directions (b). (c) and (d) 2D acoustic field considering equal pressure amplitudes in the two directions, and either ϕ=0 (c) or $\phi = \pi/2$ (d).

Results and interpretation

Fig.1b and c show images recorded in transmission mode a few seconds after an approx. 90 V voltage has been applied on the IDT pairs, with different phase shifts ϕ, leading to a pressure field of the form $\underline{p}_1(x,y,t) = 2p_0^x \cos(k_s^x x)e^{-i\omega t} + 2p_0^y \cos(k_s^y y)e^{-i(\omega t+\phi)}$ with p_0^i the pressure amplitudes and k_s^i the wave vectors in the x and y directions. We observe periodic modulations originating from the microfluid cavity with an uneven intensity possibly caused by acoustic streaming. When $\varphi = 0 \pm \pi$ (or when the frequencies in the two directions differ), a diamond like lattice of period $\Lambda_s^x \times \Lambda_s^y$ is visible, while when $\varphi \sim \pm\pi/2$, we observe a square lattice with a half wavelength period. Interestingly, we also observe similar but steady patterns originating from the PDMS that surrounds the microfluidic cavity. (Note that voids have been left onto the IDTs to prevent excessive direct acoustic attenuation).

Considering the high electrical power involved in these experiments, it appears that the major contribution to the modification of the refractive index is of thermal origin, even leading to the boiling of the fluid if the excitation time exceeded typically one minute and possibly causing permanent damages to PDMS. Now, a comparison between phase contrast images of Fig.1 and numerical simulations of Fig.2 suggests that the quantity accessed by the phase contrast microscope is indeed related to $\langle p_1^2 \rangle$. Since this is the leading term of Gorkov's acoustic potential for neutrally buoyant particles, this would explain why when adding 3μm polystyrene microbeads to the liquid they accumulate in the white regions corresponding to pressure nodes of the acoustic potential, as sketch by the blue disks on Fig.2.

Conclusion

We have shown for the first time that one can take benefit of phase contrast microscopy images to characterize the acoustic field produced by SSAWs. In this preliminary work involving high acoustic energy densities, it was found that thermal contributions were essentially responsible for the change of refractive index. Now, considering the 3D nature of the actual acoustic field in such microfluidic device, these results would benefit from further numerical insights as performed in [2], but possibly considering non isothermal conditions at the $LiNbO_3$ surface where viscous effects are dominant.

References

[1] N. Nama, R. Barnkob, Z. Mao, C. J. Kähler, F. Costanzo, and T. J. Huang. Lab on a Chip, **15**(12):2700–2709, (2015).
[2] P. K. Das, A. D. Snider, and V. R. Bhethanabotla. *Physics of Fluids*, **31**(10), (2019).
[3] F. Zernike. Monthly Notices of the Royal Astronomical Society, **94**:377–384, (1934).
[4] C. Raman and N. Nagendra Nath. Proc. Indian Acad. Sciences, Section A, vol. 2, pages 406–412 (1935).
[5] P. A. Chinnery, V. F. Humphrey, and C. Beckett. J.A.S.A, **101**(1):250–256 (1997).
[6] I. Bernard, A. A. Doinikov, P. Marmottant, D. Rabaud, C. Poulain, and P. Thibault, Lab on a Chip, **17**(14):2470–2480 (2017).
[7] F. Busse and T. Wang. The Journal of the Acoustical Society of America,**69**(6):1634–1638 (1981).
[8] C. P. Lee and T. G. Wang. The Journal of the Acoustical Society of America, **85**(3):1081–1088, 1989.

Acoustofluidics 2020
26-27 August 2020
Virtual Conference

Wireless high-frequency acoustofluidic micropump for portable drug delivery systems

Rui You[1], Xuexin Duan[1]

[1]State Key Laboratory of Precision Measurement Technology and Instruments, School of Precision Instruments and Opto-Electronics Engineering, Tianjin University, NO. 92 Weijin Road, Tianjin 300072, China
E-mail: xduan@tju.edu.cn, URL: http://www.tjumbios.com/

Introduction

With the increasing understanding about the importance of distribution and pharmaco-kinetics of therapeutic agents and the advance of microelectromechanical technologies (MEMS), modern researches strive to design and fabricate integrated controllable and high-efficiency drug delivery systems (DDS) to improve therapeutic effects[1]. As one of the executive components of the integrated DDS, the micropump contains electromechanical units for precise liquid control, which is rather difficult for miniaturization. Today, the MEMs fabricated micropump has triggered a lot of research interest, which features with small size, light weight, low power consumption, wide flow rate range, low cost and the potential for integration with other microsensors and electronic circuits[2]. However, the existing micropumps still need further optimizations before clinical applications, such as the high work voltage of piezoelectric micropumps[3], the low flow rate of electrowetting micropumps[4], and the low backpressure of acoustofluidic micropumps[5]. Here, we present a novel acoustofluidic based wireless micropump for portable DDS applications (Fig. 1A). Based on the working principles of acoustofluidics induced by the gigahertz (GHz) solid-mounted bulk acoustic resonator (SMR), we designed and fabricated the novel acoustofluidic micropump. And its feasibility for drug delivery applications were discussed and assessed.

Experimental principle and methods

As shown in Fig. 1A, the acoustofluidic based wireless micropump is composed of a GHz SMR, a micropump body, a printed circuit board (PCB), a conical capillary and an antenna. The SMR is fabricated by typical MEMS approaches[6], with a resonant frequency of 1.56 GHz and a typical pentagon structure with the sides of 114 μm. The micropump body was fabricated using a 3D-printer (Form 2™, Formlabs Inc., 35 Medford St. Suite 201, Somerville, MA 02143, USA) out of the photopolymer clear resin. The conical capillary was placed perpendicularly above the surface of the SMR with the distance of ~100 μm. The SMR generates acoustic waves in thickness-extension mode by applying voltage on the top and bottom electrodes. When contacting with liquid, the acoustic waves propagate from SMR into liquid. Then the GHz acoustic wave decays along the wave propagation axis, and the attenuation coefficient, β, is expressed as[7]:

$$\beta = b\omega^2 / \rho c^3$$

where ω is the angular frequency of the acoustic wave, c is the sound velocity, ρ is the liquid density, and $b = 0.75\mu + \mu_B$, where μ and μ_B are the shear viscosity and bulk viscosity of the fluid, respectively. The attenuation coefficient is in proportion to the square of acoustic frequency, which means GHz acoustic wave has a very short attenuation length (β^{-1}, which is 9.3μm here) and a highly concentrated energy distribution. As a result, a typical Eckart streaming could be generated above the SMR, where the jetting flow drives the liquid straight out from the device center. At this boundary situation of conical capillary, the rapid upward jet flow is confined in a narrow area and streams along the capillary, outflowing as droplets and driving the liquid to inflow, realizing unidirectional pumping (Fig. 1B). Thus, once connected with the drug reservoir, it could drive the drug liquid to flow, delivering drug to targeted area on demand.

To assess the stability and accuracy of the pumping droplets generated by the micropump under different applied powers, the high-speed camera was focused at the end port of the tube connected with the capillary, recording the continuous generation of the droplets under different powers. We assessed the performances under situations of two outlet tubes with different outer diameters of 0.8 mm and 1 mm, respectively.

Results and discussion

Here, the acoustofluidic based wireless micropump was fabricated with a very small typical dimension of ~9×9×9 mm^3 (Fig. 1C). We evaluated the performance of the GHz micropump as a droplet infusion pump, which mainly considered the drop resolution, stability, and the flow rate. Through recording the generated droplets, the volume and time of each droplet can be calculated. As shown in Fig. 2A, the volume of the pumped droplets can be tuned from ~7.0 μL to ~15.5 μL depending on the terminal boundary situation of the tube which proves the high-resolution dispensing. We then verified the applied power to the SMR from 200 to 640 mW, the droplet volumes remained the same. This indicates the pumping has a rather good stability which is actually very important to be used as a wireless micropump. Figure 2B demonstrates a wide range of adjustable infusion pumping rates ranging from 1.34 mL/min in Φ0.8 mm tube at 640 mW to 0.23 mL/min in Φ1 mm tube at 200 mW. This could satisfy most of the therapeutic requirements.

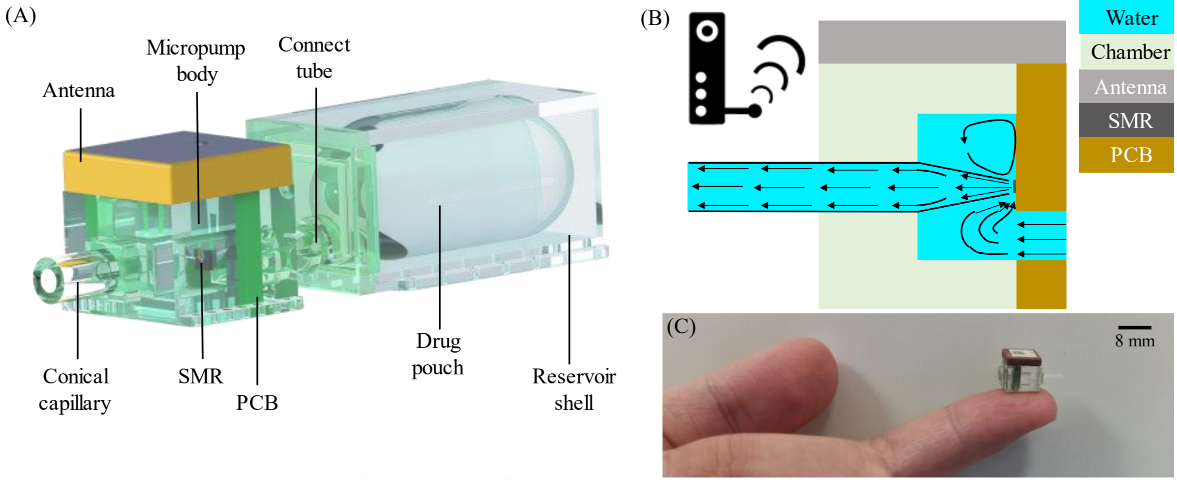

Figure 1: (A) Schematic illustration of the acoustofluidic-based wireless micropump with a drug reservoir. (B) Fluidic field of working acoustofluidic micropump. (C) Photograph of the wireless acoustofluidic micropump.

Conclusion

In summary, an acoustofluidic-based wireless-charging micropump has been developed for safe, precise and efficient drug delivery applications. We illustrated the working principle of the acoustofluidic micropump, the design and construction of the miniaturized drug delivery system. As a droplet infusion pump, it could produce droplets with different volumes tuned by the boundary situation of the outlet. A pumping resolution of 7.0 μL and a maximum flow rate of 1.34 mL/min were reached. This acoustofluidic based wireless micropump will be furtherly investigated as an integrated smart DDS for personalized medicine applications, for improving therapeutic effects and saving medical resource.

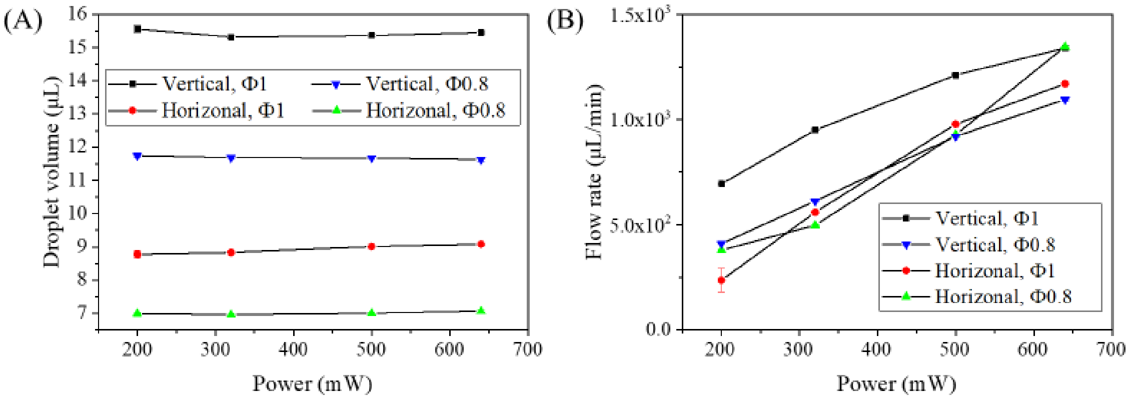

Figure 2: The volumes of droplets (A) and the flow rates of the micropump (B) through tubes with outer diameters of 0.8 and 1 mm at different postures (vertical and horizontal) under different applied powers (200, 320, 500 and 640 mW).

References

[1] P. Davoodi *et al.*, “Drug delivery systems for programmed and on-demand release,” *Adv. Drug Deliv. Rev.*, vol. 132, pp. 104–138, Jul. 2018.

[2] Y. N. Wang and L. M. Fu, “Micropumps and biomedical applications – A review,” *Microelectronic Engineering*, vol. 195, no. March. Elsevier, pp. 121–138, 2018.

[3] Q. S. Pan, L. G. He, F. S. Huang, X. Y. Wang, and Z. H. Feng, “Piezoelectric micropump using dual-frequency drive,” *Sensors Actuators, A Phys.*, vol. 229, pp. 86–93, 2015.

[4] Q. Hu, Y. Ren, W. Liu, X. Chen, Y. Tao, and H. Jiang, “Fluid flow and mixing induced by AC continuous electrowetting of liquid metal droplet,” *Micromachines*, vol. 8, no. 4, pp. 1–15, 2017.

[5] M. B. Dentry, J. R. Friend, and L. Y. Yeo, “Continuous flow actuation between external reservoirs in small-scale devices driven by surface acoustic waves,” *Lab Chip*, vol. 14, no. 4, pp. 750–758, 2014.

[6] S. Pan, H. Zhang, W. Liu, Y. Wang, W. Pang, and X. Duan, “Biofouling Removal and Protein Detection Using a Hypersonic Resonator,” *ACS Sensors*, vol. 2, no. 8, pp. 1175–1183, 2017.

[7] M. He *et al.*, “An on-demand femtoliter droplet dispensing system based on a gigahertz acoustic resonator,” *Lab Chip*, vol. 18, no. 17, pp. 2540–2546, 2018.

Acoustofluidics 2021
26-27 August 2021
Virtual Conference

Rapid Micromixing Driven by Sharp-Edge Acoustic Streaming in a Microchannel

Chuanyu ZHANG[1], Geyu ZHONG [1], Philippe BRUNET[2], Laurent ROYON[1],Xiaofeng GUO[1,3]

[1] Université de Paris, CNRS, LIED, UMR 8236, F-75006, Paris, France
E-mail : chuanyu.dream@gmail.com
[2] Université de Paris, CNRS, MSC, UMR 7057, F-75006, Paris, France
[2] Université Gustave Eiffel, ESIEE Paris, F-93162, Noisy le Grand, France

Introduction

Strong acoustic streaming can be generated inside a microchannel near sharp-edge structures. In this study, Sharp-Edge Acoustic Streaming (SEAS) micromixers with multiple sharp edge patterns actuated by kHz piezoelectric transducers are investigated. Direct Numerical Simulation (DNS) is used to numerically solve the multi-physics phenomenon involving acoustics, fluid dynamics and mass transfer. Experiments are carried out to validate the numerical results by visualization, as well as to evaluate micromixing performance with Iodide-Iodate Reactions ([1,2]).

Experiment Setup

As we have shown before [3,4], acoustic streaming can be induced around sharp edge structure at audible excitation frequency. As shown in Fig.1, an experiment setup has been built, where the piezo-transducer (of typical resonance frequency 2.5 kHz) is glued on a glass slide cover-slip and beside a PDMS micro-channel with a pattern of sharp edges. Fluorescent particles of diameter 4.9μm, two miscible fluids and two chemical solutions (acidic one : H^+,SO_4^{-2} ; alkaic one : I^-,IO_3^-,HBO_3^-) are separately injected through the channel at different experiment steps. A blue light source is put under the glass slide. The high-speed camera is mounted above the channel to capture the images and transfer data to the computer.

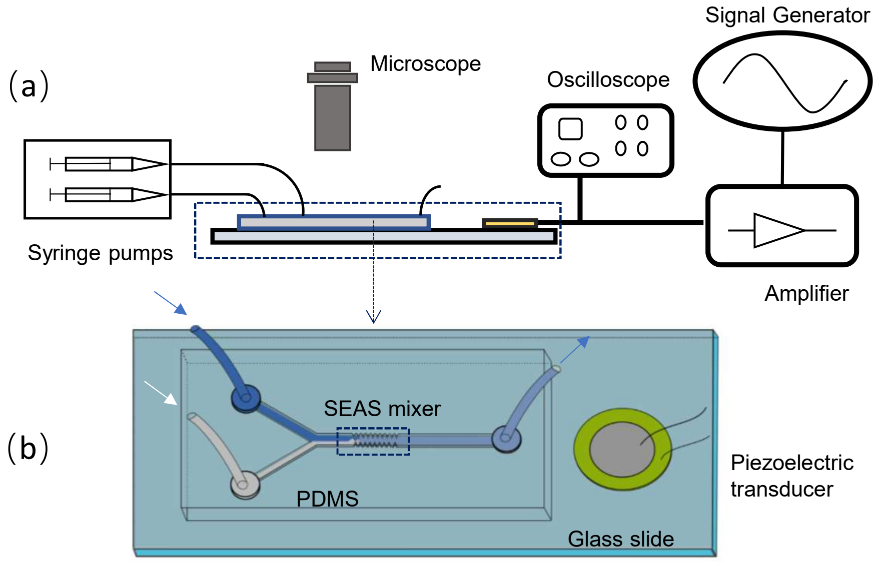

Figure 1 – The schematic of the experiment setup. The microchannel is formed between glass slide and PDMS material. The piezo-transducer is attached beside the PDMS channel.

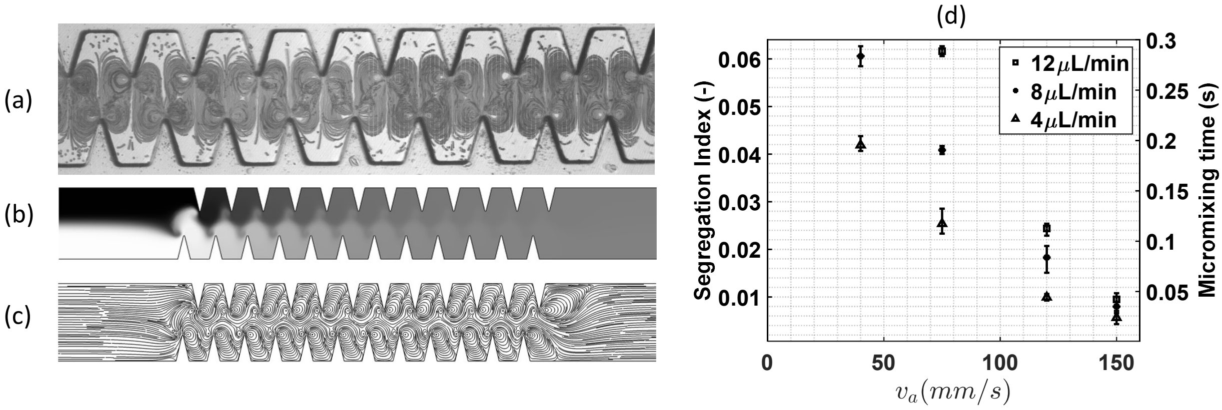

Figure 2 – (a) the stack image of particle tracers immersed in fluid ; (b) macromixing performance between two miscible fluid ; (c) streamline of streaming flow plus the main flow ; (d) the variations of micromixing time and segregation index with flow-rate and intensity of acoustic vibration field v_a.

structures, the number of sharp edges), channel throughput as well as acoustic power are among the most influential factors on the flow disturbance. As shown in Fig.2(a-c) and in [1], an optimal structure with 0.1mm spacing between two consecutive edge structure is found as a optimum value for mixing in a certain range of acoustic power, with a limited channel length.

As shown in Fig.2(c), the shape of flow streamlines from simulation results unveils the interaction between acoustic streaming and main flow, which is shown to be crucial for mixing enhancement. Following this, the micromixing time and segregation index are measured based on the Iodide-Iodate Reactions. As shown in Fig.2(d), micromixing time as short as 0.03 s can be achieved with relatively low flow-rate ($4\mu L/min$) and strong acoustic forcing ($v_a = 150mm/s$).

Finally, a comparison with literature on passive mixers confirms the micromixing performance of SEAS mixer in terms of micromixing time at low Reynolds number flow.

Conclusion

Our study demonstrates the great potential of acoustic streaming in sharp-edged microchannels, both in terms of macromixing performance between two miscible fluids or micromixing time. The spacing between two neighbouring edges plays a crucial role in the complex flow structure within the zone of edges pattern and has to be optimized in application design.

References

[1] C. Zhang, P. Brunet, L. Royon, X. Guo, Mixing intensification using sound-driven micromixer with sharp edges, Chem. Eng. J. 410 (2021) 128252.

[2] X. Guo, Y. Fan, L. Luo, Mixing performance assessment of a multi-channel mini heat exchanger reactor with arborescent distributor and collector, Chem. Eng. J. 227 (2013) 116-127..

[3] Zhang, C., Guo, X., Royon, L., Brunet, P. (2020b). Unveiling of the mechanisms of acoustic streaming induced by sharp edges. Physical Review E, 1-14,043110.

[4] C. Zhang, X. Guo, M. Costalonga, P. Brunet and L. Royon. Acoustic streaming around a sharp edge and its mixing performance characterisation. Microfluidics and Nanofluidics 23, 104 (2019)

Acoustofluidics
2021
26-27 August 2021
Virtual Conference

Selective evaporation-induced changes in the resonance behavior of a piezoacoustic inkchannel

Maaike Rump[1], Uddalok Sen[1], Roger Jeurissen, Christian Diddens[1], Hans Reinten[2], Detlef Lohse[1], Michel Versluis[1], and Tim Segers[3]

[1] Physics of Fluids group, Max-Planck Center Twente for Complex Fluid Dynamics, MESA+ Institute for Nanotechnology, and J. M. Burgers Centre for Fluid Dynamics, University of Twente, Enschede, the Netherlands
[2] Canon Production Printing, P.O. Box 101, 5900 MA Venlo, Netherlands
[3] BIOS Lab-on-a-Chip group, Max-Planck Center Twente for Complex Fluid Dynamics, MESA+ Institute for Nanotechnology, University of Twente, Enschede, Netherlands E-mail: t.j.segers@utwente.nl

Introduction

Piezoacoustic inkjet printing is a successful industrial application of acoustofluidics that allows for highly controlled, on demand, and contactless droplet deposition at picoliter volumes [1]. Today, the applications of inkjet printing reach far beyond document printing. To name a few, inkjet printing is used in solar cell printing, printing of micro-lenses, fuel cells, batteries, flat-panel and liquid-crystal displays, electronic circuit boards, rapid prototyping, and in bio-applications such as DNA and protein printing. Evidently, the inks used in most cases are multicomponent and out of equilibrium, leading to mass transport and concentration gradients in the nozzle. A typical hydrodynamic phenomenon that decreases the reproducibility of the jetted droplets (velocity, volume, and composition) is selective evaporation at the nozzle exit. Here, we study the ink channel acoustics as a function of selective evaporation induced changes in the fluid-mixture composition in the nozzle through experiments and analytical modeling. The aim is to be able to measure the composition of the ink mixture in the nozzle from the acoustic ring-down signal of the inkchannel. We find excellent agreement between the experiments and the model showing that the changes in the acoustic resonance frequency of the inkchannel are a result of changes in both density and viscosity of the fluid in the nozzle of the printhead.

Experiments

Experiments were performed on an experimental printhead with a 16 μm diameter nozzle, see Fig. 1. The model ink was composed of a mixture of 10 w.% glycerol in water. For each measurement, first, 1000 droplets were jetted using a high-amplitude pulse to ensure a homogeneous liquid mixture in the nozzle with a composition equal to the initial water-glycerol mixture. Subsequently, the jetting was stopped and the ringdown signal of the piezo in response to a half-amplitude non-jetting pulse was measured using a pulse-echo circuit connected to an oscilloscope. The time between the droplet jetted last and the low-amplitude pulse was varied from 1 ms up to 1 hour. A damped sinusoid was fitted to each ringdown signal to measure both the frequency and damping of the acoustics in the inkchannel.

Modeling

We analyze the inkchannel acoustics in the frequency domain to account for viscous dissipation. The acoustic impedance (pressure/flow rate) of a cylindrical nozzle in the frequency domain is given by [2]:

$$Z_n = -i\omega I_n \left(1 - \frac{2J_1(i^{3/2}Wo)}{i^{3/2}WoJ_0(i^{3/2}Wo)}\right)^{-1}, \tag{1}$$

with Wo the Womersley number ($R_n\sqrt{\frac{\omega\rho}{\mu}}$, with R_n nozzle radius, ω frequency, ρ density and μ viscosity), J_0 and J_1 the ordinary Bessel functions of the first kind of zeroth and first order, respectively. I_n is the acoustic inertance of the nozzle:

$$I_n = \frac{\rho L_n}{A_n}, \tag{2}$$

with L_n the length of the nozzle, and A_n the cross-sectional area of the nozzle. The same equations hold

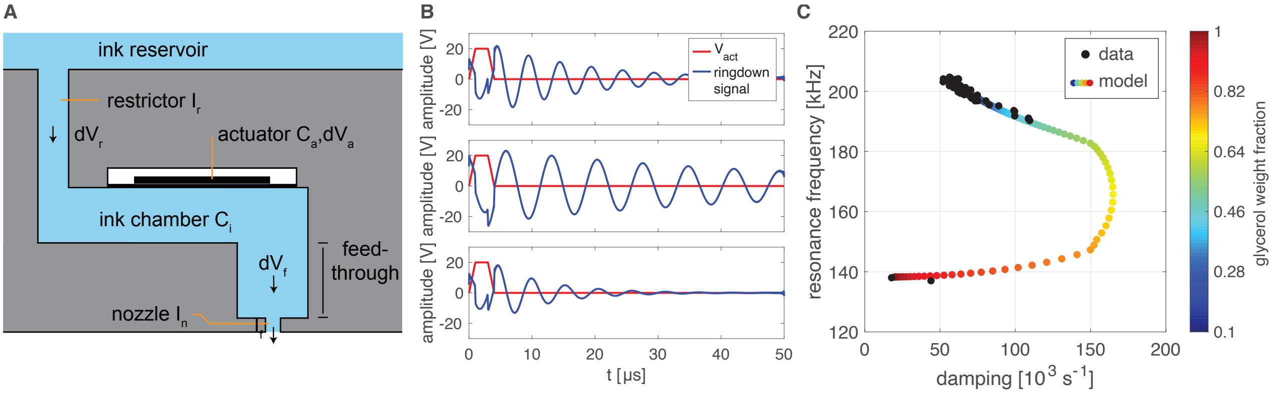

Figure 1: (A) Schematic of the employed ink channel with the ink chamber, restrictor, feedthrough and nozzle. The ink channel is driven by a piezoelectric actuator deposited on a flexible membrane. Also indicated are the inertances of the restrictor I_r, the feedthrough I_f, and the nozzle I_n. The compliances of the actuator and the ink are indicated by C_a and C_i, respectively. (B) Ringdown signals (solid blue curves) in response to the actuation pulse (solid red curve) for a glycerol weight fraction of 0.1, 0.5, and 1.0, from top to bottom, respectively. (C) Frequency versus damping of the ringdown signal from the model (colored dots) and from experiments (black dots).

for the acoustic impedance of the restrictor Z_r and the feedthrough Z_f (Fig. 1). The total compliance of the ink channel C_t (volume change per unit pressure) has contributions from the flexible piezo actuator C_a and the volume V of ink in the ink chamber: $C_i = V(\rho c^2)$, with c the speed of sound. By assuming simple harmonic motion, it follows that the acoustic impedance of the actuator and volume of ink is:

$$Z_a = \frac{1}{i\omega C_t}. \tag{3}$$

The total lumped acoustic impedance of the ink channel equals: $Z_t = \left(\frac{1}{Z_r} + \frac{1}{Z_n+Z_f} + \frac{1}{Z_a}\right)^{-1}$. Again by assuming simple harmonic motion, we derive that the piezo ringdown signal in the frequency domain is given by:

$$I(\omega) = -\omega^2\alpha^2 Z_{tot} V_p(\omega), \tag{4}$$

with α the volume change of the ink channel as a function of the driving voltage amplitude, and $V_p(\omega)$ the driving pulse in the frequency domain. Equation 4 can be inverse Fourier transformed to obtain ringdown signals in the time domain as a function of the glycerol mass fraction. The viscosity and density of a mixture of water and glycerol as a function of the glycerol mass fraction were taken from literature [3].

Results

Figure 1B shows (top to bottom) modeled piezo ringdown signals for a glycerol mass fraction of 0.1, 0.5, and 1.0, respectively. Figure 1C shows the modeled frequency of the ringdown signal as a function of its damping for a glycerol mass fraction ranging from 0.1 up to 1.0. The black dots represent experimental data points. From the comparison of the model and the experiment we learn that for an increasing glycerol mass fraction (up to 0.5), the damping increases while the frequency decreases due to the increased viscous dissipation and the increased density of the liquid in the nozzle. Note that both the damping and frequency dramatically decrease for high glycerol mass fractions. The reason is the increase of the impedance of the nozzle such that the $\frac{1}{Z_n+Z_f}$ term in Z_t becomes negligible with respect to the two other terms. As a consequence, the flow in the nozzle becomes stationary effectively decoupling the nozzle from the system, which stops the jetting.

Conclusion

The simple analytical model quantitatively predicts the resonance behavior of the ink channel as a function of compositional changes of the ink due to selective evaporation at the nozzle exit. The gained insights can be used to probe the state of the ink in the nozzle in piezoacoustic printhead.

References

[1] D. Lohse. Ann. Rev. Fluid Mech. in press, (2020)
[2] J. R. Womersley. The Journal of physiology **127**, 553-563 (1955).
[3] NIST standard reference database (2005)

Acoustofluidics
2021
26-27 August 2021
Virtual Conference

The elastic, dielectric, and piezoelectric constants of PZT transducers for acoustofluidics determined by electrical impedance spectroscopy

William N. Bodé, Fabian Lickert, and Henrik Bruus

Physics, Technical University of Denmark, Kongens Lyngby, Denmark
E-mail: winabo@dtu.dk, URL: www.fysik.dtu.dk/microfluidics

Introduction

Acoustic forces in microfluidic platforms are often driven by ultrasound actuators operating at MHz frequencies, generating acoustic waves at a wavelength comparable to the microchannel dimensions. Devices based on resonating bulk acoustic waves are often driven by piezoelectric (PZE) transducers, and a typical device consists of three components: a microfluidic chip, a coupling layer, and a transducer. Pursuing precise, accurate, and predictive simulations demands well-characterized material parameters for each device component. Inspired by the *in situ* elastic parameter fitting in Ref. [1], we present here two sets of fitted PZE material constants based on a hexagonal and a tetragonal crystal model, characterizing the commonly used Pz26 lead-zirconate-titanate (PZT) transducer.

Theory

The governing equations for the time-harmonic displacement field $\boldsymbol{u}$ and the quasi-static electric potential φ in a PZE ceramic are $\boldsymbol{\nabla}\cdot\boldsymbol{\sigma} = -\rho\omega^2\boldsymbol{u}$ and $\boldsymbol{\nabla}\cdot\boldsymbol{D} = 0$. In the Voigt notation, the stress $\boldsymbol{\sigma}$ and electric displacement $\boldsymbol{D}$ are given by the electric potential φ and the displacement field $\boldsymbol{u}$ as,

$$\left(\begin{array}{c} \sigma_{xx} \\ \sigma_{yy} \\ \sigma_{zz} \\ \hline \sigma_{yz} \\ \sigma_{xz} \\ \sigma_{xy} \\ \hline D_x \\ D_y \\ D_z \end{array}\right) = \left(\begin{array}{ccc|ccc|ccc} C_{11} & C_{12} & C_{13} & 0 & 0 & 0 & 0 & 0 & -e_{31} \\ C_{12} & C_{11} & C_{13} & 0 & 0 & 0 & 0 & 0 & -e_{31} \\ C_{13} & C_{13} & C_{33} & 0 & 0 & 0 & 0 & 0 & -e_{33} \\ \hline 0 & 0 & 0 & C_{44} & 0 & 0 & 0 & -e_{15} & 0 \\ 0 & 0 & 0 & 0 & C_{44} & 0 & -e_{15} & 0 & 0 \\ 0 & 0 & 0 & 0 & 0 & C_{66} & 0 & 0 & 0 \\ \hline 0 & 0 & 0 & 0 & e_{15} & 0 & \varepsilon_{11} & 0 & 0 \\ 0 & 0 & 0 & e_{15} & 0 & 0 & 0 & \varepsilon_{11} & 0 \\ e_{31} & e_{31} & e_{33} & 0 & 0 & 0 & 0 & 0 & \varepsilon_{33} \end{array}\right) \left(\begin{array}{c} \partial_x u_x \\ \partial_y u_y \\ \partial_z u_z \\ \hline \partial_y u_z + \partial_z u_y \\ \partial_x u_z + \partial_z u_x \\ \partial_x u_y + \partial_y u_x \\ \hline -\partial_x \varphi \\ -\partial_y \varphi \\ -\partial_z \varphi \end{array}\right). \tag{1}$$

For a tetragonal structure, C_{66} is an independent constant, whereas for a hexagonal structure it is constrained to be $C_{66} = \frac{1}{2}(C_{11} - C_{12})$. The equations are solved numerically using the weak formulation and the finite element method as in Refs. [1,2]. The hexagonal model can be reduced to a 2D axisymmetric model, whereas the tetragonal can only be reduced by eight to an octant 3D domain.

Experiment

Electrical impedance measurements of a disk-shaped PZT sample (Pz26, Meggitt Ferroperm) were performed using a USB-oscilloscope (Analog Discovery 2, Digilent) in the frequency range from 0.1 to 5 MHz in steps of 1 kHz and at an actuation voltage amplitude of 1 V. Parasitic effects of the wiring were calibrated through measurements of an open, shorted, and known-resistor configuration. The top and bottom electrode of the PZT disk were contacted through a custom-made sample holder, minimizing the contact force and area to a point in the center of the disk. The PZT disk diameter and thickness were measured to be 6.448 mm and 0.512 mm respectively, the setup is shown in Fig. 1 together with the model system.

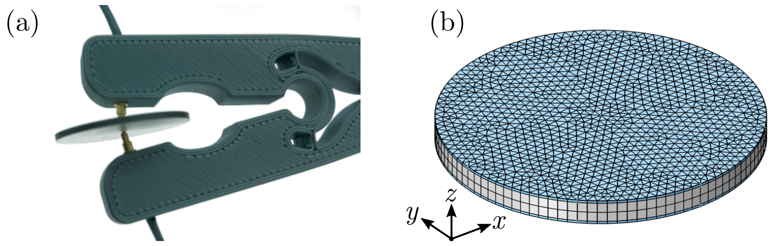

Figure 1: (a) Custom-made sample holder (dark blue) with point-contacts (Be-Cu alloy 172) for electrical impedance measurements. (b) The implemented model of the 6.448-mm-diameter PZT disk (gray) of thickness 0.512 mm with 12-µm-thick top and bottom silver electrodes (light blue). The structured finite-element mesh (black lines) with free triangles in the x-y plane is also shown.

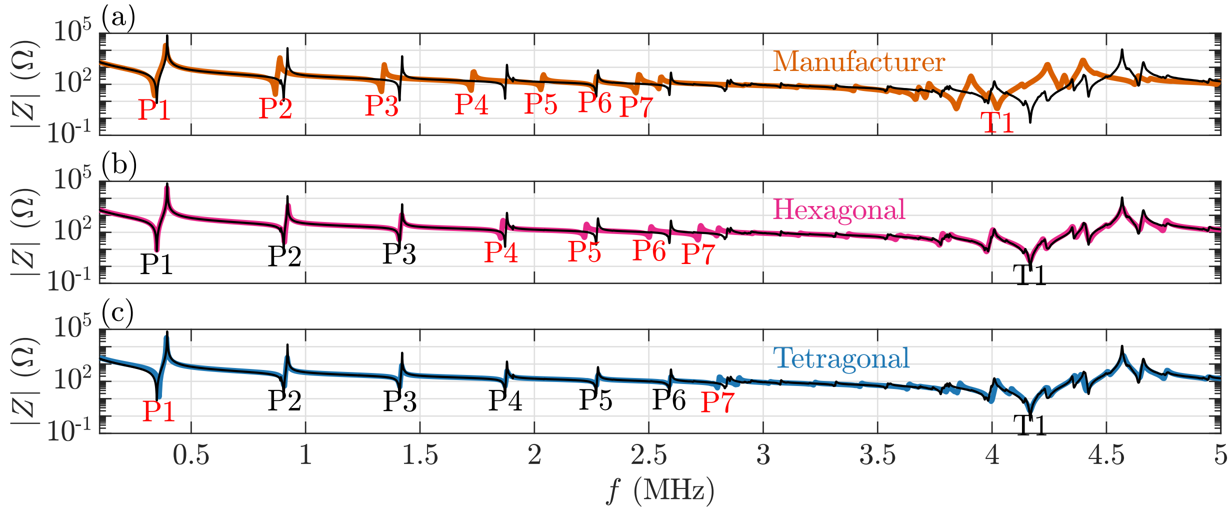

Figure 2: The measured electrical impedance spectrum (black) compared with the simulated one for (a) the manufacturer's parameters (orange), (b) a fit by the hexagonal model (purple), and (c) a fit by the tetragonal model (blue). P1-P7 are the planar radial and T1 is the thickness resonance mode. Here, a black font color indicates better than 1% agreement between simulated and measured resonance frequency, and red otherwise.

Fitting procedure

Besides the measured $\rho = 7585$ kg/m^3, ten (hexagonal) or eleven (tetragonal) parameters p_j are required to describe the piezoelectric transducer. The measured and simulated impedance spectra $Z(f)$ are used to calculate the cost function $\mathcal{C}(p_j)$, which is then minimized by a simplex search [3],

$$p_j = \{C_{11}, C_{12}, C_{13}, C_{33}, C_{44}, C_{66}\}, \{\varepsilon_{11}, \varepsilon_{33}\}, \{e_{31}, e_{33}, e_{15}\}, \tag{2a}$$

$$\mathcal{C}(p_j) = \sqrt{\sum_i \Big\{ \log_{10} |Z_{\mathrm{exp}}(f_i)| - \log_{10} |Z_{\mathrm{sim}}(f_i; p_j)| \Big\}^2}. \tag{2b}$$

Results

The simulated electrical impedance spectra from the fitted set of parameters are shown in Fig. 2(b) and (c). For each set of parameters the relative deviation $\Delta = (f_{\mathrm{sim}} - f_{\mathrm{exp}})/f_{\mathrm{exp}}$ between measured and simulated resonance frequencies are tabulated in Table 1. In Fig. 2 and Table 1, $|\Delta| < 1\%$ is marked by black and $|\Delta| \geq 1\%$ by red. The manufacturer's parameters give an average deviation of $\bar{\Delta} = -7.6\%$, the hexagonal fit yields $\bar{\Delta} = -1.3\%$, and the tetragonal fit yields $\bar{\Delta} = 0.3\%$. The corresponding parameter value sets p_{hex} and p_{tetra} for the hexagonal and tetragonal model are:

$$p_{\mathrm{hex}} = \{152, 88.4, 89.6, 136, 29.2, 31.7\}\ \mathrm{GPa}, \{965, 722\}\ \varepsilon_0, \{-3.35, 15.4, 7.89\}\ \mathrm{C/m^2}, \tag{3a}$$

$$p_{\mathrm{tetra}} = \{138, 88.4, 80.2, 136, 30.5, 26.1\}\ \mathrm{GPa}, \{990, 714\}\ \varepsilon_0, \{-2.80, 15.3, 7.90\}\ \mathrm{C/m^2}. \tag{3b}$$

Table 1: Comparison between measured and simulated resonance frequencies for each set of parameters for the first seven planar radial modes P1-P7 and the first thickness mode T1. Deviations $|\Delta| < 1\%$ are written in black and $|\Delta| \geq 1\%$ in red.

Mode f_{exp} (MHz)	P1 0.350	P2 0.904	P3 1.411	P4 1.872	P5 2.270	P6 2.590	P7 2.832	T1 4.167	$\bar{\Delta}$
Δ (manufacturer)	−2.9%	−4.0%	−5.6%	−7.9%	−11%	−13%	−14%	−3.4%	−7.6%
Δ (hexagonal fit)	0.0%	0.4%	−0.1%	−1.0%	−2.2%	−3.4%	−4.1%	0.0%	−1.3%
Δ (tetragonal fit)	2.9%	0.4%	0.1%	0.0%	−0.1%	−0.1%	−1.1%	0.0%	0.3%

Conclusion

The fitting procedure for the hexagonal model with ten parameters predicts the first three planar radial modes P1-P3 and the thickness mode T1 better than 1%, but deviates for P4-P7. The tetragonal model with eleven parameters gives a better overall result, capturing P2-P6 and T1 within 1%. The simulation result therefore suggests that the crystal structure of PZT Pz26 is tetragonal and not hexagonal. We believe that the presented impedance-spectrum fitting procedure can be generalized for *in situ* characterization of any acoustofluidic device material.

References

[1] A.G. Steckel, H. Bruus, P. Muralt, and R. Matloub, *et al.*, Phys. Rev. Appl. **16**, 014014 (2021). [pdf]
[2] N.R. Skov, J.S. Bach, B.G. Winckelmann, and H. Bruus, AIMS Mathematics **4**(1), 99-111 (2019). [pdf]
[3] N. Pérez, *et al.*, IEEE Trans. Ultrason., Ferroelectr., Freq. Control, **57**(12), 2772-2783 (2010). [doi]

Acoustofluidics
2021
26-27 August 2021
Virtual Conference

A Piezoelectric Smart Patch Operated with Machine Learning Algorithms for Effective Detection and Elimination of Condensation

Qian Zhang[1,2], Yong Wang[1,2,3], Tao Wang[1], Dongsheng Li[1], Jin Xie[1,*], Hamdi Torun[2] and Yongqing Fu[2,1,*]

[1] The State Key Laboratory of Fluid Power and Mechatronic Systems, Zhejiang University, Hangzhou 310027, China
E-mail: 11825039@zju.edu.cn
[2] Faculty of Engineering and Environment, University of Northumbria, Newcastle upon Tyne NE1 8ST, UK
[3] Key Laboratory of 3D Micro/Nano Fabrication and Characterization of Zhejiang Province, School of Engineering, Westlake University, Hangzhou 310024, China

Introduction

Condensation is a ubiquitous phenomenon, which is common in natural and built environments with a wide range of scale from kilometer-long pipelines to biological cells [1-3]. Most of the currently reported condensation detectors measure the capacitance change caused by the changes of dielectrics (e.g., formation of dew) in order to determine whether condensation occurs [4-5]. However, these detectors are susceptible to the variations of electrical characteristics of liquids and ambient humidity and also show strong nonlinearity.

In this paper, we present a flexible smart patch based on a flexible Lamb wave device and a machine learning algorithm, which can effectively detect, prevent and eliminate surface condensation. In terms of detection, condensation is generally accompanied by variations in ambient temperature and humidity, which may lead to misjudgment. Therefore, in addition to the response of the flexible device to surface condensation, the device's responses to temperature and humidity variations are also investigated for comparisons. Furthermore, several additional experiments including the condensation detection using back surface or a bent device, and detection of different types of liquids and respiration, are conducted in order to demonstrate the broad applicability of the flexible smart patch. Finally, the performance of preventing and eliminating surface condensation are studied.

Detection of condensation

Since the mass of liquid can be infinitely close to zero, a threshold is defined, which is also the minimum

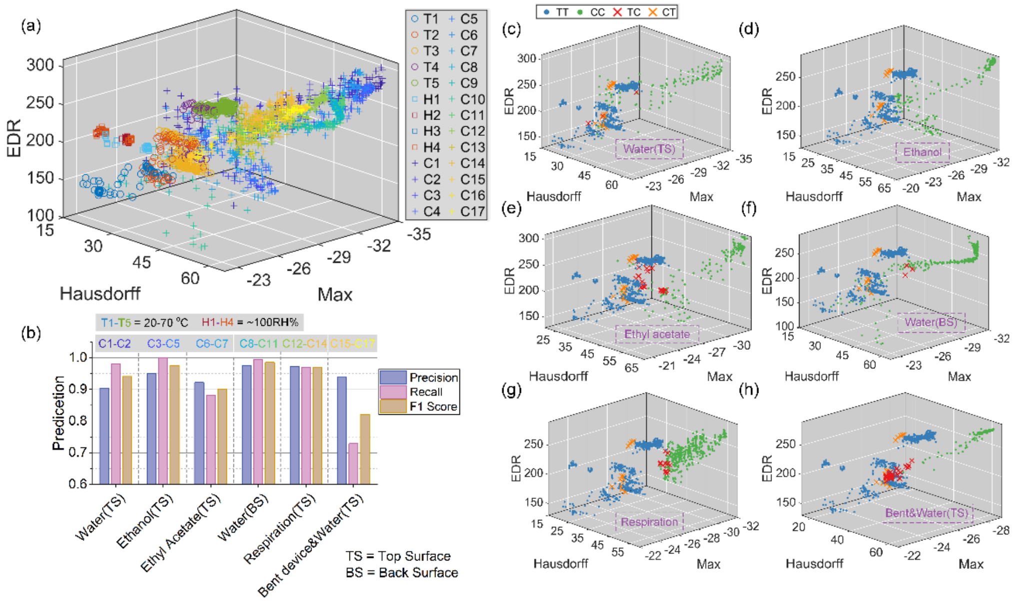

Figure 1: (a) The whole test set mapped to a selected 3-D space with coordinates of Maximum value, Hausdorff distance and EDR, which is equivalent to data preprocessing for dimension reduction. (b) The prediction results of the classification model obtained by the random forest algorithm on the six test sets corresponding to the six cases. The visualization of classification results on the six test sets, corresponding to the cases of (c) water on top side, (d) ethanol, (e) ethyl acetate, (f) water on back side, (g) respiration and (h) bent device, respectively.

detection limit. When the surface density of the liquid exceeds the threshold, it is considered that condensation have occurred. This results in the detection task into a binary classification problem, i.e., to distinguish the non-condensation (temperature change and humidity change) and condensation (mass change). In order to determine the appropriate threshold, classification preliminary tests using the following algorithm with thresholds of 0, 1.5 and 3 $\mu g/mm^2$ were separately conducted on a small part of the data set, the results of which show that the algorithm can effectively identify condensation starting from 3 $\mu g/mm^2$. Consequently, 3 $\mu g/mm^2$ is determined as the threshold in this paper. To involve more information, the S21 parameters in a frequency band (23.5-25.5 MHz) adjacent to the resonant frequency were chosen as original features. Frequency-amplitude response of S21 in this band is composed of 1601 points, which can be regarded as a 1601-dimensional vector. Then the vectors are mapped into a 3-D space with coordinates of Maximum value, Hausdorff distance and EDR (edit distance on real sequence), as shown in Fig. 1(a). After the dimension reduction of the raw S21 data, the classification model can be obtained by using the random forest algorithm and the training set, which was subsequently verified by the test sets corresponding to the six cases. The *Precision*, *Recall* and *F1 score* were then calculated by comparing the predicted results with the actual ones, as shown in Fig. 1(b). The proposed method performed well in the experiments of water (TS), ethanol (TS), water (BS) and respiration (TS), where the *Precision*, *Recall* and *F1 score* are all above 90%. Figs. 1(c) to 1(h) show the visualized classification results corresponding to the 6 various cases.

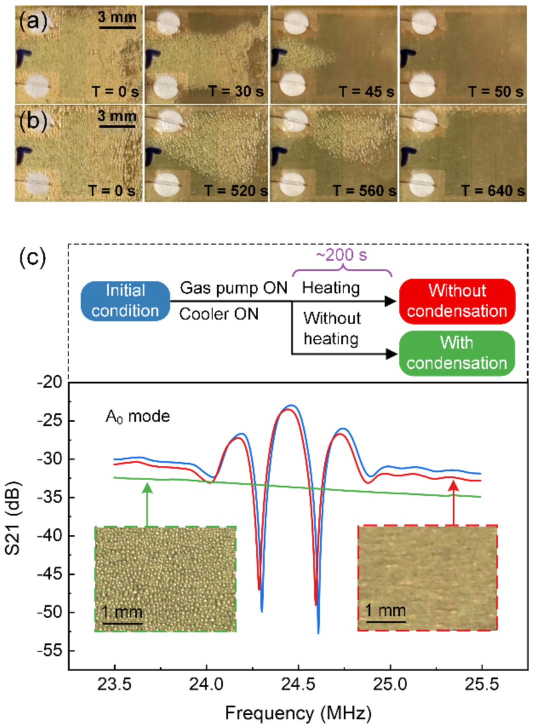

Figure 2: Photos of the evaporation process of the condensation on the surface of the flexible ZnO/Al device (a) with power input (~0.6 W) and (b) without power input. (c) After turning on the gas pump and cooler for ~200 s, the S21 spectra and photos of the ZnO/Al device with and without power input (~0.6 W).

Condensation evaporation

The heating performance is investigated for the elimination and prevention of condensation. Figs. 2(a) and 2(b) show the photos of the evaporation process of condensations with and without input of power (~0.6 W, 24.9 MHz). The room temperature and humidity are ~18 °C and ~46 RH%, respectively. It takes ~50 s for the condensation fully removed, which is only ~1/13 of that in the natural condition (~640 s). As shown in Fig. 2(c), the experiments were conducted in an environment with temperature less than dew point for ~200 s. The device can effectively prevent the condensation, which can be verified from the image of the dry surface of the sample and the S21 spectrum (red curve). On the other hand, without the power input, there are dense small droplets on the surface, and the intensity of S21 spectrum reduces (green curve).

Conclusion

In summary, through the carefully designed experiments, the capabilities of the proposed smart patch to detect and eliminate surface condensation have been investigated under various conditions. The patch has been operated using a machine learning algorithm to distinguish effective response (condensation) from false response (temperature and humidity variations). The algorithm is based on a classifier that was trained using a random forest algorithm and the S21 data after nonlinear dimensionality reduction, which performed well in six different test sets (average *Precision* = 94.40% and average *F1 score* = 93.23%). The flexible device has been shown effectively to prevent and eliminate the surface condensation with an input power of a few tenths of a watt at a frequency of ~25.3 MHz. In the experimental environment, the evaporation rate was increased up to ~13 times with an input power of ~0.6 W compared to that under natural condition. Our work demonstrates the promising prospect of proposed smart patch in broad applications including respiration detection, agricultural environmental monitoring, pipeline corrosion protection and automotive industry.

References (Times New Roman 10 pt)

[1] Cha, H. *et al.* Dropwise condensation on solid hydrophilic surfaces. *Sci. Adv.* **6**, eaax0746 (2020).
[2] Yang, Q. *et al.* Capillary condensation under atomic-scale confinement. *Nature* **588**, 250–253 (2020).
[3] Shin, Y. & Brangwynne, C. P. Liquid phase condensation in cell physiology and disease. *Science* **357**, eaaf4382 (2017).
[4] Oprea, A. *et al.* Capacitive humidity sensors on flexible RFID labels. *Sensors Actuators B Chem.* **132**, 404–410 (2008).
[5] Wei, Y. Q., Bailey, B. J. & Stenning, B. C. A Wetness Sensor for Detecting Condensation on Tomato Plants in Greenhouses. *J. Agric. Eng. Res.* **61**, 197–204 (1995).

Heat transfer mechanism due to acoustic body force under acoustic fields

Varun Kumar Rajendran[1], Mohammed Azharudeen[1] and Karthick Subramani[1]

[1]Department of Mechanical Engineering, Indian Institute of Information Technology,
Design and Manufacturing Kancheepuram, Chennai-600127, India.
E-mail: mdm20d010@iiitdm.ac.in

Introduction

In this work, we demonstrate a heat transfer mechanism using standing ultrasonic waves that can be used under microgravity and atmospheric conditions as well. The acoustic relocation phenomenon in an inhomogeneous fluid [1] is the basic underlying principle for the stated heat transfer mechanism. Here the inhomogeneity in density and speed of the sound gradient is caused due to temperature gradient and when this fluid is subjected to acoustic force it gives rise to fluid movement thereby creating a heat transfer. Acoustic waves passed perpendicular to the direction of heat transfer revealed that acoustic forces can enhance heat transfer up to 2.5 times to natural convection, and up to 11.2 compared to pure conduction. Suppression of natural convection heat transfer is observed when the acoustic waves are passed parallel to the direction of heat transfer.

Theoretical Model

A simple two-dimensional (2D) enclosure of width W (8 mm) and height H (4 mm) is considered as shown in Fig. 1 a) and b). This enclosure is maintained at a higher temperature at the bottom (T(x,-H/2)=320 K) and a lower temperature at the top (T(x,+H/2)=290 K). Water and ethanol have been considered as the working fluids in this study are subjected to an acoustic standing half-wave of wavelength λ = 2W applied along the X-axis and Y-axis as shown in Fig. 1.

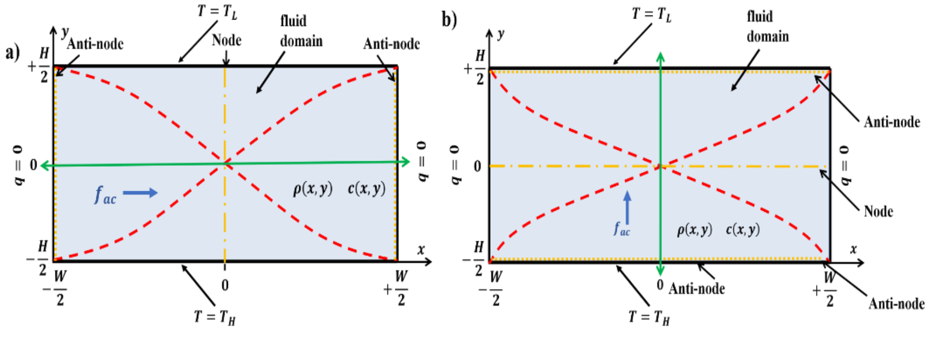

Fig. 1: Schematic of the 2-D mini channel. a) acoustic standing half-wave applied on X-axis or perpendicular to the direction of heat transfer b) acoustic standing half-wave applied on Y-axis or parallel to the direction of heat transfer. The green arrow indicates the direction of the applied acoustic wave.

Modeling Acoustic body force

The equation for acoustic force density f_{ac} in terms of density and speed of sound gradient [2],

$$f_{ac} = E_{ac}(\cos(2k_\lambda x)\,\nabla\hat{\rho} + (1 + cos\,(2k_\lambda x)\,)\nabla\hat{c}) \tag{1}$$

The gradient in density $\nabla\hat{\rho}$ and speed of sound $\nabla\hat{c}$ in this heat, transfer study is only due to temperature gradient, so Eq. 1 can be written in terms of temperature gradient and it takes the form,

$$f_{ac} = E_{ac}\nabla T\left(\cos(2k_\lambda x)\frac{1}{\rho_{avg}}\frac{\partial\rho_0}{\partial T} + (1 + cos\,(2k_\lambda x)\,)\frac{1}{c_{avg}}\frac{\partial c_0}{\partial T}\right) \tag{2}$$

Results and Discussions

A. Standing wave applied perpendicular to the heat transfer direction - Heat transfer enhancement

In this case, nodes are formed at the center, and antinodes are formed on sidewalls as shown in Fig. 2 a. Initially, the fluid is at an acoustically unstable configuration due to applied thermal boundary conditions. When an acoustic standing wave is applied perpendicular to the direction of heat transfer the acoustic force tries to bring an acoustically stable configuration, thus creates a steady fluid circulation in the entire domain and enhances heat transfer. The velocity profile for water and ethanol with and without the presence of gravity at E_{ac} = 10 J/m^3 is shown in Fig 2 a. It also must be noted that the direction of fluid circulation is different for ethanol and water. This is due to the sign and relative magnitude of the terms $\partial\rho_0/\partial T$ and $\partial c_0/\partial T$. The resultant heat transfer enhancement for this configuration for ethanol and water for various acoustic energy densities is shown in Fig. 3a.

B. Standing wave applied parallel to the heat transfer direction - Heat transfer suppression.

In this case, the nodes are formed at the center (parallel to X-axis) and antinodes are formed at the top and bottom walls as shown in Fig. 2 c. When the acoustic standing wave is applied parallel to the direction of heat transfer, only a region of the fluid domain experiences heat transfer. Again, this is due to the sign and relative magnitude of the terms $\partial\rho_0/\partial T$ and $\partial c_0/\partial T$. This incomplete convection helps to suppress heat transfer. Suppression of natural convection for ethanol and water for various acoustic energy densities is shown in Fig. 3b.

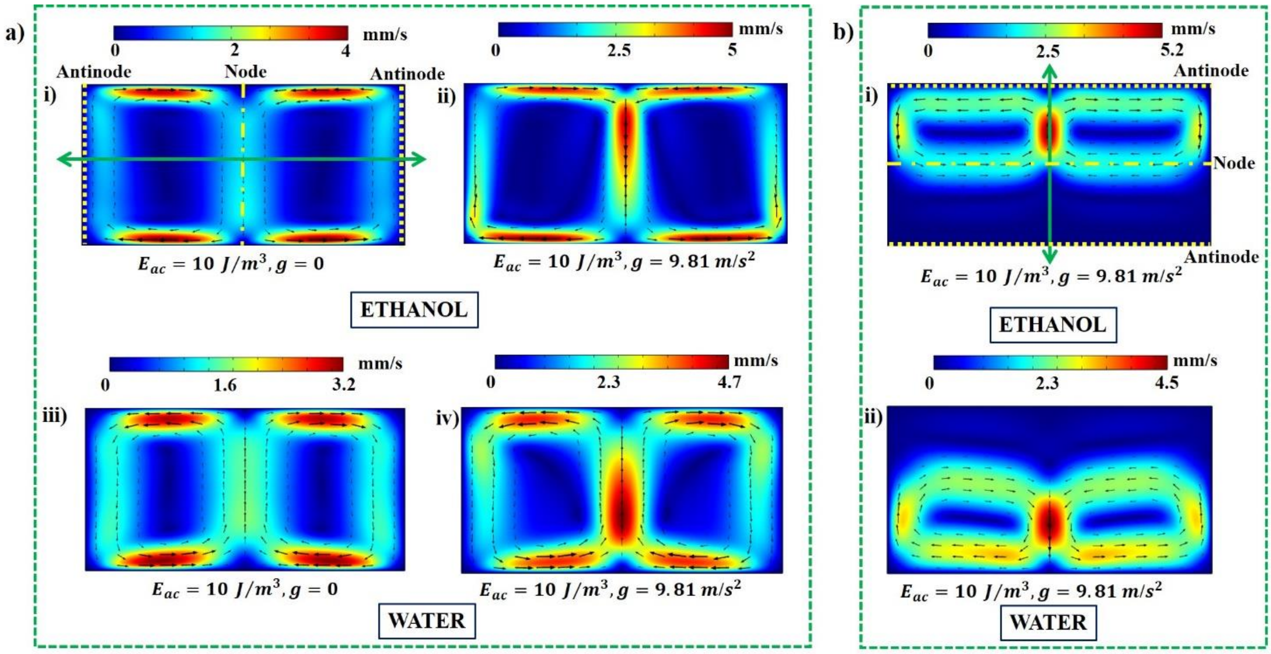

Fig. 2: Resultant heat flux when standing wave applied: a) when applied perpendicular to the direction of heat transfer–enhancement of heat transfer. b) when applied parallel to the direction of heat transfer – suppression of natural convection.

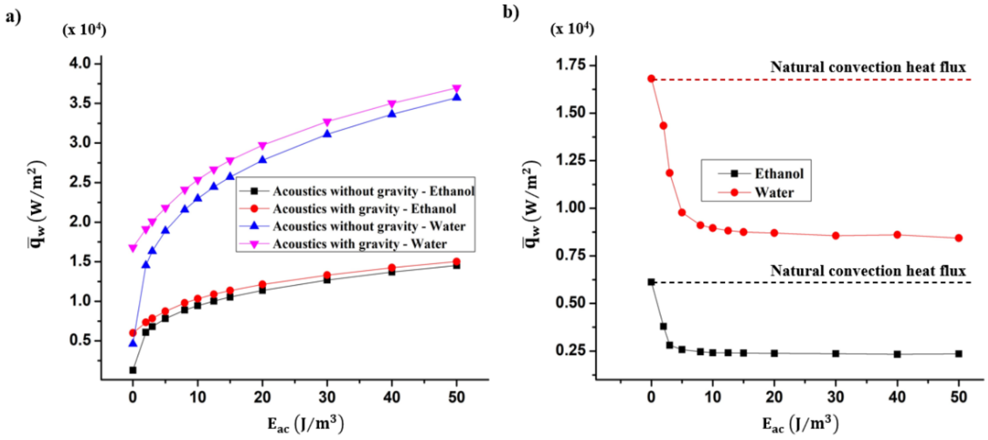

Fig 3: Resultant heat flux when standing wave applied: a) perpendicular to the direction of heat transfer–enhancement of heat transfer. b) parallel to the direction of heat transfer – suppression of natural convection.

Conclusion:

It is shown that when acoustic forces are applied perpendicular to the direction of heat transfer, it enhances heat transfer up to 11.2 times and 7.7 times in ethanol and water compared to pure conduction and 2.5 and 2.2 times in ethanol and water compared to natural convection. Also, when acoustic forces are applied parallel to the direction of heat transfer, natural convection heat transfer is suppressed by half or more for ethanol and water.

References

[1] S. Deshmukh, Z. Brzozka, T. Laurell, and P. Augustsson. Lab on a Chip **14**, 3394 (2014).
[2] J. T. Karlsen, P. Augustsson, and H. Bruus. Physical review letters **117**, 114504 (2016).

Acoustofluidics 2021
26-27 August 2021
Virtual Conference

Axial displacement of typical cells with 3D trapping in a high-frequency single beam acoustical tweezers

Zhixiong Gong[1], and Michael Baudoin[1,2]

[1]Univ. Lille, CNRS, Centrale Lille, Univ. Polytechnique Hauts-de-France, UMR 8520 - IEMN, F-59000 Lille, France
E-mail: zhixiong.gong@iemn.fr, michael.baudoin@univ-lille.fr,
URL: http://films-lab.univ-lille1.fr/michael
[2]Institut Universitaire de France, 1 rue Descartes, 75005 Paris

Introduction

High-frequency spiraling interdigitated transducers (S-IDTs) based on binary active holograms can produce focused vortex from MHz to GHz to trap microparticles [1] and cells [2], which could provide higher spatial resolution for selective trapping compared with the KHz to low MHz configuration with transducer array [3,4]. This kind of acoustical tweezers localize the acoustic energy in a small region near the focal point, which enable the selective manipulation of the targeted cells. While two dimensional demonstration of the selective manipulation of microparticles and cells in a standard microfluidic environment has been previously demonstrated [1,2], the 3D trapping ability of this design has not been revealed yet. In addition, in these previous works, the displacement of the object is obtained by the remote mechanical displacement of the transducer. In this work we show through numerical investigations (i) that S-IDTs of frequency 40 MHz enable to create a 3D radiation trap for cells and (ii) that this trap can be displaced axially without any moving part by tuning the excitation frequency.

Methods

Numerical simulations of the force exerted by the field produced by S-IDTs on a particle are performed

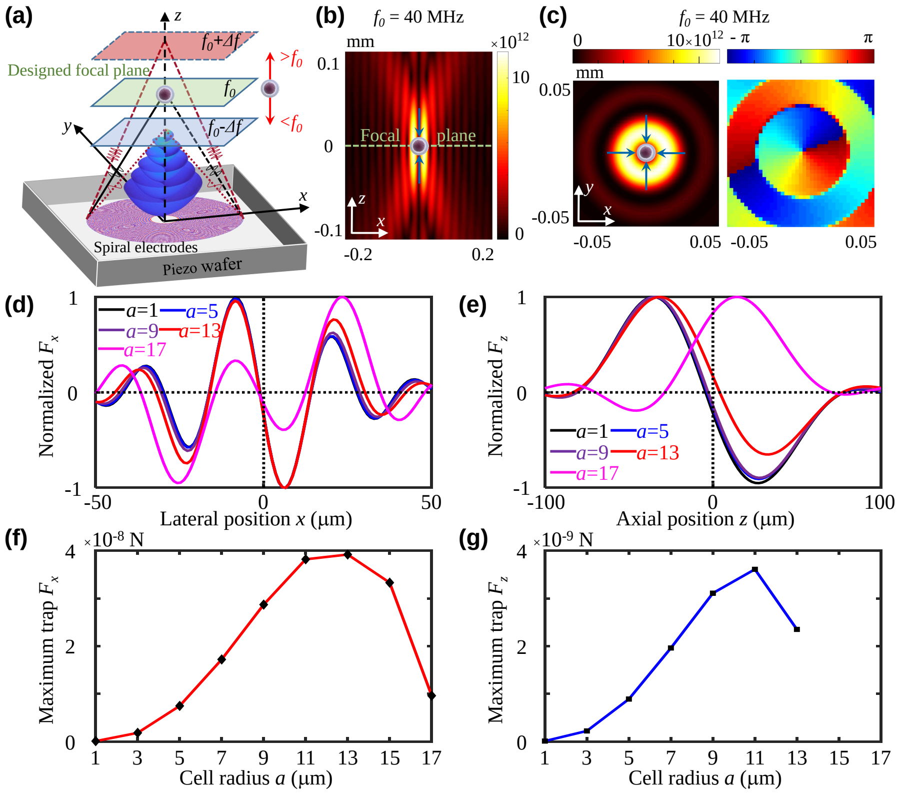

Figure 1: (a) The schematic of the high-frequency spiraling interdigitated transducers (S-IDTs) for a focsued vortex beam with the focal plane changed by tuning the excitation frequencies. The designed frequency is $f_0 = 40$ MHz. The focal plane moves away from the source plane when the excitation frequency is larger than the designed one f_0, while close to the source plane with lower excitation frequency. (b,c) the square of pressure amplitude in the propagation $(x, y = 0, z)$ and lateral $(x, y, z = 0)$ planes. The gradient forces show the potential for 3D trapping of a typical cell. (d) and (e) give the normalized lateral (at axial equilibrium positions) and axial radiation forces versus the positions for different cell radii $a = 1, 5, 9, 13,$ and 17 μm., while (f) and (g) describe the trapping forces (maximum restoring force) in Newton in the lateral and axial directions for cell radii from 1 to 17 μm.

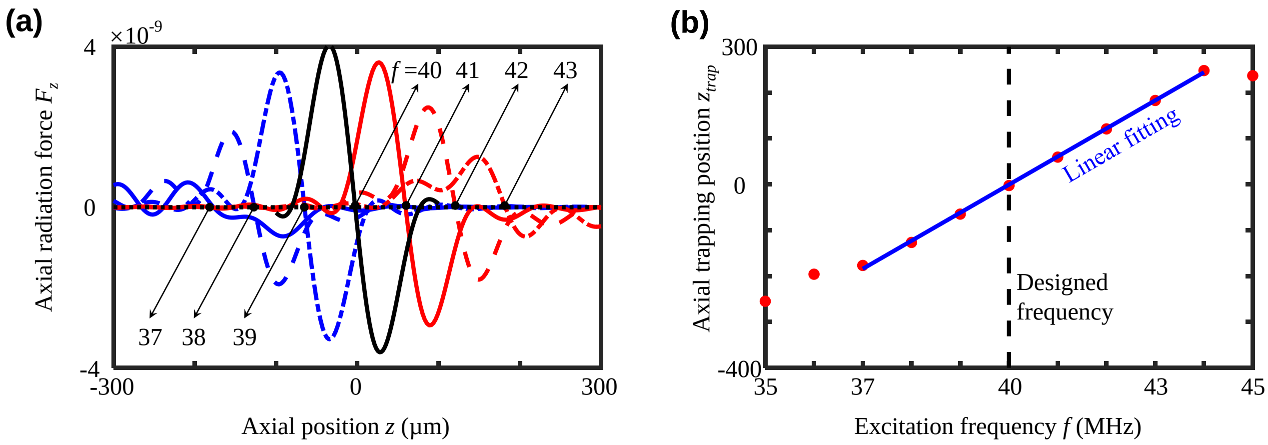

Figure 2: (a) Axial radiation force F_z versus position z for a cell with the radius $a = 11$ μm at different excitation frequencies $f = [37\text{-}43]$ MHz with the trapping positions pointed out with arrows. (b) The axial trapping positions versus the excitation frequencies. A linear relationship between the trapping position and excitation frequency is revealed around the designed frequency f_0, which provide a way to precisely displace the axial position of a cell when trapped in 3D.

based on the angular spectrum method [5,6] with our in-house code [2]. The typical cell is modeled as a liquid sphere with the acoustic parameter taken from Ref. [5]. The density and sound speed of the cell are 1100 kg/m^3 and 1508 m/s, while those of the surrounding water are 1000 kg/m^3 and 1500 m/s. The acoustic field is produced by the vibration of the S-IDTs and the acoustic pressure in the source plane is 0.1 MPa for the present simulations.

Results

The simulations show (i) that it is possible to obtain a 3D trap for cells with the radius up to 13 μm [see Fig.1] and (ii) that the axial position of the trap can be precisely displaced by switching the excitation frequency [see Fig.2]. As shown in Fig. 1(e), the pushing scattering force will dominate over the restoring gradient force when the cell radius is $a = 17$ μm so that there is no axial trapping in this case. Considering the amplitudes of the lateral and axial directions, the prior radius for 3D trapping of the cell is around $a = 11$ μm. This radius is hence chosen to study the axial trapping position with different excitation frequencies in Fig. 2. As clearly shown in Fig.2(a), the trapping position moves further away from the source when the excitation frequency is higher than the designed ($f_0 = 40$ MHz). While the trapping position moves closer to the source when the excitation frequency is lower. Furthermore, as shown in Fig. 2(b), the axial trapping positions of a typical cell have a good linear relationship with the driving frequency around the designed frequency and a 3D trap is maintained for all these positions (the lateral forces versus positions at the axial equilibrium positions for each frequency are omitted here for brevity). Note also that the axial spatial regime of precise displacement of the cell is more than 12 wavelength (40 times of the radius) with the tuning frequency at [37-44] MHz.

Conclusion and discussion

Typical cells have been demonstrated for 3D trapping and axial displacement at high frequency with theoretical model and numerical simulations [8]. The spatial resolution of the selective trapping is around one wavelength (37.5 μm) at 40MHz, which is close to the size of typical cells (5-20 μm). The axial position of the trapped cell can be precisely displaced by tuning the excitation frequency instead of physically moving the transducer or the microchannel, which can provide us one more degree of freedom to axially displace the cells with the present design of single beam acoustical tweezers.

References

[1] M. Baudoin, J.-C. Gerbedoen, O. B. Matar, N. Smagin, A. Riaud, and J.-L. Thomas. Sci. Adv. **5**, eaav1967 (2019).

[2] M. Baudoin, J.-L. Thomas, R. Al Sahely, J.-C. Gerbedoen, Z. Gong, A. Sivery, O. B. Matar, N. Smagin, P. Favreau, and A. Vlandas. Nat. Commu. **11**, 4244 (2020).

[3] D. Baresch, J.-L. Thomas, and R. Marchiano. Phys. Rev. Lett.**121**, 074301 (2018).

[4] A. Marzo, M. Caleap, Aand B.W. Drinkwater Phys. Rev. Lett. **120**, 044301 (2018).

[5] O.A. Sapozhnikov and M.R. Bailey J. Acoust. Soc. Am. **133**, 661-676 (2013).

[6] Z. Gong and M. Baudoin. J. Acoust. Soc. Am. **149**, 3469-3482 (2021).

[7] P. Augustsson, J.T. Karlsen, H.W. Su, H. Bruus, and J. Voldman Nat. Commu. **7**, 11556 (2016).

[8] Z. Gong and M. Baudoin. arXiv:2104.01089 (2021).

Acoustofluidics 2021
26-27 August 2021
Virtual Conference

A numerical simulation of pumpless-chaotic micromixer utilizing the vibration-induced flow

K. Kaneko[1], N. Ujikawa[1], Y. Hasegawa[2], T. Hayakawa[1], and H. Suzuki[1]

[1]Faculty of Science and Engineering, Chuo University, Tokyo, Japan
E-mail: kaneko@nano.mech.chuo-u.ac.jp, suzuki@mech.chuo-u.ac.jp, URL: https://nanobio.r.chuo-u.ac.jp/
[2]Institute of Industrial Science, The University of Tokyo, Tokyo, Japan

Introduction

The vibration-induced flow, in which a mean flow is induced around an object by applying a periodical vibration, has been applied for the fluid/particle micro-manipulation that does not require an external pump. We are developing a microfluidic system to realize efficient mixing of reagents in µL volume using the vibration-induced flow. In this study, we performed a numerical simulation to predict the mixing phenomena occurring in detail. By employing switching of vibration directions, we show that stretching and folding of the fluid element, a feature of chaotic advection, can be induced.

Background

In biotechnology, there are many applications to selectively capture and collect particulate matters such as protein complexes, vesicles, and bacteria using surface-modified microbeads. Because micro-scale flows in most biochips are laminar under their typical operating conditions, an active-mixing mechanism is necessary to efficiently mix these substances with small diffusion coefficients. Although many microfluidic devices have been developed that realize the collection of target nanoparticles from a sample containing miscellaneous molecular components [1], there remains a challenge in reducing the amount of samples due to the use of an external pump. Recently, a flow control technique known as vibration-induced flow is getting attracted, which requires no external pump, producing no dead volume [2, 3] (Fig. 1).

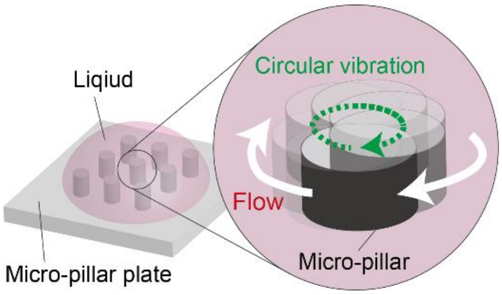

Figure 1: Conceptual diagram of the vibration-induced flow.

Thus, our goal is to develop a micromixer driven by the vibration-induced flow combined with the chaotic mixing theory [4]. In this work, we conducted a numerical simulation of the flow field in this mixer. The simulation was conducted for the micro-pillar with the cylindrical and asymmetric cross sections, to which rotational vibration with periodical switching was applied to expect the occurrence of chaotic mixing.

Procedure of numerical simulation

We solved the continuity and Navier-Stokes equations for the fluid bearing the horizontally circulating body force (centrifugal force) in the moving coordinate system fixed to the micro-pillar (Fig. 2 (a)) [5]. A periodic boundary condition was applied in the horizontal coordinates x and z. Then, the resultant time-dependent velocity field was transformed to the coordinate system at rest. The shape of a micropillar in the computational domain was introduced using a volume penalization technique [5]. From the obtained periodical flow field, we calculated the time-averaged flow field (the mean flow) by tracking fluid elements using the 4th order Runge-Kutta method. We calculated flows not only for cylindrical pillars but also for asymmetric cross-shaped pillars vibrated in different rotational directions.

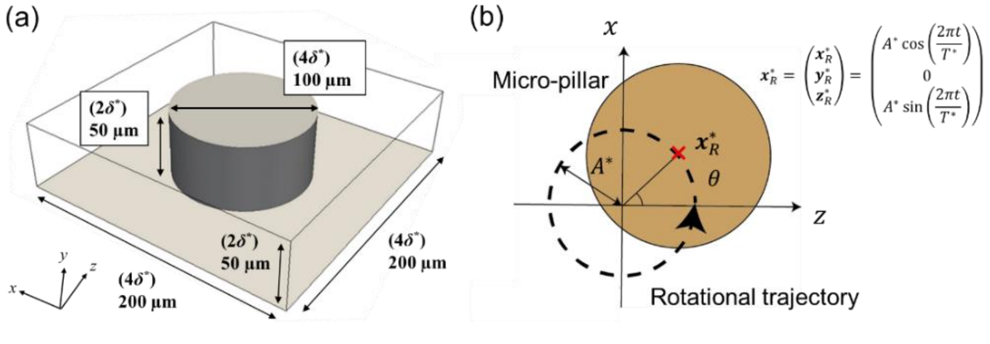

Figure 2: (a) Schematic of a coordinate system and computational domain. (b) Circular vibration of the micro-pillar. The frequency and amplitude of the vibration were set to f = 500 Hz and A = 4.0 µm, respectively.

Result and discussion

The vector plots of the average flow field at the middle of the pillar height were obtained in clockwise (CW) and counter-clockwise (CCW) directions (Fig. 3). In cylindrical cases, the flow swirled axisymmetrically around the pillars. The decrease in velocity at the top, bottom, left, and right of the pillar is due to interference with the adjacent pillar located 200 μm away. The averaged velocity vector plots for the asymmetric pillars rotated in the CW and CCW directions were also plotted (Fig. 3 (c, d)), which has the maximum velocity generated near the four tips of the pillars. In these cases, flows were slightly distorted and different between CW and CCW directions.

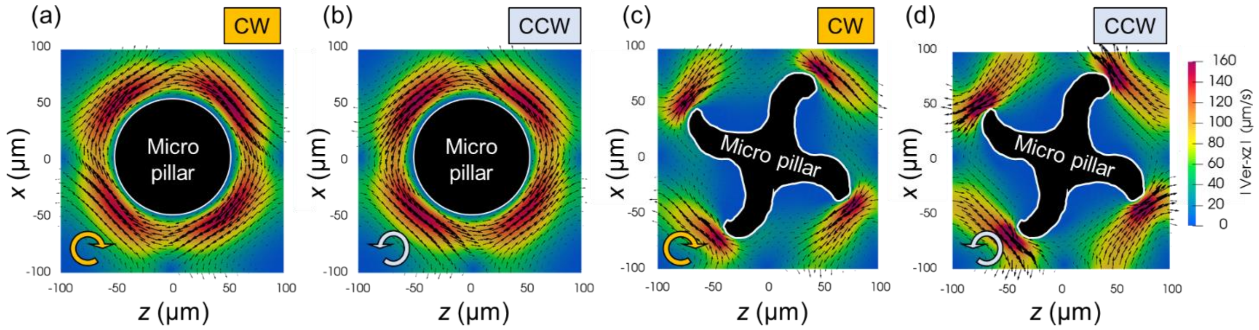

Figure 3: 2D vector plot of the averaged velocity flow field around (a, b) a cylindrical pillar and (c, d) an asymmetric pillar at height of h = 25 μm. (a, c) and (c, d) show results for CW and CCW rotational vibrations, respectively.

From the particle tracking simulation based on the above velocity fields using the 4th order Runge-Kutta method, we found that stretching and folding deformation of the fluid element, a prominent feature of chaotic advection [3], was induced only when the CW and CCW flow fields were switched at an appropriate time interval with a cylindrical (Fig. 4 (a, b, c)) and an asymmetric pillars (Fig. 4 (e, f, g)). The streamlines for CW and CCW directions were overlaid (Fig. 4 (d, h)). These diagrams revealed crossing of streamlines especially at the four internal cavities of the asymmetric pillar shape, where the folding process took place.

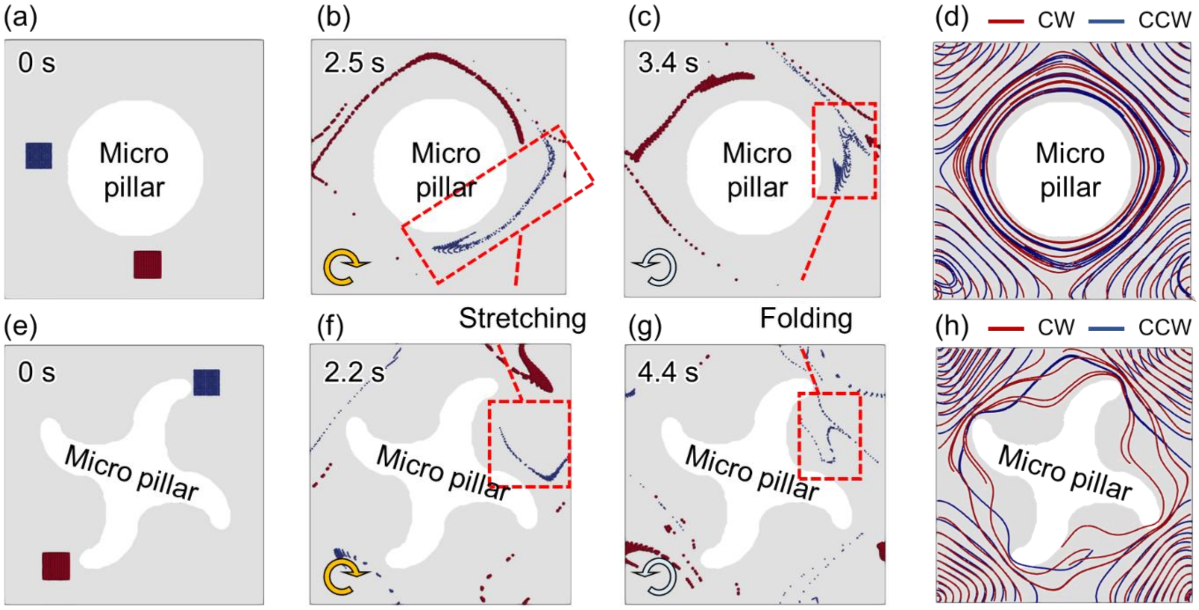

Figure 4: (a-c, e-g) Snapshots of the particle tracking simulation. The lumps of tracer particles initially located near the pillar. (d, h) Superposition of streamlines of the CW (red) and CCW (blue) flow fields. Upper figures (a, b, c, d) are for a cylindrical pillar, and bottom figures (e, f, g, h) are for an asymmetrical pillar.

Conclusion

In this work, we showed that the vibration-induced flow system is able to create a stretching and folding of the fluid element, which is an effective strategy for mixing in micro-scale flows. We will apply this chaotic theory to a micro-mixing system that realizes the efficient capturing of nanoparticles.

References

[1] Shao, H., et al., *Nat. Commun.*, **6**, 6999 (2015).
[2] Hayakawa, T. et al., *Micromachines*, **5**, 681-696 (2014).
[3] Hayakawa, T. et al., *Microflud. Nanofluid.*, **22**, 1281-1284 (2017).
[4] Stroock, A. D. et al., *Science*, **295**, 647–651 (2002).
[5] Kaneko, K. et al., *Micromachines*, **9**, 668 (2018).

Session 2 - Bio-Acoustic Systems

Invited Speaker

10:30 - 11:00

ACOUSTOFLUIDIC TECHNOLOGIES FOR TISSUE ENGINEERING
Diane Dalecki, Emma G. Norris, and Denise C. Hocking
University of Rochester, USA

Contributed Talks

11:00 - 11:10

ENABLING OFF-CHIP ANALYSIS FOR IN-DROPLET ENZYME REACTIONS USING ACOUSTOPHORESIS
Zhenhua Liu[1], Anna Fornell[1,2], and Maria Tenje[1]
[1]Uppsala University, SWEDEN and [2]Lund University, SWEDEN

11:10 - 11:20

BACTERIA PRECONCENTRATION USING AN ULTRASONIC NANOSIEVE WITHIN A MICROFLUIDIC DEVICE WITH FLUORESCENCE QUANTIFICATION
Bryan Ang, Ruhollah Habibi, Kellie Tuck, Victor Cadarso,
and Adrian Neild
Monash University, AUSTRALIA

11:20 - 11:30

ACOUSTIC DEFORMATION OF RED BLOOD CELLS
Andreas Link, Raymond Sparrow, Esther Richter,
Mustafa Zaimagaoglu, and Thomas Franke
University of Glasgow, UK

11:30 - 11:40

NON-INVASIVE NEUROMODULATION USING ULTRASOUND: MECHANISMS OF ACTION
Aditya Vasan and James Friend
University of California, San Diego, USA

11:40 - 11:50

ENDOTHELIAL CELL BRANCH FORMATION IN HYDROGEL USING TWO DIFFERENT FREQUENCY ULTRASOUNDS FOR MICROVASCULAR NETWORKS
Le Thi Huong[1], Andreas Lenshof[2], Van Thuy Duong[1], Huu Lam Phan[1],
Thomas Laurell[2], Kyo-in Koo[1]
[1]University of Ulsan, KOREA (ROK) and [2]Lund University, SWEDEN

11:50 - 12:00

USING ACOUSTOFLUIDICS TO ENGINEER SKELETAL MUSCLES
Dhananjay V. Deshmukh, Peter Reichert, Joel Zvick,
Oksana Dudaryeva, Ori Bar-Nur, Mark W. Tibbitt, and Jurg Dual
ETH Zürich, SWITZERLAND

Flash Talks

12:00 - 12:04 **ACOUSTOMICROFLUIDIC TRI-SEPARATION OF PROTEINS USING APTAMER-COATED MICROPARTICLES**
Muhammad Afzal[1], Jinsoo Park[2], Jessie S. Jeon[1], and Hyung Jin Sung[1]
[1]Korea Advanced Institute of Science and Technology (KAIST), KOREA (ROK) and [2]Chonnam National University, KOREA

12:04 - 12:08 **A BUBBLE-BASED ACOUSTOFLUIDIC DEVICE FOR THE STUDY OF ULTRASOUND THROMBOLYSIS**
Yuan Gao[1], Mengren Wu[1], Bruce Gaynes[2,3], and Jie Xu[1]
[1]University of Illinois, Chicago, USA, [2]Loyola University Medical Center, USA, and [3]Edward Hines Jr VA Medical Center, USA

12:08 - 12:12 **A SOUND IDEA TO STIMULATE CELLS: A NOVEL METHOD TO ACOUSTO-MECHANICALLY STIMULATE CELLS**
Christopher Markwell[1], Luying Feng[1], Ran Tao[1,2], Steven O'Reilly[3], Richard Fu[1], and Hamdi Torun[1]
[1]Northumbria University, UK, [2]Shenzhen University, CHINA, and [3]Durham University, UK

12:12 - 12:16 **NEURAL DIFFERENTIATION OF HUMAN EMBRYONIC STEM CELLS MEDIATED BY SURFACE ACOUSTIC WAVES**
Chao Sun[1], Jun Wei[3], Meng Cai[3], and Xin Yang[2]
[1]Northwestern Polytechnical University, CHINA, [2]Cardiff University, UK, and [3]iRegene Therapeutics Co., Ltd., CHINA

12:16 - 12:20 **SELF-ORGANIZATION OF HUMAN MESENCHYMAL STEM CELLS INTO SPHEROIDS TRAPPED IN ACOUSTIC LEVITATION**
Nathan Jeger-Madiot[1], Lousineh Arakelian[2], Niclas Setterblad[3], Patrick Bruneval[4], Mauricio Hoyos[1], Jérôme Larghero[2], and Jean-Luc Aider[1]
[1]Université de Paris-1, FRANCE, [2]Université de Paris, FRANCE, [3]Université de Paris Diderot, FRANCE, and [4]INSERM, FRANCE

12:20 - 12:24 **ACOUSTIC TRAPPING OF SUB-WAVELENGTH MICROPARTICLES AND CELLS IN RESONANT CYLINDRICAL SHELLS**
Qin Lin, Feiyan Cai, and Hairong Zheng
Chinese Academy of Sciences (CAS), CHINA

12:24 - 12:28 **ANALYSIS OF ACOUSTOPHORETIC FOCUSING USING THE OPEN-SOURCE 3D PARTICLE TRACKING TOOLBOX *DefocusTracker***
Massimiliano Rossi[1], Rune Barnkob[2], and Henrik Bruus[1]
[1]Technical University of Denmark, DENMARK and [2]Technical University of Munich, GERMANY

Acoustofluidics 2021
26-27 August 2021
Virtual Conference

Acoustofluidic Technologies for Tissue Engineering

Diane Dalecki[1,2], Emma G. Norris[2,3], and Denise C. Hocking[2,3]

[1]Department of Biomedical Engineering, University of Rochester, Rochester, NY 14627
E-mail: dalecki@bme.rochester.edu, URL: https://www.urmc.rochester.edu/labs/dalecki.aspx
[2]Rochester Center for Biomedical Ultrasound, University of Rochester, Rochester, NY 14627
[3]Department of Pharmacology and Physiology, University of Rochester Medical Center, School of Medicine and Dentistry, Rochester, NY 14642

Introduction. Acoustic fields are emerging as valuable tools to assist in the fabrication of engineered tissues and biomaterials [1-3]. Ultrasound fields offer versatility because they can interact with biological materials through both mechanical and thermal mechanisms with spatial and temporal resolution [4]. Our laboratory has innovated several ultrasound technologies to enhance fabrication of collagen-based engineered tissue constructs and biomaterials. In concert, we have developed a suite of high-frequency ultrasound imaging techniques to non-destructively visualize cellular organization and characterize collagen microstructure within three-dimensional (3D) hydrogel constructs [5]. This presentation will provide an overview of the development in our laboratory of novel ultrasound-based technologies for 3D cellular patterning, for fabrication of vascularized engineered tissue constructs, and for fabrication of collagen-based hydrogels with defined collagen microstructure and bioactivity.

Ultrasound standing wave fields for fabrication of vascularized tissue constructs. A key challenge in engineering functional artificial tissues is replicating the complex architecture present in native tissue structure. Furthermore, the organization of cells and extracellular matrix proteins within tissues can provide important signals that drive functional cell behaviors, such as cell migration, growth, and proliferation. In our laboratory, we have developed a novel technology that employs ultrasound fields to pattern cells in 3D within collagen hydrogels as a basis for fabricating complex, artificial tissue constructs [6-9].

In this technology, ultrasound standing wave fields (USWFs) are used to rapidly and non-invasively pattern cells and/or microparticles within 3D collagen-based hydrogels [6-9]. Acoustic radiation forces associated with USWFs provide non-invasive mechanical forces that rapidly drive cells to pressure nodes of the acoustic field [6-9]. The geometry of nodal regions is controlled by transducer design and positioning, and the magnitude of the acoustic radiation force is dependent upon acoustic exposure parameters and physical properties of cells. To ensure that 3D cell patterning is retained after the USWF is removed, cells are suspended within a collagen-based solution that undergoes a phase change from liquid to solid during the USWF exposure [6-9]. Using a single transducer/reflector configuration produces an USWF that patterns cells into nodal planes aligned perpendicular to sound propagation. The distance between nodal planar bands of cells is equal to ½ the wavelength of the ultrasound field, and the density of cells packed within each planar band is dependent on the acoustic pressure amplitude [6-9]. Using acoustic fields with frequency on the order of 1 MHz, we have employed this technique to pattern a variety of cells and/or microparticles within 3D collagen hydrogels with dimensions of $\sim$1 cm^3 [6-9]. We have also employed high-frequency ultrasound to visualize and characterize the resulting patterned hydrogels [9-11].

In one iteration of this acoustic patterning technology, we developed a process to create artificial microvessel networks within engineered collagen constructs [6-9]. USWFs were used to pattern endothelial cells within fabricated sample holders. Experiments investigated the influence of cell concentration, cell type, acoustic frequency, and pressure amplitude on cell patterning and microvessel formation. A 38-MHz focused ultrasound transducer was used to generate images of cell patterning within 3D hydrogels [9]. Immediately after acoustic patterning, cells were aligned in planar bands [6-9]. Within 24 h post-patterning, capillary-like sprouts began to emerge from planar bands of patterned cells [6]. Over a 10-day period, cell-mediated collagen fiber alignment was observed, and sprouts continued to develop and mature into lumen-containing, branching microvessel networks throughout the volume of the collagen hydrogel [6-9]. Histological observation confirmed vessels contained lumen and VE-cadherin staining provided evidence of intercellular junctions and microvessel integrity [9].

Importantly, the initial 3D spatial patterning of cells influences the resultant microvessel morphology [9]. Acoustic patterning of endothelial cells (HUVEC) with frequency of 1 MHz and pressure amplitude of 0.1 MPa produced dense, branching capillary-like networks with diameters of less than 25 microns [9]. Acoustic patterning at higher pressure amplitudes resulted in microvessel networks with larger diameter vessels [9]. As one example, constructs fabricated with 0.2 MPa ultrasound produced microvessels with diameters greater than 100 microns, while constructs fabricated with 0.3 MPa ultrasound were characterized by a broad distribution of microvessel diameters [9]. Interestingly, USWF patterning of endothelial cells isolated originally from small-diameter blood vessels formed larger vessels by design of initial acoustic spatial patterning [9].

Ongoing studies continue to expand this technology in new directions. Sequential acoustic patterning with different acoustic exposure parameters can be used to fabricate multi-layer composite hydrogels with different microvessel morphologies within each layer. New approaches to transducer design and USWF generation are underway. Importantly, ongoing work is focused on translating this technology to cell patterning and microvessel network formation in vivo for clinical applications.

Fabrication of bioactive collagen hydrogels using acoustic fields. Type I collagen is the primary structural component of extracellular matrices of native tissues, and engineered collagen-based hydrogels are employed in clinical therapeutics, pharmaceutical development, and tissue engineering and regenerative medicine research. The physical properties and bioactivity of collagen hydrogels are dependent on collagen microfiber structure. Collagen hydrogels fabricated in vitro typically lack the microstructure and bioactivity observed in collagen in vivo. Thus, technologies with the capacity to control collagen microstructure during hydrogel fabrication would be advantageous for producing hydrogels with designed bioactivity.

Ultrasound offers novel approaches for engineering hydrogels and biomaterials from extracellular matrix proteins [1]. In our laboratory, we have developed ultrasound-based techniques that employ mechanical and/or thermal mechanisms to non-invasively control collagen fiber microstructure and thereby influence cellular bioactivity [12-15]. Exposure of soluble collagen to ultrasound (8 MHz, 3-10 W/cm^2) during the process of collagen gel polymerization produced local changes in collagen microfiber structure [13-15]. Collagen gels exposed to ultrasound during fabrication exhibited radially aligned fibers and regions of increased collagen fiber density [13-15]. Acoustically-modified collagen hydrogels supported enhanced cell migration and cell-mediated collagen remodeling [13-14]. Similarly, skin explants seeded on acoustically-modified collagen hydrogels supported enhanced cell migration and cell-mediated collagen remodeling [13]. The effects of ultrasound on collagen microstructure were only observed when the ultrasound exposure occurred during the active phase of collagen fibril self-assembly [13-14]. Furthermore, exposing solutions of collagen and fibronectin to ultrasound during gel polymerization triggered fibronectin fibril formation and produced composite hydrogels that supported accelerated microtissue formation [15].

Conclusion. In summary, ultrasound provides innovative approaches to enhance the fabrication of engineered tissues and biomaterials. These ultrasound technologies hold exciting promise to expand the field of regenerative medicine.

References

[1] Dalecki D, Hocking DC. Ultrasound technologies for biomaterials fabrication and imaging. (Special Issue on Scaffolds for Regenerative Medicine) *Annals of Biomedical Engineering,* 43:747-761; 2015.

[2] Dalecki D, Hocking DC. “Advancing Ultrasound Technologies for Tissue Engineering” in Handbook of Ultrasonics and Sonochemistry. Editor, Muthupandian Ashokkumar, Springer, pgs. 1101-1126, 2016.

[3] Norris EG, Dalecki D, Hocking DC. Using acoustic fields to fabricate ECM-based biomaterials for regenerative medicine applications. *Recent Progress in Materials*, 2(3):24; doi:10.21926/rpm.2003018, 2020.

[4] Dalecki D. “Mechanical Bioeffects of Ultrasound” in Annual Reviews of Biomedical Engineering, Volume 6. Editor, Martin L. Yarmush, Annual Reviews, pg. 229-248, 2004.

[5] Dalecki D, Mercado KP, Hocking DC. Quantitative ultrasound for nondestructive characterization of engineered tissues and biomaterials. (Special Issue on Nondestructive Characterization of Biomaterials for Tissue Engineering and Drug Delivery) *Annals of Biomedical Engineering*, 44:636-648; 2016.

[6] Garvin KA, YousefHussien M, Helguera M, Dalecki D, Hocking DC. Spatial patterning of endothelial cells and vascular network formation using ultrasound standing wave fields. *J. Acout. Soc. Am.* 134:1483-1490; 2013.

[7] Garvin KA, Dalecki D, Hocking DC. Vascularization of three-dimensional collagen hydrogels using ultrasound standing wave fields. *Ultrasound Med. Biol.* 37:1853-1864; 2011.

[8] Garvin KA, Hocking DC, Dalecki D. Controlling the spatial organization of cells and extracellular matrix proteins in engineered tissues using ultrasound standing wave fields. *Ultrasound Med. Biol.* 136: 1919-1932; 2010.

[9] Comeau ES, Hocking DC, Dalecki D. Ultrasound patterning technologies for studying vascular morphogenesis in 3D. (Special Issue on 3D Cell Biology) *J. Cell Science*, 130:232-242; 2017.

[10] Mercado KP, Helguera M, Hocking DC, Dalecki D. Noninvasive quantitative imaging of collagen microstructure in three-dimensional hydrogels using high-frequency ultrasound. *Tissue Engineering, Part C*, 21:671-682; 2015.

[11] Mercado KP, Helguera M, Hocking DC, Dalecki D. Estimating cell concentration in three-dimensional engineered tissue constructs using high frequency quantitative ultrasound. *Annals of Biomedical Engineering,* 42:1292-1304; 2014.

[12] Garvin KA, VanderBurgh J, Hocking DC, Dalecki D. Controlling collagen fiber microstructure in three-dimensional hydrogels using ultrasound. *J. Acoust. Soc. Am.* 134:1491-1502; 2013.

[13] Norris EG, Dalecki D, Hocking DC. Acoustic modification of collagen hydrogels facilitates cellular remodeling. *Materials Today Bio*, 3:100018; 2019.

[14] Norris EG, Majeski J, Wayson S, Coleman H, Choe R, Dalecki D, Hocking DC. Non-invasive acoustic fabrication methods to enhance collagen hydrogel bioactivity. *Materials Research Express*, 6:125410; 2019.

[15] Norris EG, Dalecki D, Hocking DC. Acoustic fabrication of collagen-fibronectin composite gels accelerates microtissue formation. (Special Issue on Application of Extracellular Matrix in Regenerative Medicine) *Appl Sci,* 10(2907):1-16; 2020.

Acoustofluidics
2021
26-27 August 2021
Virtual Conference

Enabling off-chip analysis for in-droplet enzyme reactions using acoustophoresis

Zhenhua Liu[1], Anna Fornell[1,2], and Maria Tenje[1]

[1]Department of Materials Science and Engineering, Uppsala University, Uppsala, Sweden
E-mail: zhenhua.liu@angstrom.uu.se, URL: http://www.materialvetenskap.uu.se/embla
[2]MAX IV Laboratory, Lund University, Lund, Sweden

Introduction

Acoustophoresis is a commonly used technique to manipulate microbeads suspended in single-phase fluids [1]. Fornell *et al.* demonstrated that acoustophoresis can also be used to manipulate microbeads in droplets when the acoustic properties of the continuous phase match with the acoustic properties of the dispersed phase [2]. Water-in-oil droplets can be considered to be ideal vials for liquid mixing and reactions, as they allow for high throughput, low cross-contamination and low reagent consumption. Droplet microfluidics has previously been applied to study enzyme reactions [3,4]. However, these approaches are limited by on-chip detection and analysis since the enzyme is mixed with the product of the reaction inside the droplets. Here, we present an acoustofluidic chip where we can start the enzymatic reaction by injecting enzyme-coupled microbeads into the droplets containing the substrate by pico-injection and then stop the enzymatic reaction by removing the enzyme-coupled microbeads using acoustophoresis [5]. The analysis can then be performed off-chip, which allows for longer exposure times compared to performing the analysis in-line.

Experimental

The acoustofluidic chip used in this study contains droplet generation, pico-injector and three droplet splits. The width of the main flow channel is 380 µm and the height of all channels is 175 µm. The width of the side outlet channels at the droplet splits is 200 µm. The channels were dry-etched on a silicon wafer following a standard protocol and anodic bonding to a glass wafer [5]. A piezoelectric transducer (2 MHz) was glued to the chip to generate bulk acoustic standing waves in the channel. Low-temperature solder was injected as electrodes at the pico-injector. The water-in-oil droplets were generated by mineral oil as the continuous phase and 10 µM fluorescein diphosphate (substrate) as the dispersed phase. The enzyme (alkaline phosphatase) was coupled to polystyrene microbeads (5 µm in diameter) via streptavidin-biotin covalent binding and the enzyme-coupled microbeads were injected into the droplets via the pico-injector to start the enzyme reaction. The product of the reaction is fluorescein that can be separated from the droplets containing the enzyme-coupled microbeads using acoustophoresis. Prior to each of the droplet splits (marked 1-3 in Figure 1) the enzyme-coupled microbeads were focused in the center of the channel due to the acoustic focusing so that a small portion of the droplet, containing only product and no enzyme, could be collected from the side outlet channel. The three side outlet channels are placed in series along the main flow channel and they can be used independently to split the droplets (Figure 1). The fluorescein concentration in the collected droplets from each split was quantified using a fluorescence microscope.

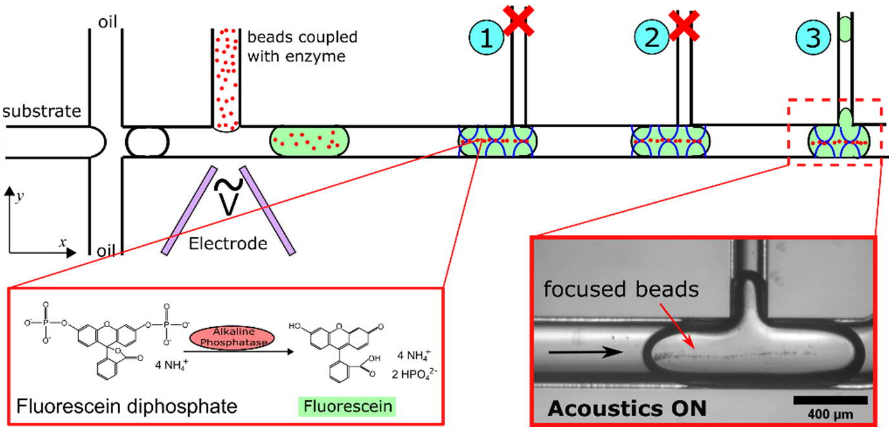

Figure 1: Schematic of the chip design and the enzymatic process. Square electrical waves (5 kHz, 100 V_{pp}) are applied on the electrodes for the pico-injection. The 5 µm enzyme-coupled microbeads are focused in the center of the droplet by standing bulk acoustic waves (1.8 MHz, 30 V_{pp}). The reaction product is separated through split 3 by blocking split 1 and split 2. The length of the reaction channel is not according to scale.

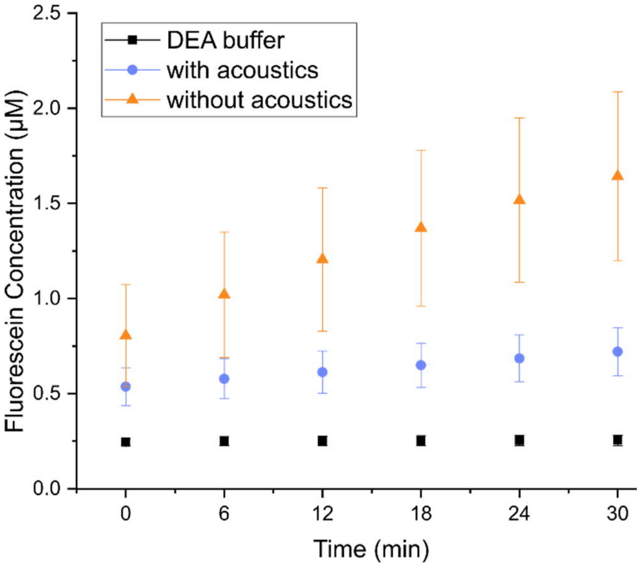

Figure 2: Fluorescein concentration in the droplets collected from split 3 with or without acoustics applied. Diethanolamine (DEA) buffer was injected into droplets containing substrate through the pico-injector as control. When no acoustics was applied, the enzyme-coupled microbeads were not separated from the collected droplets meaning that the enzymatic reaction continued in the collected droplets, as indicated by the increasing fluorescein concentration. With acoustic focusing applied, the reaction is stopped when the aliquots are taken from the droplets.

Results and Discussion

The flow rates for the continuous phase, the dispersed phase and the pico-injection were 2 µL/min, 1 µL/min and 0.5 µL/min, and only the outlet from split 3 was open for droplet collection (Figure 1). With acoustics applied, the reaction time, when the droplets flow from the pico-injection to the split 3, was 115 s. Droplets were collected from split 3 and the fluorescent intensity of the collected droplets with acoustics or without acoustics applied was measured for 30 minutes, and diethanolamine buffer was injected into droplets containing substrate through the pico-injector as control (Figure 2). With the acoustics applied the fluorescein concentration only increased slightly as most of the enzyme-coupled microbeads were removed by acoustophoresis, whereas without the acoustics applied the fluorescein concentration increased significantly over time as the reaction could continue in the collected aliquots.

Conclusion

We present a droplet acoustofluidic platform to separate the reaction product using acoustophoresis and demonstrate off-chip analysis by using the standard enzyme system alkaline phosphatase conversion of fluorescein diphosphate. Droplets containing fluorescein diphosphate were generated on-chip and the reaction was started by the pico-injection of enzyme-coupled microbeads. The reaction product was separated at the droplet split by removing the enzyme-coupled microbeads using acoustophoresis. We demonstrate that the reaction time can be fixed with the acoustics applied and the collected droplets can be taken off-chip for analysis.

References

[1] A. Lenshof, C. Magnusson and T. Laurell. Lab Chip **12**, 1210-1223 (2012).
[2] A. Fornell, F. Garofalo, J. Nilsson, H. Bruus and M. Tenje. Microfluidics and Nanofluidics **22**, 75 (2018).
[3] E. M. Miller and A. R. Wheeler. Anal. Chem. **80**, 1614-1619 (2008).
[4] S. L. Sjostrom, H. N. Joensson and H. A. Svahn. Lab Chip **13**, 1754-1761 (2013).
[5] Z. Liu, A. Fornell and M. Tenje. Biomicrofluidics **15**, 034130 (2021).

Acoustofluidics 2021
26-27 August 2021
Virtual Conference

Bacteria preconcentration using an ultrasonic nanosieve within a microfluidic device with fluorescence quantification

Bryan Ang[1,3], Ruhollah Habibi[1], Kellie Tuck[2], Victor Cadarso[1,3], and Adrian Neild[1]

[1]Department of Mechanical and Aerospace Engineering, Monash University, Melbourne, Australia
E-mail: bryan.ang@monash.edu, URL: https://www.appliedmicronanolab.com
[2]School of Chemistry, Faculty of Science, Monash University, Melbourne, Australia
[3]Centre to Impact Antimicrobial Resistance, Faculty of Medicine, Nursing and Health Sciences, Monash University, Melbourne, Australia

Introduction

Bacteria preconcentration enables the detection and quantification of bacteria cells in low abundance samples ($<10^4$ CFU/mL) which otherwise would not be possible for many traditional detection techniques such as colony counting from plate cultures, mass spectrometry and DNA amplification via PCR or LAMP [1]. Hence, a preconcentration strategy is often necessary to allow for many of these strategies to be applied. Acoustic radiation forces have been widely used within microfluidic systems to manipulate suspended matter in a dilute sample. However, in this experimental study, we employ a similar strategy as recent work by Habibi et.al [2,3], by using a packed bed of 15μm polystyrene microparticles instead, that are resonated using surface acoustic waves (SAW) at high frequency to capture bacteria cells. We determine the preconcentration efficiency of the system using *E. coli* bacteria cells by characterising the capture and release efficiencies of the microfluidic system using fluorescence microscopy. The system is able to achieve a capture efficiency of 100% and an average release efficiency of about 80% at the highest power (5.5W) of SAW activation. The system also exhibits low undesired adhesion of less than 10% for high concentrations of bacteria cells ($>10^6$ CFU/mL) and an extreme low of 1% for 10^5 CFU/mL allowing for high concentration sample retrieval for further analysis.

Working principle and device showcase

The microfluidic device consists of a PDMS channel that is bonded to piezoelectric substrate, lithium niobate with gold-deposited interdigitated transducers patterned on its surface. A packed bed of polystyrene microparticles were excited with a surface acoustic wave at 70MHz. Each microparticle vibrating within the packed bed generates an interparticle force, known as the Bjerknes force, which attracts fluorescent-stained bacteria cells as they travel through the packed bed. Figure 1 below shows the interesting observations of the packed bed before and after SAW activation for the capture of bacteria cells. The intensity of the green fluorescence is high when the SAW is on, exhibiting high efficiency of capture of bacteria cells.

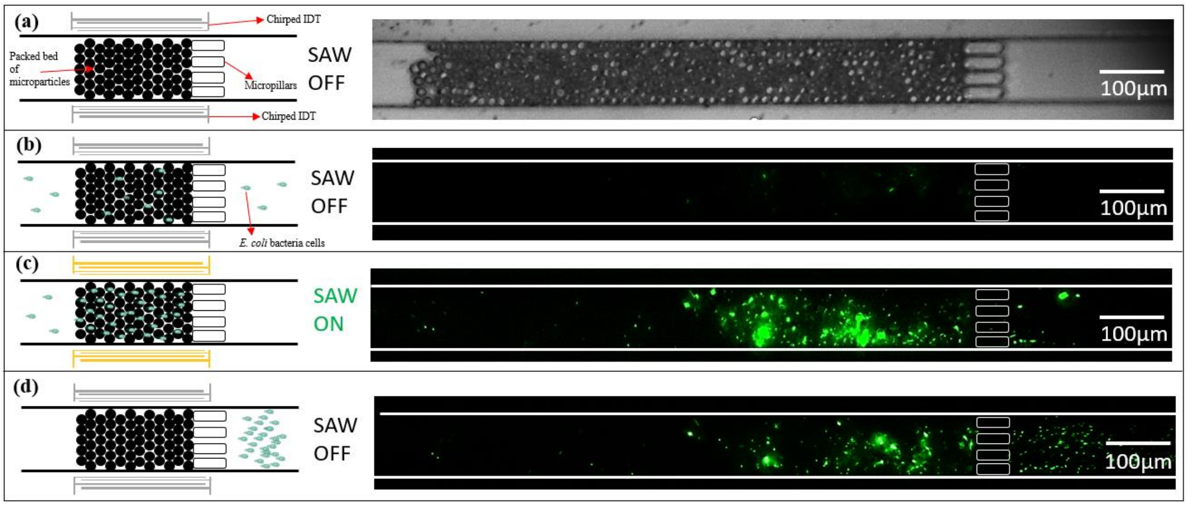

Figure 1: Schematic on the left of each panel illustrates the different stages of use of the microfluidic nanosieve that uses a surface wave activated (SAW) packed bed of microparticles to trap *E. coli* bacteria cells. The right side of each

panel shows a bright field or fluorescence microscopy image taken for each stage of the process. (a) Left: Illustration shows the packed bed of microparticles, chirped IDTs and micropillars that hold the microparticles. Right: A bright field image of the packed bed of microparticles that fill the PDMS microchannel. (b) Left: Illustration shows the introduction of bacteria cells into the channel. Right: A fluorescence microscopy image of bacteria flowing through the packed bed with little undesired adhesion without SAW activation. (c) Left: Illustration shows SAW activation and the immediate capture of bacteria cells. Right: Fluorescence microscopy image showing a large increase in fluorescence intensity within the packed bed exhibiting high efficiency capture of bacteria cells over a period of 30s. (d) Left: Illustration shows the release of bacteria cells when the SAW is turned off. Right: Fluorescence microscopy image showing the immediate release bacteria as a large batch concentrated batch when the SAW is turned off.

Preliminary results and discussion

The efficiency of the system was characterised using fluorescence microscopy for increasing powers, concentrations and flow rates. Efficiencies were calculated based on cell counts entering and leaving the packed bed during and after SAW excitation. For experiments done for flow rate and power, the concentration of cells was fixed at ~5.6x10^6 CFU/mL. As seen in Figure 2 (a), the capture efficiency shows a general increase across increasing powers, reaching 100% at the highest power used, 5.5W using a fixed flow rate of 0.05 µl/min. The release efficiency is maintained, ranging from 70-90% across the powers used. Interestingly, from Figure 2 (b), the capture and release efficiencies do not reduce at higher concentrations up to a 100-fold increase in concentration. Undesired adhesion also drastically reduces to as low as 1% at 10^5 CFU/mL. With regard to flow rate, as seen in Figure 2 (c), the capture efficiency was highest at the lowest flow rate of 0.05uL/min. Increasing the flow rates, shows gradual decrease in capture efficiency but slightly improved release efficiencies.

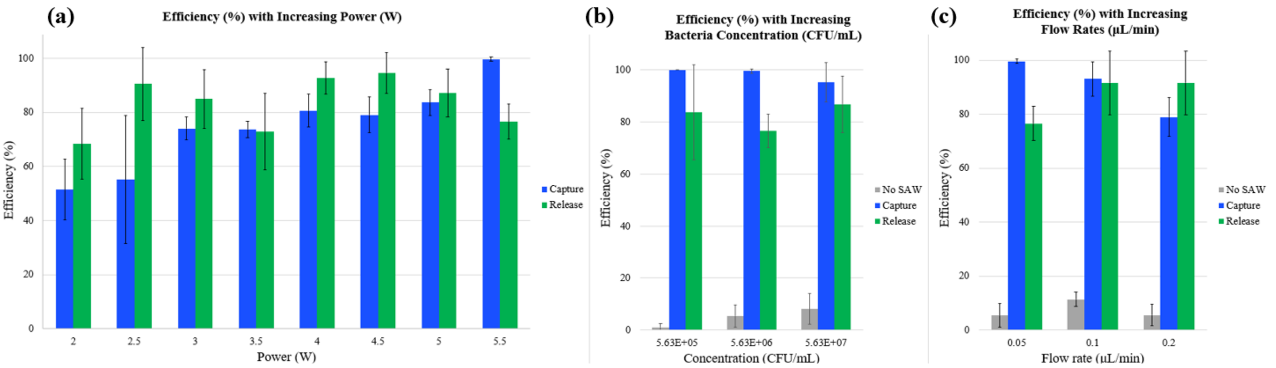

Figure 2: These graphs show the change in capture and release efficiencies across various characterized parameters of the microfluidic system. (a) Capture and release efficiency with increasing power. (b) Capture and release efficiency with increasing bacteria concentration. (c) Capture and release efficiency with increasing flow rate.

Future work

Further work is being done to explore lower concentrations down to <10^4 CFU/mL, and to verify results via collecting the preconcentrated sample for colony counting. We are also exploring a change of IDT design from chirped IDTs to straight IDTs which typically exhibit lower reflection values, which allows for more energy to be coupled into the fluid. This would allow us to use a much lower power regime and higher flow rates for higher throughput.

Conclusion

We have developed an active bacteria preconcentration microfluidic platform that is capable of completely capturing (100% capture efficiency) bacteria cells using an ultrasonic nanosieve, with a pore size 4.6 times larger than the size of the bacteria cell to be captured. The performance of the system was characterized with fluorescence microscopy and results show great promise with high capture efficiencies even for solutions with very high bacteria concentrations. The device maintains a high release efficiency of about 80% across all concentrations. The acoustic activated nanosieve also shows minimal undesired adhesion (when the SAW is inactive), of 10% or less, allowing for long-term repeated use of a single device. Overall, this ultrasonic nanosieve microfluidic platform will enable the integration of low-complexity detection systems and provides a novel alternative to preconcentration of bacteria cells.

References

[1] Zhang, D., et al. (2018). "Detection of Pathogenic Microorganisms by Microfluidics Based Analytical Methods." Analytical Chemistry **90**(9): 5512-5520.

[2] Habibi, R. and A. Neild (2019). "Sound wave activated nano-sieve (SWANS) for enrichment of nanoparticles." Lab on a Chip 19(18): 3032-3044.

[3] Habibi, R., et al. (2020). "Exosome trapping and enrichment using a sound wave activated nano-sieve (SWANS)." Lab on a Chip 20(19): 3633-3643

Acoustofluidics 2021
26-27 August 2021
Virtual Conference

Acoustic deformation of red blood cells

Andreas Link[1], Raymond Sparrow[1], Esther Richter[1], Mustafa Zaimagaoglu[1], and Thomas Franke[1]

[1]Division of Biomedical Engineering, School of Engineering, University of Glasgow, Oakfield Avenue, G12 8LT Glasgow, UK
E-mail: Thomas.Franke@glasgow.ac.uk, https://www.gla.ac.uk/schools/engineering/staff/thomasfranke/

Introduction

Mechanical properties of cells provide key insights into the type, differentiation and/or pathology of a cell.[1] The mechanical analysis of a cell population, such as a blood sample, enables meaningful biological and medical interpretation for diagnosis and monitoring of diseases. There are number of diseases which alters the mechanical properties of human red blood cells (RBCs). We demonstrate an acoustic device to mechanically probe a population of red blood cells on the single cell level.[2]

Methods

The acoustic field is exited in a microfluidic channel device (as shown in Figure 1) which is generated by a single interdigital transducer (IDT) deposited on a piezoelectric LiNbO3 substrate containing 60 finger pairs of electrodes and an aperture of 500 µm width, operating at a frequency of 162.2 MHz. A polydimethylsiloxane (PDMS) replica containing the channel features is placed on the substrate. The microfluidic design contains a U-shaped channel geometry. The bottom of the U is the section where cells are probed, the left and right arms are the inlet and outlet, respectively. The probing section has a length of $l = 200$ µm, a width of $w = 22.5$ µm and a height of $h = 10$ µm. In addition, the PDMS mould contains a cavity above the IDT to prevent damping and is separated by a wall of 60 µm to the fluid filled channel.

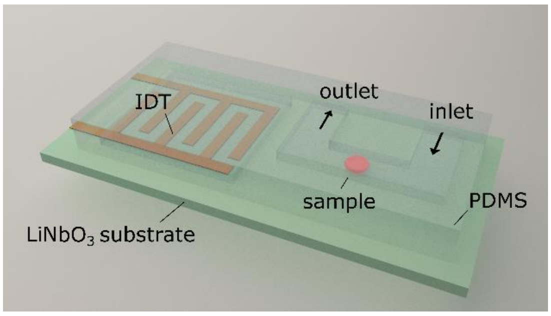

Figure 1: Schematic representation of the acoustofluidic hybrid device. The setup is composed of a structured PDMS mould aligned on top of a piezoelectric substrate. RBCs entering the microchannel through the inlet are captured in the microchannel by a stationary acoustic field. The field is generated by a planar interdigitated transducer deposited onto the substrate. Probed RBCs are released by switching off the field after measurement through the outlet tubing.[2]

The device operates by exciting a surface acoustic wave in a microfluidic channel creating a stationary acoustic wave field of nodes and antinodes.[3,4] Red blood cells are attracted to the nodes and are deformed. Using a stepwise increasing and periodically oscillating acoustic field we study the static deformation of individual RBCs one by one. We quantify the deformation by the Taylor deformation index *D*. The precision of the measurement allows to distinguish between individual cells in the suspension and provides a quantitative viscoelastic fingerprint of the blood sample at single cell resolution. The method overcomes limitations of other techniques that provide averaged values and has the potential for high-throughput.

Results and discussion

We observe an increasing deformation of the cell with increasing acoustic power as shown in Figure 2. We quantify the deformation by finding the contour of the cell and fitting it with an ellipse using an image analysis software (ImageJ). From the elliptical fit, we determine the semi-major and semi–minor axes *a* and *b*, respectively and calculate the Taylor deformation *D* according to:

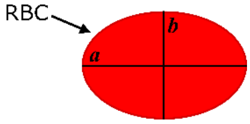

$$D = \frac{a-b}{a+b} \tag{1}$$

To improve the statistics of the measurement and verify reversibility and reproducibility, a square wave function for power input with constant amplitude. Each RBC is subjected to multiple periodic steps of deformation. The periodicity of the exciting square wave is $T = 6$ s and was chosen to be significantly larger than typical relaxation times reported in the literature (0.1 s $< \tau <$ 0.5 s).[5] To observe the deformation of RBCs, cells were viewed using bright-field microscopy and movies were recorded at high frame rates using a high-speed camera. Each movie is automatically analysed frame by frame using image and data analysis and the deformation index D is plotted against time as shown in Figure 3.

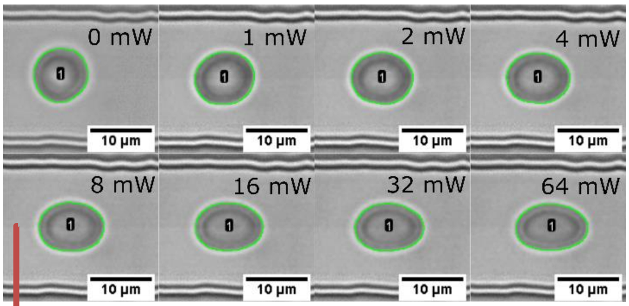

Figure 2: Micrographs and analysis of a RBC in the probing section. Without application of an acoustic field the fitted contour (green line) is nearly circular and becomes progressively elliptical by increasing the acoustic amplitudes from 1 mW to 64 mW (0 dm to 18 dBm) in doubling steps. The green contour around the cell was automatically analysed using image analysis software ImageJ and the build in function “Analyse Particles”. The RBC is labelled with a number, here cell #1. The black scale bar is 10 µm.[2]

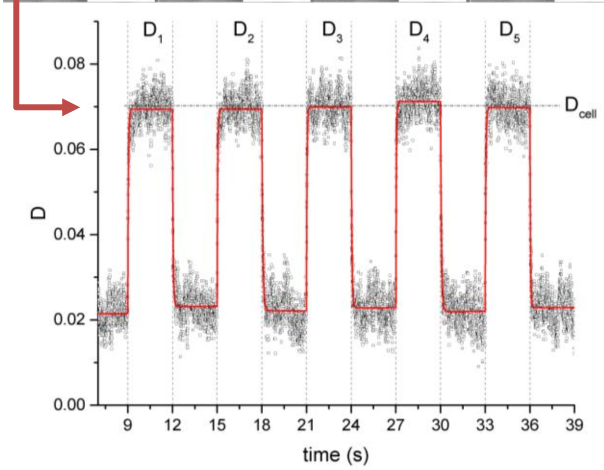

Figure 3: Deformation index D of an RBC as obtained from the contour analysis in xy-plane against time. The period of deformation and relaxation interval is $T = 6$ s. The measuring cycle was started by the trigger function of the camera at 9 s. The RBC is initially trapped using a power input of 0.8 mW (-1 dBm) and then periodically elongated by repeated steps between 8 mW (9 dBm) and 0.8 mW (- 1 dBm). Movies of the deformation at a frame rate of 250 frames/s were taken, each frame was analysed and D determined. The continuous red line in the plot indicates simple exponential fits to capture the relaxation process. D_1, …, D_5 indicates the saturation plateau value of the deformation following each power increase step and are used to determine the mean value for the deformation over 5 cycles by $D_{cell}=1/5\sum D_i$. The error of D_{cell} is calculated from the scattering of the saturation values D_i.[2]

Conclusion

A microfluidic device has been presented using standing surface acoustic waves to analyse a cell population of RBCs mechanically. This method allows to determine the elastic parameters of single RBCs, providing a viscoelastic fingerprint of the RBC sample at single cell resolution. This technique has great potential for automation for high-throughput screening of blood samples, for example, to monitor or detect disease, particularly in early stages when small numbers of diseased cells form a subpopulation. This can be used to characterize a cell population by its viscoelastic fingerprint for example to identify or monitor disease. Comparison with detailed simulations of both the acoustic field and the erythrocyte shape should be used in future, to refine the simple two parameter model presented here, and allow more specific interpretation of the transient shape deformations.

References

[1] J. Lin, D. Kim, H. T. Tse, P. Tseng, L. Peng, M. Dhar, S. Karumbayaram and D. Di Carlo, *Microsystems Nanoeng.*, **3**, 17013 (2017).
[2] A. Link and T. Franke, *Lab Chip*, **20**, 1991–1998 (2020).
[3] C. Devendran, D. J. Collins, Y. Ai and A. Neild, *Phys. Rev. Lett.*, **118**, 154501 (2017).
[4] D. J. Collins, R. O’Rorke, C. Devendran, Z. Ma, J. Han, A. Neild and Y. Ai, *Phys. Rev. Lett.*, **120**, 074502 (2018).
[5] S. Braunmüller, L. Schmid, E. Sackmann and T. Franke, *Soft Matter*, **8**, 11240 (2012).

Acoustofluidics
2021
26-27 August 2021
Virtual Conference

Non-invasive neuromodulation using ultrasound: mechanisms of action

Aditya Vasan[1], James Friend[1]
[1]Medically Advanced Devices Laboratory, Department of Mechanical and Aerospace Engineering, Jacobs School of Engineering and Department of Surgery, School of Medicine, University of California San Diego, La Jolla CA 92093 USA
E-mail: advasan@eng.ucsd.edu, URL: http://www.friend.ucsd.edu

Introduction

Non-invasive ultrasound neuromodulation has the potential to revolutionize the treatment of diseases such as Parkinson's and epilepsy(1). Although clinical trials are already underway for these conditions, there are limitations in our understanding of the underlying mechanism of action of ultrasound on neurons. We present a mathematical model that predicts neuronal activity when an ultrasound stimulus is provided and we provide experimental data that supports our model. Using novel high-speed digital holographic imaging (2), we show membrane deflection due to ultrasound can result in upto 150 nm deflection *in vitro*, corresponding to the predictions of the model.

Digital holographic imaging of membrane deflection

Conventional techniques to image cells lack phase information and typically rely on differences in intensity of light transmitted through a sample. An alternative, digital holographic microscopy (DHM), is a method that preserves phase information and this enables three-dimensional image reconstruction. We use high-speed DHM (40,000 frames per second) to visualize the real-time displacement of neuronal membranes under the influence of ultrasound. A schematic of our setup is shown in Fig. 3a. We show that deflection can range from 150 nm for neurons to as much as 250 nm for human embryonic kidney (HEK) cells *in vitro* as seen in Fig. 3b.

Membrane deflection model

Our two-dimensional model for membrane deflection assumes that the cell is fixed at the periphery. This is similar to conditions *in vitro*, where cells are adherent on a coverslip and *in vivo* where cells are attached to the extracellular matrix. Anchoring is important as it describes the characteristic length over which the range of wavemodes may occur on the membrane. The ultrasound stimulus is provided in the form of a burst, which results in a sinusoidally varying pressure field that causes membrane deflection between the anchor points. Fig. 2a is a schematic of membrane deflection due to ultrasound and Fig. 2b represents deflection at varying values of surface tension and membrane anchor length.

Model predictions of action potentials and electrophysiology

The generation of action potentials in a neuron is described by models such as the Hodgkin Huxley equation (3),

$$\frac{dV_m}{dt} = -\frac{1}{C_m}\left[I_{\text{app}} + I_{\text{Na}} + I_{\text{Kd}} + I_{\text{M}} + I_{\text{leak}}\right]. \tag{1}$$

The input to this model is typically an electrical current, but we present a modified version with an ultrasound-induced capacitive current. This occurs due to an area change between the anchor locations and leads to transmembrane capacitance changes, leading to the generation of action potentials in a neuronal model. We confirm the predictions of the model using current clamp electrophysiology.

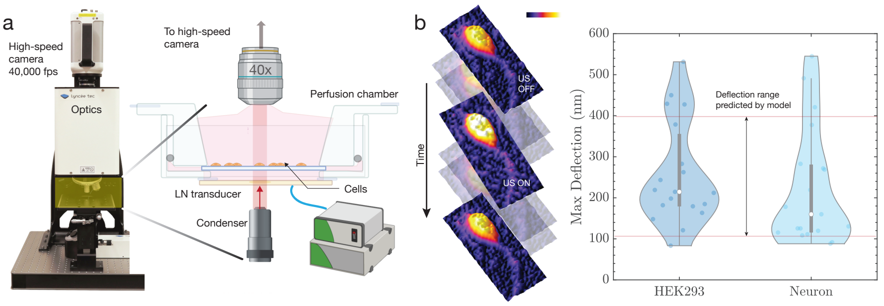

Figure 1: Deflection of neuronal membranes due to ultrasound was verified using **(a)** high-speed digital holographic microscopy. The setup enables reconstruction of **(b)** three-dimensional phase images with nanometer-scale precision, enabling estimation of deflection of HEK and neuronal membranes due to ultrasound.

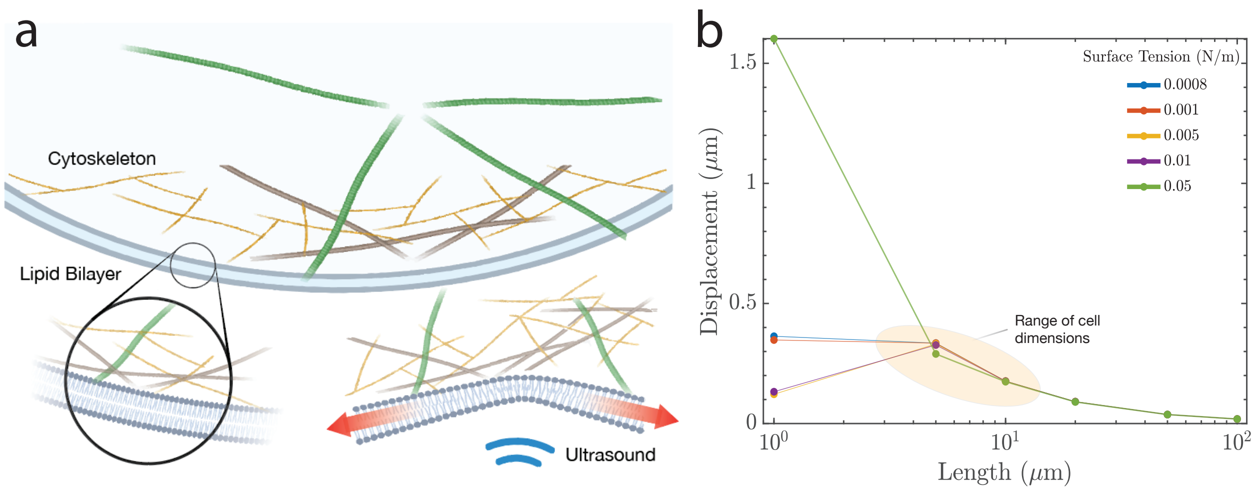

Figure 2: Ultrasound induces **(a)** membrane deflection that results in an area increase between anchor locations of the cell. This leads to downstream transmembrane voltage changes. Our **(b)** model predicts deflection range of 100-400 nm at varying values of surface tension and membrane anchor length.

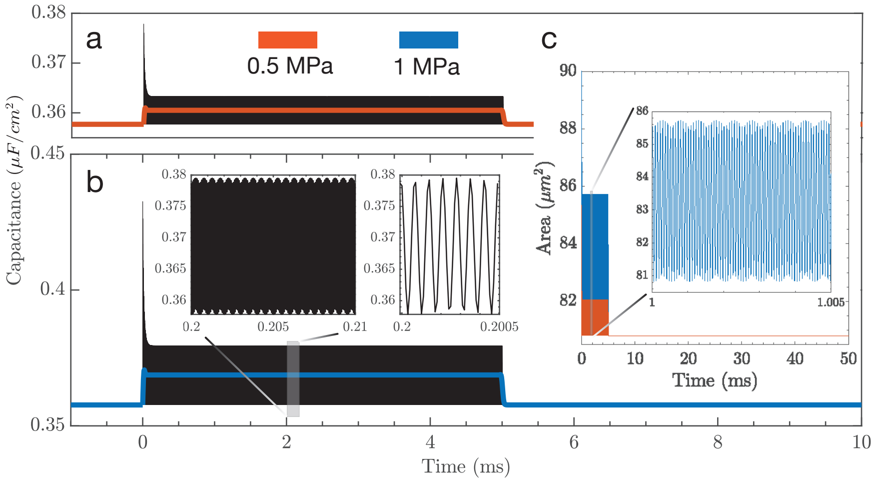

Figure 3: The mechanism of action of ultrasound on neuronal membranes involves **(a,b)** capacitance changes taking place over the stimulus duration. This is due to **(c)** a change in area occurring between the two anchor locations. The area (and hence the capacitance) change is dependent on the frequency and pressure of the ultrasound stimulus and these parameters govern whether action potentials are triggered.

Conclusion

Our model presents insights into the the generation of action potentials due to mechanical deflections and is supported by models put forth in the past (4). Taken together, these three results conclusively show that ultrasound results in the generation of action potentials due to membrane perturbations that lead to transient area changes. Our model shows that these pertubrations translate to transmembrane voltage changes and we confirm the predictions of the model using electrophysiology. We also demonstrate the use of a novel imaging technique, high-speed holography to visualize acoustic phenomenon with nanometer-scale precision.

References

[1] T. Yang, J. Chen, B. Yan, and D. Zhou, "Transcranial ultrasound stimulation: a possible therapeutic approach to epilepsy," *Medical hypotheses*, vol. 76, no. 3, pp. 381–383, 2011.

[2] U. Schnars and W. P. Jüptner, "Digital recording and numerical reconstruction of holograms," *Measurement science and technology*, vol. 13, no. 9, p. R85, 2002.

[3] L. Abbott and T. B. Kepler, "Model neurons: from hodgkin-huxley to hopfield," in *Statistical mechanics of neural networks*, pp. 5–18, Springer, 1990.

[4] T. Heimburg and A. D. Jackson, "On soliton propagation in biomembranes and nerves," *Proceedings of the National Academy of Sciences*, vol. 102, no. 28, pp. 9790–9795, 2005.

Acoustofluidics 2021
26-27 August 2021
Virtual Conference

Endothelial cell branch formation in hydrogel using two different frequency ultrasounds for microvascular networks

Le Thi Huong[1], Andreas Lenshof[2], Van Thuy Duong[1], Huu Lam Phan[1], Thomas Laurell[2, *], and Kyo-in Koo[1, *]

[1]Department of Biomedical Engineering, School of Electrical Engineering, University of Ulsan, Ulsan, Republic of Korea
E-mail: lehuong94alhp@gmail.com, URL: http://mdl.ulsan.ac.kr
[2]Department of Biomedical Engineering, Lund University, Lund, Sweden

* These authors equally contribute as corresponding authors.

Introduction

Microvasculature pervades almost all tissues and organs of the human body and supplies sufficient nutrients and oxygen to every single cell [1]. Up to date, in tissue engineering, one of the most important challenges is to generate dense vascularized networks. To do that, endothelial cells (ECs) are needed to contribute to vessel networks formation and vascular wall integrity [2]. Fabrication of branching structure with ECs is a first and important step for engineered micro-vascular networks. After constructing EC branching networks, vasculogenesis and angiogenesis sprouting are two principle mechanisms for connected vascular networks to form [3]. Previously, we reported fibroblast cell network formation using ultrasound [4]. In this work, we present branched human umbilical endothelial cell (HUVEC) patterning followed by vasculogenesis and angiogenesis.

Merging into one vessel in the acoustically aligned region as four parallel lines

Acoustofluidic device proposed in our previous work (Fig. 1) was utilized to pattern HUVEC as branch structure in alginate hydrogel [4]. Mixture of 1.5 mL of alginate (MERCK, Madison, USA) 0.5% w/v and 200 µL of 5.10^{6} cells/mL HUVECs (Cryopreserved, ATCC, Virginia, USA) was injected through our device. Four megahertz ultrasound aligned as four streams and two megahertz ultrasound aligned as one stream. Switching these two frequencies, branched structure was generated. The ultrasound-exposed mixture was extruded into CaCl$_2$ (MERCK, Madison, USA) beaker for cross-linking reaction. The generated scaffolds were embedded using 3 mg/mL type I collagen (Koken, Tokyo, Japan) hydrogel matrices (Fig. 1b), and were cultured in vascular cell basal media supplemented with an endothelial cell growth kit-VEGF (ATCC, Virginia, U.S.A.). Alginate lyase (Sigma-Aldrich, MO, USA) was added within culturing media at 1 unit/mL of final concentration for HUVECs to migrate and form vessel structure (Fig. 1c).

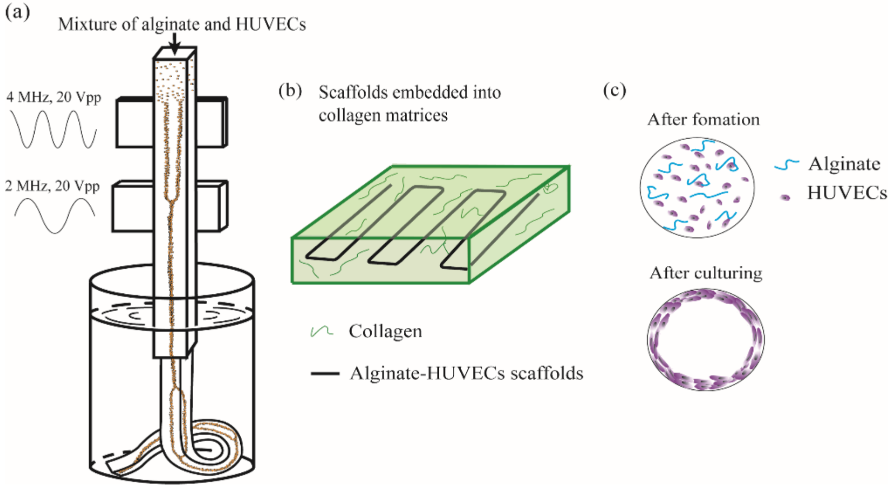

Figure 1: (a) The schematic of the acoustofluidic device for the HUVEC scaffold. (b) The schematic to embed the generated scaffolds into the 3D collagen matrices. (c) The schematic of the cross-section of the HUVEC scaffold after using alginate lyase.

We expected that four independent HUVEC vessels in the aligned region as four parallel lines by 4 MHz ultrasound. However, 550 – 600 µm diameter one vessel was observed at day 1 and day 3, as shown in Fig. 2 a and b. It was supposed that the HUVECs migrated over the initially arranged structure and merged into one vessel due to the alginate lyase. The merged vessel flowed 5 µm polystyrene particles (MicroParticles GmbH, Berlin, Germany) without any leakage at day 1, shown as orange in Fig. 2c.

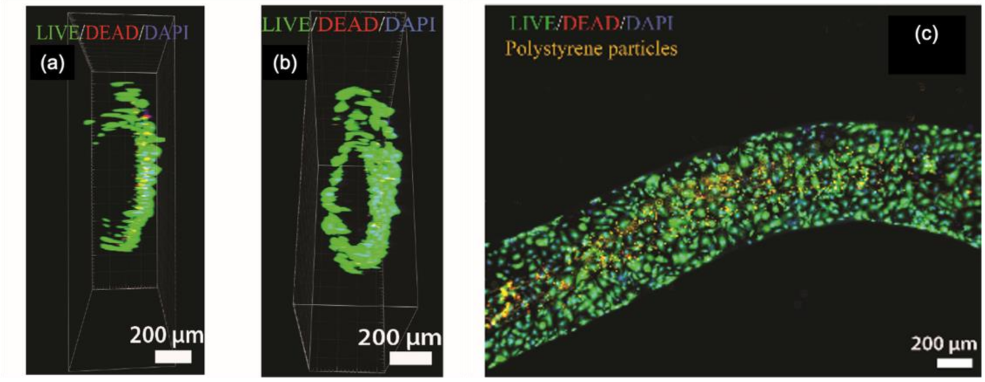

Figure 2. The confocal images of the embedded HUVEC scaffold (a) at day 1 and (b) at day 3. (c) The fluorescent image of the HUVEC scaffold during pumping.

Merging into two vessels in the acoustically aligned region as four parallel lines

In order to preserve the scaffold structure and encapsulate HUVECs in cell-migrable hydrogel without the alginate lyase, we modified our previous device, as shown in Fig. 3a. Hence, the branched HUVECs scaffold consists of two-coaxial layers. The outer layer was mixed of decellularized extracellular matrix (DECM) 12 mg/mL and alginate (MERCK, Madison, USA) 1% w/v at 8:2 of volume ratio. The core layer was mixed of DECM 12 mg/mL, alginate 0.5% w/v, and 5. 10^6 cell/mL of HUVECs (Cryopreserved, ATCC, Virginia, USA) at 8:1:1 of volume ratio, respectively. After generation, HUVECs scaffolds were incubated in vascular cell basal media supplemented with an endothelial cell growth kit-VEGF (ATCC, Virginia, USA) at 37 ºC, 5% CO_2. The culture medium was replaced every two days. During culturing, HUVECs scaffolds were collected at day 1 for checking vasculogenesis and day 3, 5, 9 for checking angiogenesis spouting by Alexa FluorTM 488 Phalloidin (F-actin) (Thermo Scientific, Massachusetts, USA) immunofluorescent staining.

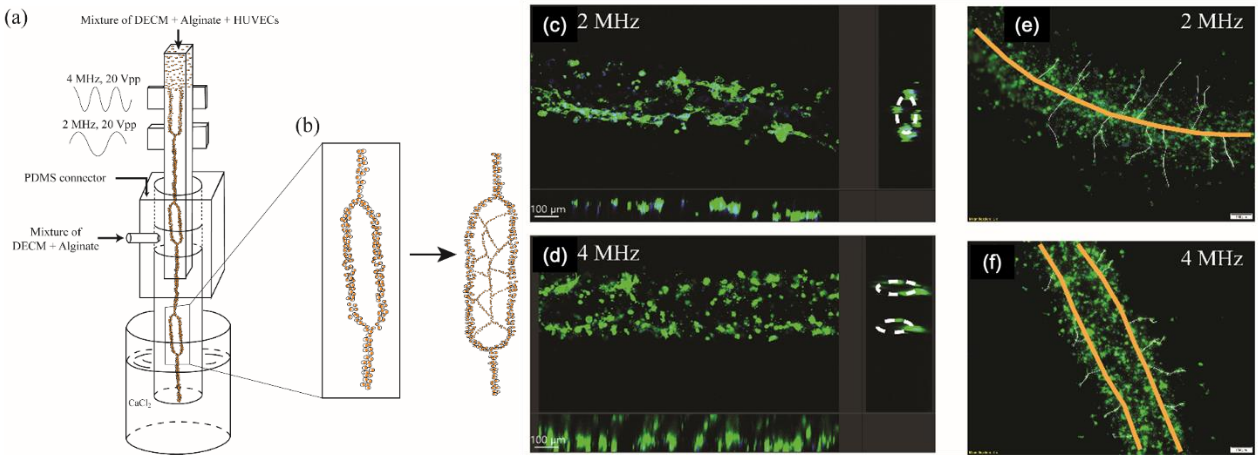

Figure 3: (a) The illustration of the branch generating device with two different frequency ultrasound transducers. (b) The expectation of the network formation. (c) The F-actin confocal images of HUEVCs scaffold at 2 MHz and (d) 4 MHz at day 1. (g) The immunofluorescent images of F-actin at 2 MHz and (h) 4 MHz at day 9.

After 1 day, it was observed that the single line cell configuration displayed a hollow structure as depicted in the z-stack insert (right) Fig. 2c. On contrary, the four-node-focused lines had reconfigured by themselves into two hollow tubes, as shown in Fig. 2d, z-stack insert (right). The sprout of HUVECs from pre-existing vessels were observed at day 9 (Fig. 2 e and f).

Conclusion

Using two different frequency ultrasounds, the HUVECs branch was generated. Using the co-axial laminar flow, two independent vessel formation was observed. Currently, authors are characterizing its functionality.

Acknowledgement

This work was supported by the Ministry of Science and ICT, Republic of Korea (2020R1F1A1075779).

References

[1] V.T. Duong, T.T. Dang, C.H. Hwang, S.H. Back, K.-i. Koo, Biofabrication **12**, 045033 (2020).
[2] S.Y. Hann, H. Cui, T. Esworthy, S. Miao, X. Zhou, S.-j. Lee, J.P. Fisher, L.G. Zhang, Translational Research **211**, 46-63 (2019).
[3] V. van Duinen, D. Zhu, C. Ramakers, A.J. van Zonneveld, P. Vulto, T. Hankemeier, Angiogenesis **22**, 157-165 (2019).
[4] K.-i. Koo, A. Lenshof, L.T. Huong, T. Laurell, Micromachines **12**, 1-12 (2021).

Acoustofluidics 2021
26-27 August 2021
Virtual Conference

Using acoustofluidics to engineer skeletal muscles

Dhananjay V. Deshmukh[1,2], Peter Reichert[1], Joel Zvick[3], Oksana Dudaryeva[2], Ori Bar-Nur[3], Mark W. Tibbitt[2], and Jurg Dual[1]

[1] Institute for Mechanical Systems, Department of Mechanical and Process Engineering, ETH Zürich, 8092 Zürich, Switzerland

[2] Macromolecular Engineering Laboratory, Department of Mechanical and Process Engineering, ETH Zürich, 8092 Zürich, Switzerland

[3]Laboratory of Regenerative and Movement Biology, Department of Health Sciences and Technology, ETH Zürich, 8603 Schwerzenbach, Switzerland

Introduction

Many tissues in our body have a specific cellular arrangement that is crucial for their proper functioning. Muscles are made up of myotubes (multinuclear contracting fibers) arranged parallel to each other. These myotubes are formed by the fusion of muscle progenitor cells (myoblasts) in a process known as myogenesis. It has been known that cell-cell contact is important to promote myogenesis in skeletal myoblasts. [1] Acoustofluidics has been used previously in a bulk acoustic wave device to produce skeletal muscle mimics with good control over the cell-cell spacing. [2] In this work, we pattern myoblasts within a hydrogel to support the growth of these cells and their differentiation into functional myotubes. We use a capillary-based device to achieve acoustic patterning in a continuous manner, extruding a hydrogel fiber with patterned cells inside. We observed the formation of myotubes by staining for myosin heavy chain (MyHC), a protein marker of mature muscle tissue. Spontaneous twitching could be observed in the myotubes formed within the hydrogels indicating the functionality of these tissue constructs.

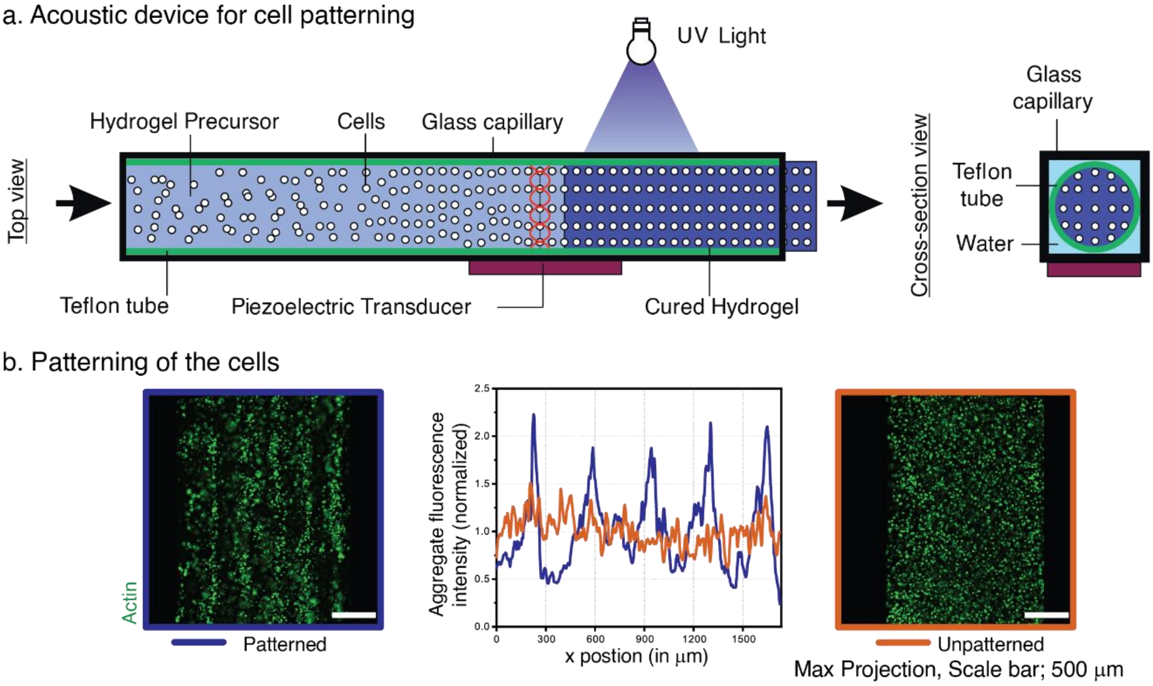

Figure 1: a. Cells in a liquid hydrogel precursor solution are patterned using an acoustic field, the patterned cell positions are retained by photo-polymerization of the hydrogel. The continuous flow in the device results in extrusion of the hydrogel fiber with patterned cells. **b.** Analysis of cell positions in patterned (left, blue) and unpatterned (right, orange) hydrogel fibers. The extruded fibers were stained after 3 days incubation. The average fluorescence intensity (middle) was calculated from maximum intensity projection of confocal z-stack images. The plots were normalized against the total fluorescence in each image

Device and methods

We engineered a Teflon-in-glass capillary device with a piezoelectric transducer glued onto it to enable acoustic manipulation (Figure 1a). The Teflon tube facilitated continuous flow of the polymerized hydrogel fibers. We could operate the device at various frequencies which facilitated control over the distance between the lines of cells. To ensure continuous polymerization of hydrogel, we used gelatin methacrylate (GelMA), a photo-polymerizable hydrogel which was polymerized using an external 405 nm light trigger (Intensity = 10 mW cm^{-2}). In our previous work, we found how addition of Matrigel improves the ability of myoblasts to form myotubes. [3] We hence used a similar hydrogel formulation (4% w/w GelMA, 0.4 mg mL^{-1} Matrigel, 1% w/w pluronics) to support myogenesis ex vivo. 0.1% w/w lithium phenyl-2,4,6-trimethylbenzoylphosphinate (LAP) was used as photoinitiator.

Primary murine myoblasts were isolated from C57BL/6J mice. Myoblasts were cultured on Matrigel-coated tissue culture plates in a medium containing equal parts high glucose DMEM and F-10 medium supplemented with 10% horse serum, 20% fetal bovine serum (FBS), 1% penicillin-streptomycin (PenStrep), and 10 ng ml^{-1} basic fibroblast growth factor (bFGF) in an incubator at 37°C. Hydrogel samples with patterned myoblasts were collected and incubated in the myoblasts culture medium. To induce myogenesis, a low serum medium consisting of knockout-DMEM with 1% MEM-NEAA, 1% GlutaMax, 1% PenStrep, 0.1% beta-mercaptoethanol, and 2% horse serum was used.

Patterning of myoblasts and formation of functional myotubes

Skeletal myoblasts were suspended in hydrogel precursor solution and patterned using the acoustic patterning device at various frequencies (2490 kHz, 2900 kHz, 6820 kHz). Since hydrogel was polymerized while still in the acoustic field, the cell patterning was retained in the samples after extrusion. (Figure 1b) Cells started fusing together and forming myotubes ~2 days post initiation of cell differentiation using low serum medium. Spontaneous contraction of myotubes was observed from 3 to 7 days post differentiation, confirming formation of functional myotubes. We also confirmed the myogenic nature of the patterned cells by staining for myosin heavy chain (MyHC). (Figure 2) Compared to unpatterned cells, patterned myoblasts showed more even formation of myotubes throughout the hydrogel fiber.

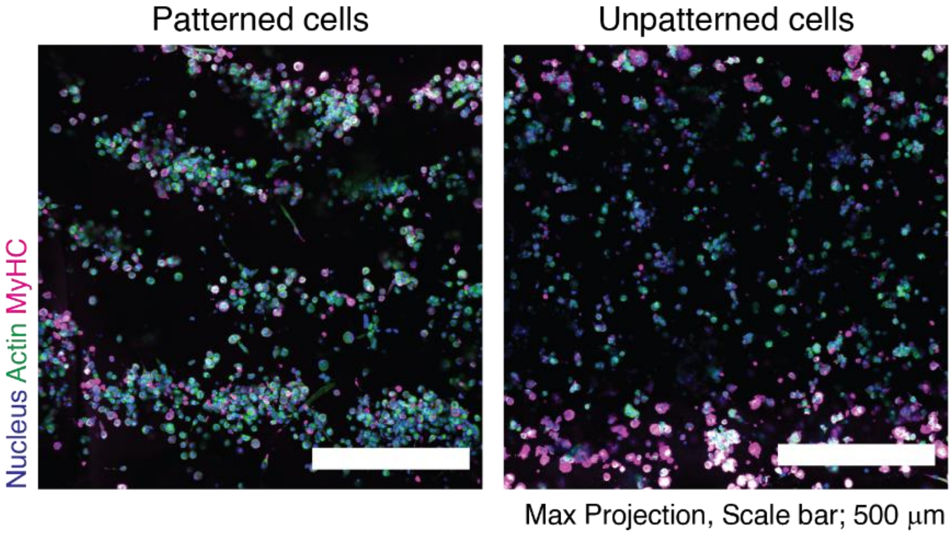

Figure 2: Formation of myotube in patterned (f = 2900 kHz) and unpatterned hydrogel samples. MyHC+ cells could be seen in regions of high localized cell density.

Conclusion

This work can be consequential in integrating the ability of spatial patterning using acoustics with the ubiquitous use of hydrogel in tissue engineering. We used acoustofluidics to pattern cells inside a hydrogel in a simple capillary device. We could also engineer skeletal myotubes by increasing the localized cell density of myoblasts, hence encouraging myogenesis. We could perform this patterning continuously and with tunable spacing between cells. Although we show engineering of muscle tissue in this work, other tissues such as tendons, ligaments, neural, vascular network or combinations thereof can be engineered using similar technology in the future.

References

[1] R. S. Krauss, G. A. Joseph, and A. J. Goel, *Cold Spring Harb. Perspect. Biol.*, vol. 9, no. 2, Feb. 2017,

[2] J. P. K. Armstrong *et al.*, *Adv. Mater.*, vol. 30, no. 43, Oct. 2018,

[3] D. V. Deshmukh *et al.*, *Bioeng. Transl. Med.*, vol. 5, no. 3, Sep. 2020,

Acoustomicrofluidic tri-separation of proteins using aptamer-coated microparticles

Muhammad Afzal[1], Jinsoo Park[2], Jessie S. Jeon[1], and Hyung Jin Sung[1]

[1]Department of Mechanical Engineering, KAIST, Daejeon, Korea
E-mail: afzal@kaist.ac.kr, URL: http://flow.kaist.ac.kr
[2]School of Mechanical Engineering, Chonnam National University, Gwangju, Korea

Introduction

Proteins are one of the essential macromolecules of human body, which are composed of polypeptide chains of amino acids. They are involved in body structure, metabolism, and many important diseases. Protein expression, detection, separation and purification play significant roles in various clinical diagnostics [1]. Conventional protein purification methods like ultracentrifugation, chromatography, enzyme-linked immune sorbent assay (ELISA) and mass spectrometry are usually labor-intensive, provide limited sensitivity and detection, and require large instrumental setups [2]. Techniques based on genetic engineering, digital ELISA, nano-materials and antigen–antibody interactions are still limited by difficult protein binding interactions and the instability of proteins. Advancements in nano-biotechnology have led the development of bio-barcode assays based on nanoparticles and single-stranded DNA aptamer which provide high stability, improved target specificity and selectivity, higher binding affinity, minimized batch-to-batch variation, and easiness in manufacturing and editing. Notable advances in bioassays and immunoassays with the use of microfluidic technologies have reduced the cost and time required for the assays, as well as the technical complexity [3]. Inertial microfluidic device depends mainly on the microchannel geometry, fluid properties and flow conditions. The magnetic separation techniques have critical limitations with respect to the magnetic label requirement and lack selectivity, which is important for multiple protein separation. In particular, the acoustic separation of microparticles based on their size, density, or shape has attracted much attention to address the limitations of conventional microfluidic separation techniques. We previously reported the acoustofluidic separation of a single target protein (thrombin) from non-targeted protein (mCardinal2) using the travelling surface acoustic wave (TSAW)-driven acoustic radiation force (ARF) [4]. Here, we propose an acoustomicrofluidic method for the tri-separation of human proteins conjugated with aptamer-coated microparticles inside a microchannel. TSAWs produced from a slanted-finger interdigital transducer (SFIT) are used to separate the protein-loaded microparticles of different sizes via the TSAW-driven ARF. We achieved simultaneous separation of proteins of three kinds (th, IgE, and mCardinal2) for the first time via the TSAW-driven ARF in the proposed acoustomicrofluidic device.

Methodology

A schematic workflow of the acoustomicrofluidic separation of thrombin (blue), IgE (purple) and mCardi-nal2 (red) is shown in Figure 1. When two kinds of the microparticle–aptamer complexes (PS6–apt15 and PS7–aptD17.4) were introduced into a mixture of target and non-target proteins, thrombin and IgE were conjugated with their specific apt15-functionalized and aptD17.4-functionalized carrier particles (green and Nile red, respectively), whereas the non-target mCardinal2 protein remained unbound in the sample solution. After formation of the microparticle–aptamer–protein complexes, the sample fluid that contained thrombin, IgE and unbound non-target mCardinal2 was introduced into the microchannel and were subjected to TSAW-induced ARF of different magnitudes upon interacting with the acoustic field.

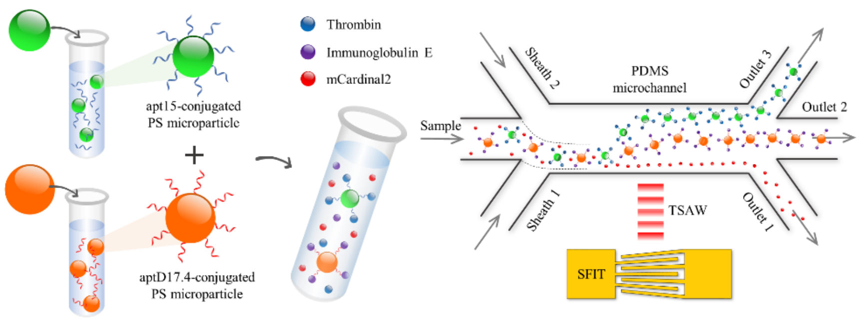

Figure 1: Schematic of the process for acoustomicrofluidic tri-separation of proteins. The targeted proteins thrombin and IgE are captured with DNA-based aptamer coated microparticles while non-target protein remains unbound. The mixture of three proteins is subjected to the TSAW-induced ARF and are thereby separated into different outlet ports in the acoustofluidic device.

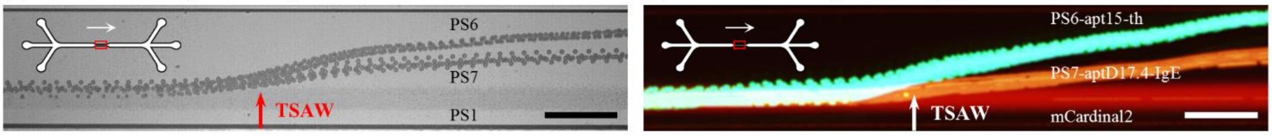
(a) Deflection zone (TSAW on)

(b) Deflection zone (TSAW on)

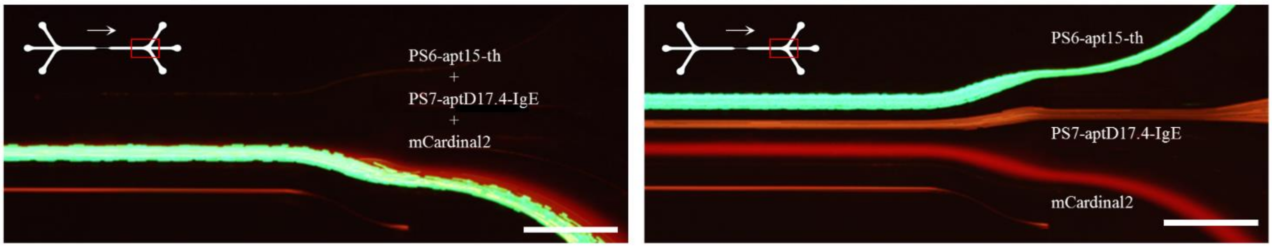
(c) Separation zone (TSAW off)

(d) Separation zone (TSAW on)

Figure 2: Acoustomicrofluidic tri-separation of microparticles and proteins. (a) Acoustomicrofluidic tri-separation of standardized non-fluorescent microparticles. (b) Acoustomicrofluidic tri-separation of targeted proteins thrombin (green) and IgE (orange), from a non-target mCardinal2 (red) protein at the TSAW deflection zone. (c) In the TSAW off mode, the targeted proteins along with non-target mCardinal2 flowed without TSAW deflection. (d) after the SFIT was actuated, targeted thrombin (green) and IgE (orange) proteins were separated from non-target mCardinal2 (red), under the influence of the ARF.

Results and discussion

Acoustomicrofluidic tri-separation of human proteins is shown in Figure 2. As proof-of-concept experiments, we first conducted acoustomicrofluidic tri-separation of non-fluorescent standardized microparticles (1, 6, and 7 µm) with a narrow size distribution, as shown in Figure 2(a). Without activation of the SFIT, the streamlines of the multiplexed protein sample solution were unaffected as all three kinds of proteins along with the sample fluid flowed into the same outlet located near the SFIT Figure 2(c). When the TSAW-induced acoustic field was activated at 117 MHz AC signal at 0.2 W, PS6–apt15–th and PS7–aptD17.4–IgE complexes in the protein sample mixture, experienced a substantial ARF; their streamlines thus translocated in the TSAW propagation direction (Figure 2(b)). PS6–apt15–th and PS7–aptD17.4–IgE complexes were deviated from their original streamline and flowed along two separate streamlines (one in the center and the other near the opposite wall). Because of its small size, the non-target mCardinal2 was not affected by the TSAW-induced ARF and thus remained in its original streamline resulting in tri-separation of proteins (Figure 2(d)). Target proteins separation efficiency was quantitatively analyzed for the samples collected at the three outlets for the TSAW off and on conditions using a hemocytometer. The purity and recovery rate were calculated using five hemocytometer images obtained from independent experiments for each sample collected at the three outlets. The purity was measured to be 99.04% for thrombin and 98.85% for IgE while the recovery rate was measured to be 97.82% for thrombin and 96.31% for IgE. These quantification measurements demonstrate high efficiency of simultaneous separation of multiple target proteins.

Conclusion

We reported an acoustomicrofluidic method for the tri-separation of human proteins from a multiplexed mixture. The target human thrombin and IgE proteins were captured by apt15- and aptD17.4-functionalized PS microparticles, respectively, and were separated from non-target mCardinal2 by TSAW-based acoustofluidic method using ARF. We expect that our proposed acoustomicrofluidic-based multiplexed protein capture and separation assay from a mixture sample can be used as a promising tool for various protein-based clinical diagnostic assays.

References

[1] N. L. Anderson. Clin. Chem. **56** (2), 177–185 (2010).
[2] S. Stepanova, V. Kasicka. Chim. Acta. **933**, 23–42 (2016).
[3] M. Wu, Y. Ouyang, Z. Wang, R. Zhang, P. H. Huang, C. Chen, H. Li, P. Li, D. Quinn, M. Dao. Proc. Natl. Acad. Sci. **114** (40), 10584–10589 (2017).
[4] R. Ahmad, G. Destgeer, M. Afzal, J. Park, H. Ahmed, J. H. Jung, K. Park, T.-S. Yoon, and H. J. Sung. Anal. Chem. **89** (24), 13313-13319 (2017).

Acoustofluidics 2021
26-27 August 2021
Virtual Conference

A bubble-based acoustofluidic device for the study of ultrasound thrombolysis

Yuan Gao[1], Mengren Wu[1], and Bruce Gaynes[2,3], Jie Xu[1]

[1]Department of Mechanical and Industrial Engineering, University of Illinois at Chicago, Chicago, IL
E-mail: ygao51@uic.edu, URL: https://xu.uic.edu/
[2]Department of Ophthalmology, Loyola University Stritch School of Medicine, Maywood, IL
[3]Edward Hines Jr VA Medical Center, Hines, IL

Introduction

Thrombosis is a common medical entity associated with many forms of cardiovascular disease including myocardial infarction and stroke. Several factors can cause thrombosis (blood clots), such as specific medications (e.g. corticosteroids), family history, obesity, smoking, and neoplastic diseases. Additionally, the recent emergence of the novel SARS-CoV-2 virus is also associated with thrombosis, which significantly increases the risk of stroke in infected individuals. The formation of a blood clot is dependent on the aggregability of RBCs. There are two models to describe RBC aggregation for the study of thrombolysis, which are bridging model and depletion model [1]. Although extensive research efforts have been made, these two seemingly contradictory models remain controversial. Therefore, new approaches are needed to better understand the underlying mechanisms of thrombosis and thrombolysis. Recently, ultrasound thrombolysis has emerged as a promising technique for thrombosis treatment by deploying acoustic waves into blood clots and proved to be effective for clot dissolution in *in vivo* and *in vitro* studies [2,3]. In this work, we introduced an acoustic bubble-based microfluidic device for experimental study of the effect of the acoustic parameters on ultrasound thrombolysis. Upon a low-frequency field, the effects of different-sized bubbles on microstreaming patterns and thrombolysis have been experimentally studied. Using image processing techniques, we quantitatively investigated the performance of thrombolysis. Additionally, the viability test proved that there are no significant detrimental effects on the blood cells after acoustic actuation. This acoustic bubble-based microfluidic platform demonstrates a promising tool for understanding RBC aggregation phenomena and quantitative analysis of ultrasound thrombolysis.

Experimental method

The acoustic bubble-based microfluidic device consists of a piezoelectric transducer and a PDMS microchannel with a microcavity structure bonded to a glass substrate. The straight PDMS channelwith a predesigned microcavity structure was designed and fabricated using standard soft lithography and mold replica technique. To activate the device, a piezoelectric transducer adhered to the glass slide, which was driven by a function generator and amplified by a voltage amplifier. Porcine whole blood was used in this experiment. To simulate blood clots, blood samples were prepared using the mixture of blood and diluted dextran 500 solution. The image sequence was captured by a high-speed for frequency sweeping, data analysis and thrombolysis visualization.

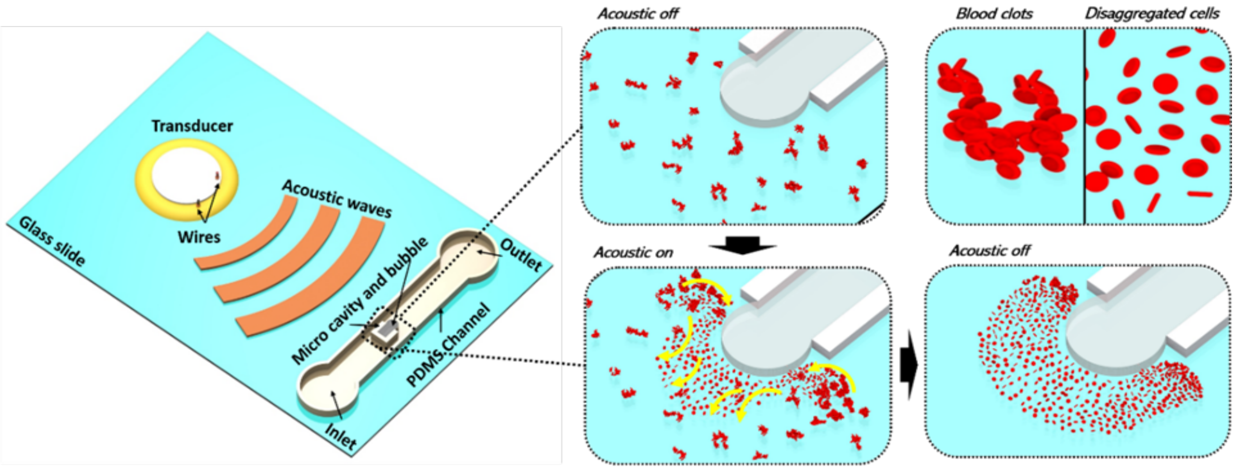

Figure 1: Schematic illustration of the working mechanism of acoustic bubble-based thrombolysis.

Results and discussion

The working mechanism of this acoustic bubble-based microfluidic platforis shown in Fig. 1. Once the blood sample inside the microchannel achieved equilibrium state, the acoustic waves were applied to actuate the device. At the bubble's resonant frequency, a strong microstreaming flow occurred around the cavity structure. Due to the microstreaming flow, the blood clots moved toward the surface of the bubble, disaggregated into single blood cells and released from the bubbles instantaneously (Fig.1). The released single cells followed the streaming pattern and stopped moving once the acoustic was off. Under acoustic bubble actuation, blood clots suspended in the microchannel experience a drag force due to the flow and a secondary radiation force from the bubble. As shown in Fig.3a, the high-speed images demonstrated the evolution of blood clots and the motion of single cells in few milliseconds.

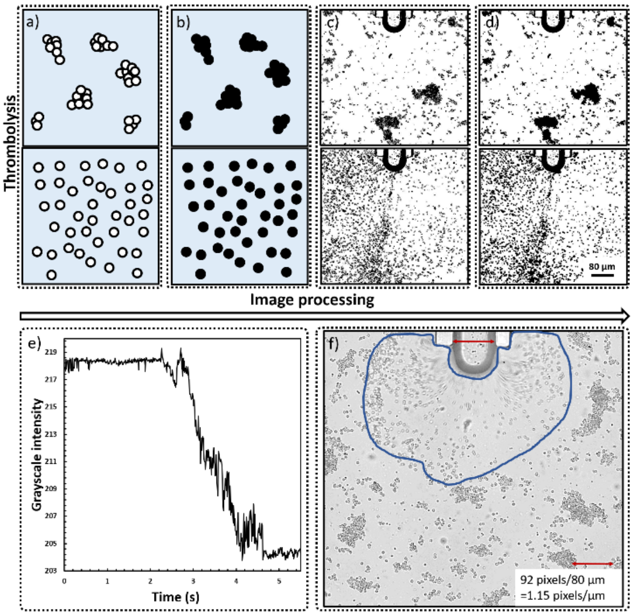

Figure 2: a),c) Cell membrane detection and binary pixels converting process. b),d) Cell contrast enhancement. e) Average grayscale intensity in the ROI versus time. f) Microstreaming area measurement.

By sweeping the frequency in a low frequency range, we found the the blood clots were almost completely lysed in the frequency range of 25-30 kHz for the 80 μm diameter bubble. To quantitively evaluate the performance of thrombolysis, the variation in the image intensity in the region of interest (ROI) and area measurement were applied. During thrombolysis, with the lysing of the blood clots, overlapping area of cells decreased and thus the average grayscale intensity (I_{ROI}) reduced (Fig. 2a-d). As shown in Figure 2e, the average grayscale intensity decreases with time of acoustic actuation. The image grayscale intensity differences at the frequecies from 25 to 30 kHz were calculated as ΔI = Ibefore - Iafter and were plotted with time (Fig.3b). The result demonstrated the optimum performance occurs at 28 kHz. To investigate the relationship of microstreaming and acoustic parameters applied on the bubble, the area of microstreaming at 2 s-actuation for different frequencies was measured (Fig. 2f). This also indicates the strongest microstreaming occurs when the driving frequency is 28 kHz (Fig.3c). Additionally, we tested effect og input voltage on the performance of thrombolysis and the viability of blood cells. We found that there is no significant impact of acoustic actuation on the cell viability with the optimum driving frequency and voltage (28 kHz and 7 Vpp).

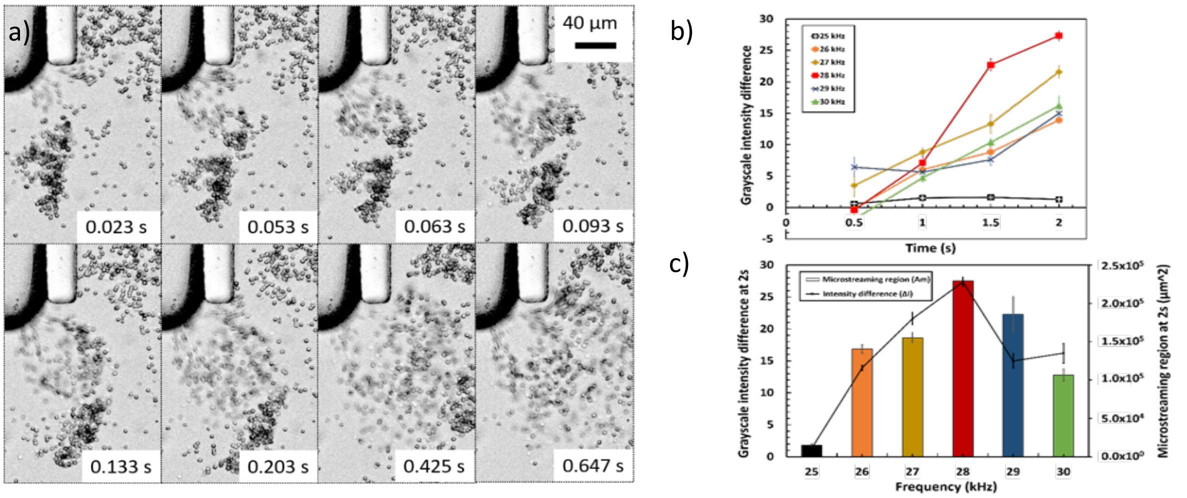

Figure 3: (a) Image sequence of the thrombolysis process captured by high-speed camera (9000 fps). (b) The average grayscale intensity difference in ROI (ΔI_{ROI}) at different frequencies. (c) Comparison of average grayscale intensity and microstreaming area at 2s-actuation.

Conclusion

This work demonstrates an acoustic bubble-based microfluidic device for the study of the effect of acoustic parameters on ultrasound thrombolysis, which is a promising platform for understanding RBC aggregation model and future development of ultrasound thrombolysis for the diagnosis and treatments of heart diseases.

References

[1] A. Pribush, D. Zilberman-Kravits and N. Meyerstein, Eur. Biophys. J. **36**, 85-94 (2007)
[2] K. Tachibana and S. Tachibana, Ultrasound angioplasty, Springer, 121-133 (1996)
[3] B. Petit, F. Yan, F. Tranquart and E. Allémann, Journal of drug delivery science and technology **22**, 381-392 (2012)

Acoustofluidics
2021
26-27 August 2021
Virtual Conference

A sound idea to stimulate cells: A novel method to acousto-mechanically stimulate cells

Christopher Markwell[1], Luying Feng[1], Ran Tao[1,2], Steven O'Reilly[3], Richard Fu[1], and Hamdi Torun[1]

[1]Department of Maths, Physics and Electrical Engineering, Northumbria University, Newcastle-upon-Tyne, United Kingdom
E-mail: christopher.markwell@northumbria.ac.uk,
[2]Shenzhen Key Laboratory of Advanced Thin Films and Applications, College of Physics and Optoelectronic Engineering, Shenzhen University 518060, China
[3] Biological Sciences, Durham University, Durham, United Kingdom

Introduction

Viscoelastic properties of human skin cells have raised great interests as important markers of skin health for diagnostic and therapeutic applications[1]. Viscoelasticity of cells can be altered by external stimuli which have been used to enhance cell proliferation, differentiation and wound healing. In this work we conducted acousto-mechanical stimulations on Normal Human Dermal Fibroblasts (NHDF) using Surface Acoustic Wave (SAW) devices. From this work we see an increase in proliferation as well as increases in stiffness and widening of the distribution. We hypothesise that from the observed changes arise through mechanosignalling pathways within the cell with the Hippo pathway of particular interest as Yap/Taz transcriptional factors due to their role in coordinating activation of fibroblasts and matrix synthesis[2]. It is expected that Yap/Taz will be more localised in the nucleus in addition to an increase in structural proteins such as Collagen and F-Actin.

Experimental set-up

Figure 1 conceptually shows the stimulation assay where NHDF cells were cultured inside of Polydimethylsiloxane (PDMS) chambers on top of the SAW devices. Four ZnO/Al SAW devices were used for this assay with frequencies ranging from 9MHz to 27MHz. We excited the cells inside the chamber using programmed surface acoustic waves during cell incubation process (37°C at 5% CO_2). A single stimulation dose corresponds to 1 minute of excitation in a duration of 5 minutes. We treated the cells with 6 doses for three times per day for a total incubation duration of two days.

Viscoelastic Properties

After the final stimulation, we measured the stiffness values of both the stimulated cells and the control ones (growing under the same circumstances without any stimulation). We used blunted pyramidal cantilever tips for the atomic force microscopy (AFM)-based measurements[3]. Our measurements

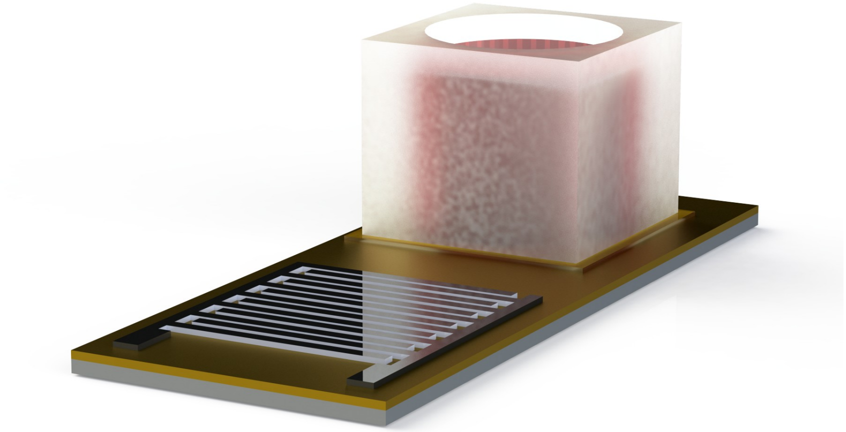

Figure 1: Conceptual render for the stimulation of cells using a SAW transducer and a PDMS chamber for use in Tissue Culture.

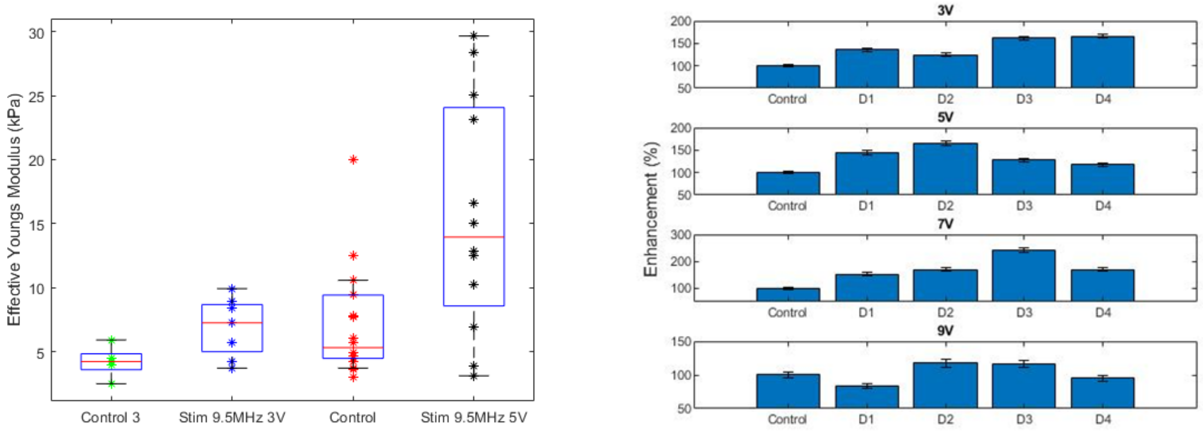

Figure 2: a) Box plot showing the differing distribution of Effective Youngs' Moduli between control cells nad stimulated cells. Each * represents the mean effective Youngs' Modulus of a cell within that set (*Left*). b) Proliferation results normalised to control, showing a statistically significant increase across all powers applied to the cells ($p<0.01$ unpaired T-test) and across all devices. With the 9V being the exception where the devices power is much higher and causes significant reduction in proliferative enhancement (all $p<0.05$ with D4 being an exception which has no statistically significant change above or below control)(*Right*).

reveal the control cells exhibit a stiffness value about 3.2 kPa (see Figure 2a for the distribution of measurements), whereas the stimulated cells exhibit an increased stiffness with a wider distribution. This set is based on three stimulated and three control cells, and between 100-200 measurements on each cell. The widening of distribution in stiffness values indicate a non-uniform effect of acousto-mechanical excitation, the exact mechanism for this is under investigation although we hypothesise that due to the cell being stressed by SAW it results in mechanosensing mechanisms in the cell activating and increasing structural proteins as well as the movement of YAP/TAZ into the cell nucleus[2].

Proliferative Results

In order to test the performance of our actuator in cell culture we look at the how cells proliferate as this is a good measure of cell function under the conditions that we impose upon the cells. The results of these experiments are plotted in Figure 2b, which are normalized to the control for each set of experiments and proliferation is plotted with respect to this value as a percentage change compared to control. Proliferation showed statistically significant changes between treated cell cultures and control we hypothesise this is due to the enhanced streaming effect as it has been shown that fluid shear stress can modulate growth factors[4] in addition to the streaming's ability to cycle new nutrients to the cell.

Conclusion

We have successfully implemented the assay exciting NHDF cells and measured their stiffnesses revealing the influence of stimulation. The assay allows the excitation of the cells with targetted acoustomechanical waves, the amplitude and the frequency of which can be controlled electronically. The assay can be integrated in conventional cell incubators for extended-time operation. We have demonstrated that the profileration of the cells can be promoted using this method. In addition, the viscoelastic properties of the cells can be altered as we measured the Youngs' Moduli of the cells against control groups. Further work will be focused on the study of the structural reformation in the cells due to the induced stimuli.

Acknowledgement

This work was financially supported by the UK Engineering, and Physical Sciences Research Council (EPSRC) grants EP/P018998/1, and Special Interests Group of Acoustofluidics under the EPSRC-funded UK Fluidic Network (EP/N032861/1).

References

[1] A. Strange, S. Aguayo, T. Ahmed, N. Mordan, R. Stratton, S. Porter, S. Parekh and L. Bozec. International Journal of Nanomedicine **2017:12**, 411-420 (2017).
[2] F. Liu, *et al.*. American Journal of Physiology - Lung Cellular and Molecular Physiology **308**, L344-L357 (2015)
[3] F. Rico, P. Roca-Cusachs, N. Gavara, R. Farré, M. Rotger, and D. Navajas. Physical Review E - Statistical, Nonlinear, and Soft Matter Physics **72**, 021914-1-021914-10 (2005).
[4] A M. Malek, G H. Gibbons, V J. Dzau, S. Izumo, Journal of Clinical Investigation **92**, 2013-2021 (1993).

Acoustofluidics
2021
26-27 August 2021
Virtual Conference

Neural Differentiation of Human Embryonic Stem Cells Mediated by Surface Acoustic Waves

Chao Sun[1], Jun Wei[3], Meng Cai[3], Xin Yang[2]

[1]School of Life Sciences, Northwestern Polytechnical University, 710072, P.R. China, E-mail: chaosun@nwpu.edu.cn
[2]Department of Electrical and Electronic Engineering, School of Engineering, Cardiff University, UK CF24 3AA, E-mail: YangX26@cardiff.ac.uk
[3]iRegene Therapeutics Co., Ltd, Wuhan, 430070, P.R. China, E-mail: Weijun@iregene.com, caimeng@iregene.com

Introduction

Current differentiation process of human embryonic stem cells (hESCs) to mature neurons is a lengthy procedure. In order to accelerate this process to facilitate the integration of neurons in cell therapies and drug screening, we develop a novel stimulation tool based on surface acoustic waves (SAWs) to accelerate neural differentiation process. This SAW stimulation device can be batch manufactured and deployed in small- to pilot-scale production of mature neurons owing to the novel SAW device fabrication technique using flexible printed circuit boards clamping with piezoelectric substrates. The hESCs are differentiating inside the SAW device for consecutive 12 days with SAW perturbation on pulse mode lasting for 10 min per day. The results show a SAW dose dependent effect in the acceleration of the differentiation process. More development and extracellular matrix-related genes are altered under low or medium SAW doses, while more cell cycle and physiological activity-related genes are regulated under high SAW dose. These findings are further confirmed by using neural stem cell markers including PAX6, SOX1, SOX2, SOX10 and NKX2-1. The expression of these markers is notably decreased in the SAW stimulation groups comparing with the control, especially the cells in the highest SAW dose group present a more mature neuron-like phenotype. The finding demonstrates the potential of using the SAW stimulation device in the acceleration of neural differentiation process and highlights the possible regulatory role of SAW stimulation in the neural cell differentiation and proliferation.

Material and methods

The assembly process of the FPCB SAW-based Cell Stimulation (FSCS) device started from placing the $LiNbO_3$ substrate bonded with the PDMS chamber into the slot on the 3D-printed holder. Then the FPCB, the silicone pad and the rectangular nut were subsequently stacked onto the substrate as shown in Figure 1.a. The reflection coefficient S_{11} of the FSCS device represents the degree of RF power reflected from the device, which was measured using a vector network analyzer (VNA, E5061B, Keysight, US). Three SAW doses produced by three RF amplitudes of 24 V, 31 V and 39 V (peak-to-peak) were applied to administrate in the hESC stimulation referring to the ultrasound power used in LIPUS studies [8b, 8c]. The RF signals were set to a pulse mode with a burst period of 1 ms, 200 pulses per burst, and 40% duty cycle. The pulse frequency was set to the Rayleigh mode frequency of individual FSCS devices. It is noted that the average voltage of the RF signal under pulse mode is much smaller than the peak-to-peak value. There were three FSCS devices applied in each dose group, and another three FSCS devices were applied as the control group. A total of twelve FSCS devices were efficiently prepared owing to the rapid prototyping ability of the FPCB technique. The three dose groups were stimulated by SAW for 10 min at the same time on each day, and for 12 consecutive days. For the three FSCS devices in the control group, hESCs were cultured using the same differentiation medium as that used in the stimulation groups, but without applying any SAW stimulation.

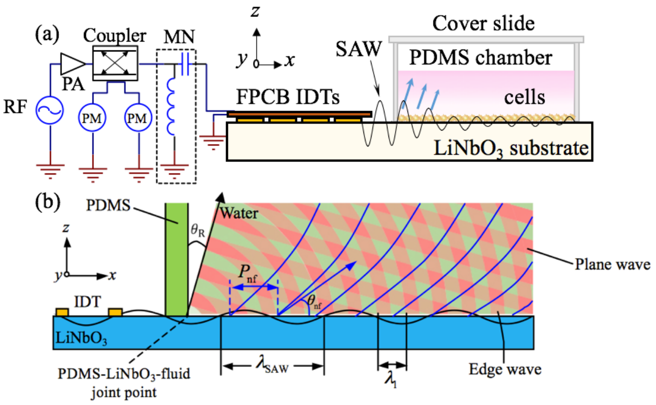

Figure 1: (a) The flexible printed circuit board (FPCB) surface acoustic wave (SAW)-based cell stimulation (FSCS) device used for cell stimulation. (b) An interdigital transducer (IDT) generates SAW propagating towards the cell chamber.

Quantitative PCR and Immunofluorescence staining were performed to identify the development stage of cultured cells.

Results and discussion

All the FSCS devices prepared by using the FPCB technique yielded a small inter-device variability in terms of Rayleigh mode frequency, i.e. 19.69±0.12 MHz (mean±SD). The S_{11} was optimized with the use of matching networks to -41.45±6.92 dB, which indicated the FSCS devices achieved the same level of frequency response as those SAW devices made through conventional photolithography technique in cleanroom.

The relative expression of NSC marker genes, *Pax6, Sox1*, *Sox10* and *Nkx2-1*, was examined by quantitative PCR (Figure 2). The expression of these NSC marker genes was decreased in at least one SAW dose group compared with the control group except *Nkx2-1*. Interestingly, it is demonstrated that the relative expression of *Sox1* gene represents a decreasing trend which is negatively correlated with the SAW power. Since these NSC markers are highly expressed in the NSC development stage and gradually decreased in relative mature neurons, these results suggest that the neural differentiation process was accelerated by SAW stimulation and thus enhanced the neural differentiation potential of stem cells. Notably, the expression of *Pax6* and *Sox10* was decreased significantly in the low or medium SAW dose groups, but not in the high SAW dose group (Figure 2a, 2c). These observations confirmed the RNA sequencing results that more stem cell development/differentiation-related genes are altered in the low and medium SAW dose groups, but not in the high SAW dose group.

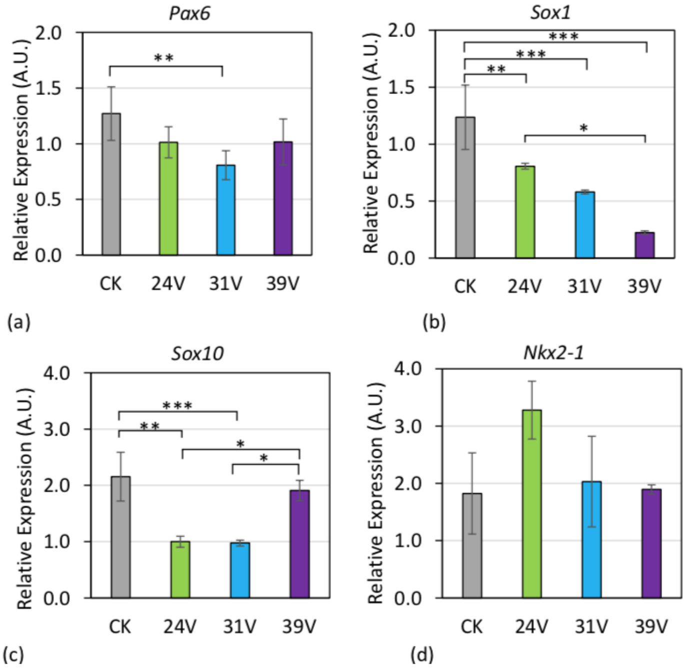

Figure 2: The quantitative PCR results for the expression of neural stem cell maker genes (a) Pax6, (b) Sox1, (c) Sox10 and (d) Nkx2-1 immediately after 12-day stimulation in the FSCS devices under three different SAW doses (*: $P<0.05$, **: $P<0.01$, ***: $P<0.005$).

Conclusion

This study presented a novel FSCS device deploying in SAW mediation of neural differentiation process of hESCs. The outcome demonstrated the capability of the device in acceleration of the maturation of neurons on a SAW dose dependent manner. The FSCS devices were fabricated through a novel process namely FPCB technique, which allowed rapid prototyping of acoustofluidic devices for batch deployment in biomedical applications. The way of SAW production in the FSCS device allows concentrating acoustic energy on the propagation surface which applies direct mechanical perturbation on the bottom of the hESCs. SAW also induces acoustic pressure and streaming in the hESC medium exhibiting shear stress on the hESC. Further analysis to the stimulated cells including quantitative PCR and immunofluorescence staining confirmed that the hESCs stimulated by high SAW dose presented a relatively more mature neuron phenotype than the control group. Altogether, the FSCS device offers a robust SAW stimulation tool for acceleration hESC differentiation towards mature neurons, which can benefit and promote the application of neurons in disease modeling, drug screening and regenerative medicine.

References

[1] Y. Gao, A. K. Fajrial, T. Yang, X. Ding, Biomaterials Science 2021, https://doi.org/10.1039/D0BM01269F.

[2] C. Sun, R. Mikhaylov, Y. Fu, F. Wu, H. Wang, X. Yuan, Z. Xie, D. Liang, Z. Wu, X. Yang, IEEE Transactions on Electron Devices 2021, 68 (1), 393, https://doi.org/10.1109/TED.2020.3039760.

Acoustofluidics
2021
26-27 August 2021
Virtual Conference

Self-organization of human mesenchymal stem cells into spheroids trapped in acoustic levitation.

Nathan Jeger-Madiot[1], Lousineh Arakelian[2], Niclas Setterblad[3], Patrick Bruneval[4], Mauricio Hoyos[1], Jérôme Larghero[2], and Jean-Luc Aider[1]

[1]Laboratoire de Physique et M´ecanique des Milieux Hétérogènes (PMMH), UMR 7636 CNRS, ESPCI Paris, PSL, Paris Sciences et Lettres University, Sorbonne Université, Université de Paris 1, Paris, 75005, France. E-mail: nathan.jeger-madiot.fr
[2]Unité de Thérapie Cellulaire, APHP, Hôpital Saint-Louis, 1 avenue Claude Vellefaux, F-75010 Paris, Université de Paris, Inserm U976 et CIC de Biothérapies CBT501, F-75006 Paris, France
[3]Technological Core facility of the Institut de Recherche Saint-Louis, Université Paris-Diderot and Inserm, Hôpital Saint-Louis, Paris, France
[4]INSERM U970-PARCC, Paris, France

Today, three-dimensional (3D) cell cultures tend to replace 2D conventional method because of their more relevant tissue-mimicking characteristics. Indeed, the 3D cell architecture (spheroïd, organoïd, etc) and the microenvironment is closer to In Vivo physiological behavior [1, 2]. Especially, the mechanic conditions of the environment will favor some cell behavior. For example, the human mesenchymal stem cells (MSC), which are adherent cells, are classically grown in 2D petri dishes until they reach the confluence.

Here we present a new approach based on multi-node acoustic levitation to grow the cells without interactions with solid walls [3]. Once the cells are suspended in their culture medium, they can be moved toward the acoustic pressure nodes where they are trapped and maintained in acoustic levitation in perfectly straight monolayers. The monolayers of cells mimic the classical confluency of the cells in 2D culture. Interestingly, by maintaining the monolayers of MSCs in culture over a 24-h period, the MSCs spontaneously self-organized from cell sheets to cell spheroids with a characteristic time of about 10 h (see Fig.1).

This approach of 3D cell culture is based on the use of the acoustic wave coupled with microfluidic. We designed a standing wave cavity to generate an important acoustic radiation force (ARF) while keeping a good optical access, which allows the observation and characterization of the self-organization dynamics. This new 3D cell culture method has been validated on MSCs over 24h experiments. The MSCs viability has been checked (see Fig.2). They also maintained the expression of their cell surface markers. Interestingly, they also show a higher differentiation capacity compared to standard 2D culture conditions.

In our acoustofluidic system, the rapid formation of spheroids mimics the high confluency of 2D cultures and spheroid formation owing to the acoustic confinement (aggregation induced by the axial and transverse components of the ARF). This approach opens the path to a better understanding of the self-organization phenomena and can be applied to many other different types of cells. It also demonstrates the use of acoustic levitation as a new method of long-term, reproducible cell culture process for scaffold-free tissue engineering purposes such as organoid formation.

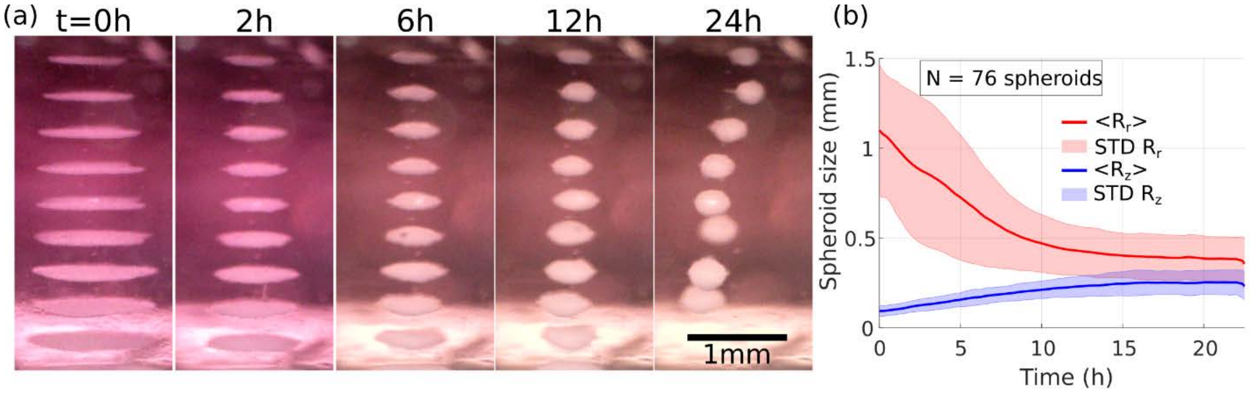

Figure 1: Self-organization of hMSCs cells sheets into spehroids shapes. (a) Time lapse snapshots of the MSC self-organization. (c) Statistic time evolution of the axial and radial dimensions of the cells aggregates.

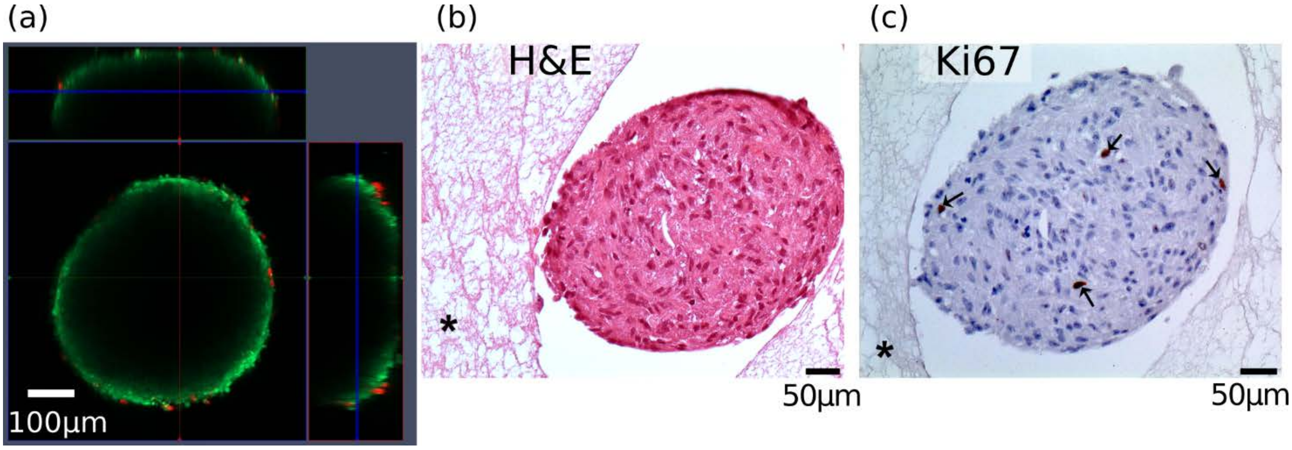

Figure 2: (a) Confocal and fluorescence imagery of a spheroid after self-organization in acoustic levitation. (b) Histology of MSC spheroids, stained with H&E for a general structure evaluation (c) and with Ki67 for the proliferation.

References

[1] Abbott, A. Biology's new dimension. Nature 424, 870–872, DOI: 10.1038/424870a (2003).

[2] Pampaloni, F., Reynaud, E. G. & Stelzer, E. H. K. The third dimension bridges the gap between cell culture and live tissue.

[3] Jeger-Madiot, N., Arakelian, L., Setterblad, N. et al. Self-organization and culture of Mesenchymal Stem Cell spheroids in acoustic levitation. Sci Rep 11, 8355 (2021). DOI: 10.1038/s41598-021-87459-6

Acoustofluidics 2020
26-27 August 2020
Virtual Conference

Acoustic trapping of sub-wavelength microparticles and cells in resonant cylindrical shells

Qin Lin[1], Feiyan Cai[1], and Hairong Zheng[1]

[1]Paul C. Lauterbur Research Center for Biomedical Imaging, Institute of Biomedical and Health Engineering, Shenzhen Institutes of Advanced Technology, Chinese Academy of Sciences, Shenzhen, China
E-mail: fy.cai@siat.ac.cn
E-mail: hr.zheng@siat.ac.cn

Introduction

Acoustic tweezers are an emerging and versatile platform for the manipulation of microparticles. Due to the advantages of low power consumption and no requirement for transparent media compared with optical tweezers, acoustic tweezers have been widely used for sorting exosomes, assembling particles, 3D volumetric displays, and so on. Acoustic tweezers based on a phased array can dynamically manipulate microparticles in real-time [1]. However, acoustic diffraction severely limits the trapping strength and the minimum size of the trapped particles in these conventional diffraction-limited systems. To strengthen the trapping ability, a series of near-field enhanced methods have been developed. For example, surface standing acoustic waves in high frequency have been successfully applied to manipulate nanoparticles and tiny biomarkers [2, 3]. These particles are usually trapped in one-dimensional linear or two-dimensional dotted patterns. Recently, artificially engineered field-based acoustic tweezers have been developed to manipulate sub-wavelength microparticles [4]. However, the complicated structure of these devices limits their portability and integration capacity. In addition, the acoustic streaming-induced drag force can be applied to manipulate microparticles with a size far smaller than the wavelength. However, these particles can not be trapped at stable positions [5]. In this work, we develop a simple cylindrical shell (CS) structure for the trapping of sub-wavelength particles with a radius as small as 1/400 of the corresponding acoustic wavelength [6]. This mechanism is attributed to the significantly enhanced acoustic radiation force originating from the resonant excitation of low order circumferential modes intrinsically existing in the cylindrical shell, this mode has a highly localized field around its surfaces. Then, we further experimentally demonstrate that particles and cells can be trapped at the inner surface of the resonant CS in a contactless and biocompatible manner.

Design and characterization of cylindrical shell sample

The schematic of the experimental setup is shown in Fig. 1(a). The CS is bonded by two micro-catheters across a PDMS wall and suspended inside a PDMS liquid cavity with approximate dimensions of $30\times30\times10$ mm^3. A quartz substrate is at the bottom of the PDMS cavity. A piezoelectric transducer (PZT) is adhered to the quartz substrate for generating acoustic waves. The manipulated PS particles and rat brain microvascular endothelial (bEnd.3) cells are injected into the CS through a syringe pump.

The cylindrical glass shell (CGS) with a thickness ratio of 4:5 (b =120 um, a=150 um) is designed to obtain optimized localized circumferential modes in the CS. The numerical and experimental transmission spectra of the CGS are shown in Fig. 1(b). It is clearly observed that there a transmission dip in both experiment and theory. The pressure fields of this resonant frequency are shown in the left panel of Fig. 1(c), which are localized at the surface of the CGS and around the circumference of the CGS with two-order. Thus, this is the second circumferential resonance mode of the CGS. To characterize the trapping ability, Gor'kov's potential formula was used to investigate the acoustic radiation forces (ARFs) exerting on PS particles with a radius of 5 um at this resonant frequency. As shown in the right panel of Fig. 1(c), it is clearly revealed that PS particles can experience a stable zero ARF at the four pressure minima in the circumferential direction [Fig. 1(d)], and experience a positive ARF in the radial direction, pulling the particles toward the inner surface of the CGS [Fig. 1(e)]. Thus, PS particles can be trapped at these four stable positions near the inner surface of the CGS at this second-order resonant frequency.

Particle and cell manipulation

Particle manipulation experiments in the resonant CGS were conducted by trapping PS particles with a radius of 5 μm, which is as small as 1/400 of the corresponding acoustic wavelength. Initially, PS particles were randomly distributed and moved by the drag force induced by the continuous fluid flow with a flow rate of 20 nl/s [Figs.2(a) and 2(c)]. When the acoustic power was turned on, the PS particles immediately accelerated toward the nearest inner wall due to the radial ARF. They then moved slowly to the stable trapping regions where the circumferential ARF is equal to zero [Figs. 2(b) and 2(d)]. Note that there seem like just two trapping regions observed in the experiment, which do not agree well with four stable trapping positions in theory. This disagreement may attribute to the experimental limitations and imperfection of the fabricated sample.

To further demonstrate the biocompatibility of this CGS system, we also trapped living bEnd.3 cells with a radius of 7.5 um. As predicted, the injected cells were immediately trapped at the inner surface of the CGS. The input power is about 0.17W, which is low enough not to damage the cells. The uptake of propidium iodide (PI) and calcein acetoxymethyl ester (Calcein AM) were then injected into the CGS to validate the viability of the manipulated bEnd.3 cells after a 24h cell culture. Figures 2(f) and 5(h) show that there is no significant difference in the viability of the manipulated cells after an exposure time of 5 min, compared to the normal cells cultured inside the CGS without the acoustic exposure [Figs 2(e) and 5(g)].

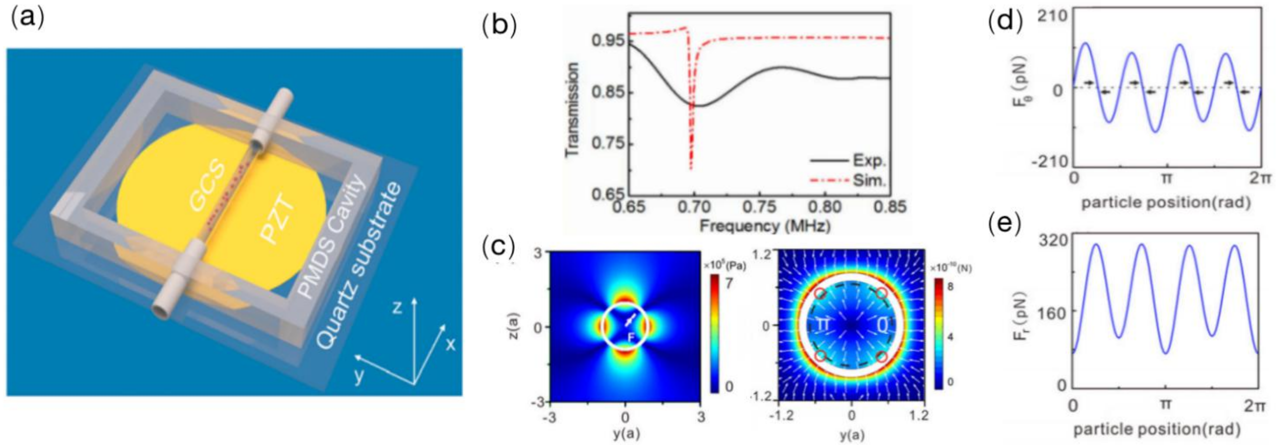

Figure 1: (a) Schematic illustration of the experimental configuration. (b) The simulated (red dashed-dotted line) anc experimental (black solid line) transmission spectra of the CGS. (c) Sound pressure field |p| (left panel) and simulatec ARF map exerted on PS particles with a radius of 5 um (right panel) at the second resonant frequency.The circumferential (d) and radial (e) components of the ARF vs the particles position moving along the black line in righ panel of (c). These red hollow circles in right panel of (c) denote stable trapping positions. Incident pressure: 0.1 MPa.

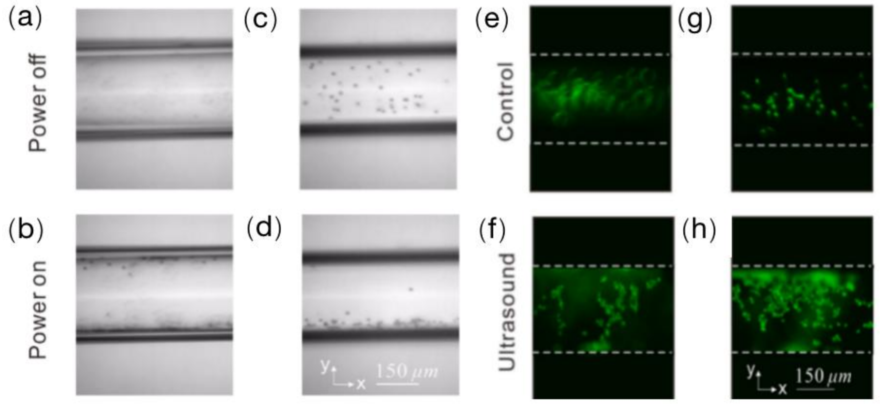

Figure 2: Time-lapse snapshots of the initial status of particles with a radius of 5 um above (a) and below (c) the central inner surface of the CGS.(b) the same as (a), and (d) the same as (c) but for the final status of trapping particles. Fluorescence micrographs of bEnd.3 cells without acoustic exposure above (e) and below (g) the central inner surface of the CGS. (f) the same as (e), and (h) the same as (g) but for bEnd.3 cells manipulated by the second resonant CGS . Input power: 0.17 W.

Conclusion

We have theoretically investigated and experimentally demonstrated the acoustic trapping of sub-wavelength particles and cells at the inner surface of a resonant CGS. This trapping effect originates from the highly enhanced ARF caused by the resonant excitation of low-order circumferential modes intrinsic to the CGS. In addition, the power used to manipulate particles is relatively small due to the strong gradient potential, which may reduce physiological damage to cells or other biological objects arising from the thermal effects. We believe that the cylindrical resonance shell-based acoustic tweezers will play a critical role in nano-scale manufacturing and biomedical applications such as bioprinting, cell culturing, and tissue engineering.

References

[1] A. Marzo and B. W. Drinkwater, Proc. Natl. Acad. Sci. U.S.A. 116(1), 84 (2019).

[2] Z. H. Tian, S. J. Yang, P. H. Huang, Z. Y. Wang, P. R. Zhang, Y. Y. Gu, H. Bachman, C. Y. Chen, M. X. Wu, Y. B. Xie, and T. J. Huang, Sci Adv. 5, 6062 (2019).

[3] K. Lee, H. Shao, R. Weissleder, and H. Lee, ACS Nano 9(3), 2321 – 2327 (2015).

[4] F. Li, F. Y. Cai, Z. Y. Liu, L. Meng, M. Qian, C. Wang, Q. Cheng, M. L. Qian, X. Liu, J. R. Wu, J. Y. Li, and H. R. Zheng, Phys. Rev. Appl. 1, 051001 (2014).

[5] D. J. Collins, Z. Ma, J. Han, and Y. Ai, Lab Chip 17, 91 – 103 (2017).

[6] Q, Lin, W. zhou, F.Y. Cai, F. Li, X. X. Xia, J. Q. Wang, D. G. Zhao , F. Yan, L. Meng and H. R. Zheng, Appl. Phys. Lett. 117, 053501 (2020)

Acoustofluidics 2021
26-27 August 2021
Virtual Conference

Analysis of acoustophoretic focusing using the open-source 3D particle tracking toolbox *DefocusTracker*

Massimiliano Rossi[1], Rune Barnkob[2], and Henrik Bruus[1]

[1] Department of Physics, Technical University of Denmark, DTU Physics Building 309, DK-2800 Kongens Lyngby, Denmark
E-mail: rossi@fysik.dtu.dk
[2] Heinz-Nixdorf-Chair of Biomedical Electronics, Department of Electrical and Computer Engineering, Technical University of Munich, TranslaTUM, 81675 Munich, Germany

Introduction

The experimental characterization of micro-acoustofluidic devices relies more and more often on single-camera particle-tracking methods based on defocusing [1,2]. Conventional 2D particle tracking methods are typically not sufficient to characterize acoustofluidic experiments, where flow fields and particle trajectories are strongly three dimensional. Defocusing methods allow to measure the three-dimensional trajectories of micro-particles and require only a single-view optical system with small depth-of-field, typically a microscopy objective [3].

DefocusTracker [4] is an open-source software for 3D particle tracking based on the well-established General Defocusing Particle Tracking (GDPT) method. The latest Version 2.0.0 was released on June 2021 and is currently available at https://defocustracking.com/defocustracker/. The evaluation procedure is based on image recognition using the normalized cross-correlation function and allows in few steps to robustly identify particle images and their depth position even with noisy images or complex background. In this work, we present an experimental analysis of vertical acoustophoretic focusing of micro-particles in a glass capillary performed with *DefocusTracker*.

Materials and methods

The acoustophoretic experiments were performed on a glass capillary with a rectangular cross-section of 2.0×0.2 mm^2 and circular side walls with a radius of curvature of 0.1 mm. Fluorescent polystyrene spheres with a diameter of 10 µm were dispersed in a solution of water and iodixanol with the same density ($\rho_\mathrm{w} = \rho_\mathrm{PS} = 1050$ kg/m^3). The acoustic actuation was provided by a piezoelectric transducer (Pz26, Meggitt A/S) glued to the capillary and driven by a sinusoidal signal with peak-to-

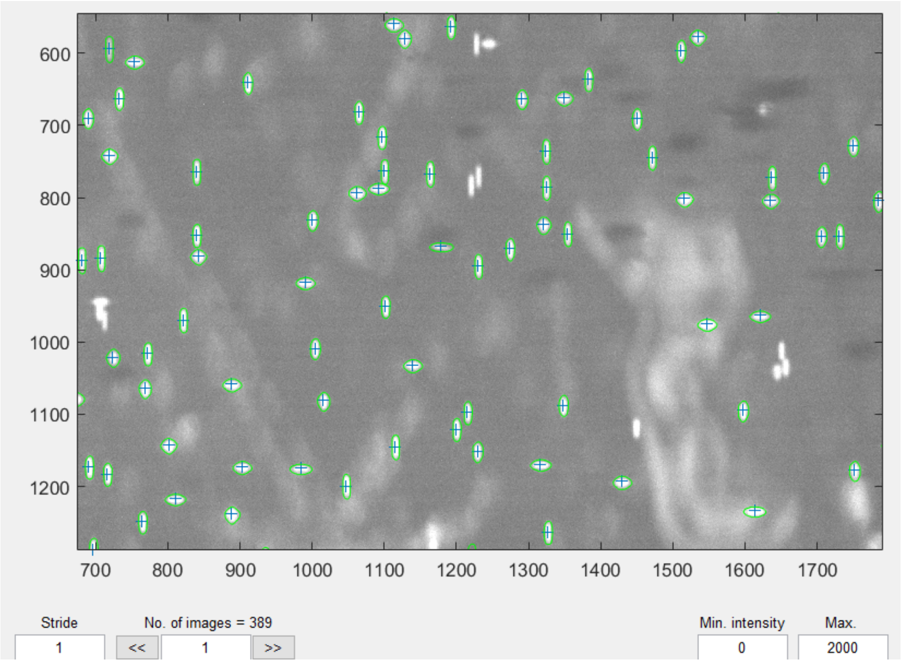

Stride 1
No. of images = 389
1
Min. intensity 0
Max. 2000

Figure 1: Particle image detection using *DefocusTracking.* A segmentation-free particle detection algorithm based on the normalized cross-correlation function allows to robustly identify defocused particle images of different shape, with no need of background removal or image pre-processing steps.

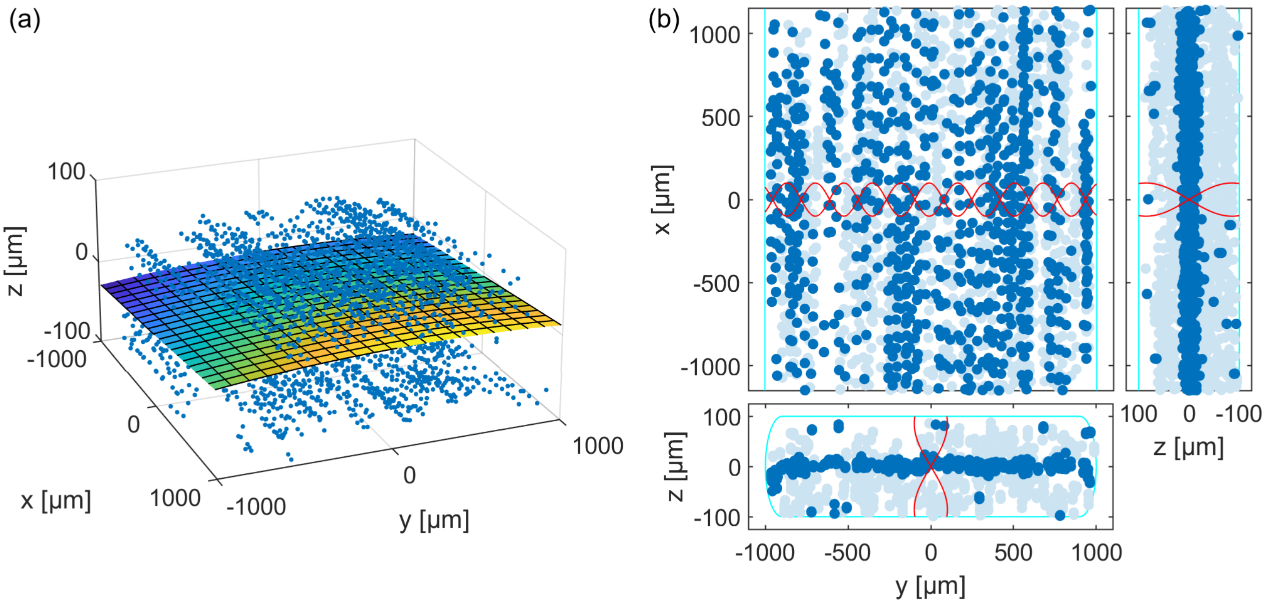

Figure 2: (a) Correction of bias errors introduced by the field curvature of the lens and the tilting of the microchannel using a reference Poiseuille flow. (b) Acoustophoretic focusing of 10-µm-diameter polystyrene particles at the resonant frequency of 4.375 MHz. Light-blue points represent particle positions without acoustic actuation, dark blue with acoustic actuation.

peak amplitude of 5 V (Analog Discovery 2). Simultaneously, a syringe pump was used to establish a pressure-driven Poiseuille flow in the microchannel. Different frequencies and flow rates were tested. An in-house epi-fluorescent microscopy system was assembled and used to acquire the images. A 5× magnification lens (Carl Zeiss AG) was used and the images were taken using a high-sensitivity sCMOS camera (pco.edge5.5, PCO AG). The illumination was provided by a high-power LED (Solis-525C, Thorlabs Inc.). The images were processed with the open-source toolbox *DefocusTracker*.

Results

A GDPT measurement relies on a set of reference calibration images at known depth positions, typically obtained by scanning sedimented particles along different depth positions . After calibration with a suitable set of calibration images, *DefocusTracker* can automatically identify similar particle images and determine their depth (Fig. 1) [5]. Bias errors introduced by the field curvature of the lens or by the tilting of the microchannel can be corrected using a reference experiment, such a Poiseuille flow, as shown in Fig. 2(a). After calibration and bias correction, the system is ready for the characterization of acoustophoretic experiments. Fig. 2(b) shows the 3D position of 10-µm-diameter polystyrene particles transported by a 50 µl/min Poiseuille flow, with (dark blue) and without (light blue) acoustic actuation. The acoustic actuation was driven at a resonance frequency of 4.375 MHz, corresponding to an acoustic node in the horizontal mid-plane, where the particles are focused. More experiments at different frequencies and flow rates will be presented and discussed in the full presentation.

Conclusion

We have used the open-source 3D particle-tracking toolbox *DefocusTracker* to characterize the acoustophoretic motion of polystyrene particles in a glass capillary. *DefocusTracker* provides a robust and easy-to-use approach for the characterization of acoustofluidic experiment and has the potential to become a widespread tool in the acoustofluidic community.

Acknowledgements

The author acknowledges financial support by the Villum Foundation under the Grant No. 00022951.

References

[1] P. B. Muller, M. Rossi, A. Marin, R. Barnkob, P. Augustsson, T. Laurell, C. J. Kähler, and H. Bruus. Phys. Rev. E **88**, 023006 (2013).
[2] W. Qiu, J. T. Karlsen, H. Bruus, and P. Augustsson. Phys. Rev. Applied **11**, 024018 (2019).
[3] R. Barnkob and M. Rossi. Exp. Fluids **61**, 1-14 (2020).
[4] R. Barnkob and M. Rossi. arXiv preprint, arXiv.org/abs/2102.03056 (2021).
[5] M. Rossi and R. Barnkob. Meas. Sci. Technol. **32**, 014001 (2020).

Session 3 - Physical Acoustics

Invited Speaker

08:10 - 08:40 **EXPLOITING PHASE SINGULARITIES TO STABLY TRAP INDIVIDUAL MICROBUBBLES**
Diego Baresch
Université de Bordeaux, FRANCE

Contributed Talks

08:40 - 08:50 **SELF-ORGANIZATION BY ACOUSTIC CONTRAST FACTOR IN ACOUSTICALLY PACKED BEDS OF WHOLE BLOOD AND IN-LINE REMOVAL OF RED BLOOD CELLS**
Richard Soller, Ola Jakobsson, and Per Augustsson
Lund University, SWEDEN

08:50 - 09:00 **MEAN ACOUSTIC FIELDS IN ACOUSTOFLUIDICS: RADIATION FORCE AND TORQUE ON SUBWAVELENGTH AXISYMMETRIC PARTICLES**
Everton B. Lima, Giclênio C. Silva, Marcos Sales, Ana Leite,
Ueslen Rocha, and Glauber T. Silva
Federal University of Alagoas, BRAZIL

09:00 - 09:10 **SUPPRESSION OF ACOUSTIC STREAMING BY AC ELECTROOSMOSIS: THEORY AND SIMULATION**
Bjørn G. Winckelmann and Henrik Bruus
Technical University of Denmark, DENMARK

09:10 - 09:20 **EFFECTS OF A LASER-INDUCED THERMAL GRADIENT ON THE ACOUSTIC STREAMING FIELD**
Franziska Martens, Wei Qiu, Andreas Ehn, and Per Augustsson
Lund University, SWEDEN

09:20 - 09:30 **QUALITATIVE CHANGES IN THE STREAMING PATTERN AT HIGH ACOUSTIC ENERGY DUE TO FRICTION-INDUCED HEATING IN THE VISCOUS BOUNDARY LAYERS**
Jonas H. Joergensen[1], Wei Qiu[2], and Henrik Bruus[1]
[1]Technical University of Denmark, DENMARK and
[2]Lund University, SWEDEN

09:30 - 09:40 **MEASURING THE TEMPORAL DIFFERENCE IN BUILD UP BETWEEN THE ACOUSTIC RADIATION FORCE AND ACOUSTIC STREAMING WITH AN OPTICAL TWEEZER**
Christoph Goering and Jürg Dual
ETH Zürich, SWITZERLAND

Flash Talks

09:40 - 09:44
EFFECTS OF SHAPE AND WILLIS COUPLING ON ACOUSTIC RADIATION FORCE AND TORQUE
Shahrokh Sepehrirahnama[1], Sebastian Oberst[1,2], Yan Kei Chiang[1,2], and David A. Powell[1,2]
[1]*University of Technology Sydney, AUSTRALIA and*
[2]*University of New South Wales, AUSTRALIA*

09:44 - 09:48
EFFECT OF AXIAL PRIMARY RADIATION FORCE ON THE DYNAMICAL MOTION OF A PAIR OF MICROPARTICLES ALONG THE PRESSURE NODAL PLANE
Sazid Z. Hoque, Amal Nath, and Ashis K. Sen
Indian Institute of Technology (IIT), Madras, INDIA

09:48 - 09:52
GENERALIZED POTENTIAL FOR ACOUSTIC INTERACTION FORCE
Shahrokh Sepehrirhnama[1], and Kian-Meng Lim[2]
[1]*University of Technology Sydney, AUSTRALIA and*
[2]*National University of Singapore, SINGAPORE*

09:52 - 09:56
MICROSTREAMING AND ACOUSTIC INTERACTION FORCES BETWEEN TWO PARTICLES IN A STANDING WAVE WITHIN A VISCOUS FLUID
Alen Pavlic, Lorenzo Ermanni, and Jürg Dual
ETH Zürich, SWITZERLAND

09:56 - 10:00
3D3C FLOW MEASUREMENTS OF THE ACOUSTICALLY INDUCED VORTEX STRUCTURES IN A STANDING SURFACE ACOUSTIC WAVE FIELD
Sebastian Sachs, Christian Cierpka, and Jörg König
Technische Universität Ilmenau, GERMANY

10:00 - 10:04
BURGERS-RICCATI PHYSICS OF FAST BULK ACOUSTIC STREAMING
Jeremy Orosco and James Friend
University of California, San Diego, USA

10:04 - 10:08
SPECULAR-REFLECTION CONTRIBUTIONS TO DYNAMIC RADIATION FORCES ON HIGHLY REFLECTING SPHERES AND CYLINDERS: SIMPLIFIED ANALYSIS
Philip L. Marston[1], Timothy D. Daniel[1,2], and Auberry R. Fortuner[1]
[1]*Washington State University, USA and*
[2]*Naval Surface Warfare Center Panama City Division, USA*

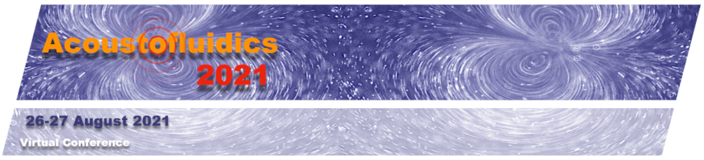

Exploiting phase singularities to stably trap individual microbubbles

Diego Baresch

Mechanical Engineering Institute (I2M), Physical Acoustics Laboratory, CNRS, Université de Bordeaux, France

Introduction

Acoustic wavefields possessing a singular phase can be synthesised in a gas or a liquid by engineering the emitted wavefront [1-3]. An acoustic vortex is a beam for which the wavefront is spiralling around the propagation axis where the phase goes undefined, and the acoustic pressure vanishes as a consequence of destructive interference. In this talk I will provide an overview of our recent efforts to model, control and exploit the acoustic radiation force [4,5] arising when vortex beams interact with isolated particles. In particular, we have reported vortex beams enable to generate a gradient force converging towards the focus in all directions of space [6], thereby demonstrating the first acoustic analogue to optical tweezers [7]. For small particles relative to the driving wavelength, the trap stability stems from the annihilation of the monopolar oscillation mode which usually leads to a strong repulsive force for elastic particles located at the focus of axisymmetric beams. This notable behaviour has recently been investigated in the context of individual microbubbles whose exceptionally rich and strong monopolar dynamics is central to all the manipulation strategies reported so far; but is also responsible for their main limitations. In contrast, vortex beams were shown to enable stable trapping, precise positioning and manoeuvring in three-dimensions without relying on monopolar bubble dynamics, therefore providing a new stable parametric space for bubble manipulation. Overall, this approach shows promise for pinpoint 3D-manipulation of individual microbubbles in complex environments, with important implications in applications such as drug delivery, microfluidics, sonoporation or sonoluminescence.

The acoustic gradient force in vortex beams

For a small particle relative to the driving wavelength $a/\lambda \ll 1$, where a is the particle radius, the gradient component of the acoustic radiation force dominates [6]:

$$\vec{F_a} = -\frac{1}{2}\left\{\Re(\alpha_m)\frac{1}{2\rho c^2}\vec{\nabla}|p_a|^2 - \Re(\alpha_d)\frac{1}{2}\rho\vec{\nabla}|\vec{v_a}|^2\right\}, \tag{1}$$

where p_a and $\vec{v_a}$ are the first order acoustic pressure and velocity field taken at the particle centre respectively. ρ is the host liquid density and c the speed of sound. $\Re$ denotes the real part of complex quantities. α_m and α_d are two acoustic strength parameters associated to the monopolar and dipolar oscillation modes of a spherical particle. For the special case of a bubble, the following expressions can be found [8]:

$$\Re(\alpha_m) = \frac{4}{3}\pi a^3 \frac{K}{K_b}\frac{\omega_0^2(\omega^2-\omega_0^2)}{(ka\omega^2)^2+(\omega^2-\omega_0^2)^2} \tag{2}$$

$$\Re(\alpha_d) = 4\pi a^3\left(\frac{\rho_b-\rho}{2\rho_b+\rho}\right). \tag{3}$$

$K=\rho c^2$ and $K_b=\rho_b c_b^2$ are the propagation medium and gas bulk modulii respectively, ρ_b the gas density and $\omega_0=(3K_b/\rho a^2)^{1/2}$ and ω the natural oscillation frequency of the bubble (or Minnaert resonance frequency) and driving frequency respectively.

A bubble located off-axis of the vortex beam will undergo monopolar oscillations, and will be driven by a force proportional to $|\vec{\nabla}p_a|$ towards, or away from, the propagation axis, for bubbles driven above or bellow resonance respectively. This behaviour is well documented for bubbles located near the nodes or antinodes of a standing wave levitation apparatus. When the bubble reaches the propagation axis, z, vortex beams create the specific condition for which $|p_a|=0$ and $\frac{\partial|p_a|^2}{\partial z}=0$ simultaneously at a distance $r=\sqrt{x^2+y^2}=0$ from the axis. Under these conditions, the axial force exerted by a

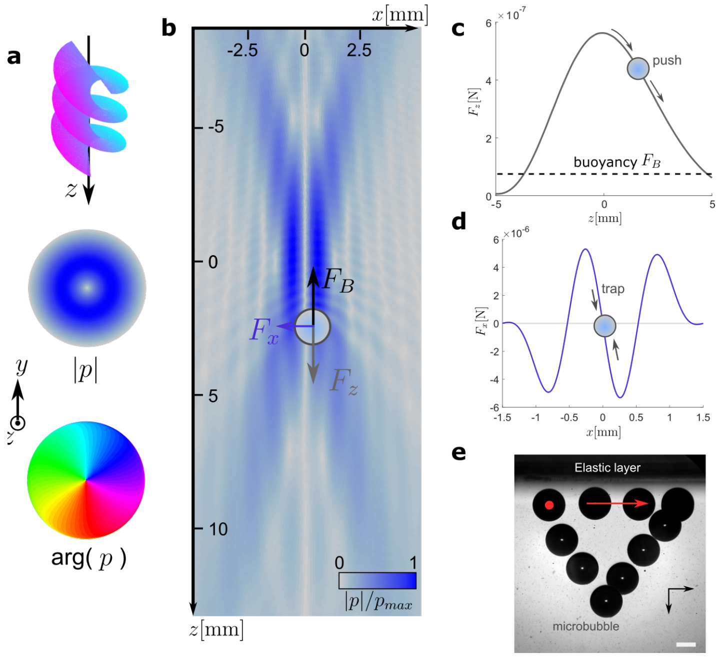

Figure 1: a) Spiralling wavefront, lateral pressure magnitude and phase of a focused vortex beam. b) An individual bubble scattering the incident focused vortex beam generates a lateral trapping force (c) and a net pushing force (d) countering the bubble's buoyancy. e) Timelapse sequence of a bubble manoeuvred in 2D with the single-beam vortex trap.

vortex beam written as $p_a = \tilde{p}(r,z)e^{i(m\theta-\omega t)}$, where m quantifies the beam helicity, reads

$$F_z = \frac{\Re(\alpha_d)}{4\rho\omega^2}\frac{\partial}{\partial z}\left|\frac{\partial \tilde{p}}{\partial r}\right|^2. \tag{4}$$

In a focused vortex beam, the axial force pushes the bubble downstream from the focus. This force is of weaker magnitude compared to the lateral trapping force (by approximately 3 orders of magnitude), but remains sufficient to counter the upward buoyancy force at moderate acoustic power. The pushing and lateral acoustic forces act together to stabilise the bubble position in three dimensions.

Vortex generation and manipulation of individual microbubbles

We generated vortex beams with a focused array of 8-individual piezoelectric transducers ($f = 2.25$MHz). Each transducer is driven with independent amplitude and phase to engineer the spiralling wavefront. Individual bubbles were generated by the *in situ* electrolysis of water setting a size range between 10 and 500 microns. The largest bubbles were obtained by the subsequent coalescence of multiple bubbles entering the trap. The largest bubbles stand out of the range for which the acoustic force can be described by the gradient force introduced in the previous paragraph. Nevertheless, we have observed stable trapping forces for bubbles with a radius comparable to the driving wavelength [8]. A bubble trapped at a unique equilibrium position can subsequently be manoeuvred by displacing the array of transducers with micron resolution.

Conclusion

Microbubbles find several promising applications in advanced ultrasonic therapies, drug delivery, sonochemsitry or microfluidic lab-on-chip design. For all these applications, and considering the large buoyancy force of a bubble at the microscale, it is desirable to remotely control the bubble position and dynamics. We have shown a vortex beam acoustical trap allows to exert sufficient forces to drive individual bubbles towards the propagation axis and arrest the rising buoyancy force, enabling their precise 3D manipulation. Our results suggest microbubbles can be controlled in complex environments, which could lead to *in vitro* and *in vivo* manipulation, opening new perspectives for biomedical research.

References

[1] BT. Hefner and PL. Marston. Journal of the Acoustical Society of America **106**, (1999).
[2] J-L. Thomas and R. Marchiano. Physical Review Letters **91**, (2003).
[3] A. Marzo and B. Drinkwater. Proceedings of the National Academy of Sciences **116**, (2019).
[4] D. Baresch, J-L. Thomas, and R. Marchiano. Journal of the Acoustical Society of America **133**, (2013).
[5] D. Baresch, J-L. Thomas, and R. Marchiano. Journal of Applied Physics **113**, (2013).
[6] D. Baresch, J-L. Thomas, and R. Marchiano. Physical Review Letters **116**, (2016).
[7] A. Ashkin *et al.* Optics Letters **11**, (1986).
[8] D. Baresch and V. Garbin. Proceedings of the National Academy of Sciences **117**, (2020).

Acoustofluidics 2021
26-27 August 2021
Virtual Conference

Self-organization by acoustic contrast factor in acoustically packed beds of whole blood and in-line removal of red blood cells

Richard Soller, Ola Jakobsson, and Per Augustsson

Lund University, Department of Biomedical Engineering, Lund, Sweden
E-mail: per.augustsson@bme.lth.se, URL: https://bme.lth.se/staff/augustsson-per/per-augustsson/

Introduction

Blood is an extremely diverse and crowded suspension of cells and particles and about 40% of the blood volume consists of red blood cells (RBC) making it time consuming to isolate rare from blood by most available microfluidic methods. To address this need, we have studied the behavior of blood cells when they become densely packed by a sound field. Considering packed RBCs not as single cells but as a medium, our hypothesis is that cells or particles trapped inside packed RBCs have an acoustic contrast factor that is dependent on the RBC properties and that they tend to re-organize predictably according to their acoustic properties. We demonstrate this reorganization in stop-flow experiments, and we show that this principle can be exploited for separation of rare cells directly from undiluted whole blood. This type of separation could form an initial stage of refinement in a series of purification steps for accessing rare cells such as white blood cells or circulating tumor cells. This is our first report of this discovery and we have found no prior publications on the subject, and we therefore think that it should be of considerable interest to the acoustofluidic community.

Experimental arrangement

We used a Glass-Silicon-Glass chip with a 150 µm × 374 µm × 50 mm (h×w×l) main channel with trifurcated in- and outlets (Fig. 1). It was actuated by a glued-on piezoceramic transducer by 1 ms sweeps of 1.93 to 1.96 MHz with amplitudes ranging from 3 V_{pp} to 15 V_{pp}, resulting in a single node standing wave in the channel center. When necessary, the chip was cooled by air flow. Whole blood was driven through the channel by a syringe pump, another syringe with PBS was used for flushing if necessary. Blood was pre-filtered with a 70 µm nylon cell strainer to avoid clogging the chip and spiked 1:10 with a suspension containing Jurkat cells stained with Calcein Deep Red AM ester or 10 µm fluorescent glass beads or 10- or 5-µm fluorescent polystyrene (PS) beads. Images and videos were acquired with a microscope. Stop flow experiments with beads, Jurkat cells, and red blood cells were conducted with open outlets. Inline removal of blood cells from Jurkat cells were conducted by controlling the output flow-rate ratios at the center or side outlets with a syringe in pull configuration while the other outlet was open for sample collection. Collected cell samples were analyzed with a flow cytometer.

Results and discussion

We first performed stop flow experiments to study how RBCs pack in an acoustic field and where beads or cells will migrate during packing. Fig. 2 shows the packed RBCs and positions of cells and beads over time during acoustic focusing. Jurkat cells (Fig. 2A and B), which are bigger than RBCs but which we also assume to have a lower compressibility and density, migrate to the interface between the packed RBCs and the plasma, while the less compressible, and higher-density 10-µm-glass beads (Fig. 2C) migrate to the center of the packed red blood cells. 10-µm-PS-beads move to a node inside the RBC bed and execute small streaming rolls inside the packed RBC (Fig. 2D) while the 4-µm-PS beads stream across the whole packed RBCs (Fig. 2E). Our preliminary hypothesis is that the packed RBCs, being soft and slippery, acts as a semi-continuous medium that determines an altered acoustic contrast factor for particles trapped inside. Jurkat cells have a negative acoustic contrast factor inside the RBC bed while having negative contrast in the outside plasma. Hence, inside the packed RBCs they migrate in the direction of the pressure anti-node and stop at the RBC-plasma border. 10-µm-glass beads have a positive acoustic contrast factor inside the RBC bed and move to the pressure node while the 10-µm- and 4-µm-PS beads have only a slight positive acoustic contrast factor, which drives them to the pressure node but makes them also susceptible to the slow rotation of the RBCs due to acoustic streaming.

We then studied if cells that accumulate at the RBC-plasma interface can be skimmed off at the trifurcated outlet of our chip and be separated from RBCs. We collected output samples from the center and side outlets, for a range of flow rate ratios, at a throughput of 100 µl/min. Figure 3A shows the concentrations of Jurkat cells and RBCs in the output sample relative to the input sample. We were able to decrease the RBC concentration to ~20% relative to the input sample while recovering ~76% of the Jurkat cells (Fig. 3B) and thereby achieving a 10-fold relative enrichment of Jurkat cells (Fig. 3C).

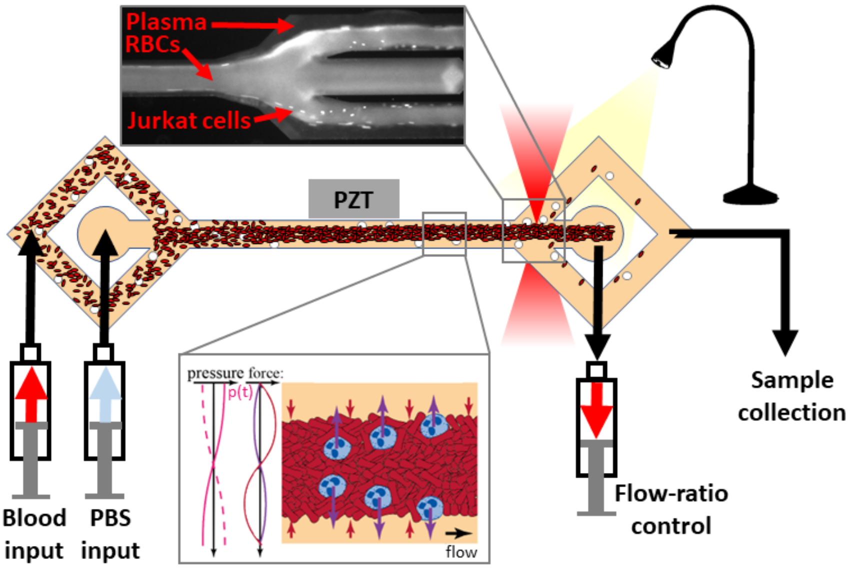

Figure 1: Setup used for separation of Jurkat cells from RBCs by acoustic packing and skimming. Samples were collected from the side outlets (shown) and from the center outlet (not shown). For stop-flow experiments both outlets were open. The PBS syringe is for rinsing the system between runs.

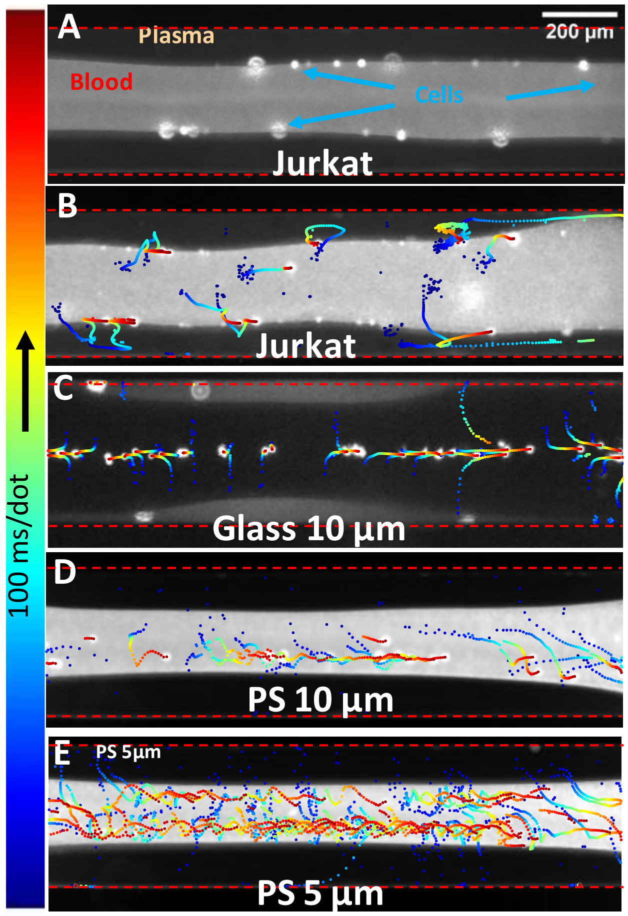

Figure 2: (A) Blood spiked with Jurkat cells after acoustic packing. Red dotted line indicates the channel walls. (B) Blood spiked with Jurkat cells, (C) 10 µm glass beads, (D) 10 µm PS beads, (E) and 5 µm PS beads after acoustic packing. Dots mark fluorescent particle positions in consecutive video frames.

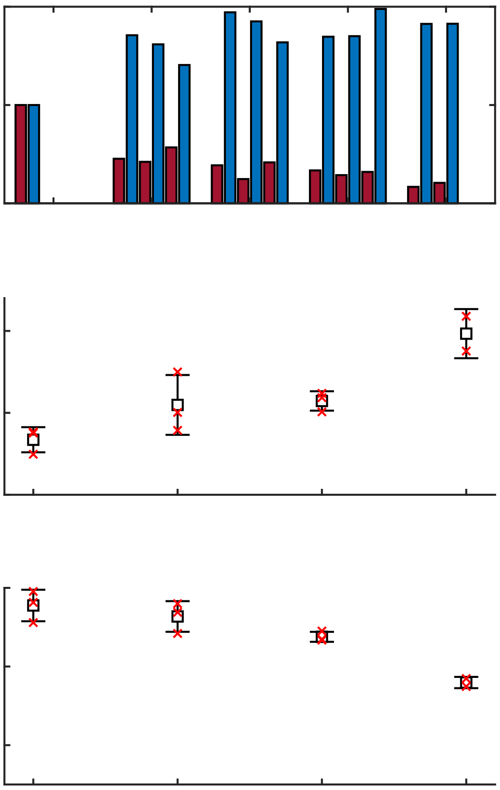

Figure 3: (A) Relative concentrations of Jurkat cells and RBCs before and after skimming, (B) Jurkat cell recovery rate and (C) Jurkat cell enrichment rate. Red crosses: Single measurements.

Conclusion

We showed that particles and cells in acoustically focused packed particles organize predictably according to their local acoustic contrast factor in the packed bed. The fact that we observe streaming particle paths inside the packed cells indicate that the packed RBCs are subject to acoustic streaming. We also showed that this can be used as an initial separation step for higher throughput acoustic separation of rare particles.

Acoustofluidics 2021
26-27 August 2021
Virtual Conference

Mean acoustic fields in acoustofluidics: radiation force and torque on subwavelength axisymmetric particles

Everton B. Lima[1], Giclênio C. Silva[1], Marcos Sales[2], Ana Leite[2], Ueslen Rocha[1,3] and Glauber T. Silva[1]

[1]Physical Acoustics Group, Institute of Physics, Federal University of Alagoas, Maceió, Brazil
[2]Laboratory of Bioenergetics, Institute of Chemistry, Federal University of Alagoas, Maceió, Brazil
[3]Group of Nanophotonics and Images, Institute of Physics, Federal University of Alagoas, Maceió, Brazil
E-mail: gtomaz@fis.ufal.br, URL: www.if.ufal.br/~gaf

Introduction

Active methods to handle, move, position, and pattern microparticles and cells in acoustofluidic devices are vastly based on the acoustic radiation force phenomenon. This effect arises when the linear momentum of an ultrasonic wave changes due to scattering and absorption caused by a particle immersed in a fluid. When the incoming wave energy stationary varies in space (throughout the fluid), a subwavelength particle (much smaller than the wavelength) is subjected to a gradient force. Ultrasonic waves with no spatial variation in energy, such as traveling plane waves, give a push on microparticles. Another effect that appears in non-isotropic particles is the acoustic radiation toque that aligns or spins the particle. The radiation force and torque are referred to as *the mean-acoustic fields* in acoustofluidics.

Based on the dipole approximation for the scattering wave expansion, exact solutions to the mean acoustic fields have been obtained only for particles with spherical [1,2] and spheroidal [3] shapes. Nonetheless, several types of cells have more elaborate shapes than these simple geometries. The solution for complex-shaped particles is based on numerical techniques such as the finite element method. Naturally, determining the particle dynamics with numerical methods is a compute-intensive task. The complete understanding of the mean fields is at the heart of developing novel methods for microparticle handling in acoustofluidic microenvironments. Here, we present a theoretical description of the mean acoustic fields exerted on an axisymmetric particle, e.g., with an axis of symmetry for rotations, immersed in a Newtonian fluid. More emphasis will be given to the fields produced by incoming waves with non-homogeneous intensity, e.g., ultrasonic standing waves. In this case, the radiation force is given by the incident wave's kinetic and potential energy gradient. The force also depends on the acoustic analog to the electric and magnetic polarizability tensor of the particle. Acoustic polarizabilities are obtained by numerically solving the wave scattering by the particle. The general expression of the radiation torque is more involving and is related to the momentum flux tensor of the incident wave and the gyroacoustic factor that is a measure of the torque efficiency. Our model is used to describe the mean acoustic fields generated by a standing wave on a red blood cell (RBC) immersed in blood plasma. Theoretical predictions for the RBC trap location and equilibrium orientation are in agreement with experimental results obtained in a polymeric chip.

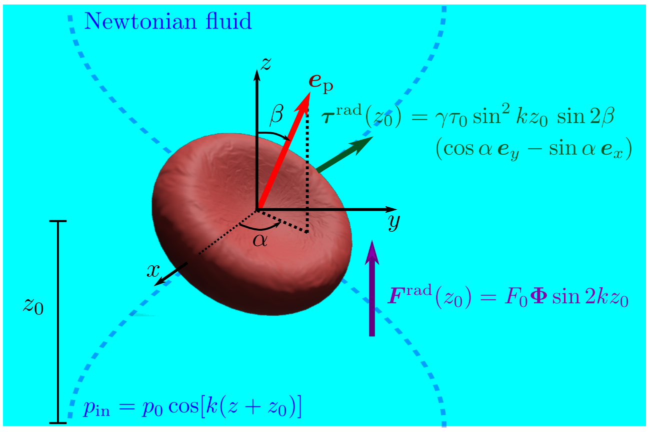

Figure 1: An RBC is considered the subwavelength axisymmetric particle, on which the mean acoustic fields of a standing plane wave (light-blue dashed line) actuate. The spatial configuration of the RBC is determined by the direction of its axis of symmetry, which is given the unit vector $\boldsymbol{e}_{\mathrm{p}}$ (red arrow). The angles α and β are the orientation angles concerning a laboratory system O_{xyz} (black arrows) placed at the geometric center of the particle. The expressions of the wave pressure (p_{in}), radiation force ($\boldsymbol{F}^{\mathrm{rad}}$, purple arrow) and torque ($\boldsymbol{\tau}^{\mathrm{rad}}$, green arrow) are presented.

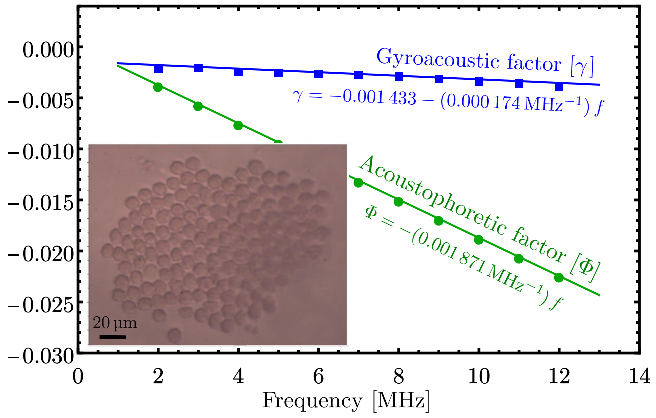

Figure 2: The gyroacoustic and acoustophoretic factors computed for a RBC in blood plasma versus frequency. The solid lines represent a linear fit of the obtained data. Inset: optical micrograph of trapped RBCs in a half-wavelength polymeric resonator operating at 3.4 MHz at room temperature. The axis of symmetry of the RBCs is aligned with the standing wave axis (coming out of the page).

Physical model

Assume a subwavelength axisymmetric particle in a fluid of density ρ_0 and compressibility β_0. The particle scatters an incoming wave of pressure amplitude p_{in}, fluid velocity $\boldsymbol{v}_{\text{in}}$, angular frequency ω, and wavenumber k. In Fig. 1, we depict an RBC as the axisymmetric particle whereon the mean acoustic fields are applied. The particle orientation concerning a fixed laboratory frame O_{xyz} is described by the azimuthal (α) and polar (β) angles.

The acoustic radiation force exerted by a stationary wave on the particle located at $\boldsymbol{r} = \boldsymbol{r}_0$ is given by [4]

$$\boldsymbol{F}^{\text{rad}}(\boldsymbol{r}_0) = \boldsymbol{\alpha}^{\text{m}} \cdot \nabla E_{\text{pot}}(\boldsymbol{r}_0) + \boldsymbol{\alpha}^{\text{d}} \cdot \nabla E_{\text{kin}}(\boldsymbol{r}_0). \tag{1}$$

This equation shows that the acoustic kinetic $E_{\text{kin}} = \rho_0 |\boldsymbol{v}_{\text{in}}|^2/4$ and potential $E_{\text{pot}} = \beta_0 |p_{\text{in}}|^2/4$ energy densities pumped into the fluid are transformed into force through their gradient projection onto the acoustic monopole ($\boldsymbol{\alpha}^{\text{m}}$) and dipole ($\boldsymbol{\alpha}^{\text{d}}$) polarizability tensors of the particle.

Consider a standing plane wave distributed along the z axis, with pressure $p_{\text{in}} = p_0 \cos[k(z + z_0)]$, where p_0 is the pressure magnitude, z_0 is the particle position relative to the pressure antinode at $z = 0$. As shown in Fig. 1, the standing wave produces the mean acoustic fields on the RBC. The expressions of the mean fields are also presented in Fig. 1, where $F_0 = AE_0$ and $\tau_0 = VE_0$, with A and V being the cross-section area (perpendicular to the axis of symmetry) and volume of the particle, respectively. The parameters which depend on how the particle scatters the incoming wave are $\boldsymbol{\Phi}$ is the acoustophoretic vector, and γ is the gyroacoustic factor. In turn, these parameters are related to the mechanical and thermodynamic properties of the particle and fluid. The factors $\boldsymbol{\Phi}$ and γ can be determined by computing the monopole and dipole coefficients of the multipole expansion of the scattered wave. The scattering coefficients are computed from the projection of the scattered pressure onto the angular part of the corresponding mode (monopole and dipole). The scattered pressure is obtained via the finite element method using the computer-aided engineering software COMSOL Multiphysics (Comsol, Inc., Sweden).

Results

We compute the acoustophoretic and gyroacoustic factors for the RBC in blood plasma (see Ref. [4]). The finite element result is shown in Fig. 2. We see that both parameters are negative and vary linearly with frequency f. A negative acoustophoretic factor means that the RBC will be trapped in a pressure node. Moreover, having $\gamma < 0$ says the RBC axis of symmetry will be aligned with the standing wave axis ($\beta = 0$). These qualitative predictions are confirmed by experimental observation of trapped RBCs in a half-wavelength acoustic resonator, as shown in the inset.

Conclusions

We present a mean acoustic field theory for axisymmetric particles immersed in a Newtonian fluid. Our model is valid for acoustic waves of an arbitrary wavefront. Thermoviscous effects of the surrounding fluid and particle can be readily accounted for in the model by including them in the finite element numerical simulations of scattering.

References

[1] H. Bruus, Lab Chip **12**, 1014-1021 (2012).
[2] G. T. Silva and B. W. Drinkwater, J. Acoust. Soc. Am. **144**, EL453-459 (2018).
[3] E. B. Lima and G. T. Silva, arXiv:2104.06090, (2021) [J. Acoust. Soc. Am. (to be published)].

Acoustofluidics 2021
26-27 August 2021
Virtual Conference

Suppression of acoustic streaming by AC electroosmosis: theory and simulation

Bjørn G. Winckelmann and Henrik Bruus

Department of Physics, Technical University of Denmark, 2800 Kongens Lyngby, Denmark
E-mail: winckel@dtu.dk , URL: http://www.fysik.dtu.dk/microfluidics

Introduction

Controlling sub-micrometer particles in acoustofluidic devices is often impeded by acoustic streaming. The acoustic streaming is typically driven from the boundary of the fluid channel through the thin viscous boundary layer. We use analytical calculations and numerical simulations to study efficient suppression of the streaming by another type of boundary-driven streaming used in microfluidics, namely AC electroosmosis. We predict that a suitable implementation of such electroacoustic streaming, can reduce the total steady streaming amplitude in the bulk of a typical rectangular acoustofluidic channel by two orders of magnitude.

Electroacoustic streaming

As illustrated in Fig. 1, we suggest a novel design idea for an acoustofluidic setup with integrated electrodes at the top and bottom of the fluid channel for generating AC electroosmotic streaming. The principal idea is to use a controlled electroosmotic streaming in a dilute aqueous suspension of ions to counteract the inevitable acoustic streaming generated by actuating a standing acoustic half-wave resonance. As demonstrated in our recent paper [1], the electroacoustic streaming emerging from the combined acoustic and electroosmotic actuation is well described by a Stokes flow with an acoustic body force and the two independent slip velocities, acoustic and electroosmotic, even at relevant electroosmotic actuation voltages around five times the thermal voltage $k_\mathrm{B}T/e$, well into the non-linear regime. Denoting the time-averaged streaming field $\langle \boldsymbol{v}_2 \rangle$ and the corresponding pressure field $\langle p_2 \rangle$, the governing equations and boundary conditions at the fluid-solid boundary of the channel $\boldsymbol{r} = \boldsymbol{s}_0$ are,

$$0 = \boldsymbol{\nabla} \cdot \langle \boldsymbol{v}_2 \rangle, \tag{1a}$$

$$\boldsymbol{0} = -\boldsymbol{\nabla} \langle p_2 \rangle + \eta_\mathrm{fl} \nabla^2 \langle \boldsymbol{v}_2 \rangle + \boldsymbol{f}_\mathrm{b}^\mathrm{ac}, \tag{1b}$$

$$\langle \boldsymbol{v}_2 \rangle = \langle \boldsymbol{v}_{2,\mathrm{slip}}^\mathrm{ac} \rangle + \langle \boldsymbol{v}_{2,\mathrm{slip}}^\mathrm{eo} \rangle, \quad \text{for } \boldsymbol{r} = \boldsymbol{s}_0. \tag{1c}$$

Here, $\langle \boldsymbol{v}_{2,\mathrm{slip}}^\mathrm{ac} \rangle$ and $\langle \boldsymbol{v}_{2,\mathrm{slip}}^\mathrm{eo} \rangle$ denote the acoustic and the electroosmotic slip velocity, respectively. The slip velocities and the acoustic body force $\boldsymbol{f}_\mathrm{b}^\mathrm{ac}$ can be calculated after solving two independent first-order problems, one describing the harmonic pressure field p_1 and the acoustic vibrational velocity $\boldsymbol{v}_1$, and the other describing the first-order electrical potential ϕ_1^bk as in Refs. [1,2]. The idea is to apply an electroosmotic slip velocity of the form $\langle \boldsymbol{v}_{2,\mathrm{slip}}^\mathrm{eo} \rangle = -\langle \boldsymbol{v}_{2,\mathrm{slip}}^\mathrm{ac} \rangle$ to suppress boundary-driven

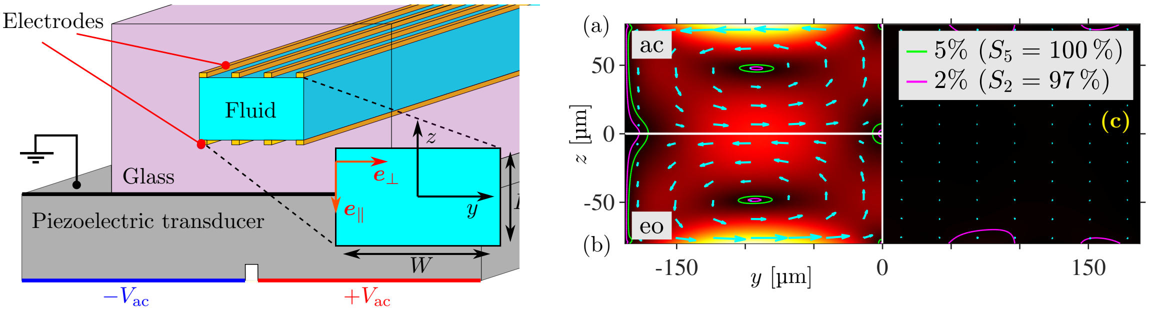

Figure 1: (Left) The principal design idea: a fluid channel embedded in an elastic solid, actuated acoustically by a piezoelectric transducer and electroosmotically by electrodes at the fluid boundary. (Right) Color plot of the streaming amplitude, from zero (black) to maximum (white), and 2% and 5% velocity contours. (a) Acoustic streaming from a standing half-wave in an ideal hard-wall channel. (b) AC electroosmotic streaming from the surface potential V_surf, Eq. (2). (c) The resulting suppressed electroacoustic streaming, from Ref. [1].

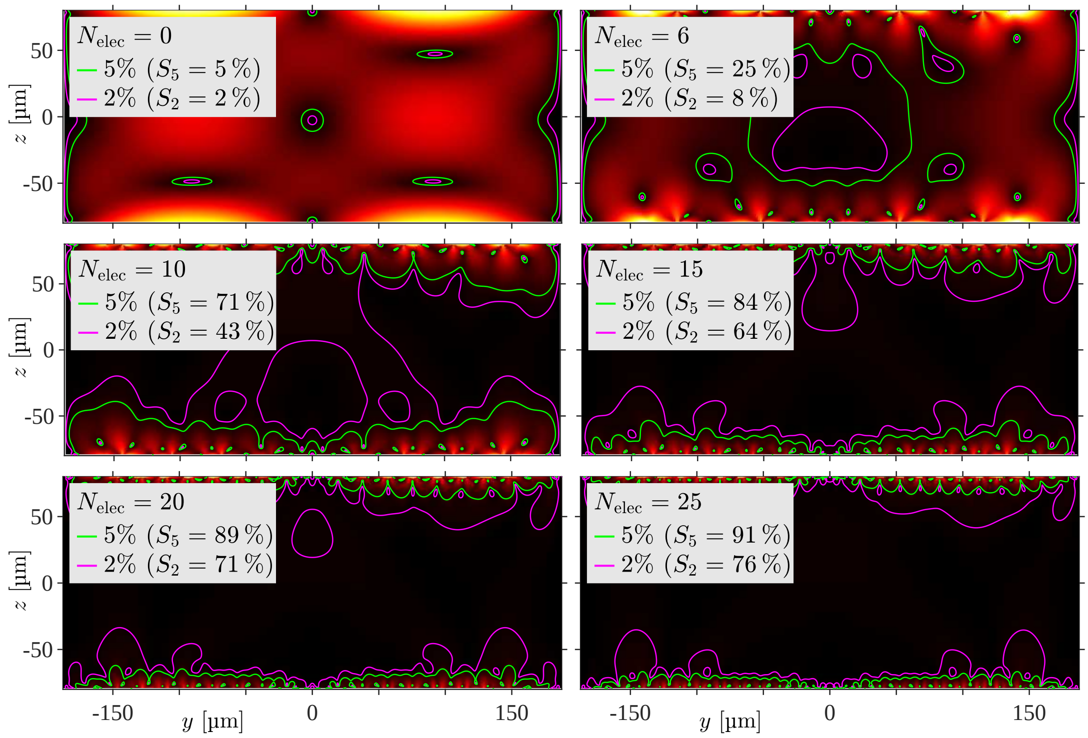

Figure 2: The electroacoustic streaming for an increasing number N_{elec} of discrete electrodes for electroosmotic actuation in the numerical 2D simulations. The model also includes a piezoelectric transducer for acoustic actuation, an elastic surrounding solid, and a dilute aqueous suspension of ions. Adapted from Ref. [1].

streaming. We demonstrate that for a binary ionic suspension, the typical Rayleigh boundary-driven streaming generated by a standing acoustic half-wave in an acoustically hard channel, can be efficiently suppressed by actuating AC electroosmosis with a surface potential at $z = \pm\frac{1}{2}H$ of the form,

$$V_{\mathrm{surf}}(y, \pm\tfrac{1}{2}H) = V_0\big[\sin(k_n y) + \mathrm{e}^{\mathrm{i}\vartheta}\sin(k_{n+1}y)\big], \quad k_n = \frac{2n+1}{W}\,\pi, \quad \text{for} \quad n = 0, 1, 2 \dots. \tag{2}$$

Here, ϑ describes a phase difference between the two sinusoidal modes, which can be optimized analytically, and $z = \pm\frac{1}{2}H$ denotes the top and bottom walls of the rectangular channel shown in Fig. 1. The side walls are left unactuated electrically. Choosing the amplitude $V_0 \sim 125\,\mathrm{mV}$, leads to suppression of typical acoustic streaming velocities $\sim 100\,\mathrm{µm/s}$. The suppressed streaming in this ideal case is illustrated in Fig. 1, where the parameter S_n describes the fraction of the cross-sectional area that has a streaming amplitude below $n\,\%$ of the Rayleigh-streaming amplitude.

2D system simulations including transducer, elastic walls, and discrete electrodes

As a more realistic 2D model, see Fig. 1, we now include a piezoelectric transducer for acoustic actuation, an elastic solid (glass), a dilute aqueous suspension of ions, and discrete electrodes for electroosmotic actuation. The acoustomechanical parts of the simulations are described in Ref. [3]. A discretized version of the surface potential in Eq. (2) is subsequently applied to the discrete set of electrodes to actuate the fluid electroosmotically. The resulting suppressed streaming is illustrated in Fig. 2 for an increasing number N_{elec} of electrodes at the top and bottom surfaces. It is seen that a moderate number $N_{\mathrm{elec}} \sim$ 15-25 leads to suppression of the streaming below $2\,\%$ of the Rayleigh-streaming amplitude in large parts of the channel. For typical channel dimensions, this is achievable with electrode widths of $W_{\mathrm{elec}} \gtrsim 10\,\mathrm{µm}$, which is feasible with standard clean-room techniques.

Conclusion

We suggest a novel design idea for acoustofluidic chips with integrated AC electroosmosis for suppressing acoustic streaming. The principal idea is backed up by an ensuing theoretical and numerical analysis. It is found that the acoustic streaming in the bulk of a rectangular acoustofluidic channel can be suppressed by two orders of magnitude with a suitable implementation of electroosmosis.

References

[1] B.G. Winckelmann and H. Bruus. J. Acoust. Soc. Am. **149**, 3917 (2021). [pdf]
[2] J.S. Bach and H. Bruus. J. Acoust. Soc. Am. **144**, 766 (2018). [pdf]
[3] N.R. Skov, J.S. Bach, B.G. Winckelmann, and H. Bruus. AIMS Math **4**, 99-111 (2019). [pdf]

Acoustofluidics 2021
26-27 August 2021
Virtual Conference

Effects of a Laser-induced Thermal Gradient on the Acoustic Streaming Field

Franziska Martens[1], Wei Qiu[1], Andreas Ehn[2] and Per Augustsson[1]

[1]Department of Biomedical Engineering, Lund University, Lund, Sweden
Email: franziska.martens@bme.lth.se, bme.lth.se/research-pages/nanobiotechnology-and-lab-on-a-chip
[2]Department of Combustion Physics, Lund University, Lund, Sweden

Introduction

Inhomogeneities in density and compressibility in fluids in acoustofluidic devices lead to an acoustic body force acting on the fluids [1]. We recently showed that such inhomogeneities can be introduced not only through molecular concentration gradients [1-3] but also by inducing a thermal gradient in the fluid [4]. Establishing a spatially confined heat source, falling below the measures of acoustofluidic channels, opens the possibility to generate thermal fields, precise enough for highly localised flow patterns to develop with potential applications for single particle manipulation. To achieve this, we guided a focused laser beam into an absorbing liquid in an acoustically actuated microchannel and studied the resulting streaming field. We observed a more confined streaming pattern compared to our recent study [4] and we also provide novel data for the transient decay of the streaming velocity after shutting off the laser light source.

Materials and Methods

As shown in Fig.1, the 785 nm wavelength laser light was focused to a spot size of 60 µm, heating the liquid inside the silicon glass channel (375 µm wide, 150 µm high). The laser pulse duration and average power were 303 ms, (3.3 Hz) and 20 mW respectively. The optical absorption of Indo-Cyanin green (ICG) dye matches the laser wavelength and was therefore added to a dilute suspension of 1 µm sized, green fluorescent (ex. 468 nm, emi. 508 nm) tracer particles. The pressure field within the channel was established by a piezo-electric transducer run at 1.98 MHz during stopped flow. The streaming field was recorded at a frame rate of 33 fps and 17 ms exposure time. The images were analysed via 2D particle image velocimetry (PIV) using a MatLab-based open source algorithm, PIVlab [5] and were averaged over 85 measurements.

Results

The dye in the liquid absorbs the laser light at its spectral peak, following the Beer-Lambert law with the most energy being absorbed at the top of the channel where the laser light enters the cavity. Apart

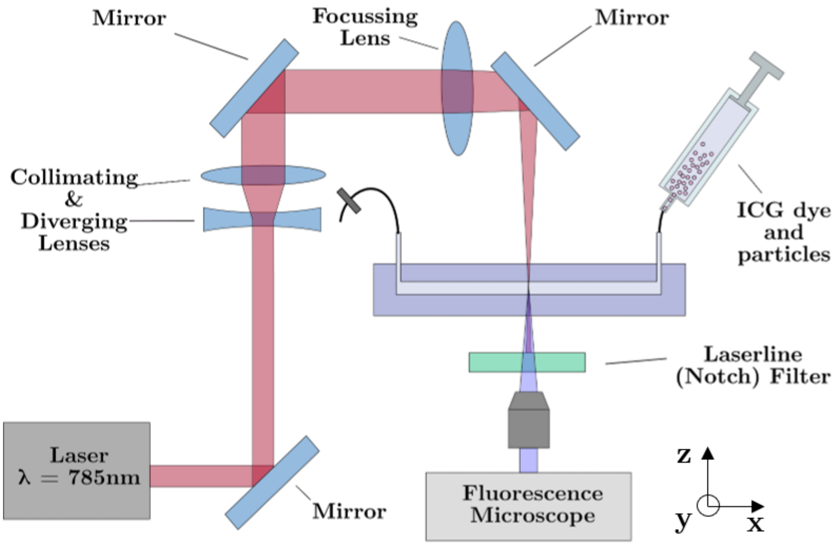

Figure 1: The setup comprises a lens system to enlarge, collimate and focus the beam to achieve the 60 µm spot size. Guided by mirrors, the laser light is shone onto the chip from the top, where it is absorbed by the ICG dye and therefore heats the liquid, causing convection rolls. Fluorescent tracer particles indicate the movement of the liquid which is imaged with a fluorescence microscope. The camera is triggered to record as soon as one laser pulse ends.

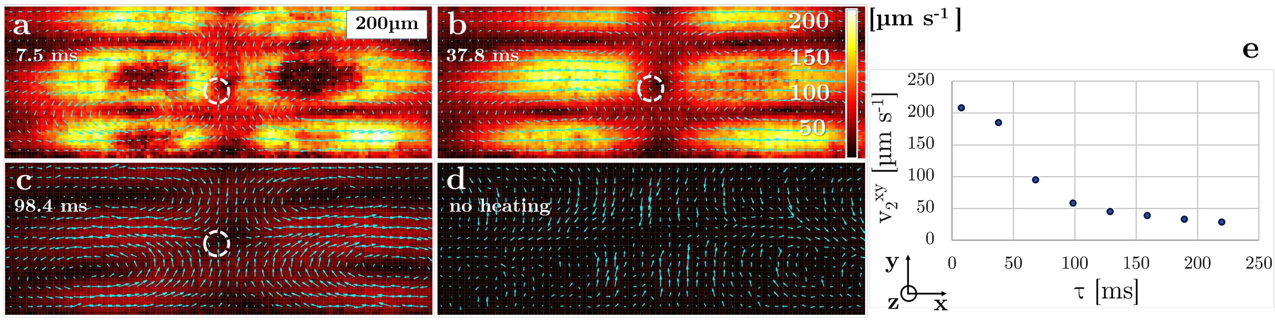

Figure 2: Top-view of the streaming fields for constant acoustic actuation after a single laser shot at times: **(a)** τ = 7.5 ms **(b)**, τ = 37.8 ms and **(c)** τ = 98.4 ms. Laser spot size is indicated by rings. **(d)** Acoustic streaming without heating but ultrasound actuation only, $v = 13.04\,\mu\mathrm{m\,s}^{-1}$. **(e)** Decrease in streaming velocity after a laser pulse ended.

from the acoustic Rayleigh streaming, the two main mechanisms of the fluid motion are due to the laser-induced thermal gradient. The Rayleigh-Bénard convection, caused by gravity and the temperature dependent density and compressibility of the fluid, acts, as well as an acoustic body force, caused by the acoustic field and the temperature dependent density and compressibility of the fluid. Laser heating, compared to LED heating, as conducted in previous experiments [4], allows a denser energy distribution ($7.1\,\frac{\mathrm{W}}{\mathrm{mm}^2}$) with increased local precision. Consequently, the expected temperature gradient is spatially more defined than a heat gradient created with a non-coherent light source. Within the microchannel, this affects predominantly the gradient in the length dimension (x-axis). Since the gradient along y is dominated by the high thermal conductivity of the side walls relative to the water, the thermal gradient across the channel will assume a similar profile in both LED- and laser heating experiments. The roll size in the channel length direction (x) can, however, stretch arbitrarily far based on the spot size.

Due to the optical configuration, with the laser directed towards the camera, it was not possible to measure the flow field while the laser was active. Instead, we recorded a sequence of images from the moment of turning the laser off. Fig.2(a-c) shows the transition of the flow field from four distinct streaming rolls, present around the centre of the laser spot, in comparison to Fig.2(d) that shows the Rayleigh streaming at the mid height x-y-plane for ultrasound only. As the temperature gradient flattens out at long times (110 ms), the rolls' centres move out along the x-direction and become elongated. Compared to previous results with a broader, collateral optical heating [4], the streaming pattern in the x-direction is more compact due to the steeper slope of the gradient by precision laser heating. In the y-direction however, the difference in the gradients' slope is not sufficient to influence the streaming pattern and is therefore not observable in the conducted measurement.
By analysing the decay of the maximum streaming velocity over time, Fig.2(e), we can conclude that the accelerated velocity is only observable for 90 - 110 ms after disabling the laser heating while the initial velocity is more than six times faster than the steady state, no-light, Rayleigh streaming velocity. Due to the microscale dimensions of the chip, the heat dissipates rapidly via thermal conduction through the side walls and the colder liquid around the laser spot.

Conclusion

The presented results demonstrate the accelerating effect of precisely located, energy dense heating on the acoustic streaming velocity and indicate changes in the streaming pattern during the heating process. The streaming velocity was observed to decrease exponentially, and the laser light source enabled a more confined streaming pattern compared to a light source of larger spot size. The exact temperature gradient, as well as the recording of the streaming pattern during the heating process are topics of our ongoing investigations. We believe that the ability to tailor a combined acoustic- and thermal field both spatially and temporally can become a new tool for precise control of single particles and to drive localised flow fields at the microscale.

References

[1] J. T. Karlsen, P. Augustsson, H. Bruus *Phys. Rev. Lett.* **117**, 114504 (2016)
[2] J. T. Karlsen, W. Qiu, P. Augustsson, and H. Bruus, *Phys. Rev. Lett.* **120**, 054501 (2018).
[3] W. Qiu, J. T. Karlsen, H. Bruus and P. Augustsson *Phys. Rev. Applied* **11**, 024018 (2019)
[4] W. Qiu, J. H. Jørgensen, E. Corato, H. Bruus, P. Augustsson *Phys. Rev. Lett.* **in press**, 2103.10192 (2021)
[5] W. Thielicke and E. Stamhuis, J. Open Res. Softw. 2, 1 (2014)

Acoustofluidics
2021
26-27 August 2021
Virtual Conference

Qualitative changes in the streaming pattern at high acoustic energy due to friction-induced heating in the viscous boundary layers

Jonas Helboe Joergensen[1], Wei Qiu[2], and Henrik Bruus[1]

[1] Department of Physics, Technical University of Denmark, Kongens Lyngby, Denmark
[2] Department of Biomedical Engineering, Lund University, Lund, Sweden
E-mail: jonashj@fysik.dtu.dk, URL: http://www.fysik.dtu.dk/microfluidics

Introduction

We present a theoretical, numerical, and experimental study of non-linear effects in microscale acoustofluidic devices at high acoustic energies. Normally, models describing microscale acoustofluidics are based on perturbation theory, but in this study we show that the pattern of the acoustic streaming in a microfluidic channel undergoes qualitative changes at high acoustic energy densities. We present modeling, a physical explanation, and experimental validation for this non-linear energy dependency spanning two orders of magnitude. This phenomenon is of fundamental interest, and it is important when designing high-throughput acoustofluidic devices relying on high acoustic energy densities.

Experimental and simulation setup

The experiments were performed using a long straight microchannel of width $W = 375$ µm and height $H = 133$ µm in a glass-silicon chip, see Fig. 1. The chip is actuated from below with a piezoelectric transducer at 1.97 MHz generating a half-wave-resonance in the fluid chamber. For each given acoustic energy density E_ac, the acoustic streaming was measured at 10 to 60 fps by tracking the motion of 0.5-µm-diameter particles using a defocusing-based 3D particle-tracking technique [1].

To simulate the systems an iterative solver has been used together with a thermoviscous model with effective boundary conditions, it is a extension of the model presented in our recent paper [2]. We avoid 3D modeling and just simulate the 2D cross-section, because in this long channel, the pressure and streaming fields only vary slightly in the length direction of the chip. The iterative solver enables us to go beyond the perturbation regime and simulate non-linear effects.

Results and discussion

The experimental and simulation results as a function of the acoustic energy density E_ac is shown in Fig. 2. At low E_ac, Fig. 2(a), the streaming is the classical boundary-driven streaming with four streaming rolls. However, friction in the boundary layers generates heat, thus providing a heat source at the bottom and at the top of the channel. At the bottom of the channel, the silicon effectively transports the heat away, whereas the glass lid at the top of the channel is a bad heat conductor, and therefore the temperature increases there, Fig. 2(f). Thus, a temperature gradient is established, which creates a gradient in the compressibility and density that in turn is known to spawn an inhomogeneous acoustic body force $\boldsymbol{f}_\mathrm{ac}$ in the fluid [2,3],

$$\boldsymbol{f}_\mathrm{ac} = -\frac{1}{4}\,|\boldsymbol{v}_1|^2\,\boldsymbol{\nabla}\rho_0(T_0) - \frac{1}{4}\,|p_1|^2\,\boldsymbol{\nabla}\kappa_{s0}(T_0) = -\frac{1}{4}\big(\,|\boldsymbol{v}_1|^2\,\partial_T\rho_0 + |p_1|^2\,\partial_T\kappa_{s0}\big)\boldsymbol{\nabla}T_0. \tag{1}$$

Firstly, because both density and compressibility decrease with temperature, and because $\big|\partial_T\rho_0\big| \ll \big|\partial_T\kappa_{s0}\big|$, it follows that $\boldsymbol{f}_\mathrm{ac}$ points towards the high temperature region and is strongest at the pressure antinodes at the sides of channel. As a result see Fig. 2(c)–(d), the acoustic force tends to create two big streaming rolls placed side by side that pulls fluid in towards (away from) the center at

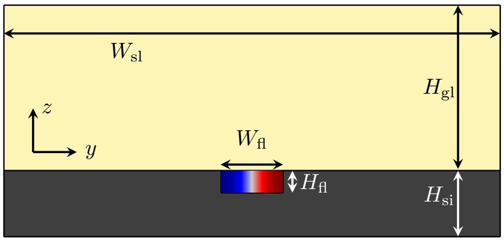

Figure 1: Sketch of the cross-section of the rectangular channel of width $W_\mathrm{fl} = 375$ µm and height $H_\mathrm{fl} = 133$ µm. The channel is etched into a silicon wafer of width $W_\mathrm{sl} = 3$ mm and height $H_\mathrm{si} = 400$ µm and is covered by a glass lid of height $H_\mathrm{gl} = 1$ mm. The system is actuated at the bottom surface of the silicon base with a frequency of $f_0 = 1.911$ MHz resulting in the excitation of a half-wave-resonance in the fluid chamber.

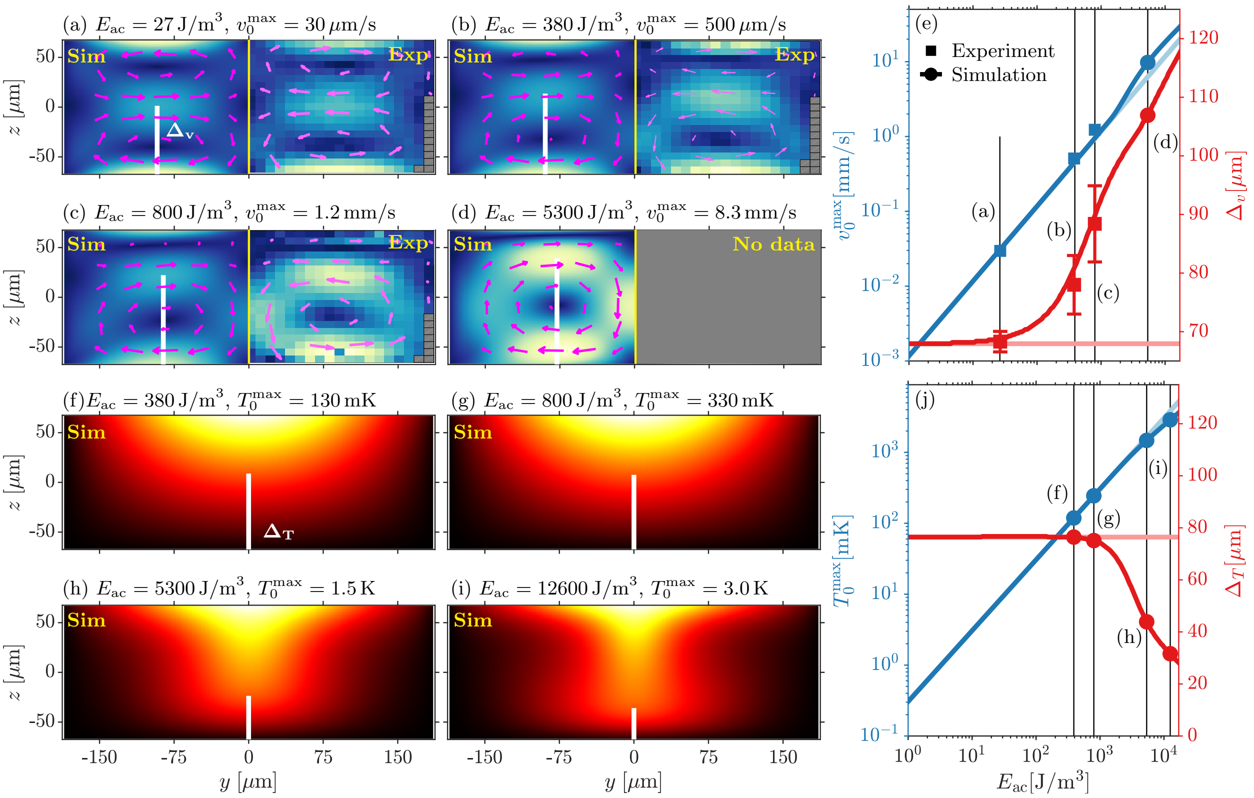

Figure 2: Simulation and experimental results for the stationary fields in a rectangular acoustofluidics channel. (a)-(d) Color and vector plots of the streaming field at four different acoustic energy densities E_{ac}. For each E_{ac}, simulations (sim) are shown to the left and experimental results (exp) to the right, and Δ_v (the distance from the channel bottom to the maximum horizontal velocity pointing towards the center of the channel) is shown by the white bar. (e) The cross-over from boundary- to bulk-driven streaming seen in the quantities v_0^{max} and Δ_v, with both simulations and experimental data. The error bars on the streaming velocity and acoustic energy density in the experiments are within the square marker. The round markers note where the fields shown in (d) and (f)-(i) are positioned. (f)-(i) Color plots at four values of E_{ac} of the simulated temperature, and Δ_T (the height where the temperature is half of T_0^{max}) is shown by the white bar. (j) The cross-over from a heat-diffusion-dominated to a convection-dominated temperature field seen in the quantities T_0^{max} and Δ_T.

the top (at the bottom) of channel. Secondly, the acoustic body force and thus the bulk-driven streaming has a quadratic energy dependence, $\propto E_{ac}^2$, whereas the boundary-driven streaming only has a linear dependence, $\propto E_{ac}$, so at high acoustic energy densities, the bulk-driven streaming will become dominant. In Fig. 2(a)-(d) is shown how the streaming changes from four to two streaming rolls as the energy density increases, with a cross-over for $E_{ac} \approx 800$ J/m^3. This cross-over is shown qualitatively in Fig. 2(e) by the maximum streaming velocity v_0^{max} and the geometrical quantity Δ_v defined as the height above the bottom edge with the maximum velocity towards pressure node.

When the streaming becomes fast, convection becomes important and alters the temperature field. Fig. 2(f)-(j) show the non-linear effects on the temperature field. At low and medium acoustic energy density E_{ac}, the heating occurs at the glass lid because glass is a bad heat conductor compared to silicon. As E_{ac} increases, the streaming velocity increases, and the convective heat-transport becomes important, clearly seen in Fig. 2(h)-(i), where the temperature field is notably altered at high E_{ac}. In Fig. 2(j), this cross-over is shown in the maximum temperature T_0^{max} and the geometrical quantity Δ_T describing the pattern of the temperature field.

Conclusion

We have theoretically understood and modeled non-linear effects and observed them experimentally. The non-linear effects in this particular system are important at acoustic energies in the order of 1000 J/m^3, which is high but achievable. In conclusion non-linear effects in the acoustic streaming can be important when designing devices needing a high acoustic energy such as high-throughput devices, which our iterative solver is capable of computing in 2D and 3D.

References

[1] R. Barnkob, C. J. Kähler, and M. Rossi. Lab Chip **15**, 3556 (2015).
[2] J.H. Joergensen, and H. Bruus. J. Acoust. Soc. Am. **149**, 3599-3610 (2021).
[3] J. T. Karlsen, P. Augustsson, and H. Bruus. Phys. Rev. Lett. **117**, 114504 1-6 (2016).

Acoustofluidics
2021
26-27 August, 2021
Virtual Conference

Measuring the temporal difference in build up between the acoustic radiation force and acoustic streaming with an optical tweezer

Christoph Goering[1] and Jürg Dual[1]

[1]Institute for Mechanical Systems, ETH Zürich, Switzerland
E-mail: goering@imes.mavt.ethz.ch, URL: https://expdyn.ethz.ch

Introduction

We report a new method for measuring the build up time of the acoustic streaming (AS) and the acoustic radiation force (ARF) in an acoustic standing pressure field. The drag force from AS and the ARF are the two main effects for the controlled manipulation of objects within an acoustofluidic device. For large objects the ARF dominates over AS because the ARF scales with the radius of the spherical object cubed (ARF $\propto R^3$) whereas the drag force from AS scales linearly to the radius (AS $\propto R$). For small objects the latter dominates the ARF. The drag force form AS is in most cases undesired because it can counteract the ARF.

Castro and Hoyos [3,4] reduced the steady-state streaming velocity in the xy-plane (see Figure 1) by applying a pulsed excitation of the piezo electric transducer (PZT). Muller and Bruus [5] investigated numerically the effects of a pulsed excitation on the build up of AS and the ARF in a two dimensional fluid cavity without surrounding structure (yz-plane in Figure 1). They found that a pulsed excitation does not result in a decrease of streaming velocity but rather in a delay of its build up.

Here, we use the high temporal resolution ($\Delta t = 0.8\,\mu\text{s}$) of an optical tweezer (OT) to measure the build up of the ARF and Rayleigh streaming versus time. Our OT has previously been used in the context of direct force measurements in bulk acoustofluidic devices [1,2]. During the measurements we switch the laser of the OT off in order to measure the movement of the particle due to AS and the ARF only, i.e. without additional optical trapping forces. After the measurement the laser is switched on for precise spatial (re-)positioning within the acoustic field.

Methodology

We measure on a single spherical silicon-dioxide particle of radius 1.03 µm in the same plane where Muller and Bruus performed their simulations. The excitation frequency $f_{\text{ex}} = 4.015\,\text{MHz}$ creates a standing wave pressure mode with 16 nodal lines. Before measuring the time evolution, we measure the steady-state forces within the device to select the measurement points where the drag force from AS and the ARF are perpendicular to each other and maximized, respectively.

The build up times for AS and the ARF can be estimated as

$$\tau_{\text{AS}} = \frac{1}{2\nu} L^2 \quad \text{and} \quad \tau_{\text{ARF}} = \frac{Q}{2\pi f_{\text{ex}}}$$

where ν is the kinematic viscosity of the fluid, L half the height of a streaming roll, and Q the quality factor of the device [5]. For our device with $Q \approx 36$, water at room temperature ($\nu = 0.890\,\text{mm}^2\,\text{s}^{-1}$), and AS rolls over the whole channel height ($L = 50\,\mu\text{m}$), τ_{AS} and τ_{ARF} are approximately 1.4 ms and

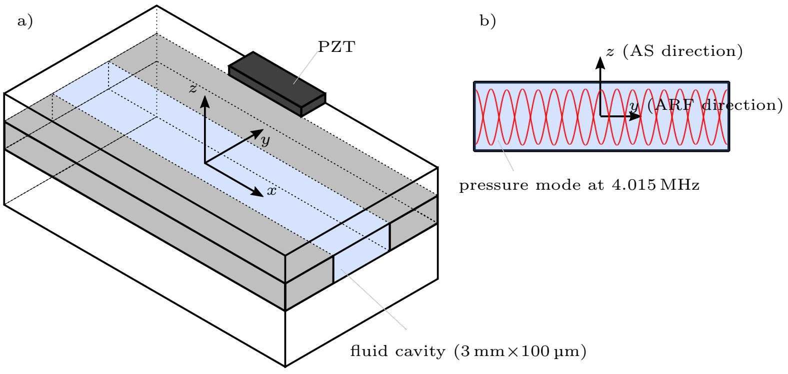

Figure 1: a) Schematic of acoustofluidic glass-silicon-glass device. b) Plane of measurements with schematic 16 nodal line pressure mode at the excitation frequency of 4.015 MHz.

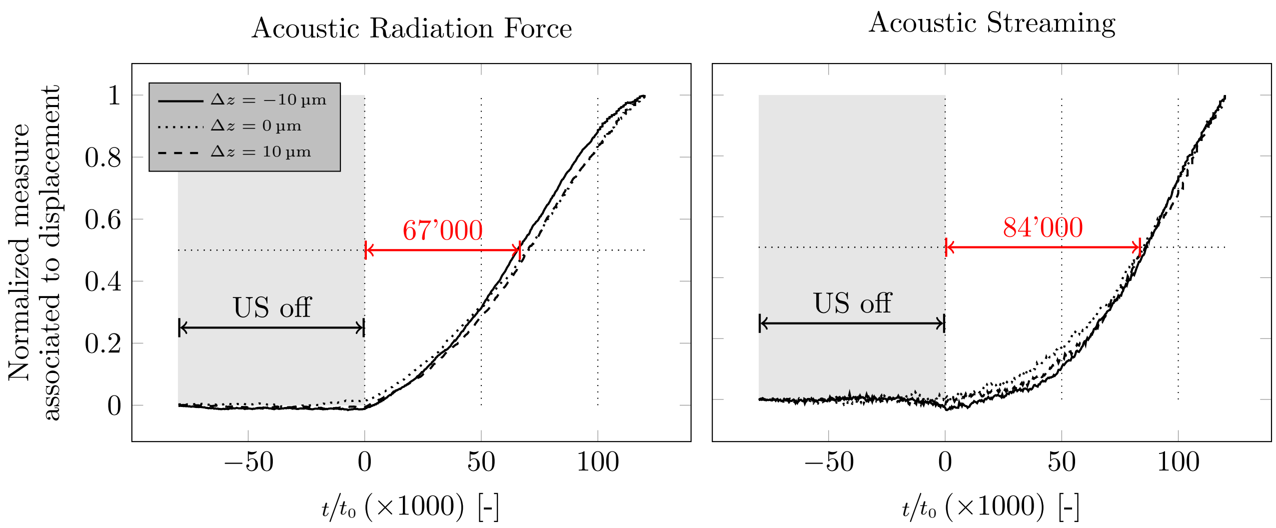
Acoustic Radiation Force

Acoustic Streaming

Figure 2: Normalized measure linearly related to particle displacement for three different points where the ARF dominates in y-direction (left plot) and the AS in z-direction (right plot). The x and y coordinates are for all three measurement points the same, just the z-coordinate is different. The left plot is the evolution of the ARF and the right plot of AS measured at the same time on the same particle. For all three points per plot the respective lines show the same behavior over time. The particle reaches 50% of its final ARF induced displacement at the end of the measurement after 67’000 excitation periods whereas for AS it takes about 17’000 periods longer to reach 50%.

1.4 µs, respectively, i.e. they differ by three orders of magnitude. Hence, a high temporal resolution is advantageous to capture the build up of both effects. For both forces the inertia of the particle can be neglected.

For the time evolution experiments, we measure with our setup ($\Delta t = 0.8\,\mu\mathrm{s} \approx 0.5\,\tau_{\mathrm{ARF}}$) at least every fourth excitation period $t_0 = {}^{1}/_{f_{\mathrm{ex}}} \approx 0.25\,\mu\mathrm{s}$. In the end, we monitor the movement of the particle using the quadrant photo detectors of the OT for 200’000 periods where the first 70’000 periods are before the ultrasound (US) is switched on. The measurement needs to be stopped after 200’000 periods in order to reliably recapture the particle with the OT. The evolution of AS and the ARF are recorded simultaneously.

Results and Discussion

Figure 2 shows the evolution of AS and ARF for three different measurement points. In total, we measured at 4 different x, y-positions with 3 different heights, each. For each position we average 75 measurements at the same point to reduce noise. For all measurement points we found similar results. We normalize each line to their respective traveled distances at the end of the measurement to simplify the comparison. In addition, we use the 50% mark as criteria for computing their build up time difference.

One can see, that as soon as the US is switched on (${}^{t}/_{t_0} = 0$), the ARF induced motion starts. However, the AS induced motion is around 17’000 periods ($\approx 4.4\,\mathrm{ms}$) slower in reaching the linear behavior, compared to the ARF induced motion.

Conclusion

We measured for the first time on a single spherical particle the evolution of the ARF and AS induced displacement with a very high time resolution, respectively.

Our results show that the temporal build up difference between AS and ARF of 4.4 ms is significantly larger than indicated by the results from the numerical study by Muller and Bruus [5] and also larger than the approximation of $\tau_{\mathrm{AS}} \approx 1.4\,\mathrm{ms}$. This difference might explain why a pulsed excitation can indeed decrease/prevent the build up of streaming as shown by Castro and Hoyos [3,4]. First results with a pulsed excitation show a strong reduction of AS depending on the pulse parameters while the ARF is still acting on the particle.

References

[1] S. Lakämper, A. Lamprecht, I.A.T. Schaap, and J. Dual. Lab on a Chip **15**, 290-300 (2015).
[2] A. Lamprecht, S. Lakämper, T. Baasch, I.A.T. Schaap, and J. Dual. Lab on a Chip **16**, 2682-2693 (2016).
[3] A. Castro and M. Hoyos. Ultrasonics **66**, 166-171 (2016).
[4] M. Hoyos and A. Castro. Ultrasonics **53(1)**, 70-76 (2013).
[5] P. Muller and H. Bruus. Physical Review E **92**, 063018 (2015).

Acoustofluidics 2021
26-27 August 2021
Virtual Conference

Effects of shape and Willis coupling on acoustic radiation force and torque

Shahrokh Sepehrirahnama[1], Sebastian Oberst[1,2], Yan Kei Chiang[1,2], and David A. Powell[1,2]

[1]Centre for Audio, Acoustics and Vibration, University of Technology Sydney, Sydney, Australia
E-mail: shahrokh.sepehrirahnama@uts.edu.au, URL: https://profiles.uts.edu.au/shahrokh.sepehrirahnama
[2]School of Engineering and Information Technology, University of New South Wales, Canberra, Australia

Introduction

In acoustophoresis, sub-wavelength objects are often regarded as particles to indicate their small size and the regime of dynamic balance in an incident pressure field [1]. This particle view of the objects was studied theoretically by simplifying the geometry to that of spheres (highest-order of symmetry), spheroids, cylinders, disks and other axisymmetric shapes, or the Cassini oval shape for the study of red blood cells. These geometries limit our understanding of the effects of anti-symmetric features of real-life objects on their experienced acoustic radiation force and radiation torque. In this work, we present a quantification of anti-symmetric shape effects by using the concept of acoustic Willis coupling and formulating the acoustic radiation force and torque for 3D object of arbitrary shape.

Theoretical formulation

The monopole-dipole scattering moments M and $\mathbf{D}$ of objects with arbitrary shape can be expressed as

$$p_s \approx -\omega^2 \Omega M G + \omega^2 \boldsymbol{\nabla} \cdot \Big[\Omega \mathbf{D} G\Big], \qquad G = G(kr) = \frac{e^{jkr}}{4\pi r}, \qquad \begin{bmatrix} M \\ \mathbf{D} \end{bmatrix} = \frac{1}{\Omega} \begin{pmatrix} \alpha_{pp} & \boldsymbol{\alpha}_{pv}^T \\ \boldsymbol{\alpha}_{vp} & \boldsymbol{\alpha}_{vv} \end{pmatrix} \begin{bmatrix} p_i \\ \mathbf{v}_i \end{bmatrix}, \tag{1}$$

where p_s denotes the scattering pressure field, p_i and $\mathbf{v}_i$ denote the incident pressure and velocity fields, respectively, $\boldsymbol{\alpha}$ is the polarizability tensor, Ω denote the object's volume, r is the radial distance from the centroid of the object, and ω and k denote the circular frequency and wavenumber, respectively. $\boldsymbol{\alpha}_{pv}$ and $\boldsymbol{\alpha}_{vp}$ denote the Willis coupling coefficients, which are related according to the reciprocity principle [2]. By using Gor´kov's approach [3], we derived the acoustic radiation force $\mathbf{F}$ and torque $\mathbf{T}$ for an arbitrarily shaped object, as expressed in Eq. (2).

Numerical study

The polarizability tensor for the non-spherical shapes in Fig. 1 is obtained from numerical solution of their scattering response, as outlined in [4]. The real and imaginary parts of the non-zero and

$$\begin{aligned}
\mathbf{F} =& \mathbf{F}_{sym} + \mathbf{F}_{asym} \\
& \mathbf{F}_{sym} = -\Big\langle \frac{\alpha_{pp}}{2\rho_f} \boldsymbol{\nabla}\big[p_i^2\big] \Big\rangle + \Big\langle j\omega \boldsymbol{\alpha}_{vv} \mathbf{v}_i \cdot \boldsymbol{\nabla} \mathbf{v}_i \Big\rangle \\
& \mathbf{F}_{asym} = \Big\langle \frac{1}{\rho_f} \boldsymbol{\alpha}_{pv} \cdot \big[p_i \boldsymbol{\nabla} \mathbf{v}_i - \mathbf{v}_i \boldsymbol{\nabla} p_i\big] \Big\rangle, \\
\mathbf{T} =& \mathbf{T}_{sym} + \mathbf{T}_{asym} \\
& \mathbf{T}_{sym} = \Big\langle j\omega p_i \boldsymbol{\alpha}_{vp} \times \mathbf{v}_i \Big\rangle \\
& \mathbf{T}_{asym} = \Big\langle j\omega \big[\boldsymbol{\alpha}_{vv} \mathbf{v}_i\big] \times \mathbf{v}_i \Big\rangle,
\end{aligned} \tag{2}$$

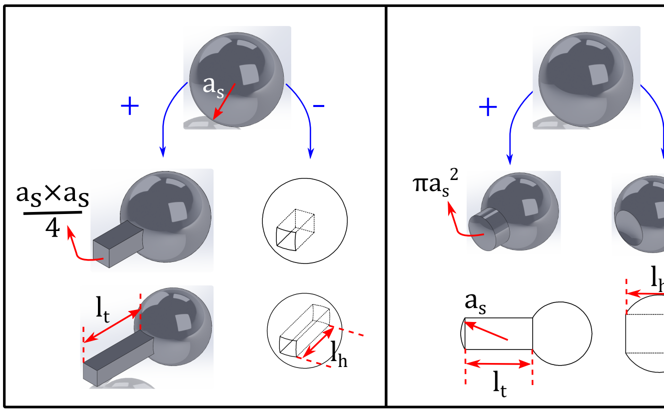

Figure 1: The geometries with engineered anti-symmetry were designed from a reference sphere by adding a protrusion (tail) or intrusion (hole) with square cross section.

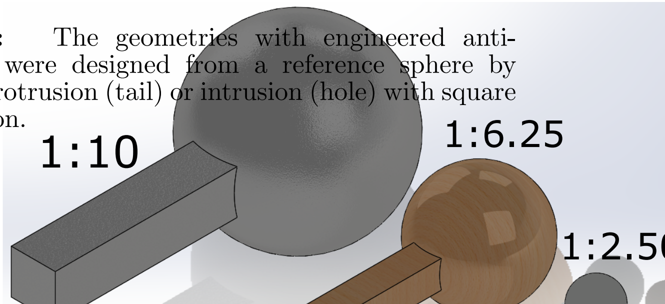

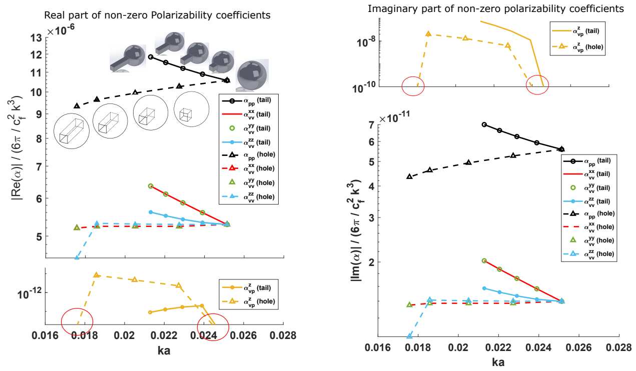

Figure 2: Real and imaginary parts of the non-zero polarizability coefficients, normalized by the theoretical upper bound [2,5], for a series of non-spherical objects with tails and holes. The length of the tails and depth of holes are ranging from 0 to $2a_s$ with a_s denoting the radius of the spherical component of the shape. When the hole depth is 0 or $2a_s$, the shape retains its symmetry along the length direction resulting in zero Willis coupling, as indicated by the red circles in the panels.

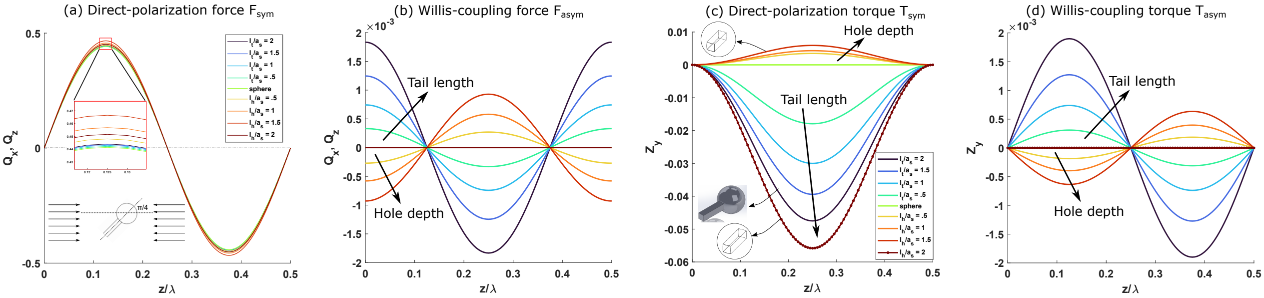

Figure 3: Study of the partial components, (a) F_{sym} and (b) F_{asym}, of the radiation force and, (c) T_{sym} and (d) T_{asym}, radiation torque for non-spherical shape with a tail or hole of square cross section at locations along the half wavelength span in a plane standing wave. The object's orientation is $\pi/4$ with respect to the incidence direction.

normalized polarizability coefficients are shown in Fig. 2. It was found that the shape modification in the length direction generates non-zero Willis coupling coefficients; however their magnitudes are less than the theoretical upper bound [2]. Nonetheless, the presence of Willis coupling effects lead to the partial force and torque, denoted by $\mathbf{F}_{asym}$ and $\mathbf{T}_{asym}$ respectively, and depicted in Fig. 3. Considering the normalization $\mathbf{Q} = \mathbf{F}/E_{in}k\Omega$, $\mathbf{T} = \mathbf{F}/E_{in}\Omega$, and the characteristic length $a = \Omega/\Gamma$ with Γ denoting the surface area, we found that the effects of shape on the radiation torque is much larger than for the force, which exhibits a negligible variation for the given set of non-spherical shapes compared against a reference sphere. The Willis-coupling partial force is at least two orders of magnitude smaller than the partial force $\mathbf{F}_{sym}$ due to direct polarizabity coefficients. However, the partial torques T_{sym} and T_{asym} are approximately of the same order of magnitude, implying significant effects of Willis coupling on the acoustic radiation torque. Hence, shape effects should be accounted for to describe the dynamic balance of an object in acoustic radiation force and radiation torque fields.

Conclusion

We developed a formulation of acoustic radiation force and radiation torque for arbitrarily shaped objects by incorporating the effects of anti-symmetric geometry features through Willis coupling. By introducing the characteristic dimension as ratio of volume over surface area, we showed that acoustic radiation torque is more sensitive to the shape effects for the given geometries; while such effects are negligible on the radiation force. If the induced Willis coupling increases, both the radiation force and torque will be dominated by the anti-symmetric features of the shape. Subsequently, the coordinates of the zero-force and zero-torque locations will be determined by the sum of their partial forces. This implies that objects could be trapped at distances away from the pressure/velocity nodes in a plane standing wave field, depending on the anti-symmetric features of their shapes.

References

[1] H. Bruus, Lab on a Chip 11, 3742 (2011).
[2] A. Melnikov, Y. K. Chiang, L. Quan, S. Oberst, A. Alù, S. Marburg and D. Powell, Nature Comm. **10**, 1–7 (2019).
[3] S. Sepehrirahnama, and K.-M. Lim, Physical Review E **102**, 043307 (2020).
[4] S. Sepehrirahnama, S. Oberst, Y. K. Chiang, and D. Powell, Arxiv , 1–8 (2021).
[5] J. Jordaan, S. Punzet, A. Melnikov, A. Sanches, S. Oberst, S. Marburg, D. Powell, Applied Physics Letters, 113, 224102 (2018)

Acoustofluidics 2021
26-27 August 2021
Virtual Conference

Effect of axial primary radiation force on the dynamical motion of a pair of microparticles along the pressure nodal plane

Sazid Z. Hoque[1], Amal Nath[1], and Ashis K. Sen[1]

[1]Department of Mechanical Engineering, IIT Madras, Chennai, India
E-mail: ashis@iitm.ac.in, URL: http://www.ashislab.in

Introduction

Manipulation of micro-objects by utilizing the ultrasonic acoustic waves on lab on a chip device is known as microscale acoustofluidics. The average nonlinear effects due to the interaction of incident and scattered wavefield from a particle leads to the primary radiation force [1]. When multiple particles are present inside a microchannel, there is a force due to the re-scattering of sound waves, known as secondary or interparticle radiation force [2].
Apart from the above forces, another force exists due to the spatial variation of the acoustic pressure field along a channel, defined as axial primary radiation force. The non-uniformity of pressure amplitude may be due to diffraction effects, the variation of the thickness of the coupling layer, or the transducer's non-uniform performance [3]. Here, we elucidate the insight into the dynamical behaviour of particles along the pressure nodal plane due to the competition between the axial primary radiation force and interparticle force for a pair of particles using numerical simulations and experiments.

Theoretical modelling

Fig. 1 shows schematic of the simulation domain of the particle's pair and various forces acting on them. Considering a 1D standing wave, we can write the incoming velocity potential as,

$$\phi_{in} = \frac{p_a(x)}{\rho_0 ck} cos(k_y y) cos(\omega t) \tag{1}$$

where $p_a(x)$ is the position-dependent pressure amplitude varying along the axial direction (i.e., x-direction), k_y is the wavenumber of the standing wave, ρ_0 is the density, c is the speed of sound, ω is the angular frequency of the wave, and t denotes time.

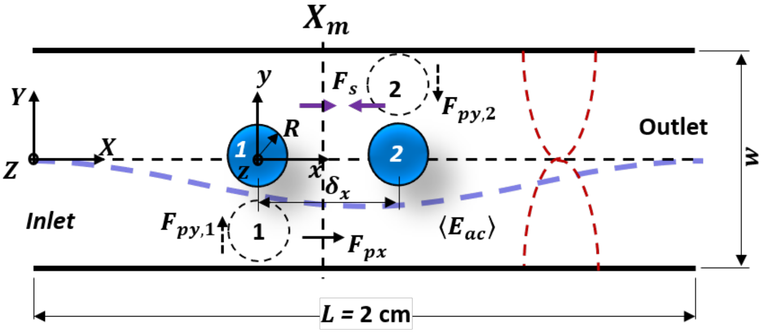

Figure 1: Schematic of the simulation domain of a pair of particle showing the different forces acting on the particles initially placed away from the pressure nodal plane. The sinusoidal variation of time-average energy density, $\langle E_{ac} \rangle$ along the channel length is indicated.

The acoustic force potential on a particle of radius R within the Rayleigh limit can be expressed in terms of incoming velocity potential and using eqn. (1) we can simplify the expression as,

$$U = 2\pi R^3 \rho_0 \left[\frac{p_a^2}{6\rho_0^2 c^2} f_1 cos^2(k_y y) - \frac{1}{4\rho_0 c^2 k_y^2} \left(\frac{\partial p_a}{\partial x} \right) f_2 cos^2(k_y y) - \frac{1}{4} \frac{p_a^2}{\rho_0^2 c^2} f_2 sin^2(k_y y) \right] \tag{2}$$

where f_1 and f_2 are the monopole and dipole scattering factors of a particle defined in terms of density and compressibility ratio of the particle. The average force acting on the particle positioned at (x, y) is given by the negative force potential, i.e., $\mathbf{F} = F_{px} e_x + F_{py} e_y = -\nabla U$. Here, F_{px} and F_{py} are the axial primary radiation force and transverse primary radiation force respectively. The interparticle force, F_s acting on the particle's pair is modelled using the theoretical expression developed by Silva and Bruus [2].

Results and discussion

Three distinct dynamical motion are observed depending on the initial position of the particle pair along the pressure nodal plane. The well-defined regimes are, Regime I. particles are attracted to each other, Regime II. particle 2 oscillates about its position, while particle 1 moves towards particle 2, and Regime III. Particle's pair moves along the same direction and also approaches each other. Fig. 2 depicts the time variation of the positions of the particles (i.e., x_c^* vs. t^*) and the interdistance between them (i.e., δ_x^* vs.t^*) positioned at $X_m^* = 0.004, 0.006$ and 0.02 along the pressure nodal plane. The global position (see Fig. 1) of the center of the particles pair is normalized with the length of the microchannel, $X_m^*{=}X_m/L$, while the interdistance between the particles is scaled with the particle radius, $\delta_x^* = \delta_x/R$. Time is nondimensionalized with the ratio of particle radius square to that of kinematic viscosity, i.e., $t^* = t(4\nu/R^2)$ [2].In Regime I, when the particles are placed initially near the microchannel's inlet with $X_m^* = 0.004$, we observed that both the particles move towards each other. Initially, the interdistance decreases linearly with normalized time t^*, $\delta_x^* \propto (t^*)^{-1}$. After a critical time, i.e., $t^* < 25 \times 10^3$, interparticle distance decreases rapidly, i.e., $\delta_x^* \propto (t^*)^{-2}$ (see Fig. 2(a)). At this location, the F_{px} is negligible, and the F_s dominates the motion of particles. Fig. 2(b) shows the Regime II where the particle 2 oscillates about its position while particle 1 attracted towards particle 2. Since at time $t^* = 0$, the axial primary force and the interparticle force acting on particle 2 balances each other, the particle 2 remains at rest. Still, the axial primary force and interparticle radiation force acting on particle 1 are in the same direction (towards the right), and therefore it moves towards particle 2.

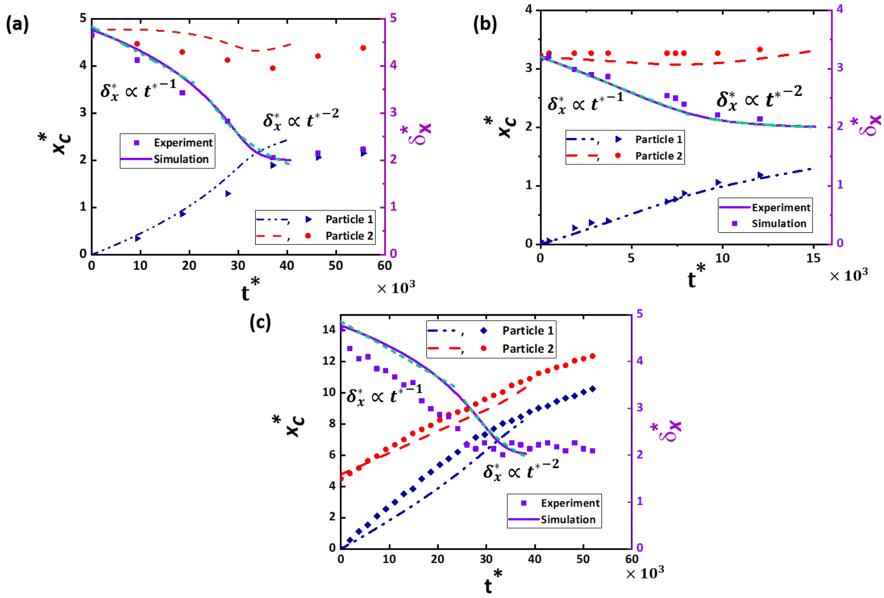

Figure 2: Comparison of the time variation of the positions of the centers of the particles (i.e., x_c^* versus time t^* from simulations and experiments) and the interdistance between a pair of $25\mu m$ particles (i.e. δ_x^* vs. t^* from simulations and experiments). (a) Regime I: Both the particles approach each other, (b) Regime II: particle 2 at rest initially and oscillates while particle 1 moves towards particle 2, and (c) Regime III: Both the particles move along the direction of decreasing $\langle E_{ac} \rangle$ and also approach each other.

In Regime III, as we further placed the pair of particles with $X_m^* = 0.02$, and $\delta_x^* = 4.5$, we observed that the particles move along the pressure nodal plane while they come close to each other (see Fig. 2(c)). The F_{px} dominates for both particle 1 and 2 and they move towards the point where $\langle E_{ac} \rangle$ is minimum. The migration of both the particles predicted by the simulations positioned at $X_m^* = 0.004, 0.006$,and 0.02, is in good agreement with the experimental observations within 10%.

Conclusion

We provided an improved understanding of axial primary radiation force and the dynamical motion of a pair of particles. Our results revealed that the axial primary force is proportional to the particle size and acts along the direction of a positive energy density gradient. It is found that the interdistance between a pair of particles decreases linearly with time, $\delta_x^* \propto (t^*)^{-1}$ up to a critical time beyond which point the interdistance decreases as $\delta^* \propto (t^*)^{-2}$.

References

[1] T. Laurell, F. Petersson, and A. Nilsson, Chem. Soc. Rev. **36**, 492 (2007).
[2] G.T. Silva and H. Bruus, Phys. Rev. E - Stat. Nonlinear, Soft Matter Phys. **90**, 1 (2014).
[3] S. M. Woodside, B. D. Bowen, and J. M. Piret, AIChE J., **43**, 1727-1736, (1997).
[4] H. Bruus, Lab Chip, **12**, 1578 (2012).

Acoustofluidics
2021
26-27 August 2021
Virtual Conference

Generalized potential for acoustic interaction force

Shahrokh Sepehrirhnama[1] and Kian-Meng Lim[2]

[1]Centre for Audio, Acoustics and Vibration (CAAV), University of Technology Sydney, Sydney, Australia
[2]Department of Mechanical Engineering, National University of Singapore, Singapore
E-mail: limkm@nus.edu.sg

Introduction

In ultrasound particle manipulation, interparticle forces become significant when the interparticle distances are comparable to particle size or the particles are close to their trapping locations where the primary radiation force becomes negligible. In this work, we present a generalize potential that can be used to evaluate interparticle forces among multiple spherical particles subject to an external acoustic field.

Formulation for force potentials

For a single sphere (radius a, density ρ, and compressibility κ) in a fluid medium (with density ρ_f and compressibility κ_f) subject to an external incident field (p_{in} and $\mathbf{v}_{\text{in}}$), the acoutic radiaton force can be calculated by Eq. (1). This accounts for only the monopole and dipole terms, which is valid in the Rayleigh limit [1]. The monopole and dipole coefficients are $\alpha = 1 - \frac{\kappa}{\kappa_f}$ and $\beta = \frac{2(\rho-\rho_f)}{2\rho+\rho_f}$, respectively.

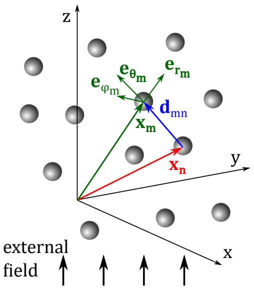

Figure 1: Schematic of an ensemble of N spheres in an external field.

$$\mathbf{F}^{\text{rad}} = 2\pi a^3 \rho_f \Big\langle \beta\ \mathbf{v}_{\text{in}} \cdot \boldsymbol{\nabla} \mathbf{v}_{\text{in}} \Big\rangle - \frac{4\pi a^3}{3} \kappa_f \Big\langle \alpha\ p_{\text{in}} \boldsymbol{\nabla} p_{\text{in}} \Big\rangle \tag{1}$$

For an ensemble of N spheres in an external field, we can generalize the incident field on a particular sphere n as $\hat{p}_n$ and $\hat{\mathbf{v}}_n$. This incident field is the sum of the external field (p_0 and $\mathbf{v}_0$) and scattered fields from other spheres m (p_m and $\mathbf{v}_m$), excluding sphere n itself.

$$\hat{p}_n = p_0 + \sum_{\substack{m=1\\ m\neq n}}^{N} p_m \qquad \hat{\mathbf{v}}_n = \mathbf{v}_0 + \sum_{\substack{m=1\\ m\neq n}}^{N} \mathbf{v}_m \tag{2}$$

We may use this incident field to obtain the radiation force $\mathbf{F}_n$ acting on sphere n in a similar form as Eq. (1):

$$\mathbf{F}_n = 2\pi a_n^3 \rho_f \Big\langle \beta_n \hat{\mathbf{v}}_n \cdot \boldsymbol{\nabla} \hat{\mathbf{v}}_n \Big\rangle_{\mathbf{x}=\mathbf{x}_n} - \frac{4\pi a_n^3}{3} \kappa_f \Big\langle \alpha_n \hat{p}_n \boldsymbol{\nabla} \hat{p}_n \Big\rangle_{\mathbf{x}=\mathbf{x}_n}. \tag{3}$$

Here, a_n, α_n and β_n are the radius, and monopole and dipole coefficients of sphere n, respectively, that may be distinct for each sphere. Following the steps in [2], we further split the force into the primary force $\mathbf{F}_n^0$ due to the external field and the interaction forces $\mathbf{F}_n^m$ acting on sphere n due to another sphere m.

$$\mathbf{F}_n^0 = -\boldsymbol{\nabla} G_n^0; \quad G_n^0 = \Omega_n \Big\langle \frac{\kappa_f}{2} \alpha_n p_0^2 - \frac{3}{4} \rho_f \beta_n v_0^2 \Big\rangle_{\mathbf{x}=\mathbf{x}_n} \tag{4}$$

$$\mathbf{F}_n^m = -\boldsymbol{\nabla} G_n^m; \quad G_n^m = \Omega_n \Big\langle \kappa_f \alpha_n \big(p_m p_0 + \frac{1}{2} \sum_{\substack{l=1\\ l\neq n}}^{N} p_m p_l \big) - \frac{3}{2} \rho_f \beta_n \big(\mathbf{v}_m \cdot \mathbf{v}_0 + \frac{1}{2} \sum_{\substack{l=1\\ l\neq n}}^{N} \mathbf{v}_m \cdot \mathbf{v}_l \big) \Big\rangle_{\mathbf{x}=\mathbf{x}_n} \tag{5}$$

The forces are expressed as the gradient of potentials, with G_n^0 giving the classical Gorkov's potential for the primary force. The generalized potential G_n^m gives the interaction force acting on sphere n due

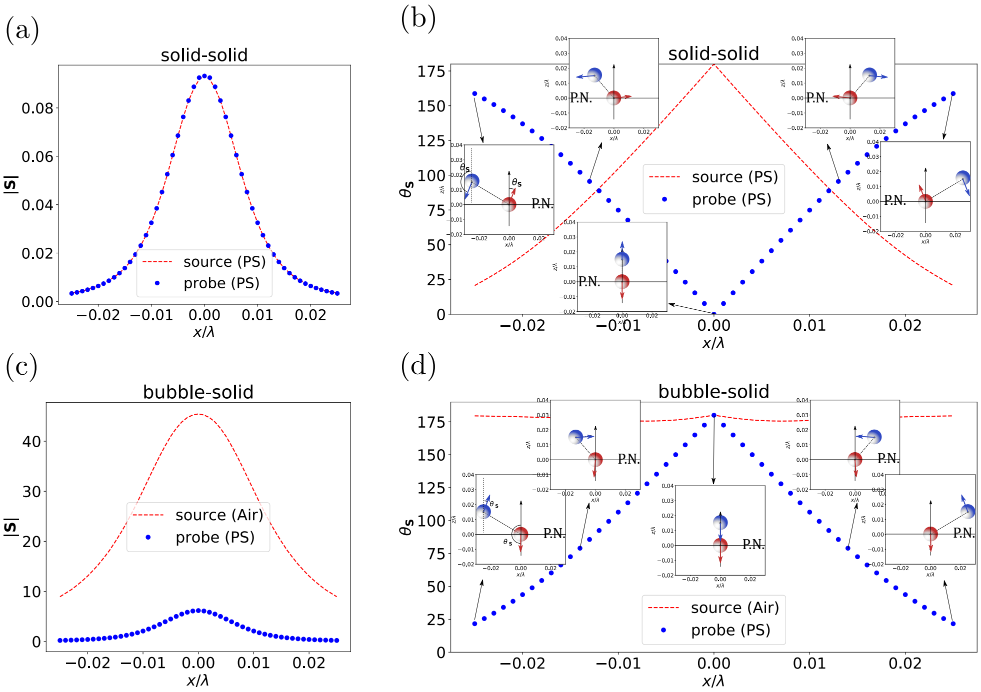

Figure 2: Interaction forces acting on probe and source spheres, with probe sphere is shifted parallel to the nodal plane at a perpendicular distance of $3a$. For two solid spheres, magnitudes (Panel a) are equal and directions (Panel b) are opposite, but this not the case for the bubble-solid interaction (Panels c and d). Figures adapted from Ref. [2].

to the scattered field from sphere m. The cross terms ($p_m p_l$ and $\mathbf{v}_m \cdot \mathbf{v}_l$) are typically small and can be neglected; the remaining terms in the interaction potential give the same expression as reported in [3]. It is noted that the scattered fields (p_m and $\mathbf{v}_m$) from all spheres need to be solved in a fully coupled manner before they are used in the potentials (G_n^0 and G_n^m).

Interparticle forces between similar and dissimilar spheres

Using the above formulation, we calculated the interparticle forces for two cases: (i) between two polystyrene beads in water (solid-solid) and (ii) between a polystyrene bead and air bubble (bubble-solid). The source sphere is placed at the pressure nodal plane of a standing wave, while the probe sphere is moved over a horizontal line above the nodal plane (Fig. 2). For the solid-solid case, the interaction forces are found to be equal and opposite. For the bubble-solid case, the mutual interaction forces are distinctly different. The air bubble (source sphere) exhibits a strong monopole scattering, while the scattered field of the bead is dominated by dipole scattering. This difference in the scattering patterns results in the unequal interaction forces. The interaction force acting on the air bubble is larger than the force acting on the bead by one to two orders of magnitude. Due to the break in symmetry in the scattering patterns of two spheres of different properties, the usual notion that interaction forces being an equal and opposite pair (similar to Newton's third law) is not valid here.

Conclusion

We presented a generalized potential function, an extension of the classical Gorkov potential, that can be used to calculate the acoustic interaction force between spheres. It takes into account the interaction among the scattered fields from all spheres as well as the external field. While the formulation is applicable to multiple spheres, results for two spheres (solid-solid and bubble-solid) have been presented here for illustration. The results show that the interaction force is equal and opposite for two identical spheres, but differ significantly for spheres with different properties.

Acknowledgments

This work was supported by the Ministry of Education, Singapore, through the National University of Singapore, Faculty of Engineering (Tier 1 Grant R-265-000-652-114).

References

[1] H. Bruus Lab on a Chip **12**, 1014-1021 (2012).
[2] S. Sepehrirhnama, K.M. Lim Physical Review E **102**, 043307 (2020).
[3] G.T. Silva, H. Bruus Physical Review E **90**, 063007 (2014).

Acoustofluidics
2021
26-27 August 2021
Virtual Conference

Microstreaming and acoustic interaction forces between two particles in a standing wave within a viscous fluid

Alen Pavlic[1], Lorenzo Ermanni[1], Jürg Dual[1]

[1]Institute for Mechanical Systems, Swiss Federal Institute of Technology Zurich, Zurich, Switzerland
E-mail: apavlic@ethz.ch, URL: http://www.expdyn.ethz.ch

Introduction

Acoustophoresis represents one of a few contactless methods for handling microparticles and cells, rendering the understanding of fundamental forces behind it very important. Effects of viscosity on the primary acoustic radiation force (ARF) are already well understood and can become dominant for a heavy particle when the viscous boundary layer thickness δ surpasses the radius of the particle, redefining the stable positions of the particle in a standing wave [1,2]. This strange behaviour was attributed to the contribution of the microstreaming, since considering the viscosity at the level of acoustic scattering [3] yields only a minor correction to the inviscid theory [4]. However, the influence of the viscosity and particularly the influence of the microstreaming between two particles on the acoustic interaction force (AIF) is deemed important [5], but not yet well understood. We extend the numerical model from Baasch et al. [2] to investigate the microstreaming field around two particles in a standing wave and compute the AIF that results from the re-scattering as well as from the microstreaming interactions. The results partially agree with the inviscid AIF theory by Silva and Bruus [6], and reveal interesting phenomena beyond, where the microstreaming dominates the interactions between the two particles. The results are relevant for multi-particle acoustofluidic systems, as for example the seed-particle-based trapping of nanoparticles and bacteria [7].

Theory and numerical model

The AIF is the force acting on a particle in an acoustic wave solely due to the presence of another particle nearby, excluding the hydrodynamic interactions due to movements of other particles. The AIF arises from the re-scattering of the waves [6] and also from the interactions between the microstreaming fields surrounding the two particles [5]. As a basis for the computation of the AIF, we compute the ARF on a single particle in the two-particle configuration through

$$\boldsymbol{F}_{\mathrm{rad}} = \int_S \left[-\langle p_2 \rangle \boldsymbol{I} + \eta \left(\boldsymbol{\nabla} \langle \boldsymbol{v}_2 \rangle + (\boldsymbol{\nabla} \langle \boldsymbol{v}_2 \rangle)^{\mathrm{T}} \right) + \left(\eta_{\mathrm{B}} - \frac{2}{3} \eta \right) (\boldsymbol{\nabla} \cdot \langle \boldsymbol{v}_2 \rangle) \boldsymbol{I} - \rho_0 \langle \boldsymbol{v}_1 \boldsymbol{v}_1 \rangle \right] \cdot \boldsymbol{n} \, dS \,, \tag{1}$$

with second-order pressure $\langle p_2 \rangle$, second-order (streaming) velocity $\langle \boldsymbol{v}_2 \rangle$, equilibrium density ρ_0, dynamic viscosity η, bulk viscosity η_{B}, and first-order (acoustic) velocity $\boldsymbol{v}_1$. The whole expression is integrated over a static surface S with surface normal $\boldsymbol{n}$, enclosing the particle. The time average over a period of oscillation is denoted by $\langle \quad \rangle$. The integration from eq. (1) is then repeated for a case without the additional particle, and the difference between the two forces is the AIF.

The contribution to the AIF from the acoustic re-scattering is captured in the Reynolds stress in eq. (1), namely $\rho_0 \langle \boldsymbol{v}_1 \boldsymbol{v}_1 \rangle$. Furthermore, through the Reynolds stress, the re-scattering also affects the source terms for the equations of acoustic streaming, the solutions to which are $\langle \boldsymbol{v}_2 \rangle$ and $\langle p_2 \rangle$.

The numerical model capable of capturing the scattering and streaming phenomena was built based on the finite element method framework of COMSOL Multiphysics® v. 5.6 (COMSOL AB, Stockholm, Sweden), following the approach of Baasch et al. [2]. For extraction of the AIF, three simulations are needed for each case: a simulation with two interacting particles present in the computational domain, and two single-particle simulations, one for each of the two particles. The AIF is then computed as the difference between the ARF in the two-particle configuration and the ARF in the single-particle configuration. The two particles are positioned along the direction of the pressure gradient of a plane standing wave, which enables the use of axial symmetry, reducing the computational cost.

Results and discussion

We consider two polystyrene spheres with density of $1050\,\mathrm{kg\,m^{-3}}$ and pressure- and shear-sound speeds of $2400\,\mathrm{m\,s^{-1}}$ and $1150\,\mathrm{m\,s^{-1}}$, respectively, suspended in water with density of $997\,\mathrm{kg\,m^{-3}}$, sound speed of $1502\,\mathrm{m\,s^{-1}}$, and dynamic viscosity of $0.85\,\mathrm{mPa\,s}$. The spheres are placed in a plane standing wave along the direction of the pressure gradient. One of the particles – Particle 1 – is always placed at the pressure node, since the AIF relative to the ARF is usually most significant there. Furthermore, the standing wave in water is defined by the pressure amplitude of $0.5\,\mathrm{MPa}$ and the frequency (f) of $0.5\,\mathrm{MHz}$. The characteristic viscous boundary layer thickness corresponds to $\delta = \sqrt{\eta/(\pi f \rho)} = 0.74\,\mathrm{\mu m}$.

In Fig. 1, we analyze the microstreaming around two particles with radii of 5 μm (Particle 1) and 0.5 μm (Particle 2), while the interparticle distance is decreased from 10μm in Fig. 1(a), to 1 μm in Fig. 1(c). The patterns in Fig. 1(a) indicate that the initial pattern of four vortices along the z-axis, between the two particles, transforms to two vortices when the particles are 3 μm apart in Fig. 1(b), and lastly, to a single vortex in Fig. 1(c), when the particles are only 1 μm apart, revealing strong microstreaming interactions.

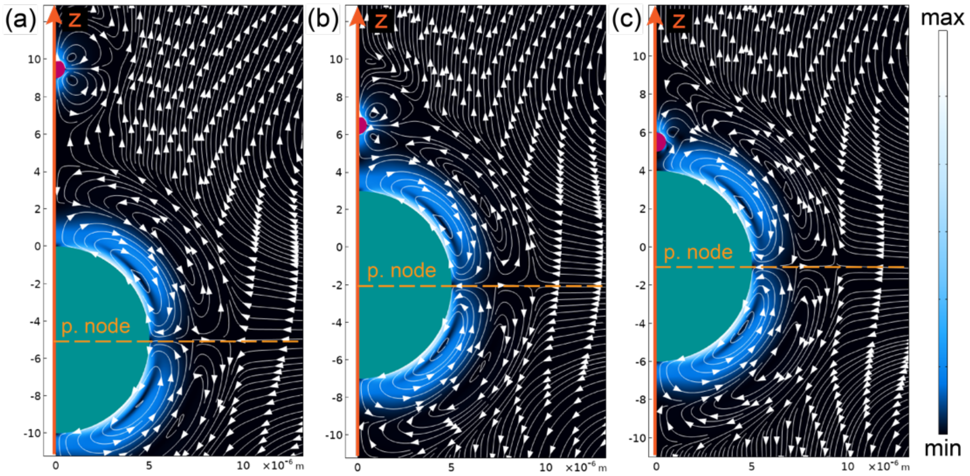

Figure 1: The Eulerian microstreaming patterns for a pair of polystyrene spheres in water. Particle 1 (green) of 5 μm radius is always at the pressure node (dashed line) of a 0.5 MHz standing wave that is imposed along the z-axis, axis of symmetry. Position of Particle 2 (red) of 0.5 μm radius is varied to yield the interparticle distance of: (a) 10 μm, (b) 3 μm, and (c) 1 μm. Colorbar indicates the min.-max. streaming velocity magnitude.

The impact of the microstreaming on the AIF is analyzed in Fig. 2, for two polystyrene particles, where Particle 2 is approaching Particle 1 which is fixed at a pressure node of the standing wave. When the two particles are of the same radius, 5 μm in Fig. 2(a), the AIF from our model qualitatively agrees with the inviscid theory by Silva and Bruus [6], confirming the repulsion of the approaching particle. The agreement is especially good at the interparticle distances above 4 μm. However, for a smaller Particle 2, the microstreaming contribution can change the sign of the AIF and of the total force, resulting in the attraction of Particle 2 to Particle 1. This is shown in Fig. 2(b), for 0.5 μm radius of Particle 2 (same case as in Fig. 1).

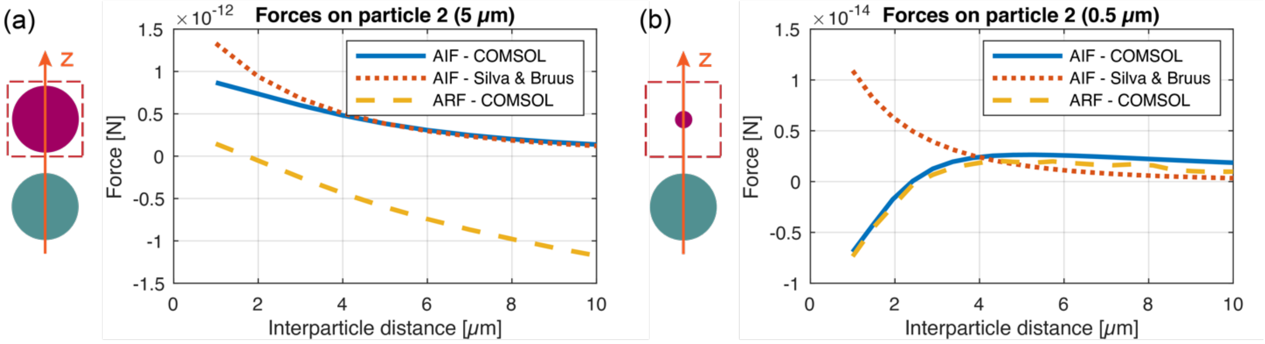

Figure 2: Acoustic forces along the z-axis acting on Particle 2 (red) for different interparticle (surface to surface) distances to Particle 1 (green) of 5 μm radius that is placed at a pressure node of a 0.5 MHz standing wave in water. Both particles are from polystyrene. AIF – COMSOL represents the interaction force from our numerical model that accounts for the microstreaming; AIF – Silva & Bruus is the interaction force from the reference inviscid theory [6]; ARF – COMSOL is the total force on Particle 2 from our model. (a) Acoustic forces on Particle 2 of 5 μm radius. (b) Acoustic forces on Particle 2 of 0.5 μm radius. The negative sign of a force implies an attraction of Particle 2 to Particle 1, whereas the positive sign implies repulsion.

Conclusion

We demonstrated the significance of the microstreaming contribution to the AIF, by predicting that a particle approaching another particle at a pressure node of a standing wave, experiences attraction to the particle at the pressure node in a direction transverse to the pressure node. Such attraction has not been recognized before and could, for example, enhance the acoustic trapping of nanoparticles and bacteria [7].

References

[1] A. A. Doinikov. Proc. Royal Soc. A **447(1931)**, 447-466 (1994).
[2] T. Baasch, A. Pavlic, and J. Dual. Phys. Rev. E **100(6)**, 061102 (2019).
[3] M. Settnes and H. Bruus. Phys. Rev. E **85(1)**, 016327 (2012).
[4] K. Yosioka and Y. Kawasima. Acta Acustica united with Acustica **5(3)**, 167-173 (1955).
[5] S. Sepehrirahnama, F. S. Chau, and K. M. Lim. Phys. Rev. E **93(2)**, 023307 (2016).
[6] G. T. Silva and H. Bruus. Phys. Rev. E **90(6)**, 063007 (2014).
[7] B. Hammarström, T. Laurell, and J. Nilsson. Lab on a Chip **12(21)**, 4296-4304 (2012).

Acoustofluidics 2021
26-27 August 2021
Virtual Conference

3D3C flow measurements of the acoustically induced vortex structures in a standing surface acoustic wave field

Sebastian Sachs[1], Christian Cierpka[1], and Jörg König[1]

[1]Institute of Thermodynamics and Fluid Mechanics, Technische Universität Ilmenau,
P.O. Box 100565, D-98684 Ilmenau, Germany
E-mail: sebastian.sachs@tu-ilmenau.de, URL: http://www.tu-ilmenau.de/ttd

Introduction

By utilizing standing surface acoustic waves (sSAW), particle trajectories can be systematically manipulated under the influence of acoustic streaming and the acoustic radiation force (ARF). While the latter enables a fractionation of particle suspensions based on the location of stationary pressure nodes and antinodes, the acoustically induced fluid flow has a negative effect on the purity of the fractionation in many microfluidic systems [1,2]. Especially when particles are involved which motion is only weakly affected by the ARF, the acoustically excited flow needs to be considered in the design of appropriate devices and have been investigated numerically in previous studies [3,4]. While experimental results has been reported with microchannels with a width of one wavelength λ_{SAW} of the sSAW only [5], this work extends the state of research by 3D velocity measurements in a standing wave field with multiple pressure nodes along the channel width and height. Based on the variation of the frequency, channel height and electrical power, the influence on the structure and velocity of the flow is discussed both in the center and outer regions of the sSAW-field.

Experimental setup

The acoustically induced particle motion was investigated in straight microchannels made of Polydimethylsiloxan (PDMS, see Fig. 1) with a width of 500 μm and heights ranging from 85 μm to 480 μm. To excite a standing wave field within the fluid, the respective channel was centrally positioned between two interdigital transducers (IDTs) on a 128° YX $LiNbO_3$ substrate. Through different geometries of the IDTs, SAWs were generated applying resonance frequencies f in the range from 25.72 MHz to 194.8 MHz. To reduce the influence of the ARF on the particle motion, the density of the fluid (mixture of 80 % v/v de-ionized water and 20 % v/v glycerol) was adjusted to that of the suspended 1.14 μm polystyrene particles. In that way, reliable velocity measurements of the acoustically excited flow were enabled with a low acoustic contrast factor. A pulsation-free main flow was imposed externally by using a syringe pump (neMESYS, cetoni GmbH). During the measurements the 3D trajectories of the particles were determined by astigmatism particle tracking velocimetry (APTV) [6].

Results and discussion

Fig. 2 illustrates the spatially and time averaged velocity fields in the center (ROI2) of the sSAW for frequencies of 194.8 MHz (a) and 25.72 MHz (b). Since the particle motion in this region is translation invariant with respect to the main flow direction (y), a spatial averaging over the entire measurement range of 800 μm was performed using voxel sizes of $10 \times 800 \times 10\ \mu m^3$ and Gaussian-weighted interpolation of the randomly distributed velocity vectors. Acoustically excited vortex structures are clearly visible, which symmetrically extend from the sidewalls as Eckart streaming over the entire channel for f = 194.8 MHz. The angle ϑ between the outer and inner vortices amounts to approx. 24.2°, and is

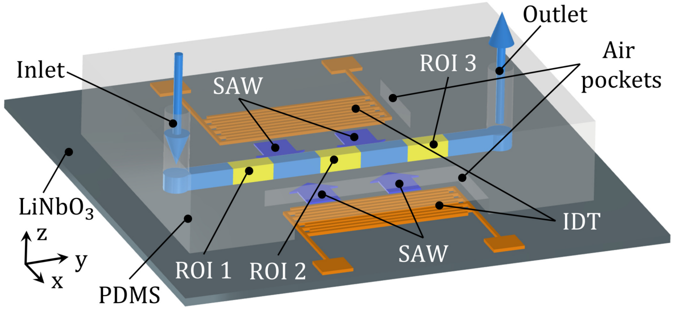

Figure 1: Schematic representation of the microfluidic platform with the channel made of PDMS, the $LiNb0_3$ substrate and the IDT structures. The propagation direction of the SAW is indicated by arrows and the three distinct regions of interest (ROI) are highlighted in yellow.

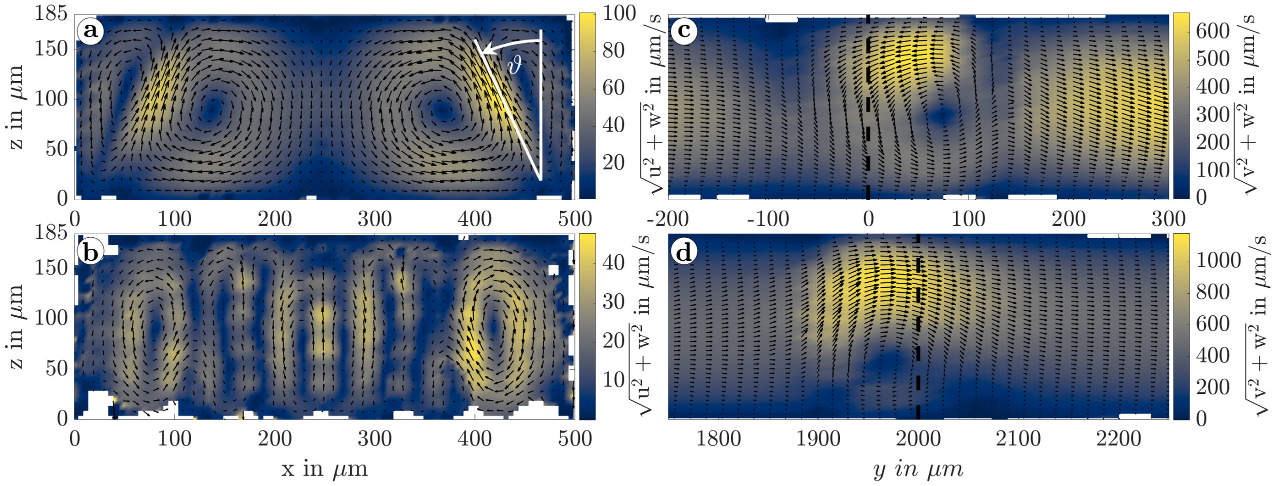

Figure 2: Experimental results of acoustically induced particle motion perpendicular to the main flow in ROI2 for a frequency of 194.8 MHz (a) and 25.72 MHz (b). The electrically imposed power was about 20 mW in each case, the channel height about 185 μm and the width approx. 500 μm. The flow in sectional planes at the beginning (c, ROI1, $x' = 250$ μm) and end (d, ROI3, $x'' = 160$ μm) of the sSAW-field reveals additional vortex structures in main flow direction (y). In those cases the channel geometry remained constant while the electrical power was increased to approx. 154 mW at 194.8 MHz. The dashed lines mark the beginning and the end of the aperature of the IDTs, respectively. Please note the different scaling of the color bars and vectors.

thus close to the theoretically expected Rayleigh angle of 23.4°. As the frequency decreases, typical vortices develop only near the channel walls in Fig. 2b, while several small vortex pairs form in the central region of the channel. This trend shows the influence of traveling wave components, which are limited to the edge regions of the channel due to the lower attenuation at $f = 25.72$ MHz, while the particle trajectories in the middle are dominated by the standing wave field. At the same time, the attenuation length of the bulk acoustic wave (BAW) increases, resulting in less energy being coupled into the fluid and a nonlinear decrease in the flow velocity.

Vortex structures with inverse sense of rotation are visible at the beginning (ROI1) and end (ROI3) of the sSAW in Fig. 2c and 2d, respectively. These arise due to pressure gradients in y-direction, and cause a variation of the velocity component v in main flow direction locally, due to recirculation. With increasing power, the vortices extend further into the channel and displace the imposed main flow, resulting in a local increase of the particle velocity. The vortex centers are always located within the aperture of the IDTs in the considered parameter range. Due to the interaction with the imposed flow, a central vortex at the beginning and two separate vortex structures in the lower corners of the channel at the end of the sSAW are formed. Based on the measurement results, a structural analysis of the complex three-dimensional flow is possible for the first time.

Conclusion

The structure of the acoustically induced flow in the center and in the outer regions of the sSAW has been characterized experimentally by comprehensive velocity measurements. Thereby, the influence of travelling wave components on the formation and extension of the local vortices under the variation of the excitation frequency was demonstrated. Further investigations revealed complex 3D vortex structures at the beginning and at the end of the sSAW. During the conference, additional results on the variation of the channel height and the electrical power will be shown. The presented investigations provide important information for the design of acoustofluidic devices, e.g. for particle fractionation.

Acknowledgement

The authors thank the Deutsche Forschungsgemeinschaft (DFG) for financial support within the priority program SPP2045 "MehrDimPart" (CI 185/8-1).

References

[1] P. Sehgal and B. J. Kirby. Analytical Chemistry **89**, 12192-12200 (2017).

[2] M. Wu, Z. Mao, J. Chen, H. Bachman, Y. Chen, J. Rufo, L. Ren, P. Li, L. Wang and T. J. Huang. Advanced Functional Materials **27**, 1606039 (2017).

[3] C. Devendran, T. Albrecht, J. Brenker, T. Alan and A. Neild. Lab on a Chip **16**, 3756-3766 (2016).

[4] N. Nama, R. Barnkob, Z. Mao, C. J. Kähler, F. Costanzo and T. J. Huang. Lab on a Chip **15**, 2700-2709 (2015).

[5] R. Barnkob, N. Nama, L. Ren, T. J. Huang, F. Costanzo and C. J. Kähler. Phys. Rev. Applied **9**, 014027 (2018).

[6] C. Cierpka, R. Segura, R. Hain and C. J. Kähler. Meas. Sci. Technol. **21**, 045401 (2010).

Acoustofluidics 2020
26-27 August 2020
Virtual Conference

Burgers-Riccati physics of fast bulk acoustic streaming

J. Orosco[1] and J. Friend[1,2]

[1]Department of Mechanical and Aerospace Engineering, University of California San Diego, La Jolla, California, USA
[2]E-mail: jfriend@ucsd.edu, URL: http://friend.ucsd.edu/

Introduction

We outline a theoretical approach to acoustofluidic modeling that affords the user greater generality than classical methods by its direct, explicit consideration and exploitation of all spatiotemporal scale disparities. The method is applied to a one-dimensional problem of semiinfinite extent that is conventionally classified as "fast streaming." We show that transient fast bulk acoustic streaming is explained by a forced viscous Burgers equation. Steady streaming therefore corresponds to a Riccati equation. A number of simple expressions are derived that characterize the fundamental flow characteristics. The theory is validated with a broad comparative survey of results from the recent literature.

Theory and main results

Our framework finds its origins in the efforts of Blekhman [1], Thompson [2], and others [3] toward uncovering the peculiar and often counterintuitive behaviors of nonlinear rigid-body systems (*i.e.*, temporal ODEs) subject to high-frequency inputs. Known as the Method of Direct Partition (or Separation) of Motions, the novel approach works by partitioning the nondimensionalized temporal derivatives into two timescales: "slow" and "fast," where explicit notions of fast and slow—as well as conditions for applicability of the method—were first rigorously described by Blekhman [1].

In order to leverage the insights of these past authors and yet extend them into the domain of continuum mechanics, we show that one can justify (physically and mathematically) a partitioning of nondimensional temporal and spatial operators:

$$d_t = \varepsilon\, \partial_t + \partial_\tau, \tag{1a}$$

$$d_x = q_\lambda\, \partial_x + \partial_\xi, \tag{1b}$$

where t and τ are the "slow" streaming and "fast" acoustic nondimensional time scales, respectively. Similarly, x and ξ are the "large" streaming and "small" acoustic nondimensional space scales. Here, $q_\lambda = \lambda/x_s \ll 1$ is a small parameter characterizing the spatial disparity between the streaming space scale, x_s, and the acoustic wavelength, λ. The parameter $\varepsilon = S^{-1} \ll 1$ is given in terms of a Strouhal number, $S = \omega\, t_s$, and characterizes the difference between the streaming timescale, t_s, and the acoustic timescale, ω^{-1}.

For the fast streaming scenario, we also show that nondimensionalized field variables may be partitioned in a framework-relevant fashion:

$$u_x = u_x^{(a)} + q_p\, S\, u_x^{(s)}, \tag{2a}$$

$$\rho - 1 = M_a\, \rho^{(a)} + M_s\, \rho^{(s)}, \tag{2b}$$

where $q_p = \xi_p/x_s \ll 1$ characterizes the disparity between the particle displacement, ξ_p, and the streaming space scale. The density scaling utilizes the acoustic Mach number, $M_a = \omega\, \xi_p/c$, as well as a streaming Mach number, $M_s = U_s/c$, where c is the speed of sound in the fluid. The pressure partition is determined by the isentropic equation of state, $\widetilde{P} = \widetilde{P}(\widetilde{\rho})$ (tilde indicates dimensional variables), which we find sufficient to expand at first order: $\widetilde{P} - P_0 = c^2\, (\widetilde{\rho} - \rho_0)$.

By applying the method to the isentropic Navier-Stokes equations, one obtains a finite term expansion in terms of the scale disparities. The leading order equations determine the acoustic field:

$$\mathcal{A}\, u^{(a)} = \partial_\tau F, \tag{3}$$

where we have defined the linear acoustic field operator $\mathcal{A} = \partial_\tau^2 - \partial_\xi^2 - 2\,\theta\, \partial_\tau \partial_\xi^2$, which is realized entirely within an acoustic spatiotemporal basis. The nondimensional parameter $\theta = \mu_l\, \omega / 2\, \rho_0\, c^2$ is related to the attenuation per unit wavelength, $(k\,\delta_a)^{-1}$. We take $F_x = 0$ since the source of the motions is the vibrating origin. At higher order, one recovers a forced viscous Burgers streaming equation:

$$\partial_t u^{(s)} + u^{(s)}\,\partial_x u^{(s)} = \mu\,\partial_x^2\,u^{(s)} + \eta_m^{-1} f_R(x), \tag{4}$$

where $f_R(x) = -\langle u^{(a)}\partial_x u^{(a)}\rangle_{\xi,\tau}$ is the Reynolds stress associated with the acoustic wave, μ is a nondimensional viscosity, and η_m is a maximum acoustic-to-streaming tranduction efficiency. Here $\langle(\,\cdot\,)\rangle_{\xi,\tau}$ denotes the spatiotemporal average of $(\,\cdot\,)$ taken over the wave periodicity. The separation of time scales allows us to take such an average while leaving the transient streaming effects intact. Selected results for modeling axial Eckart flow with Eq.(4) are provided in Fig. 1 for two different forcing scenarios. In the steady streaming limit, $t \to \infty$, one has Riccati's equation,

$$\begin{aligned} q_\lambda\,(\partial_x\,u^{(s)} - \partial_x\,u^{(s)}|_{x=0}) - \frac{R}{2}\,\left(u^{(s)}\right)^2 \\ = \frac{R}{\eta_m}\int_0^x \langle u^{(a)}\partial_x u^{(a)}\rangle_{\xi,\tau}\,dx, \end{aligned} \tag{5}$$

where R is a Reynolds number for the streaming flow. A number of simple-yet-fundamental relations can be derived directly from Eq. (5).

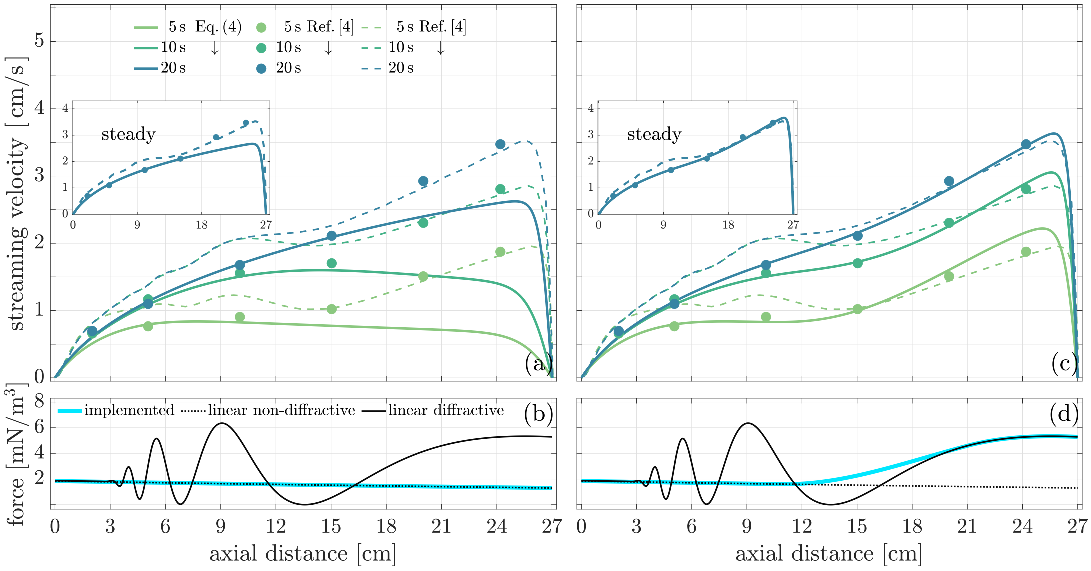

Figure 1: Large-amplitude ("fast") axial Eckart streaming. (a) Viscous Burgers streaming model with $\mu \approx 0.018$ and (b) Reynolds stress derived from a linear, non-diffractive pressure field. (c) Viscous Burgers streaming model with $\mu \approx 0.013$ and (d) composite Reynolds stress derived from a linear non-diffractive pressure field in the leading half of the domain and a linear diffractive pressure field in the latter half of the domain. All other parameters follow from Ref. [4]. Steady profile evolution—which starts at the source and proceeds monotonically toward the distal boundary—leads to spatially progressive profile dependence. Thus, forcing in the leading section of the model of Ref. [4] cannot be altered without significantly perturbing model fidelity in the latter domain half.

Conclusion

By leveraging the drastic spatiotemporal disparities concomitant to systems encountered in modern acoustofluidics research, a method has been developed and demonstrated for extracting the dynamics of interest from the highly nonlinear governing equations.

References

[1] I. I. Blekhman, *Vibrational Mechanics: Nonlinear Dynamic Effects, General Approach, Applications* (World Scientific, River Edge, NJ, 2000).

[2] J. J. Thomsen, *Vibrations and Stability: Advanced Theory, Analysis, and Tools*, 2nd ed. (Springer-Verlag, Berlin Heidelberg, 2003).

[3] G. P. Chini, Z. Malecha, and T. D. Dreeben, J. Fluid Mech. **744**, 329 (2014).

[4] T. Kamakura, T. Sudo, K. Matsuda, and Y. Kumamoto, J. Acoust. Soc. Am. **100**, 132 (1996).

Acoustofluidics 2021
26-27 August 2021
Virtual Conference

Specular-reflection contributions to dynamic radiation forces on highly reflecting spheres and cylinders: simplified analysis

Philip L. Marston[1], Timothy D. Daniel[1,2], and Auberry R. Fortuner[1]

[1]Physics and Astronomy Dept., Washington State University, Pullman, Washington, 99164-2814, USA
E-mail: marston@wsu.edu, URL: https://physics.wsu.edu
[2]NSWC PCD, 110 Vernon Avenue, Panama City, FL, 32407

Introduction

It has been recognized for decades that double sideband suppressed carrier modulation (DSB-SCM) acoustic illumination gives rise to acoustic radiation pressures that oscillate at a single low frequency [1-5]. Unfortunately, calculation of quantities of interest using partial-wave series (PWS) solutions can be complicated even when the ultrasonic size parameter k*a* is small [6, 7]. Here a novel geometric method of evaluating dynamic forces on highly reflecting spheres and cylinders having k*a* >> 1 is summarized [8, 9]. For the case of plane-wave illumination simple approximations of the magnitude and phase of the modulated radiation force are obtained. The approximations are supported by PWS comparisons and provide a simple way of understanding how the magnitude and phase of such forces depend on the modulation frequency.

Dimensionless progressive-wave radiation force function Y_P

For steady unmodulated progressive acoustic waves having an intensity I_0 there is a commonly used normalization that allows the radiation force on a sphere or on a right-circular cylinder to be expressed as proportional to I_0 and a dimensionless function Y_P and geometric factors reviewed in [8, 9]. What is less well known is that when k*a* >> 1, for smooth highly reflecting spheres and cylinders, the radiation force can be approximated by evaluating a factor that depends on the reflectivity at normal incidence and the Y_P for fixed-rigid spheres and cylinders. (At large k*a*, geometric constructions give in the fixed-rigid sphere and cylinder cases using the standard normalization Y_P of 1 and 4/3, respectively [8, 9].) Figure 1 (from [8]) shows an example for the case of a solid aluminum cylinder in water. This example is relevant to some applications.

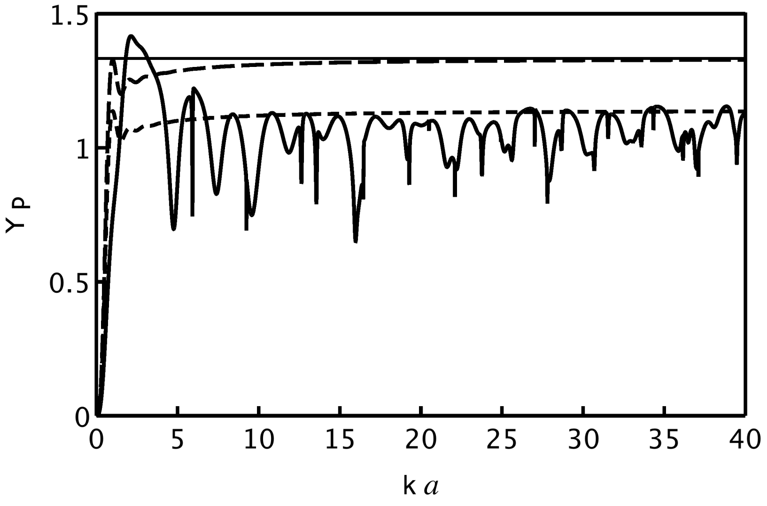

Figure 1: The radiation force function Y_P for steady acoustic illumination of a cylinder is plotted as a function of the cylinder's k*a*. The solid curve is the PWS result for an aluminum cylinder in water. The curve with long dashes is for a fixed rigid cylinder which approaches the geometrically computed line $Y_P = 4/3$ when k*a* is large. The curve with short dashes is the rigid result scaled by a factor [8] associated with partial reflection at normal incidence. The specular contribution is dominant on the average when k*a* is large.

Dimensionless progressive-wave radiation force function for DSB-SCM plane-wave illumination Y_T

In the case of highly reflecting spheres and cylinders illuminated by DSB-SCM plane waves having k*a* >> 1 it is possible to analytically modify the geometric approach considered in Fig. 1 to account for the temporal modulation of the illumination. The geometric analysis builds on Herrey's formulation of radiation stresses on tilted reflecting surfaces supported by her experiments [10]. It is necessary to account for the temporal modulation of the illumination in the situation considered here. The needed integrals can be done analytically. In the case of a perfectly reflecting circular cylinder, the resulting time-dependent dimensionless radiation force function Y_T is reduceable to expressions involving Struve functions, Bessel functions, and elementary trigonometric functions [8]. Similarly in the case of a perfectly reflecting sphere the resulting time-dependent dimensionless radiation force function Y_T is reduceable to expressions involving Bessel functions and elementary trigonometric functions [9]. These are not formal series solutions, but they are still valuable because they have simple physical interpretations that explain the magnitude and phase of the modulated radiation force. Furthermore, these approximations show how to design the phase of the illuminating sidebands in such a way as to reduce the dependence of the phase of the modulated radiation force on the modulation frequency. These approximations also show why the dynamic part of the radiation force decreases with increasing modulation frequency for highly reflecting spheres and cylinders. In certain cases, PWS solutions are available and numerical comparison of the PWS solutions with the specular approximation results support the relevance of those results when appropriate [8,9].

Conclusion

We have analytically evaluated geometric approximations for the specular reflection contributions to static and dynamic radiation forces on spheres and cylinders [8,9]. The approximations provide helpful insight into static and dynamical progressive wave radiation forces.

References

[1] P. L. Marston and R. E. Apfel, Bull. Am. Phys. Soc. **22**, DFD-1283 (1977).
[2] P. L. Marston and R. E. Apfel. Journal of Colloid and Interface Science **68**, 280–286 (1979).
[3] P. L. Marston and R. E. Apfel. J. Acoust. Soc. Am. **67**, 27–37 (1980).
[4] P. L. Marston and S. G. Goosby. Physics of Fluids **28**, 1233–1242 (1985).
[5] P. L. Marston, J. Quant. Spectroscopy & Radiative Transfer **254**, 107226 (2020).
[6] P. L. Marston. J. Acoust. Soc. Am. **67**, 15–26 (1980).
[7] P. L. Marston, S. E. LoPorto-Arione, and G. L. Pullen. J. Acoust. Soc. Am. **69**, 1499–1501 (1981).
[8] P. L. Marston, T. D. Daniel, A. R. Fortuner, I. P. Kirsteins, and A. T. Abawi. “Specular-reflection contributions to static and dynamic radiation forces on circular cylinders,” J. Acoust. Soc. Am. **149**, 3042-3051 (2021).
[9] P. L. Marston, T. D. Daniel, and A. R. Fortuner. “Specular-reflection contributions to dynamic radiation forces on highly reflecting spheres,” J. Acoust. Soc. Am. (accepted for publication, 2021).
[10] E. M. J. Herrey. J. Acoust. Soc. Am. **27**, 891-896 (1955).

Session 4 - Acoustic Manipulation

Invited Speaker

10:30 - 11:00

INTELLIGENT ACOUSTOFLUIDICS FOR ENGINEERING HUMAN BRAIN ORGANOIDS
Hongwei Cai, Zheng Ao, and Feng Guo
Indiana University, USA

Contributed Talks

11:00 - 11:10

ACOUSTICALLY EXCITED CHANNEL WALLS FOR MICROBIOLOGICAL APPLICATIONS
Michael Gerlt, Nino Läubli, Peter Ruppen, Moritz Leuthner,
Michel Manser, Alexander Wüthrich, Bradley Nelson,
Sven Panke, and Jürg Dual
ETH Zürich, SWITZERLAND

11:10 - 11:20

SELECTING THE OPTIMAL BUFFER FOR ACOUSTIC PARTICLE SEPARATION
Thierry Baasch and Thomas Laurell
Lund University, SWEDEN

11:20 - 11:30

ACOUSTIC RADIATION FORCE ON ELASTIC MICROBEADS EXPERIENCING RESONANT SPHEROIDAL VIBRATIONS IN A VISCOUS FLUID
Amir Tahmasebipour, Matthew R. Begley, and Carl D. Meinhart
University of California, Santa Barbara, USA

11:30 - 11:40

CONTACTLESS ADDITIVE MANUFACTURING USING ACOUSTIC LEVITATION
Iñigo Ezcurdia[1], Rafael Morales[2], Marco A.B. Andrade[3],
and Asier Marzo[1]
[1]Public University of Navarre, SPAIN, [2]UltraLeap Ltd., UK, and
[3]University of São Paulo, BRAZIL

11:40 - 11:50

ON-DEMAND DROPLET GENERATION USING BULK ACOUSTIC WAVE
E. Hemachandran[1], Thomas Laurell[2], and Ashis Kumar Sen[1]
[1]Indian Institute of Technology, Madras, INDIA and
[2]Lund University, SWEDEN

11:50 - 12:00

SWARMING BEHAVIORS OF MICROMOTORS POWERED BY BUBBLE OSCILLATION
Xiaolong Lu[1], Ying Wei[1], Hui Shen[1], and Wenjuan Liu[2]
[1]Nanjing University of Aeronautics and Astronautics, CHINA and
[2]Nanjing Tech University, CHINA

Flash Talks

12:00 - 12:04 **CONTROLLED TRANSPORT AND MERGING OF INDIVIDUAL DROPS IN CLOSED CHANNEL ACOUSTOFLUIDIC DEVICES**
Kyriacos Yiannacou and Veikko Sariola
Tampere University, FINLAND

12:04 - 12:08 **PARTICLE TRAPPING IN MICROFLUIDIC SHAPED TRAPS EXPOSED TO BULK ACOUSTIC STANDING WAVES**
Lokesh Malik, Amal Nath, and Ashis Kumar Sen
Indian Institute of Technology, Madras, INDIA

12:08 - 12:12 **PARTICLE FOCUSING IN POLYMER-BASED ACOUSTOFLUIDIC DEVICES: AN EXPERIMENTAL AND NUMERICAL STUDY**
Fabian Lickert[1], Mathias Ohlin[2], Henrik Bruus[1], and Pelle Ohlsson[2]
[1]Technical University of Denmark, DENMARK and
[2]AcouSort AB, SWEDEN

12:12 - 12:16 **CELL-BASED MICROROBOT MANIPULATION BY MULTIELEMENT FOCUSED ULTRASOUND PHASED ARRAY**
Hiep Xuan Cao, Van Du Nguyen, Daewon Jung, Han-Sol Lee, Byungjeon Kang, Jong-Oh Park, and Chang-Sei Kim
Chonnam National University, KOREA (ROK)

12:16 - 12:20 **FOURIER ACOUSTICAL TWEEZERS: SYNTHESIZING ARBITRARY RADIATION FORCE USING NON-MONOCHROMATIC WAVES ON DISCRETE-FREQUENCY BASIS**
Yu Zhang and Xiasheng Guo
Nanjing University, CHINA

12:20 - 12:24 **GENERATION AND TRANSFER OF POLYDISPERSE DROPLETS USING LOW POWER SURFACE ACOUSTIC WAVES**
Krishnadas N. Nampoothiri, Niladri S. Satpathi, and Ashis K. Sen
Indian Institute of Technology, Madras, INDIA

12:24 - 12:28 **DROPLET IMPACT DYNAMICS ON HYDROPHOBIC AND SLIPPERY LIQUID-INFUSED POROUS SURFACES CONTROLLED BY PROPAGATING SURFACE ACOUSTIC WAVES**
Luke Haworth[1], Mehdi H. Biroun[1,2], Prashant Agrawal[1], Bethany Orme[1], Glen McHale[3], Mohammad Rahmati[1], Hamdi Torun[1], and Richard YongQing Fu[1]
[1]Northumbria University, UK, [2]University College London, UK, and
[3]University of Edinburgh, UK

Acoustofluidics
2021
26-27 August 2021
Virtual Conference

Intelligent Acoustofluidics for Engineering Human Brain Organoids

Hongwei Cai, Zheng Ao, and Feng Guo

Department of Intelligent Systems Engineering, Indiana University, Bloomington, IN 47405, United States
E-mail: fengguo@iu.edu

Abstract

Acoustofluidics, fusion of acoustics and microfluidics, offers a unique means to manipulate cells and handle liquids for broad applications in life sciences and medicine. However, challenges remain for current acoustofluidic devices and systems to maintain excellent performance due to a multiplicity of factors including device-to-device variation, manual operation conditions, environmental factors, sample-to-sample variability, etc. To address these challenges, we propose a new concept "intelligent acoustofluidics".[1] The conceptual system involves acoustofluidic device design, sensor fusion, and intelligent controller integration. The intelligent acoustofluidic system has a better performance in terms of automation, robustness, and accuracy, once comparing with current acoustofluidics. As a proof-of-concept application, we developed intelligent acoustofluidic systems for engineering human brain organoids.

Introduction

Acoustofluidics offer a unique means to manipulate cells and handle liquids by integrating acoustic waves into microfluidic devices or lab-on-a-chip systems.[2-5] For example, acoustic radiation force has been employed in microfluidics for the trapping, transportation, separation, sorting, and enrichment of cells.[6-9] Moreover, acoustic streaming has been utilized for liquid pumping, moving, and mixing [10, 11]. Acoustofluidics have unique features and advantages: (1) This method is biocompatible, and enables contactless and label-free manipulation; (2) Acoustofluidics devices are simple, compact, and inexpensive, and can be fabricated in a mass-producible fashion; (3) Acoustofluidic devices can be adopted into a portable and user-friendly system for portable and daily usage in the research lab or hospital. However, current acoustofluidic devices and systems have not yet fully exploit their translational potential, due to several hurdles including device-to-device variation, environmental and temporal factors, manual operation and intervention. There is an urgent need to develop automated and standardized acoustofluidic systems for basic research and translational applications in real-world settings.

Machine learning (ML) may shine news lights for improving current acoustofluidics because ML enables computer algorithms to learn from experience. Recent pioneer attempts are made to combine a variety of ML methods with microfluidic devices and lab-on-a-chip systems for broad applications in biomedical sciences and engineering.[12, 13] Recently, reinforcement learning (RL) method has been used for dynamic microfluidic system control.[14, 15] For example, a RL-based automated control system was developed for the precise regulation of dynamic laminar flow and microfluidic droplet generation.[14] Compared to manual operation, this RL-based system demonstrated a significant improvement in consistency, robustness, and repeatability during long-term experiments. Therefore, ML methods, especially RL algorithms, are promising to address the above-discussed acoustofluidic challenges.

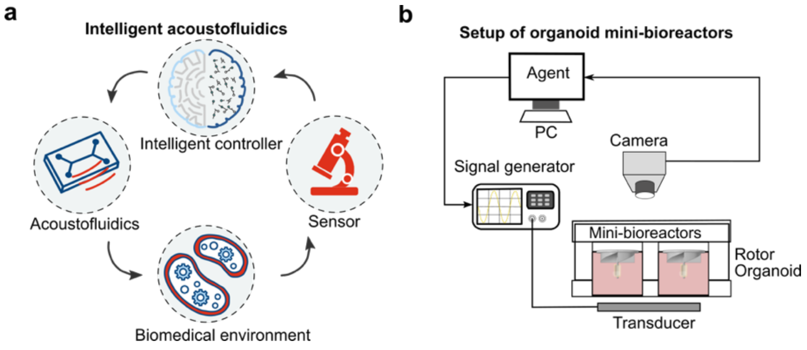

Figure 1: (a) "Intelligent Acoustofluidics" involve acoustofluidic device design, sensor fusion, and intelligent controller integration. The agent (RL controller) observes the biomedical environment through the sensors and outputs actions to the acoustofluidic devices based on the observations. The environment is actively driven by the actions of acoustofluidic devices, and a reward signal representing the quality of the action is returned based on the environmental changes. (b) Illustration of intelligent acoustofluidics for engineering human brain organoids.[1]

Results and Discussion

Herein, we report a conceptual system ‘intelligent acoustofluidics', which involves the development of automated systems with the support of acoustofluidic devices, sensors, and intelligent controllers to interact and learn from biomedical environments (**Figure 1a**). To improve organoid culture, we developed a system consisting of three components (**Figure 1b**): (1) rotors via an acoustic spiral phase plate (ASPP) regulated by RF signals, (2) a CCD camera to track rotational actions and collect dynamic data to the controller, and (3) an RL-based controller for tracking and closed-loop regulation of rotation of organoids/rotors. After training RL-based controller using simulation and experimental environments, our system can take in the observations (e.g., rotor rotational speed) from the camera and output actions (e.g., acoustic signals) to control rotor rational dynamics. By maximizing the rewards, our system can improve its performance and control the rotor at the desired rotational speed for improving organoid culture.

Conclusion

We introduce a novel concept of intelligent acoustofluidics. As a demonstration, we developed an intelligent acoustofluidic system for culturing human brain organoid. In the future, we believe the novel intelligent systems will offer excellent performance over active devices and advance fields of microfluidics, and biomedical systems.

References

[1] H. Cai, Z. Ao, Z. Wu, S. Song, K. Mackie, and F. Guo, “Intelligent acoustofluidics enabled mini-bioreactors for human brain organoids,” *Lab Chip,* vol. 21, no. 11, pp. 2194-2205, Jun 1, 2021.

[2] H. Bruus, J. Dual, J. Hawkes, M. Hill, T. Laurell, J. Nilsson, S. Radel, S. Sadhal, and M. Wiklund, “Forthcoming Lab on a Chip tutorial series on acoustofluidics: Acoustofluidics—exploiting ultrasonic standing wave forces and acoustic streaming in microfluidic systems for cell and particle manipulation,” *Lab on a Chip,* vol. 11, no. 21, pp. 3579-3580, 2011.

[3] J. Friend, and L. Y. Yeo, “Microscale acoustofluidics: Microfluidics driven via acoustics and ultrasonics,” *Reviews of Modern Physics,* vol. 83, no. 2, pp. 647-704, 06/20/, 2011.

[4] A. Ozcelik, J. Rufo, F. Guo, Y. Gu, P. Li, J. Lata, and T. J. Huang, “Acoustic tweezers for the life sciences,” *Nature Methods,* vol. 15, no. 12, pp. 1021-1028, 2018/12/01, 2018.

[5] M. Wiklund, R. Green, and M. Ohlin, “Acoustofluidics 14: Applications of acoustic streaming in microfluidic devices,” *Lab Chip,* vol. 12, no. 14, pp. 2438-51, Jul 21, 2012.

[6] F. Guo, Z. Mao, Y. Chen, Z. Xie, J. P. Lata, P. Li, L. Ren, J. Liu, J. Yang, M. Dao, S. Suresh, and T. J. Huang, “Three-dimensional manipulation of single cells using surface acoustic waves,” *Proc Natl Acad Sci U S A,* vol. 113, no. 6, pp. 1522-7, Feb 09, 2016.

[7] A. Marzo, and B. W. Drinkwater, “Holographic acoustic tweezers,” *Proceedings of the National Academy of Sciences,* vol. 116, no. 1, pp. 84, 2019.

[8] N. Garg, D. Boyle, A. Randall, A. Teng, J. Pablo, X. Liang, D. Camerini, and A. P. Lee, “Rapid immunodiagnostics of multiple viral infections in an acoustic microstreaming device with serum and saliva samples,” *Lab on a Chip,* vol. 19, no. 9, pp. 1524-1533, 2019.

[9] Z. Ao, H. Cai, Z. Wu, J. Ott, H. Wang, K. Mackie, and F. Guo, “Controllable Fusion of Human Brain Organoids Using Acoustofluidics,” *Lab on a Chip*, 2021.

[10] S. Weydert, S. Girardin, X. Cui, S. Zürcher, T. Peter, R. Wirz, O. Sterner, F. Stauffer, M. J. Aebersold, S. Tanner, G. Thompson-Steckel, C. Forró, S. Tosatti, and J. Vörös, “A Versatile Protein and Cell Patterning Method Suitable for Long-Term Neural Cultures,” *Langmuir,* vol. 35, no. 8, pp. 2966-2975, 2019/02/26, 2019.

[11] Y. Gao, M. Wu, Y. Lin, W. Zhao, and J. Xu, “Acoustic bubble-based bidirectional micropump,” *Microfluidics and Nanofluidics,* vol. 24, no. 4, pp. 1-10, 2020.

[12] J. Riordon, D. Sovilj, S. Sanner, D. Sinton, and E. W. K. Young, “Deep Learning with Microfluidics for Biotechnology,” *Trends in Biotechnology,* vol. 37, no. 3, pp. 310-324, 2019/03/01/, 2019.

[13] S. Momtahen, F. Al-Obaidy, and F. Mohammadi, "Machine Learning with Digital Microfluidics for Drug Discovery and Development." pp. 1-6.

[14] O. J. Dressler, P. D. Howes, J. Choo, and A. J. deMello, “Reinforcement Learning for Dynamic Microfluidic Control,” *ACS Omega,* vol. 3, no. 8, pp. 10084-10091, 2018/08/31, 2018.

[15] K. Latifi, A. Kopitca, and Q. Zhou, “Model-Free Control for Dynamic-Field Acoustic Manipulation Using Reinforcement Learning,” *IEEE Access,* vol. 8, pp. 20597-20606, 2020.

Acoustofluidics 2021
26-27 August 2021
Virtual Conference

Acoustically excited channel walls for microbiological applications

Michael Gerlt[1], Nino Läubli[2], Peter Ruppen[3], Moritz Leuthner[1], Michel Manser[1],
Alexander Wüthrich[2], Bradley Nelson[2], Sven Panke[3], and Jürg Dual[1]

[1]Mechanics and Experimental Dynamics, D-MAVT, ETH Zürich, Zürich, Switzerland
E-mail: gerlt@imes.mavt.ethz.ch, URL: http://www.expdyn.ethz.ch
[2]Multi-Scale Robotics Lab, D-MAVT, ETH Zürich, Zürich, Switzerland
[3]Bioprocess Laboratory, D-BIOL, ETH Zürich, Basel, Switzerland

ABSTRACT

This work presents a novel concept for acoustofluidic cell manipulation: thin vibrating channel walls. Improved etch recipes enable us to produce thin walls between two microfluidic channels, fabricated in silicon or via PDMS casting, that can be used for challenging microbiological applications. We demonstrate the medium exchange for bacteria utilised for transformation, single-cell rotation for 3D imaging, and rapid fluid mixing.

Introduction

Manipulation of cells in microfluidic systems is highly relevant for various microbiological applications. In this work, we present a novel device design based on thin vibrating channel walls, enabling us to tackle several research challenges simultaneously. First, we developed novel etch recipes allowing us to produce slim structures down to a depth of 200 µm and reducing the etch lag to below 1.5% [1]. Then, we utilised these improved etch recipes to fabricate two microfluidic channels close together leading to a thin channel wall that can be excited by acoustic waves. We utilised these channel wall vibrations for bacteria trapping and successive medium exchange [2], single-cell rotation and rapid fluid mixing [3].

Experimental

The devices are produced in a standard cleanroom environment. A piezoelectric element (piezo) matched to the resonance of the thin wall in between the microfluidic channels is glued to the devices and connected to a wave generator and power amplifier for excitation. We utilised E. Coli bacteria (~2 µm length, ~1 µm diameter), polystyrene particles (10 µm diameter), and HeLa cells (~ 15 µm diameter) for the experimental verification. For our numerical investigations we used the FEM software COMSOL Multiphysics.

Results and Discussion

By acoustically exciting a 13 µm wide silicon wall located between 180 µm deep water and air-filled channels with a frequency of 1.8 MHz, we can trap bacteria (Fig. 1). The trapping at the wall occurs due to the generation of a Gor'kov potential minimum at the wall and streaming rolls that exhibit a point of coalescence (Fig. 2). Our acoustofluidic chip is capable of retaining 47 ± 3% of the bacteria at a flow rate of 10 μL min^{-1}. After trapping, the cells are transferred from culture medium into deionized water, allowing us to electrically shock them (electroporation) to deliver exogenous genetic material into the bacterial cell (transformation). With this approach, we achieved a transformation efficiency of $8\text{x}10^5$ CFU per µg of plasmid DNA [2], presenting a significant step towards automated genome engineering.

The same design concept can be applied to perform particle attraction, single-cell rotation, and microfluidic mixing in a PDMS device, exhibiting a wall thickness $T = 5$ µm and a height $H = 50$ µm (Fig. 3), thereby resembling an embedded microbubble. The wall is excited at 70 kHz, leading to a Gor'kov potential minimum at the thin wall and one streaming vortex filling the entire channel height (Fig 4). At an excitation voltage of 3 V_{PP}, HeLa cells can be rotated at a steady speed of 8 rpm, a task crucial for 3D cell imaging. Finally, multiple vibrating walls can be utilised for rapid fluid mixing. At an excitation voltage of 20 V_{PP}, the average mixing time and length were 376 ms and 800 µm, respectively [3].

Conclusion

In this work, we present a novel acoustofluidic concept capable of addressing various essential microbiological tasks such as bacteria trapping, single-cell rotation, and microfluidic mixing. The high flexibility of the device concept - functioning in various materials and frequency ranges - renders the concept highly interesting for a wide range of fields, especially but not limited to microbiology.

References

[1] M.S. Gerlt, N.F Läubli, M. Manser, B.J. Nelson, J. Dual, Micromachines 2021, 12, 542.
[2] M.S. Gerlt, P. Ruppen, et al., submitted to LOC, preprint: 10.26434/chemrxiv.14564529.v1.
[3] N.F. Läubli, M.S. Gerlt, et al., submitted to Analytical Chemistry, preprint: 10.26434/chemrxiv.14252393.v1

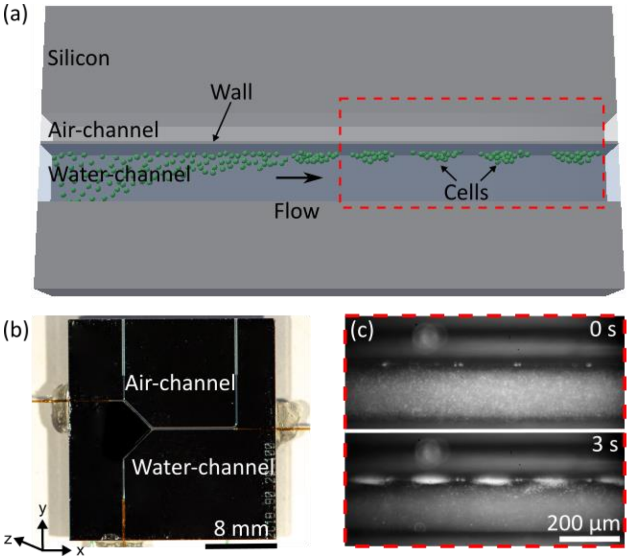

Figure 1: (a) Sketch of the device (not to scale). (b) Photograph of the acoustofluidic device. A piezoelectric element is glued underneath the device. (c) Micrograph series of bacteria trapping. Upon excitation of the piezo with a frequency of 1.7 MHz and 46 V_{PP}, the E.coli bacteria (in white) were pressed against the channel wall.

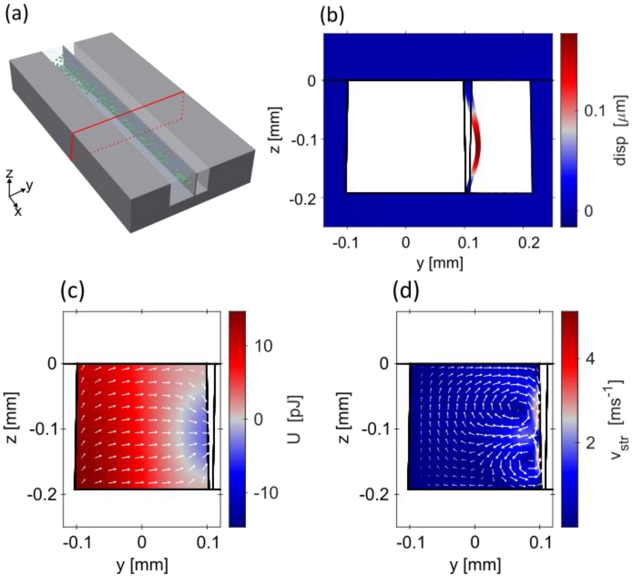

Figure 2*:* Numerical modelling of the silicon device. (a) Sketch of the device with a red plane indicating the cross-section used for device simulations. Numerical results of the (b) exaggerated displacement, revealing a bending mode of the channel wall, (c) Gor'kov potential with acoustic radiation force (white arrows), indicating that cells are attracted to a position at half the height of the channel wall, and (d) streaming velocity with streaming field (white arrows), indicating that cells are trapped at a position at half the height of the channel wall, which has been experimentally verified. All simulations were carried out at an excitation frequency of 1.8 MHz.

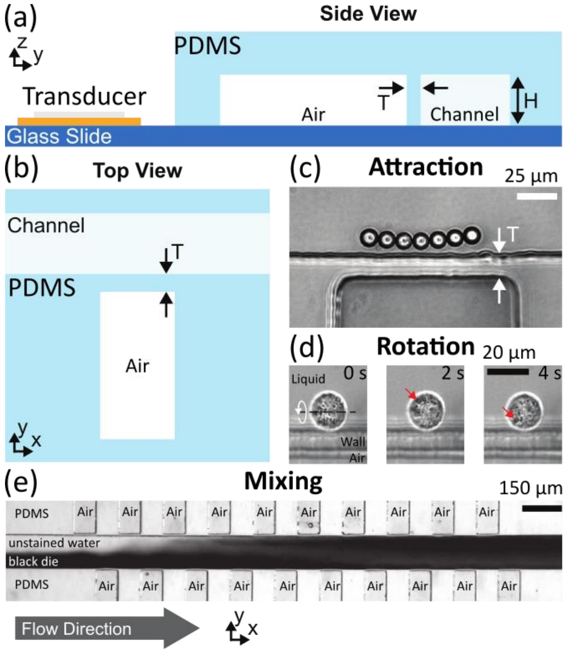

Figure 3: Sketch of the (a) side and (b) top view of the device design in PDMS. (c) Attraction to the thin wall, (d) controlled rotation of a HeLa cell with 15 µm diameter close to the thin wall, and (e) rapid microfluidic mixing, using multiple thin walls. The devices exhibit a height H = 50 µm and a wall thickness T = 5 µm.

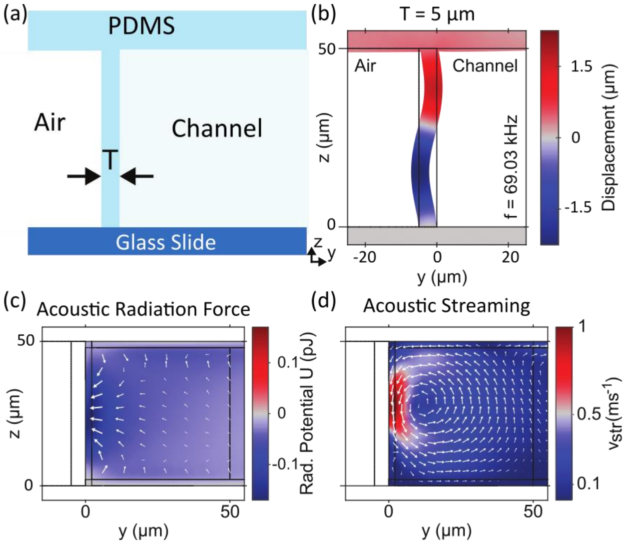

Figure 4: Numerical modelling of the PDMS device. (a) Zoom of the device's side view sketch. Numerical results of the (b) displacement, (c) Gor'kov potential with acoustic radiation force (white arrows), and (d) streaming velocity with streaming field (white arrows) at an excitation frequency of 69 kHz. The thin wall exhibits an S-shaped bending mode with a displacement node at half the height of the wall, to which particles are attracted, as can be seen in the results for the acoustic radiation force. Further, a streaming vortex is generated, which can be used for particle and cell rotation (see Fig. 3 (d)).

Acoustofluidics 2021
26-27 August 2021
Virtual Conference

Selecting the optimal buffer for acoustic particle separation

Thierry Baasch[1], and Thomas Laurell[1]

[1]Department of Biomedical Engineering, Lund University, Lund, Sweden
E-mail: Thierry.Baasch@bme.lth.se

Introduction

We theoretically investigate how the buffer can be tuned to maximize the acoustic separation efficiency. In their experimental study, Urbansky et al. [1] enriched mononuclear cells from blood using acoustophoresis. This separation was impossible in water due to a large overlap of acoustic mobilities of the mononuclear and red blood cells. However, the separation is possible in stock isotonic Percoll (SIP) solution of 70% or higher. The buffer can be tuned, and selecting the correct buffer is crucial to obtain high separation efficiencies. In this work, we investigate the optimal buffer selection theoretically.

Methods and theory

We focus our investigation on the acoustic particle separation done in a lab-on-a-chip device as shown in Fig. 1a [1]. The particles enter the device through the prefocusing chamber where the λ mode is used to concentrate all the particles into small pre-focused bands. The band then enter the separation channel where the different species are displaced by acoustic forces. If the device is tuned correctly then one species exits through the center outlet while the other exits through the side outlet.
We describe the dynamics of a particle inside the separation channel by the following ordinary differential equations

$$v_y = -\frac{2ka^2\Phi E_{\mathrm{ac}}}{3\eta}\sin 2ky, \quad v_x = A\sum_{n\ \mathrm{odd}}^{\infty}\left({}^{1}\!/_{n^3}\left[1-\frac{\cosh\left({}^{n\pi y}\!/_{h}\right)}{\cosh\left({}^{n\pi w}\!/_{2h}\right)}\right]\right)\sin\left({}^{n\pi z}\!/_{h}\right), \tag{1}$$

$$A = \frac{48Q}{\pi^3\,(hw)\,(1-0.63({}^{h}\!/_{w}))}, \tag{2}$$

where we used the total flowrate Q, the acoustic contrast factor Φ, the wavenumber k, the particle radius a, the fluid viscosity η, the acoustic energy density E_{ac}, the particle velocities in x and y direction v_x and v_y, respectively, the channel height h and the channel width w. The differential equations can be reformulated to be independent of the time and then solved by separation of the variables, which yields

$$L\cdot B = F(y_0, y_e), \quad F(y_0, y_e) = \int_{y_0}^{y_e}\sum_{n\ \mathrm{odd}}^{\infty}\left\{\left({}^{1}\!/_{n^3}\left[1-\frac{\cosh\left({}^{n\pi y}\!/_{h}\right)}{\cosh\left({}^{n\pi w}\!/_{2h}\right)}\right]\right)\frac{\sin\left({}^{n\pi}\!/_{2}\right)}{\sin\left({}^{2\pi y}\!/_{w}\right)}dy\right\} \tag{3}$$

$$B = -\,\Phi a^2\alpha\frac{\pi}{w}\frac{\pi^3\,(hw)\,(1-0.63\,({}^{h}\!/_{w}))}{24\cdot 3}, \quad z = {}^{h}\!/_{2}, \quad k = {}^{\pi}\!/_{w}, \quad \alpha = \frac{E_{\mathrm{ac}}}{Q\eta}, \tag{4}$$

where L denotes the length of the separation channel, y_0 and y_e are the lateral positions at the inlet and outlet of the separation channel, respectively. This allows a graphical solution of the particle lateral position at the outlet of the separation channel (Fig. 1b). A good separation is achieved when the lateral distance between the species is large at the outlet. Of course, α can be tuned to a certain degree, or at least made smaller if a smaller driving voltage is applied. It is thus sufficient to theoretically investigate the maximal lateral distance between the species inside the channel for a maximal applied voltage.

In practice, the species have ranges of material properties and the optimal separation can only be solved computationally. To investigate the separation performed by Urbansky et al. [1], we modelled the red blood cells to have a density $\rho = 1100\,\mathrm{kg\,m^{-3}}$, compressibility $\kappa = 334\,\mathrm{TPa^{-1}}$ and diameter between $7\,\mu\mathrm{m}$ to $8\,\mu\mathrm{m}$ [1–2]. The mononuclear cells were modelled to have density $\rho = 1054\,\mathrm{kg\,m^{-3}}$, compressibility $\kappa = 393\,\mathrm{TPa^{-1}}$ and diameter between $6\,\mu\mathrm{m}$ to $20\,\mu\mathrm{m}$ [1–2]. The E_{ac} was set to $100\,\mathrm{Pa}$

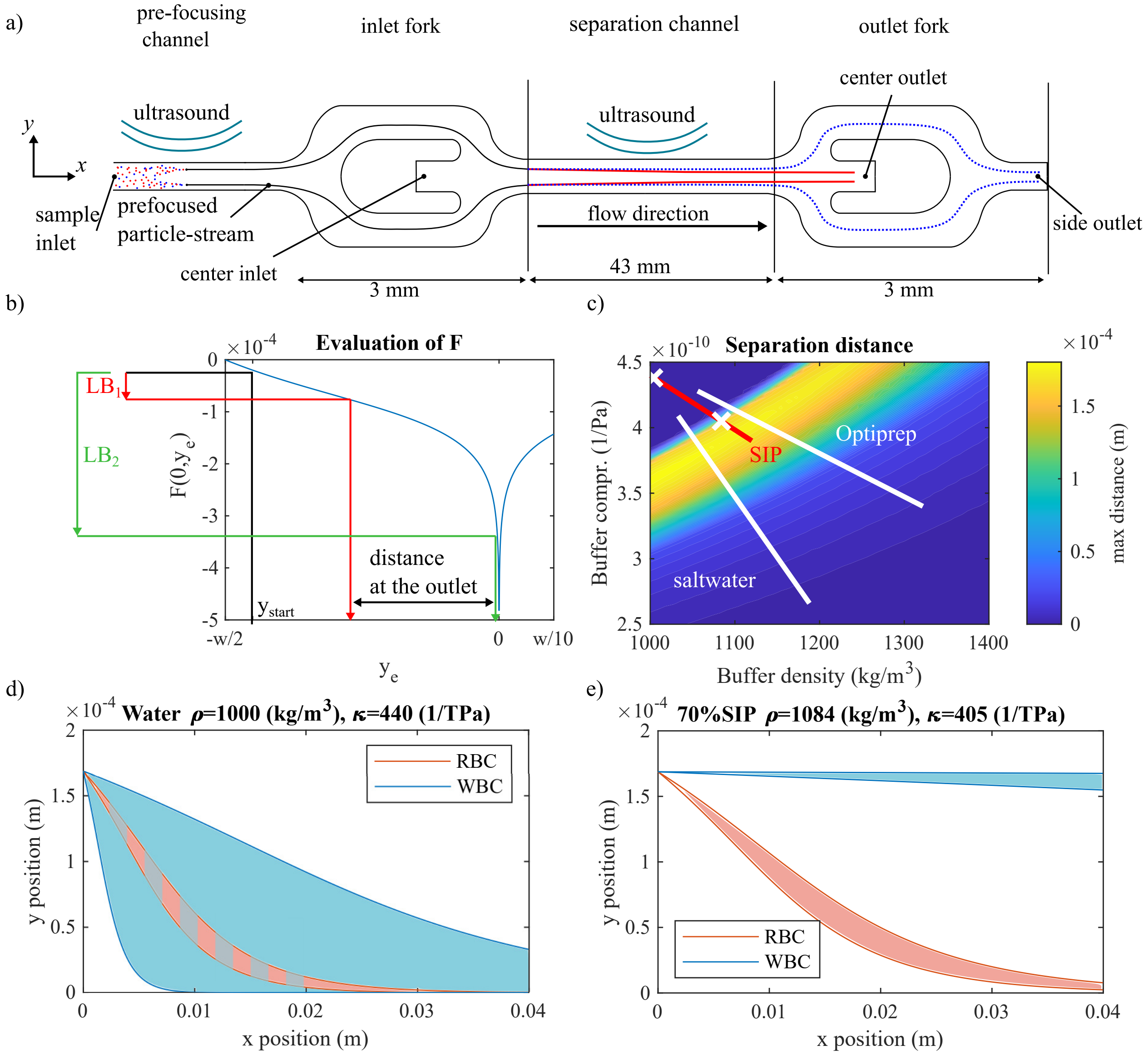

Figure 1: a) Acoustic separation device, b) Graphical solution of the particle dynamics, c) SIP dilutions used by Urbansky et al. [1], red line. Water and 70% SIP denoted by white crosses). White lines indicates max. separation distance in salt water and Optiprep at different concentrations , d, e) separation of mononuclear cells (WBC) from red-blood cells (RBC) in water and 70% SIP, respectively.

and the flowrate to $400\,\mu\mathrm{L\,min}^{-1}$. Under these conditions, we investigated the maximal separation distance throughout the whole separation channel (Fig. 1c). We found that water performs poorly (top left cross Fig. 1c and Fig. 1d), while 70% SIP leads to a nice separation (lower right cross Fig. 1d and Fig. 1e). Furthermore, Urbansky et al. [1] stated in their work that, even though the separation was still successful, it worked less well for very high SIP concentrations, which is confirmed in Fig. 1c.

Conclusion

In this project, we are investigating the buffer choice to optimize the acoustic particle separation. To this end, we apply both numerical and analytical methods, consider the range of material properties of the samples and the possibility to tune the actuation voltage. Our results agree with the experimental findings by Urbansky et al. [1].

References

[1] A. Urbansky, P. Ohlsson, A. Lenshof, F. Garofalo, S. Scheding, and T. Laurell. Scientific reports **7**, 1–9 (2017).
[2] K. W. Cushing, F. Garofalo, C. Magnusson, L. Ekblad, H. Bruus, and T. Laurell. Analytical chemistry **89**, 8917–8923 (2017).

Acoustofluidics 2021
26-27 August 2021
Virtual Conference

Acoustic radiation force on elastic microbeads experiencing resonant spheroidal vibrations in a viscous fluid

Amir Tahmasebipour[1], Matthew R. Begley[1,2], and Carl D. Meinhart[1]

[1] Department of Mechanical Engineering, University of California Santa Barbara, Santa Barbara, CA, USA
E-mail: atahmasebipour@uucsb.edu, URL: https://sites.engineering.ucsb.edu/~microflu/
[2] Materials Department, University of California Santa Barbara, Santa Barbara, CA, USA

Introduction

Acoustophoresis is established as a robust, gentle and label free active method of microparticle manipulation by using ultrasound in microfluidic devices [1]. In an efficient acoustofluidic device, strong resonant acoustic fields are necessary to generate enough energy density in the small fluidic channels [2]. The acoustic field in the fluid is scattered from and transmitted through any suspended particle and due to the non-linear physics of fluids it gives rise to the so-called Acoustic Radiation Force (ARF). Accurate calculation of forces acting on particles is required for effective control, therefore, ARF has been studied analytically for various particle sizes with respect to the acoustic wavelength and thermo-viscous boundary layers, δ_t and δ_v, in a viscous fluid [3]. Similar to the harmonic pressure field in the channel, the scattered acoustic field from the particle is a result of the fluid-structure interaction at the vibrating particle walls. Therefore, it is logical to pay attention to the existing research focused on different modes and characteristics of resonant vibrations of a spherical particle are studied [4, 5]. In this work, first we use a damped, 3D numerical model of a single elastic particle to show spheroidal and breathing eigenmodes of a freely vibrating sphere and explore the effects of solid mechanical properties on the eigenfrequencies. We then extend our simulation to include a suspended particle in a viscous fluid with a standing half wave background field to analyze the scattered acoustic pressure as the particle goes through a vibrational resonance. We note that the effects of these resonant motions cause meaningful fluctuations in the acoustic energy, damping and ARF affecting the microparticle.

Theory

The physics of the fluid and solid domains are governed by a perturbation theory analysis of the Navier-Stokes and linear solid mechanics equations, respectively [2-3]. Naturally, momentum transfer between a sound field and an object give rise to the ARF generalized by acoustic contrast factor Φ and the time-averaged pressure $\langle p^2\rangle$ and velocity $\langle v_i v_i\rangle$ fields as $\mathbf{F}^{\mathrm{rad}} = -\boldsymbol{\nabla} U^{\mathrm{rad}}$, attracting the particles to the minima of the potential field,

$$U^{\mathrm{rad}} = \frac{4}{3}\pi a^3\left[f_1\frac{\kappa_{\mathrm{fl}}}{2}\langle p^2\rangle - f_2\frac{3\rho_{\mathrm{fl}}}{4}\langle v_i v_i\rangle\right] \text{ and } \Phi = \frac{f_1}{3} + \frac{f_2}{2}, \tag{1}$$

where f_1 is the monopole and f_2 is the dipole acoustic scattering coefficient for particles with radius a, suspended in a fluid of density ρ_{fl} and compressibility κ_{fl}. From a numerical simulation of a finite sized particle in a background pressure field, the radiation force is calculated by integrating the kinetic, hydrostatic and convective momentum fluxes on S, the unperturbed surface of the particle [3],

$$F_{\mathrm{num}}^{\mathrm{rad}} = \int_S \left(\frac{\rho_{\mathrm{fl}}}{2}\langle v_i v_i\rangle \boldsymbol{n} - \frac{\kappa_{\mathrm{fl}}}{2}\langle p^2\rangle\boldsymbol{n} - \rho_{\mathrm{fl}}(\boldsymbol{n}\cdot v_i)v_i\right) dS, \tag{2}$$

where $\boldsymbol{n}$ is the normal vector out of the particle. The resonant frequency of the breathing mode of a freely vibrating sphere is found by solving the following equation [5],

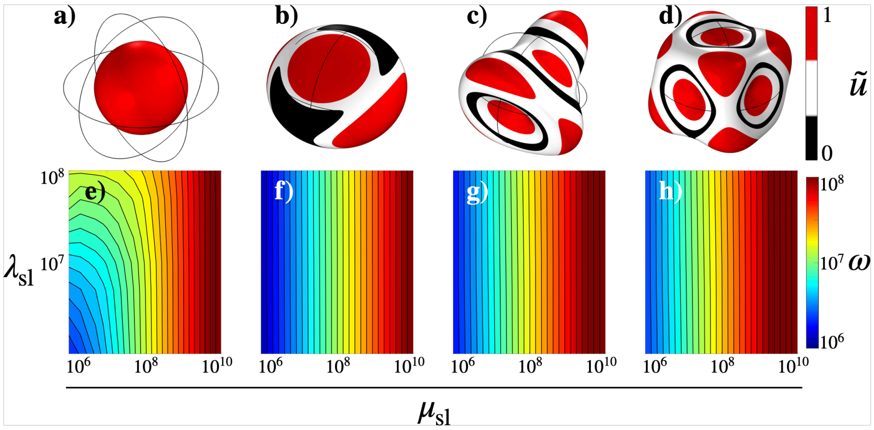

Figure 1: Normalized displacement field of a sphere under (a) the first breathing mode (b)-(d) three fundamental spheroidal modes. (e)-(g) Logarithmic contour maps of the angular frequency corresponding to breathing and spheroidal modes shown in (a)-(d), respectively. The contour maps show angular frequency of resonant vibration with respect to the first (λ^{sl}) and second (μ^{sl}) Lamé parameters.

$$\frac{\gamma_\mathrm{s}\, a}{\tan(\gamma_\mathrm{s}\, a)} = 1 - \frac{\gamma_\mathrm{s}^2\, a^2}{4}\left(\frac{c_\mathrm{l}}{c_\mathrm{t}}\right)^2 \text{ where } \gamma_\mathrm{s} = \frac{\omega}{c_\mathrm{l}}, \tag{3}$$

while c_l and c_t are the longitudinal and transverse speeds of sound in the solid. A streamlined look at the spheroidal modes reveals that their angular frequency is closely related to the latter $\omega \sim 2\pi\, c_\mathrm{t} a^{-1}$.

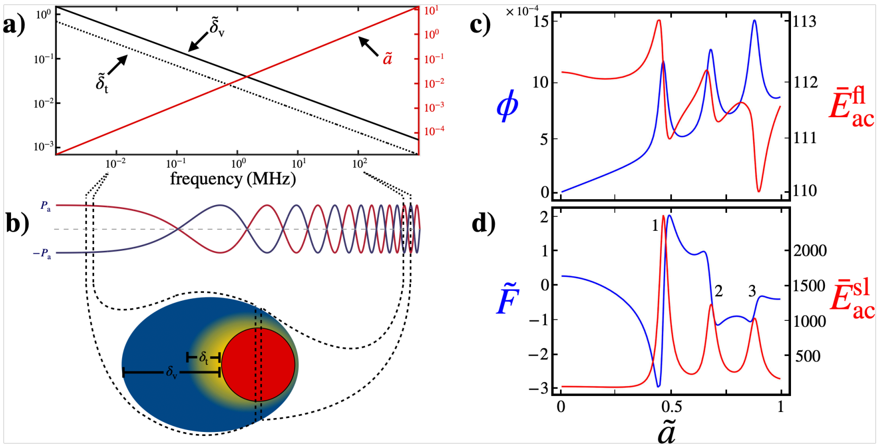

Figure 2: (a) Frequency variation of relative thermal and viscous BL with respect to radius a on the left and relative particle size to wavelength on the right. (b) Change in qualitative standing wavelength and BL with respect to a constant size particle as the frequency increases from left to right. (c) Changes of numerically calculated damping factor ϕ (blue) and average fluid acoustic energy density (red) and (d) ARF deviation from theory $\tilde{F}$ (blue) and average solid acoustic energy density (red) with increasing radius ratio $\tilde{a}$ for a 10 μm radius polystyrene particle.

Results and discussion

In Fig. 1, various mode shapes of harmonic vibrations of a sphere are presented. Breathing and spheroidal modes, due to particle surface displacement, contribute to the acoustic scattering whereas torsional resonant modes leave the surface unperturbed and therefore are not included in this work. For some solid particle materials of interest to acoustophoresis the lowest spheroidal resonance frequency falls within the MHz range. For example, polystyrene in water is chosen to be studied in a frequency range where the thermal and viscous boundary layers are small relative to the particle radius and the ideal fluid approximation is valid (Fig. 2a & b)[3]. As the actuation frequency increases, a 10 μm polystyrene sphere undergoes resonant vibrational modes. The first resonant peak shown in Fig. 2d corresponds to the vibrational mode of Fig. 1b and is signified by a notable increase in acoustic energy density in the solid. Approaching and crossing this peak, causes a significant deviation from small particle ARF predictions that is displayed as $\tilde{F} = {F^\mathrm{rad}}^{-1}(F_\mathrm{num}^\mathrm{rad} - F^\mathrm{rad})$. A similar trend to the solid energy is seen in the overall damping factor ϕ since the viscous energy loss is directly related to the particle wall velocity and displacement (Fig. 2c) [6]. For the purpose of acoustophoresis it is desired to keep the particle sizes within the range of manipulation which for a standing wave is limited to half a wavelength. This idea motivates the chosen range of frequencies in this study.

As the larger $\tilde{a} = 2a\lambda^{-1}$ are investigated peaks 2 and 3 show up corresponding to higher modes of spheroidal vibrations displayed in Fig. 1c & d. In all cases, the acoustic energy density in the fluid is impacted by the scattered fields from the particle. This quantity is shown to increase and decrease across a particle resonance based on the constructive and destructive superposition of the background and scattered acoustic pressure.

Conclusion

We have used 3D numerical simulations to estimate and characterize microsphere resonant vibrations in a viscous fluid. We found that resonances of an elastic sphere can heavily impact the scattered acoustic field, viscous damping and acoustic radiation force experienced by the microparticle when excited at frequencies relevant to acoustophoresis applications. These results show an abrupt change, and in some cases reversal, of ARF behavior of microbeads. These findings are of significant value to fields that are focused on manipulating soft elastic particles in acoustofluidic devices, such as, life sciences, bio 3D printing and cell sorting.

References

[1] P. Augustsson, C. Magnusson...and T. Laurell. Anal. Chem., **84**, 7954-7962 (2012)
[2] A. Tahmasebipour, L. Friedrich, M. Begley, H. Bruus, C. Meinhart. J. Acoust. Soc. Am., **148**, 359-373 (2020)
[3] J. T. Karlsen and H. Bruus. Phys. Rev. E., **92**, 043010 (2015)
[4] L. Saviot. J. Phys. Chem. B, **111**, 7457-7461 (2007)
[5] V. Galstyan, O. Pak and H. Stone. Phys. Of Fluids, **27**, 032001 (2015)
[6] P. Hahn, J. Dual. Phys. Fluids, **27**, 062005 (2015)

Acoustofluidics 2021
26-27 August 2021
Virtual Conference

Contactless Additive Manufacturing using Acoustic Levitation

Iñigo Ezcurdia[1], Rafael Morales[2], Marco A. B. Andrade[3] and Asier Marzo[1]

[1]UpnaLab, Public University of Navarre, 31006 Pamplona, Spain
E-mail: inigofermin.ezcurdia@unavarra.es, URL: https://upnalab.com/inigo-ezcurdia-phd/
[2]UltraLeap Ltd, Bristol BS2 0EL, UK
[3]Institute of Physics, University of São Paulo, São Paulo 05508-090, Brazil

Introduction

Acoustic Levitation can hold and manipulate multiple small objects of different materials without direct contact [2]. Beads, threads, and fabric have been used as levitation primitives for the assembly of tangible and articulated levitated structures[3][1]. Here, we show how acoustic levitation could be used for contactless additive manufacturing using spherical particles and elongated segments as the building parts. To enable this, a novel algorithm to manipulate elongated segments in position and orientation will be developed. We explore how the building parts can be assembled with pre-applied adhesive, adhesive added during the manufacturing process, two-part adhesives and melting or welding. We will evaluate the suitability of using two opposed arrays, three arrays placed in a triangle, or four arrays placed orthogonally as a way to place particles around the piece that is being manufactured. We highlight the reduction of cross-contamination, the capability to manufacture inside closed containers from the outside, the support of multiple materials on different phases and the removal of the need for supports. These techniques can be leveraged for the microfabrication of electromechanical components and in-vivo additive manufacturing.

Additive manufacturing with levitated particles

We plan to design an additive manufacturing method involving several particles. This method sticks particles together on a static foundation that is inside the construction volume. Multiple particles will be manipulated by acoustic levitation and placed on the foundation, to construct a complex piece particle by particle (bottom row of Figure 1). It is necessary to consider the presence of the piece being manufactured as an obstacle in the domain that will scatter sound and interfere with the acoustic levitation. Different arrangements will be checked to understand to what degree is possible to trap particles around obstacles and corners.

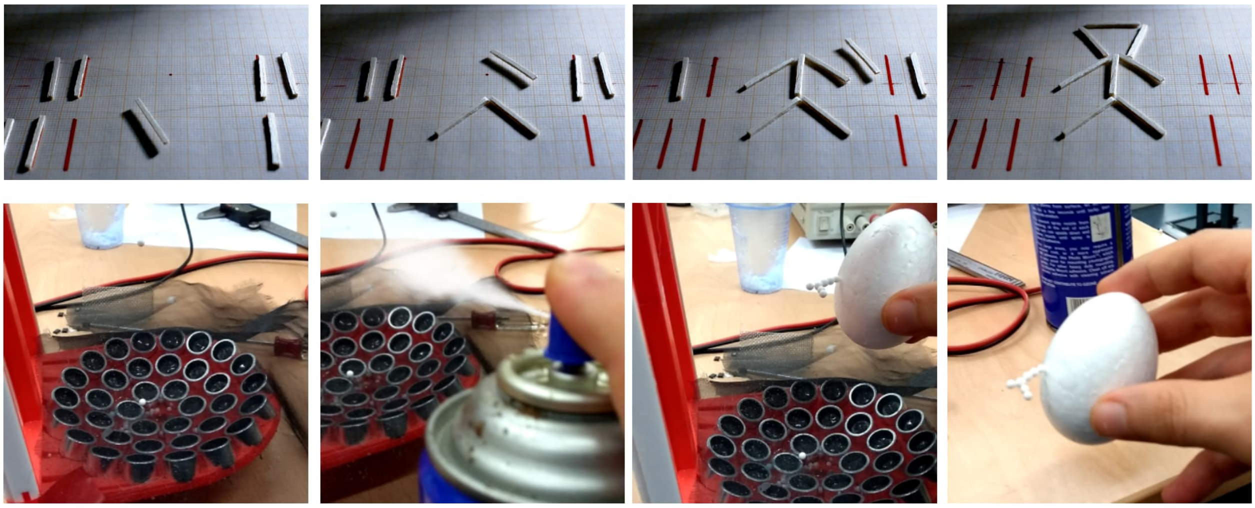

Figure 1: Top) Assembly process levitating individual sticks. Each stick is levitated, rotated, and positioned individually to build a stick-person. Bottom) Levitating particles are sprayed with glue, moved and stack, a big sphere is use as a fundation.

Adhesion techniques

Beads and elongated segments must be attached together to obtain a final solid piece. We propose four different techniques to adhere beads and segments together. In the first technique, we place a bead in the trap and then spray it with glue, then the bead is moved into its target position and attached to the ongoing piece, some time is left for letting the glue dry, this process is repeated for each sphere that composes the final piece (Figure 1.bottom). For the second technique, beads and sticks will be soaked with glue on specific areas before being introduced into the construction volume. For our third approach, two-component adhesives will be used, two droplets will be levitated and mixed in mid-air before being translated into the target area in the piece. For the fourth technique, we use a focused heat source such as a laser or halogen lamp to melt or fuse together elements in contact.

Torque on elongated segments

We expect to use elongated segments as an additional construction primitive. Lightweight wooden sticks can be levitated, translated, and rotated using one phased array over a reflective surface (Figure 1). We aim to extend this manipulation technique to provide 6 DoF manipulation: 3 axis translation and 3 axis rotation. The sticks can be attached to other particles or sticks. With simulations we have seen that the torque generated on a stick can be approximated by the torque generated on a series of joined spheres (Figure 2), making the optimization problems considerably simpler.

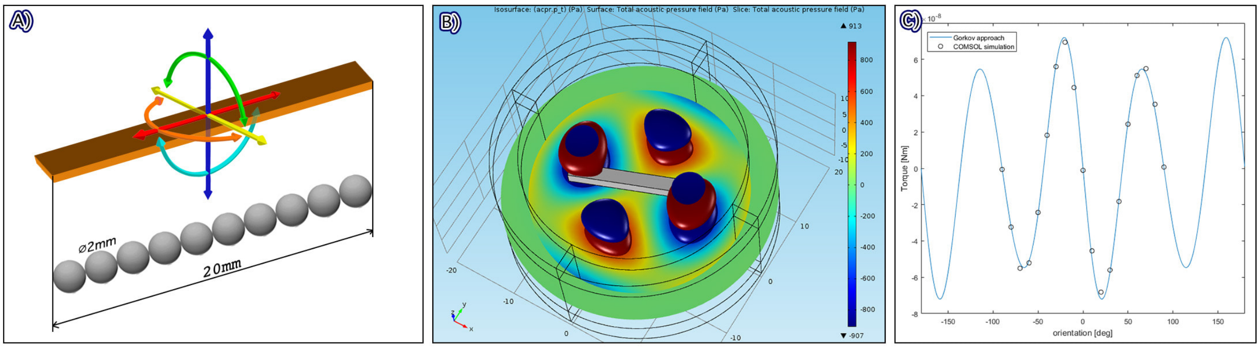

Figure 2: A) In the top a solid stick is shown and on the bottom its approximation as a series of discrete spheres. B) Incident acoustic field and a solid stick inside C) Simulation of the torque depending on the orientation of the stick: solid line is the approximation by spheres, the hollow circles are the simulation of a solid stick using COMSOL multi-physics. Good agreement was found and for both torque was converging.

Arrangements of the Phased Arrays

Three different arrangements will be evaluated to understand to what degree is possible to trap and manipulate particles around the piece that is being built inside the levitator.

When using two opposed arrays we expect limitations to place a bead above or below a solid piece that is being built, as these areas are completely occluded from the sound emitters despite diffraction. These limitations can be mitigated by using three arrays placed in a triangular shape. Finally, four arrays will be placed orthogonally. In this case, the entire construction volume will remain reachable for the beads and elongated segments.

References

[1] Andreas Rene Fender, Diego Martinez Plasencia, and Sriram Subramanian. Articulev: An integrated self-assembly pipeline for articulated multi-bead levitation primitives. In *Proceedings of the 2021 CHI Conference on Human Factors in Computing Systems*, pages 1–12, 2021.

[2] Asier Marzo and Bruce W Drinkwater. Holographic acoustic tweezers. *Proceedings of the National Academy of Sciences*, 116(1):84–89, 2019.

[3] Rafael Morales, Asier Marzo, Sriram Subramanian, and Diego Martínez. Levipropos: Animating levitated optimized fabric structures using holographic acoustic tweezers. In *Proceedings of the 32nd Annual ACM Symposium on User Interface Software and Technology*, pages 651–661, 2019.

Acoustofluidics
2021
26-27 August 2021
Virtual Conference

On-demand droplet generation using bulk acoustic wave

E. Hemachandran[1], T. Laurell[2], and A. K. Sen[1]

[1]Department of Mechanical Engineering, Indian Institute of Technology Madras, Chennai, India
E-mail: hemachandranw@gmail.com, URL: http://www.ashislab.in/
[2]Department of Biomedical Engineering, Lund University, Lund, Sweden

Introduction

On-demand droplet generation from continuously flowing fluid has profound applications in rare event encapsulation studies. The active droplet generation is very much essential when the job is to produce droplets at a specific time. For droplet generation, surface acoustic wave (SAW) devices have been explored for both on-demand generation[1], and size control[2], but bulk acoustic wave (BAW) devices have not been explored yet. Here, we demonstrate on-demand droplet generation from co-flowing fluids using BAW. Our experimental observations reveal that in order to generate droplets from continuously flowing fluids; First, the system must be maintained in the acoustic relocation conditions (configuration must be acoustically unstable and $C_{ac} \gg 1$). Second, interfacial tension must exceed the viscous force of the co-flowing phases.

Theory

When two fluids of miscible nature (no interfacial tension between them) flows in a microchannel due to low Reynolds number flows, the element of instability and non-linearity is not present. However, for a fluid of immiscible nature, the interfacial tension can introduce non-linearity and instability. Acoustic relocation was observed for fluids of miscible nature, even with a 0.1% difference in impedance between the flowing fluids[3]. However, in the case of immiscible fluids, acoustic relocation was only observed once the acoustic radiation force acting at the immiscible interface exceeds the interfacial tension between the co-flowing fluids[4,5]. The acoustic capillary number $(\mathrm{C_{ac}})$ which characterizes the competition between interfacial tension and acoustic radiation force is defined as $C_{ac} = F_{ac}/F_{int} \sim E_{ac}\Delta\hat{z}\,\mathrm{w}/\gamma$, where E_{ac} is the acoustic energy density, $\Delta\hat{z}$ is the impedance contrast between the fluids, w is the width of the microchannel, γ is the interfacial tension between the fluids.

On-demand droplet generation from co-flowing fluids is illustrated in Figure 1. Co-flowing fluids between the aqueous and oil phase were established. The acoustic standing wave is created inside the microchannel by attaching the piezoelectric transducer beneath the microchannel. The standing wave generates an acoustic radiation force at the immiscible fluid interface, which moves the high impedance stream (aqueous phase) towards the acoustic pressure node (channel center). During the process of the acoustic relocation, droplets were produced provided that interfacial tension force exceeds the viscous force. By making the central streamline enter into the oil phase outlet, the produced droplets were collected at the oil phase outlet. Once the acoustic field is turned off, co-flowing fluids state re-emerges.

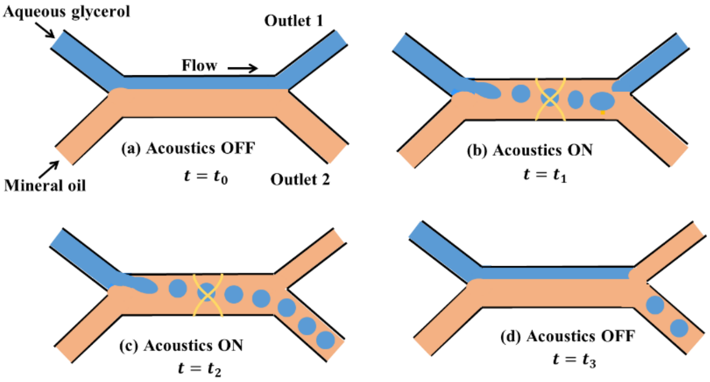

Figure 1: Schematic illustration of on-demand droplet generation using BAW. a) oil and aqueous phase were co-flowing while an acoustic field in off condition b) upon turning on the acoustic field when $C_{ac} \gg 1$, $\mu u \ll \gamma$, droplets were produced, since droplets are having positive contrast factor, produced droplets were pushed towards the acoustic pressure node c) keeping the acoustic field, droplet were continuously produced at the upstream, making the central streamline enter into the outlet by selecting appropriate flow rate, produced droplets were isolated towards the oil phase outlet. d) Once the acoustic field is turned off co-flow state re-emerges again.

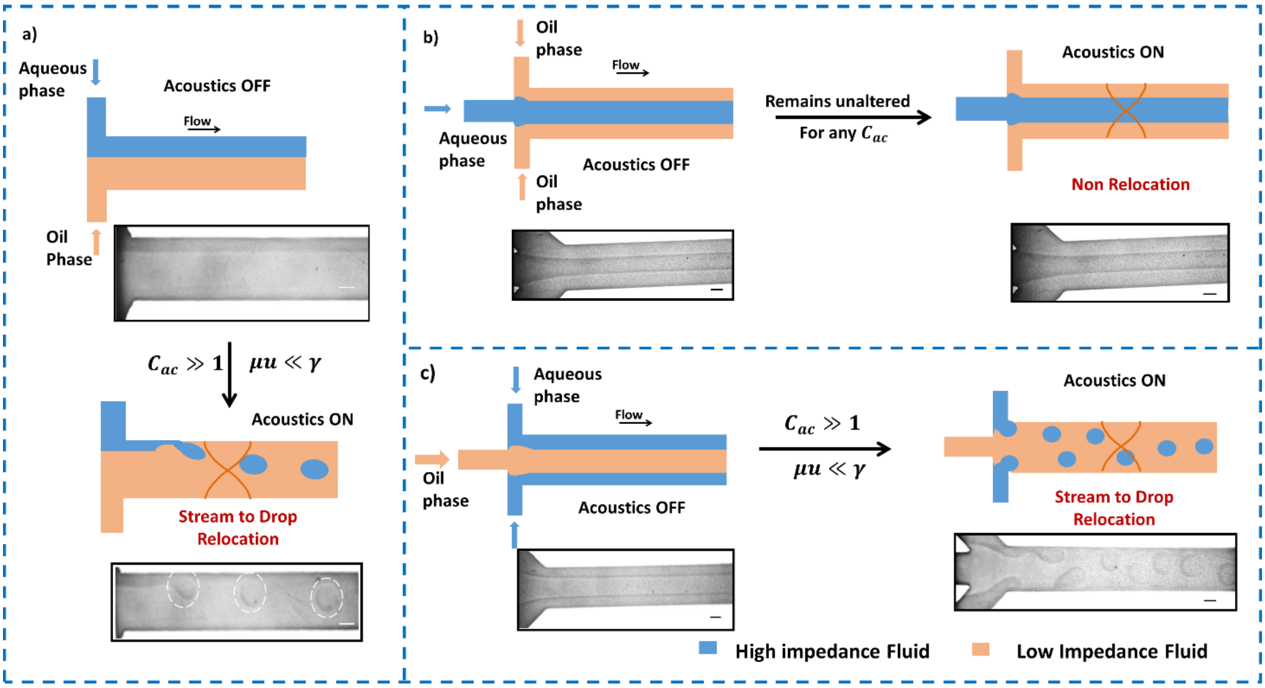

Figure 2: Effect of BAW on different channel configurations. a) Aqueous and oil phase are co-flowing in bifurcation inlet configuration, upon $C_{ac} \gg 1$, due to interfacial tension, which seeks to minimize the interfacial area, droplets were produced from co-flowing fluids. b) Trifurcation inlet - high acoustic impedance at the center surrounded by the low acoustic impedance fluids on sides; this configuration remains unaltered regardless of the acoustic and interfacial tension force between the fluids. c) Trifurcation inlet with low impedance at the center and high impedance at the sides. Once acoustic radiation force exceeds the interfacial tension force and interfacial tension dominates the viscous force, droplets were produced from both sides on side inlets and moves towards the center by the acoustic forces.

Results and discussion

The effect of bulk acoustic standing half-wave on immiscible fluids is presented. Experiments in two different channels, such as bifurcation inlet and trifurcation inlet configurations are outlined in Figure 2. When aqueous and oil phases are co-flowing in a bifurcation inlet channel at the following flow conditions ($Q_{oil} = 45\,\mu L/min$, $Q_{aq} = 5\,\mu L/min$, $Ca_{mi} = 0.2$ and $Ca_{aq} = 0.17$), the interfacial force ($\gamma = 3\,m\,\mathrm{N}/m$) dominates the viscous force($(\mu u)_{avg} = 0.66\,m\,\mathrm{N}/m$). since $(\mu u)_{avg} \ll \gamma$ and $C_{ac} \gg 1$, onset of instability by interfacial tension seeks to minimize the interfacial area due to which droplets are formed in the process of relocating high impedance fluid to the center, as shown in Figure 2(a). In the trifurcation microchannel, we performed experiments for two different fluid configurations, one with low acoustic impedance fluid at the central inlet surrounded by high acoustic impedance fluids at the two side inlets as shown in Figure 2(b) and other with high acoustic impedance at the center inlet surrounded by low acoustic impedance fluid from the two side inlets, as shown in Figure 2(c). We observe that upon onset of the bulk acoustic waves, the configuration with high acoustic impedance fluid at the central inlet of the microchannel remains the same, regardless of the acoustic force density and interfacial tension between the fluids, as shown in Figure 2(b). when high acoustic impedance fluids are at the sides of the microchannel, aqueous droplets were produced from the sides, as shown in Figure 2(c). Using the same acoustic force, droplets were moved towards the center of the microchannel and isolated at the oil flow outlet, as shown in Figure 1(c).

Conclusion

We found that droplets could be generated in an on-demand manner from co-flowing fluids using BAW. For the generation of droplets, the system should be maintained in an acoustically unstable configuration, and interfacial tension force should dominate viscous forces. Droplet could be isolated by using the same acoustic force which produced them. The proposed on-demand droplet generation can be a useful tool for rare event isolation.

References

[1] D. J. Collins, T. Alan, K. Helmerson and A. Neild, Lab Chip, **13**, 3225-3231 (2013)
[2] L. Schmid and T. Franke, Lab Chip, **13**, 1691–1694 (2013)
[3] S. Deshmukh, Z. Brzozka, T. Laurell and P. Augustsson, Lab Chip, **14**, 3394-3400 (2014).
[4] E. Hemachandran, S. Karthick, T. Laurell and A. K. Sen, EPL (Europhysics Lett.), **125**, 54002 1-7 (2019).
[5] E. Hemachandran, T. Laurell and A. K. Sen, Phys. Rev. Appl., **12**, 044008 1-13 (2019).

Acoustofluidics
2021
26-27 August 2021
Virtual Conference

Swarming behaviors of micromotors powered by bubble oscillation

Xiaolong Lu[1*], Ying Wei[1], Hui Shen[1], and Wenjuan Liu[2]

[1] State Key Laboratory of Mechanics and Control of Mechanical Structures, Nanjing University of Aeronautics and Astronautics, Nanjing, Jiangsu 210016, China
E-mail: long_8446110@nuaa.edu.cn
[2] College of Materials Science and Engineering, Nanjing Tech University, Nanjing, Jiangsu 211816, China

Introduction

Microrobots that could perform precise manipulations in micro/nano scale have attracted tremendous attention in past decades for helping human beings to explore the unknown nanoworld.[1] Among several representative geometries of micromotors, tubular micromotors have aroused scientific concerns for their unique structural asymmetry featured with different inner and outer surfaces, therefore hold considerable promise for diverse applications.[2] However, the interactions among individual tubular micromotor and the collective behavior of such assembled group have been rarely exploited because of the comparatively fast motions coupled with immense disturbance flow around bubbles.

Here, we report an acoustically-powered superfast locomotion methodology for tubular micromotor swarms assembled by the ultrasound (US) oscillation of self-generated bubbles. With the applied ultrasound, micromotor individuals are headed by the attached oxygen bubbles to swim towards high pressure spots by the primary Bjerknes force. Subsequently, the bubble heads interact with each other by the secondary Bjerknes force to rapidly fuse into a big bubble core, serving as the collection center for attracting more micromotor individuals to join a dandelion-like swarming. The ultrafast microswarm growth and locomotion strategy offers a new paradigm for constructing distinct dynamic assemblies and rapid transmission of artificial microrobots, paving the way to a myriad of promising applications.

Untethered swimming

The tubular micromotors were synthesized by template-assisted electrodeposition. The elemental distributions of C, S, O and Mn in Figure 1a confirm the fabrication of PEDOT/MnO_2 micromotors. In addition, SEM images in Figure 1b show a typical PEDOT/MnO_2 micromotor with an appearance size of 15 μm in length and 5 μm in outer diameter. Single micromotor mobility with/without US fields were tested and compared in Figure 1c. It is obvious from non-US results (Figure 1c-i) that one bubble is generated at the opening of micromotor and then undergo an increased expansion to 20 μm in 150 ms, when no propulsion of the micromotor is observed. On the other hand, the applied US (Figure 1c-ii) with 101 kHz frequency and 10 V voltage would create a standing wave acoustic field in operating reservoir. The resultant pressure gradient in turn applies a primary Bjerknes force on the self-generated bubble.[3] With such asymmetrical radiation force, the connected micromotor is dragged to swim in a remarkable long distance (~ 100 μm) in 80 ms. The US-trigged robust swimming strategy was further evaluated using the transient velocity versus operating time. It is observed from Figure 1d that the micromotor-bubble systems without US maintains immobile during the test.

The implementation of ultrasound enables the micromotor-bubble systems to experience a fast accelerating phase and relocate with the maximum velocity of 3.6 mm/s in a short time. Furthermore, there is slight difference for transient velocity variations of different micromotor samples, which maybe caused by the irregular defects at the opening ends of micromotor individuals during the electrodeposition. But, the similar acceleration process and fast response to the same ultrasound stimuli indicate such untethered swimming could be repeated. These results confirm that ultrasound is an effective stimuli to drive MnO_2 tubular micromotors swimming in surfactant-free 1% H_2O_2 solutions.

Group schooling

The individual micromotors conjoint with bubbles are ultrasonically driven to swim. Consequently, such bubble heads could also response to the variance of acoustic pressure from neighbored bubbles due to the secondary Bjerknes force and thus move together until fusing into a big one. With this big vibrating bubble yielded from interaction of self-generated small bubbles, a number of micromotors are therefore able to join in and perform group schooling, as the schematic showing in Figure 2a.

The group schooling behavior is further quantified by exploring the dependence of bubble core diameter and number of joined micromotor units upon the operating time, as illustrated in Figure 2b. The diameter of the bubble core is increased to 55 μm as the operating duration increase to 280 ms. In terms of the amount of gathered micromotors, it displays a similar trend as the diameter curve does. However, it is worth noting that the number of gathered micromotor units maintains stable since 100 ms and restarts to rise after 250 ms. This could be explained that most micromotors suspending around the bubble core have been readily gathered even though the bubble core for schooling still expands during this time period. When the bubble expands to a stabilized size, it will detach from the bottom plate and relocate to a new position. Then, additional micromotors would be gathered by the bubble core to perform group schooling. After the group schooling, micromotors carried by oscillated bubbles could then autonomously swarm at a superfast speed. The average speed of the swarming is around 50 mm/s, which is 100 times higher than that of conventional bubble-propelled tubular micromotors.

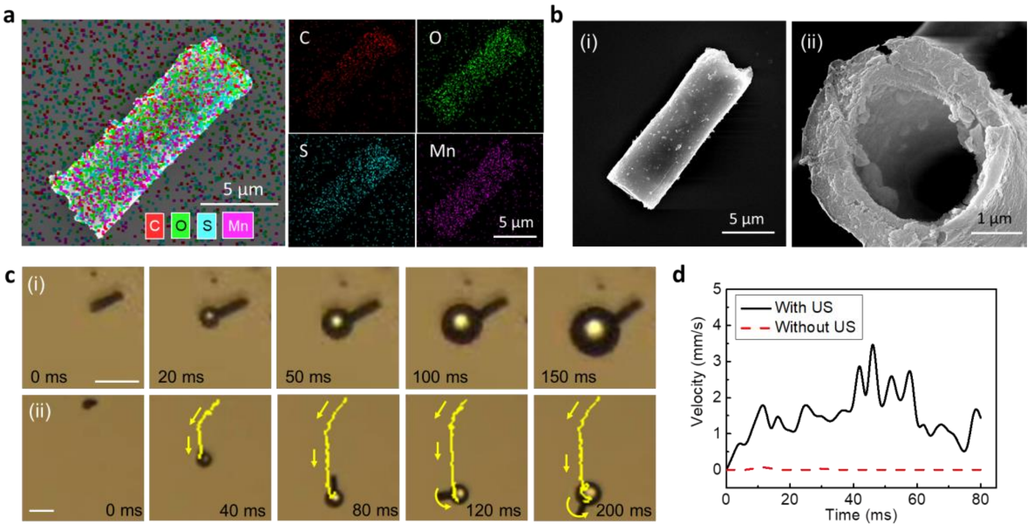

Figure 1: Untethered swimming of PEDOT/MnO_2 micromotor individuals powered by oscillation of self-generated bubbles. a) EDS elemental mapping of a PEDOT/MnO_2 micromotor showing the components of C, O, S and Mn, respectively. b) SEM images of a tubular PEDOT/MnO_2 micromotor (i) and its detailed construction at the opening end (ii). c) Sequential images captured from Video S1 showing the dynamic microbubble generation and resultant swimming of micromotors (i, scale bar: 10 µm.) without ultrasound and (ii, scale bar: 20 µm.) with ultrasound. d) Ultrasound dominance on the swimming velocity of bubble-propelled micromotor individuals

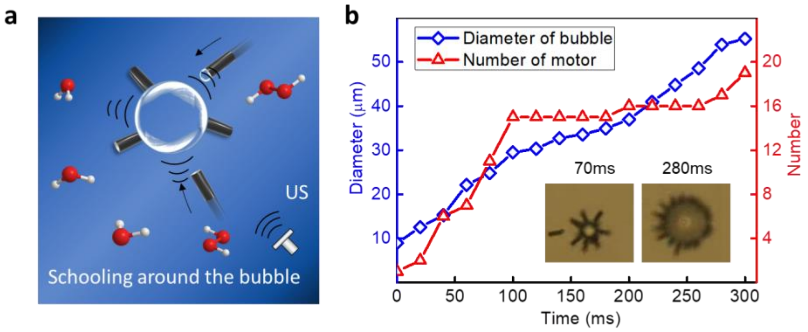

Figure 2: Schooling behavior of PEDOT/MnO_2 micromotor individuals around fused bubbles in ultrasound field. a) Schooling schematic of multiple PEDOT/MnO_2 micromotors triggered by ultrasound induced oscillation of fused oxygen bubbles. b) Microbubble diameter and number of collected micromotors vs operating time.

Conclusion

In summary, we presented a superfast strategy for growing dandelion-like microswarms from tubular micromotors and driving them to move freely by oscillating self-generated bubbles in ultrasound field. The electrodeposited tubular MnO_2 micromotors have been selected to efficiently decompose H_2O_2 and generate oxygen bubbles, which could oscillate with the external ultrasound stimuli. Driven by the primary Bjerknes force, the bubble-micromotor individual could rapidly swim in surfactant-free environment where most bubble-propelled micromotors cannot move effectively. With the fusion of multiple bubbles by secondary Bjerknes force, a large bubble is constructed and acts as the collection core to accomplish the group schooling for a number of micromotors suspending around it. Accordingly, a dandelion-like microswarm would thus be accomplished. The superfast swarming protocol will open a new avenue for bubble-propelled micromotors locomotion with surfactant independence, which would be significant for micromotor groups to enhance the propulsion power in complex environments.

References (Times New Roman 10 pt)

[1] J. Wang, *Nanomachines: fundamentals and applications*, John Wiley & Sons, 2013.
[2] B. Xu, B. Zhang, L. Wang, G. Huang, Y. Mei, Adv. Funct. Mater. 2018, 28, 1705872.
[3] T. Leighton, A. Walton, M. Pickworth, European Journal of Physics 1990, 11, 47.

Acoustofluidics
2021
26-27 August 2021
Virtual Conference

Controlled Transport and Merging of Individual Drops in Closed Channel Acoustofluidic Devices

Kyriacos Yiannacou[1] and Veikko Sariola[1]

[1]Faculty of Medicine and Health Technology, Tampere University, Tampere, Finland
E-Mails: kyriacos.yiannacou@tuni.fi, veikko.sariola@tuni.fi, URL: http://research.tuni.fi/bmr-group

Introduction

Handling small volumes of fluid (< 1 µl) is challenging using traditional, pipette-based methods. For handling smaller volumes of fluid, transporting droplets suspended in an immiscible phase inside microfluidic chips has been proposed.[1] However, most methods reported so far rely on passive transport of droplets in microfluidic flows, limiting the control over the position of individual drops. Merging has been achieved by applying electric[2] or acoustic field[3] when two drops meet near a specific location. A more versatile method that would allow transport and merge individual droplets at will, would enable more complex chemical synthesis and analyses in such a chip. In this work, we present controlled ultrasonic manipulation of droplets in closed-channel microfluidic chips, using a single transducer in a closed loop manner. The droplets are tracked using machine vision and manipulated through defined routes/points by a machine learning algorithm. In each cycle, the algorithm chooses which frequency to apply, using only the information it has learned since the manipulation started. In our previous work, we use this method to manipulate single and multiple polystyrene particles in closed-channel microfluidic chips;[4] here, we extend this method to the transport and merging of water drops suspended in oil inside microfluidic chips. We show that this method is robust to changes in droplet sizes, and to the number of discrete actuation frequencies. This work paves way towards more programmable and reconfigurable microfluidic chips, where fluid volumes in the 100 pl range can be controllably manipulated for lab-on-a-chip applications.

Methods

A schematic of our experimental setup is shown in Figure 1a. The apparatus consists of a glass microfluidic chip with three inlets and a single outlet, a piezoelectric transducer (CTS-Noliac, NCE 46, 15mm × 15mm × 2mm) mounted on the backside of the chip, a camera (Basler acA2040-120uc) to image the droplets inside the chip, a computer running the machine vision and control algorithm, an arbitrary waveform generator (PCI-5412, National Instruments), an amplifier (1400L, Electronics and Innovation), and a syringe pump (Aladdin, World Precision Instruments). Inside the chip, there is a rectangular chamber with dimensions of 7 mm × 6 mm × 0.15 mm.

The droplets were produced using an external flow focusing device with an orifice width of 80 µm.[5] The continuous phase (2.25 vol% Span80 in hexadecane oil) was infused at rates of 15-30 µl/min, and the dispersed phase (dyed DI-water) was infused at a rate 10µl/min using a syringe pump. The different flow rates for the continuous phase were used to produce the different sized droplets.

The control routine used for the droplet manipulation is the ε-greedy algorithm from our previous work.[4] Briefly, at each control cycle, any random frequency (discrete number of frequencies in the range

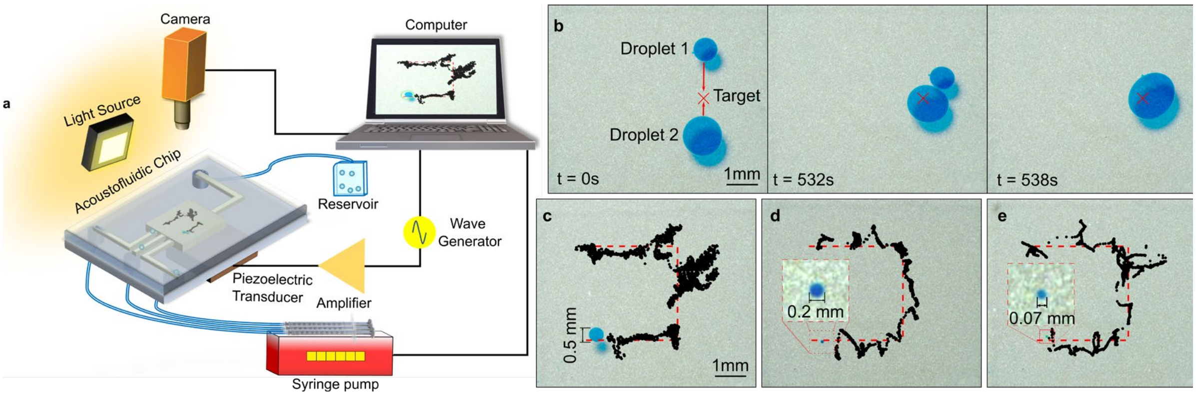

Figure 1. a) Schematic diagram of the experimental setup. **b)** Timestamps of droplet manipulation and merging. The droplets are guided to a single target point, where the droplets merge due to ultrasonic vibrations. **c-e)** Controlled manipulation of water drops in hexadecane oil with sizes **c)** 500 µm, **d)** 200 µm, sand **e)** 70 µm.

of 65-700 kHz) is chosen with a probability of ε (exploration). Otherwise (with a probability of 1 – ε), the frequency with the highest expected reward is chosen (exploitation).[4,6] The expected reward is simply how many micrometers (pixels) that frequency moved all the droplets towards their target points in the past, on average. The averaging used exponentially decaying weights: recent observations were given more weight than old observations. Details of the algorithm are reported in our previous paper.[4]

Results

To test if we can transport and merge droplets using the proposed method, we pumped two drops into the chamber (diameters: 1.25 mm and 0.76 mm). The controller was given the task of bringing both drops to the target point (Figure 1b). The controller successfully guided the droplets towards the target point (Figure 1b). However, the drop interfaces are stable, and the two drops do not spontaneously merge, at least not consistently. To induce merging of the drops, we performed continuous excitation of the chamber with ultrasound, disrupting the drop interfaces and causing the two droplets to merge (Figure 1b). These experiments show that two drops can be transported and merged using our setup.

To test what sizes of drops can be transported using our method, we designed a U-shaped route for the droplets to follow, and pumped drops of various volumes in the chamber. The diameters of the drops were 70 µm, 200 µm and 500 µm, corresponding to volumes of approximately 200 pl, 5 nl and 30 nl (assuming drops smaller than chamber height are approximately spheres and drops larger than the chamber height are approximately disks). All different sized drops were successfully manipulated (Figure 1c-e). The manipulation of the 500 µm drop was slower (130 minutes) than the manipulation of the two smaller drops (67 minutes for the 70 µm drop, and 64 minutes for the 200 µm drop). Overall, this shows that the method is robust to drop size changes, and that at least drops with diameters in the 70 µm – 500 µm range can be manipulated with our method.

Finally, we tested how many different discrete frequencies are necessary for the manipulation. In these experiments, we again manipulated a 100 nl droplet along a U-shaped path, but the number of discrete frequencies N was varied. We tested $N = 30$, $N = 50$ and $N = 75$. With all the tested numbers of frequencies, the manipulation was successful (Figure 2). These results indicate that our method is robust and not sensitive to the number of frequencies. Thus, optimizing this parameter very carefully is not critical for performing successful manipulation.

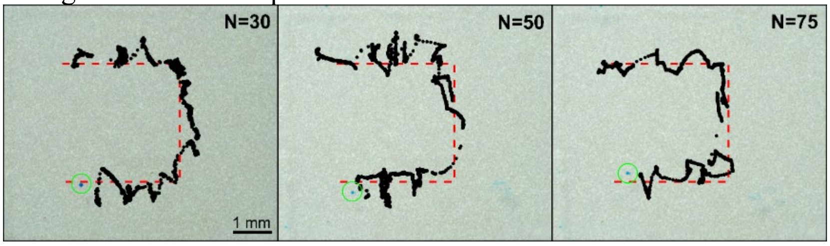

Figure 2. Controlled manipulation of droplets with different numbers of frequencies *N*.

Conclusions

In this work, we have demonstrated controlled 2D manipulation of single and multiple droplets inside closed-channel microfluidic chips using bulk acoustic waves from a single piezoelectric transducer. The method uses closed-loop control, based on machine vision tracking of the droplets and machine learning. We demonstrated controlled merging of two drops, and the manipulation of water drops of various sizes and with varying number of frequencies.

The advantage of our method is that it can successfully transport and merge droplets without any prior learning events or calibration experiments. Our method can adapt to changes (e.g. drop size and the number of frequencies) and still complete the manipulation task. We attribute this robustness to the machine learning algorithm: the machine learning algorithm does not know anything about the chamber at the start of the experiment, so it will adapt to using whatever frequencies that work in this particular situation. Our method paves the way towards robust acoustic manipulation of droplets in lab-on-a-chip applications, for potential uses in e.g. drug discovery, bioreactors, and diagnostics.

References

1. Teh, S. Y., Lin, R., Hung, L. H. & Lee, A. P. Droplet microfluidics. *Lab on a Chip* vol. 8 198–220 (2008).
2. Chou, W. L., Lee, P. Y., Yang, C. L., Huang, W. Y. & Lin, Y. S. Recent advances in applications of droplet microfluidics. *Micromachines* vol. 6 1249–1271 (2015).
3. Bussiere, V. *et al.* High-throughput triggered merging of surfactant-stabilized droplet pairs using traveling surface acoustic waves. doi:10.1021/acs.analchem.9b03521ï.
4. Yiannacou, K. & Sariola, V. Controlled Manipulation and Active Sorting of Particles Inside Microfluidic Chips Using Bulk Acoustic Waves and Machine Learning. *Langmuir* acs.langmuir.1c00063 (2021) doi:10.1021/acs.langmuir.1c00063.
5. Lashkaripour, A., Rodriguez, C., Ortiz, L. & Densmore, D. Performance tuning of microfluidic flow-focusing droplet generators. *Lab Chip* **19**, 1041–1053 (2019).
6. Kuleshov, V. & Precup, D. Algorithms for multi-armed bandit problems. *J. Mach. Learn. Res.* **1**, 1–48 (2014).

Acoustofluidics 2021
26-27 August 2021
Virtual Conference

Particle trapping in microfluidic shaped traps exposed to bulk acoustic standing waves

Lokesh Malik[1], Amal Nath[1], and Ashis Kumar Sen[1]

[1]Micro Nano Bio- Fluidics Unit, Fluid Systems Laboratory, Department of Mechanical Engineering, Indian Institute of Technology Madras, India
E-mail: lokeshiitmadras@gmail.com

Introduction

Development in bio-particle handling microfluidic systems is subject to advancements in efficient techniques of trapping them. Contactless and gentle trapping [1] platform offered by the ultrasonic standing wave technology makes it an attractive tool for widespread biotechnological applications [2]. In the present study, we numerically demonstrate and experimentally validate a contactless acoustofluidic trapping technique based on the standing bulk acoustic waves (BAW) generated inside a uniquely designed chamber here referred to as the 'shaped trap' that enables the particle to experience axial primary radiation force (PRF) along the flow direction as its main trapping force. Axial PRF opposing the flow (beyond the nodal plane) tends to immobilize the particle eventually getting it trapped at a unique off-node trapping site precisely controlled by extensive variations in particle size (D), flow rate (Q), and acoustic energy density (E_{ac}).

Shaped Trapping Setup – Overview and Possibilities

Particle trapping in one-dimensional (1D) and two-dimensional (2D) BAW actuated shaped traps is fundamentally studied where 1D and 2D represent the number of dimensions in which the standing wave is generated having pressure nodal plane at the center of the trapping chamber and antinodal plane at the chamber walls. Out of all configurations (see fig. 1-c to -f), 1D-S (schematic shown in fig. 1-b) is chosen for

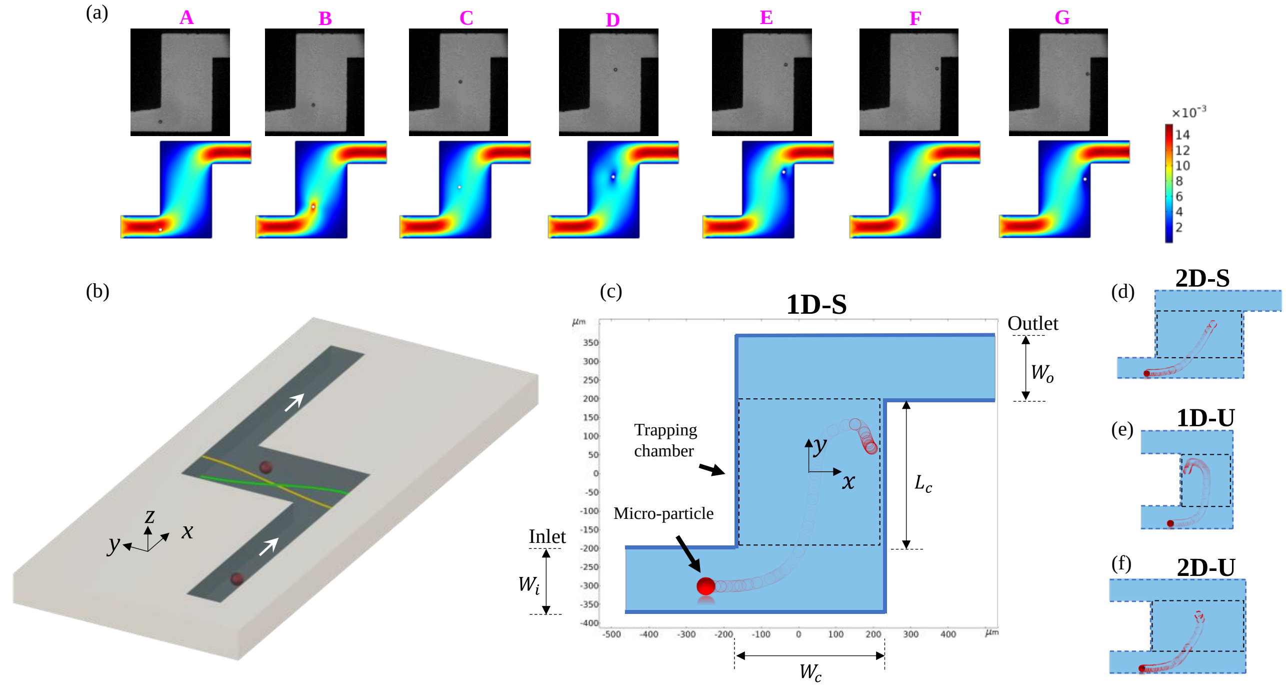

Figure 1: (a) Comparison of experimental snapshots and velocity contours at time instants A, B, C, D, E, F and G. The colour legend refers to the magnitude of velocity in m/s. (b) A schematic of the 1D-S trapping chamber design indicating the flow direction, standing half wave generation and typical shape of the 1D-S trap. (c) 1D BAW actuated S shaped (1D-S) trapping set-up with $W_i = W_o = 175\ \mu m$ and $W_c = L_c = 400\ \mu m$. (c-f) Simulation domain showing all configurations for the first harmonic mode acoustic trapping (pressure nodal plane at $y = 0$) considered for the study with $W_c = 750\ \mu m$ for 2D traps, other dimensions being the same as of 1D traps. Trajectories (red circles) of particles trapped in various configurations for similar flow and field conditions have been shown.

experimental validation. Inside the chamber, particle experiences axial PRF in the flow direction in all configurations and additionally in the direction perpendicular to it only in case of 2D traps. In case of 1D traps, the axial PRF competes with the y direction fluidic drag resulting in a typical U-turn motion, after which the particle gets trapped above the nodal plane near the left (1D-U) or right wall (1D-S). Whereas in case of 2D traps, axial PRFs compete with the x and y direction fluidic drags and unlike 1D traps, particle in spite of approaching the walls, hangs in the middle of the chamber (see fig. 1-d, f). The competing effects inside the chamber are quantified using a dimensionless energy parameter β (acoustic to viscous energy ratio $=E_{ac}D\phi/U/\eta$) where ϕ, U and η are acoustic contrast factor, particle's average velocity in the chamber, and fluid's viscosity, respectively. A trapping case with β = 60 ($E_{ac} = 120 J/m^3, D = 25\ \mu m, Q = 15\ \mu l/$min) is chosen to explain the particle's travel via simulations and experiments performed on 1D-S trap as shown in fig. 1-a. Experimental snapshots and velocity contours at different instants qualitatively reveal particle's journey inside the chamber. Particle's entry to the chamber, maximum acoustic force, node crossover, U-turn begin, U-turn peak, U-turn end and trapping are represented by instants A, B, C, D, E, F and G, respectively.

Regime study, characterization of trapping location and particle trajectories

Studies related to trapping regimes and trapping location with extensive variations in E_{ac}, Q, D and W_i, performed across all configurations reveal that whether the particle gets trapped or not, is independent of the type of configuration and is solely dependent on β. As shown in fig. 2-a, the shaded region pertains to the trapping region demarcating a critical flip-over between the trapping and non-trapping regimes at $\beta_{cr} = 38$.

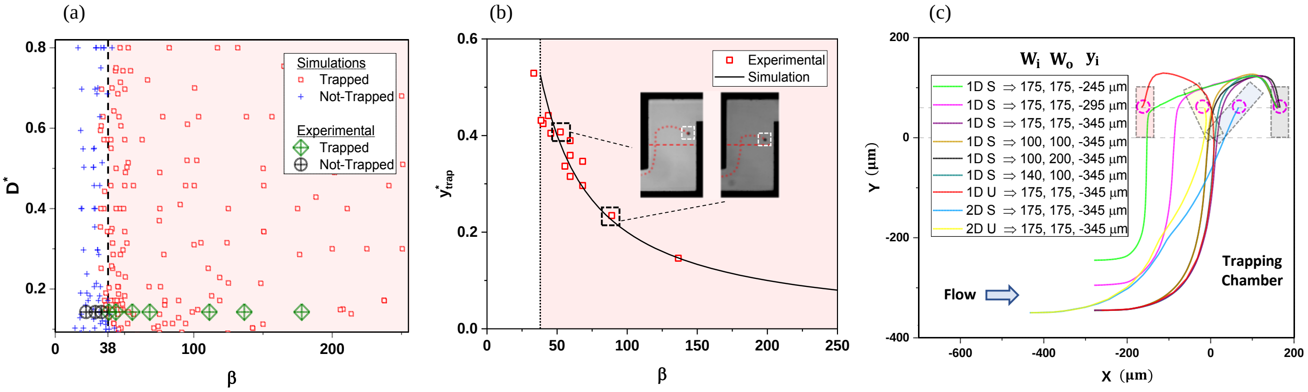

Figure 2: (a) Regime plot revealing two important regimes – trapping, non-trapping. (b) Characterisation of trapping location $y^*_{trap} = 20/\beta$ with $R^2 = 0.9$ (c) Explanation of the variations in trajectory and trapped location for $\beta = 45$.

β_{cr} is independent of D^*, where D^* $(= D/W_i)$ is the particle diameter non-dimensionalised with W_i. Since, the presence of x direction axial PRF inside the chamber in 2D configurations doesn't affect the y coordinate of the trapping location, y_{trap} is found to be configuration independent thus extensively characterised ($y^*_{trap} = 20/\beta$, see fig. 2-b) in the present study while x_{trap} is found to be configuration dependent, as shown in fig. 2-c. Experimental data points pertaining to the trapped and non-trapped cases shown in fig. 2-a, b are found to be in decent agreement with the numerical findings. The variations in the particle's trajectory and trapping location inside the chamber are studied considering a case with $\beta = 45$. Particle's trajectory inside the chamber for a particular configuration majorly depends on the initial streamline of the particle, y coordinate of which is designated by y_i in fig. 2-c, however interestingly the final trapped location (y^*_{trap}) remains unaffected to the change in initial streamline. Also, it can be clearly seen that the variation in the inlet and/ or outlet widths has very little effect on the trajectory of the particle, whereas the final trapped location is absolutely unchanged with the width variations. Depending on the type of configuration, the trapped particles are retained all along the chamber at different x locations but at the same y location. Starting from left to right, the shaded region shown in fig. 2-c corresponds to the trapping zones (brought about by a range of β values) pertaining to 1D-U, 2D-U, 2D-S and 1D-S configurations, respectively.

Conclusion

Contactless particle trapping inside shaped traps utilizing the axial PRF as the main trapping force is demonstrated on a microfluidic platform. With extensive variations in the operating parameters (E_{ac}, Q, D and W_i) across all the configurations, the ratio of the competing effects β is utilized to characterize trapping thus identifying two distinct regimes – trapping ($\beta > 38$) and non-trapping ($\beta < 38$). The y component of the final trapped location is found to vary as $y^*_{trap} = 20/\beta$ (maximum being 0.53 at $\beta = \beta_{cr}$), dependent only on β and independent of the configuration type, whereas x_{trap} is found to be independent of β and dependent on the configuration type. Finally, the effect of the particle's initial streamline, chamber dimensions and configuration (chamber shape) on particle's trajectory and final trapped location is explored.

References

[1] J. Svennebring, O. Manneberg, P. Skafte-Pedersen, H. Bruus, and M. Wiklund, Biotechnol. Bioeng. **103**, 323 (2009)

[2] M. Evander and J. Nilsson, Lab Chip **12**, 4667 (2012)

Acoustofluidics
2021
26-27 August 2021
Virtual Conference

Particle focusing in polymer-based acoustofluidic devices: An experimental and numerical study

Fabian Lickert[1], Mathias Ohlin[2], Henrik Bruus[1] and Pelle Ohlsson[2]

[1]Department of Physics, Technical University of Denmark, Kongens Lyngby, Denmark
E-mail: fabianl@dtu.dk, URL: www.fysik.dtu.dk/microfluidics
[2]AcouSort AB, Lund, Sweden, URL: www.AcouSort.com

Introduction

The use of polymer-based microfluidic chips in the area of acoustofluidics presents many opportunities, such as reducing mass production cost, easier integration into diagnostic polymer cartridges, and rapid prototyping capabilities. Acoustofluidic devices made from polymers are, however, not established in the field yet, partially due to the lack of design rules, and glass or silicon devices are dominating in applications such as particle focusing. Moiseyenko and Bruus [1] numerically explored the concept of whole-system ultrasound resonances (WSUR) as the underlying mechanism in polymer-based devices, causing a standing half-wave-like pressure field inside the microfluidic channel, which is leading to particle focusing in the center of the channel. We showed recently that this prediction agrees well with experimental data [2]. In this work, we compare by simulation and experiment, two microfluidic chips made from PMMA, differing only in their thickness h_PMMA and otherwise being nominally identical. In Fig. 1(a) is shown an overview of the entire device, including a piezoelectric transducer and a 20-µm-thin glycerol coupling layer.

Numerical simulation

Numerical simulations for devices with chip thickness $h_\mathrm{PMMA} = 1.18$ mm and $h_\mathrm{PMMA} = 1.68$ mm are performed using the software COMSOL Multiphysics 5.5. The electric potential φ inside the PZT, the displacement $\boldsymbol{u}$ in the solid materials, as well as the pressure fields $p_{1,\mathrm{fl}}$ and $p_{1,\mathrm{cpl}}$ inside the fluid channel and the liquid coupling layer are obtained from the simulations and shown in Fig. 1(b) and (c). Details on the implementation as well as the material parameters can be found in Ref. [2]. We calculate the focusability $\mathcal{F}$ based on the resulting fields, describing the relative number of particles that are focused within 10% of the channel center.

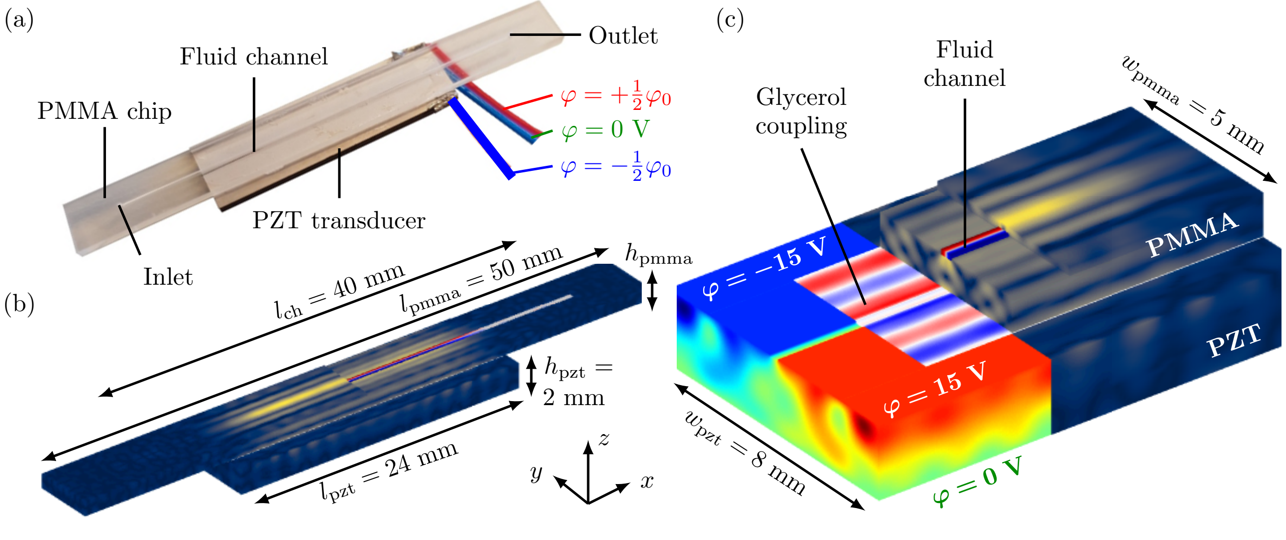

Figure 1: (a) Image of the PMMA chip, containing a 375-µm-wide and 150-µm-high microfluidic channel, coupled to a piezoelectric transducer through a 20-µm-thin glycerol layer. (b) Numerical results for the device with $h_\mathrm{PMMA} = 1.18$ mm at the resonance frequency $f_1^\mathrm{sim} = 1.17$ MHz, showing the displacement field $\boldsymbol{u}$ from 0 (blue) to 50 nm (yellow) and the acoustic pressure $p_{1,\mathrm{fl}}$ inside the channel from -700 kPa (blue) to 700 kPa (red). (c) Cut-view of the simulation results, showing the displacement field, the electric potential, as well as the acoustic pressure inside the channel and the glycerol coupling layer.

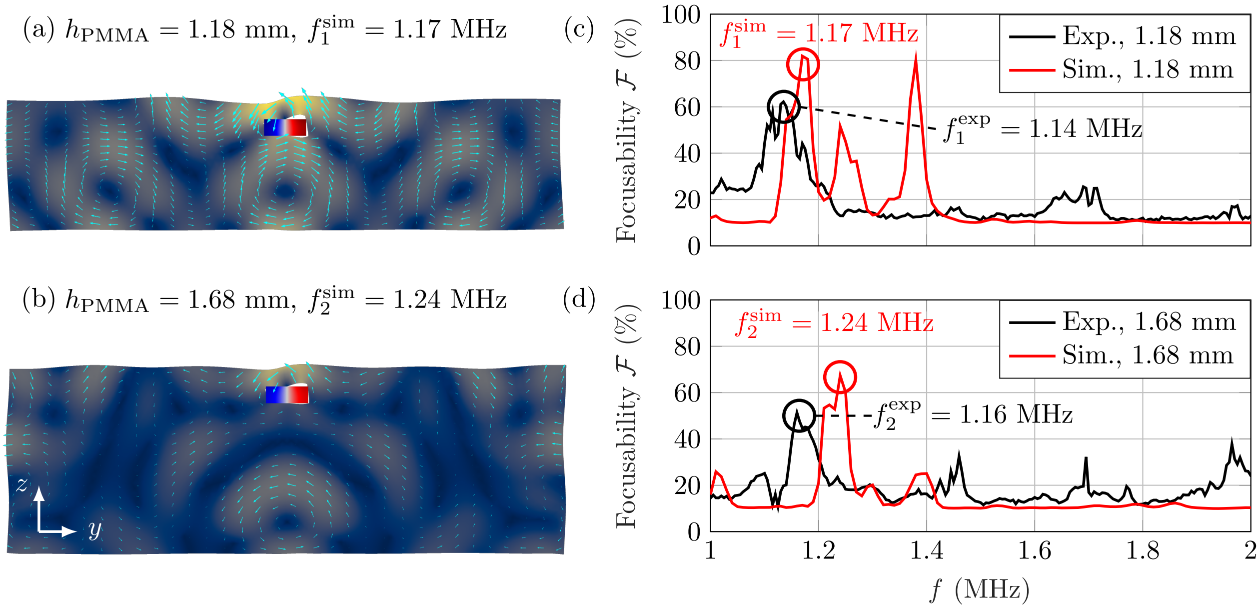

Figure 2: (a) Cross-section of the simulated displacement field $\boldsymbol{u}$, scaled by a factor of 1000, inside the 1.18 mm chip. (b) Simulated displacement field inside the 1.68 mm PMMA chip. (c) Comparison of the measured and simulated focusability in the frequency range from 1 to 2 MHz for the 1.18 mm thick chip. The simulations predict good focusing of about 80% of the particles at a frequency of $f_1^{\mathrm{sim}} = 1.17$ MHz, while the experimental results slightly deviate by 2.6% from this frequency. (d) Measured and simulated focusability spectrum for the 1.68 mm thick chip. The measured focusability is below the value which has been observed for the thinner chip and the simulated resonance frequency of $f_2^{\mathrm{sim}} = 1.24$ MHz deviates by 6.9% from the experimental value.

Comparison with experimental results

We verify our numerical results by performing focusing experiments on 4.8 µm-diameter polystyrene particles in a solution consisting of 84% (v/v) water and 16% (v/v) iodixanol and calculating the experimental focusability $\mathcal{F}_{\mathrm{exp}}$. During the focusability measurement an anti-symmetric actuation voltage with a peak-to-peak amplitude of $\varphi_0 = 30$ V and a flow rate of 10 µL/min is used, while the device is kept at a constant temperature of $T = 20$ ℃. The results are summarized in Fig. 2. The simulated displacement field of the 1.18-mm-thin chip in Fig. 2(a) reveals a vortex of the displacement field below the fluid channel, coupled with strong lid motion above the channel, while the displacement field in Fig. 2(b) shows an overall weaker response with lower displacement amplitudes in the thicker PMMA chip, suggesting that it is not a strong WSUR which is being actuated in the latter case. In Fig. 2(c) and (d) a comparison between the simulated and measured focusability spectrum is given. The simulated focusablity has been re-scaled to match the experimentally determined acoustical energy density E_{ac}, where a measured value of $E_{\mathrm{ac}} = 13\ \mathrm{J\,m^{-3}}$ has been used for the 1.18 mm chip and a value $E_{\mathrm{ac}} = 10\ \mathrm{J\,m^{-3}}$ has been assumed preliminary for the 1.68-mm-thick PMMA chip. In terms of the focusability our model predicts best focusing results at $f_1^{\mathrm{sim}} = 1.17$ MHz for the thinner 1.18 mm chip, deviating only 2.6% from the measured highest focusability at $f_1^{\mathrm{exp}} = 1.14$ MHz. For the 1.68 mm chip we experimentally observe lower focusability and our simulated frequency of maximum focusability $f_2^{\mathrm{sim}} = 1.24$ MHz deviates by 6.9% from the experimental value $f_2^{\mathrm{exp}} = 1.16$ MHz.

Conclusion

Acoustophoretic particle focusing in two different PMMA-based devices is presented, and the results have been predicted numerically and verified experimentally. Our simulation model captures the basic physics of the device and opens the possibility for further design improvements, which ultimately will allow to achieve higher flow rates in polymer-based particle separation platforms.

Acknowledgments

This work is part of the Eureka Eurostars-2 joint programme E!113461 AcouPlast project funded by Innovation Fund Denmark, grant no. 9046-00127B, and Vinnova, Sweden's Innovation Agency, grant no. 2019-04500, with co-funding from the European Union Horizon 2020 Research and Innovation Programme.

References

[1] R. P. Moiseyenko, and H. Bruus. Phys. Rev. Appl. **11**, 014014 (2019). [pdf]
[2] F. Lickert, M. Ohlin, H. Bruus, and P. Ohlsson. J. Acoust. Soc. Am. **149**, 4281-4291 (2021). [pdf]

Acoustofluidics 2021
26-27 August 2021
Virtual Conference

Cell-based microrobot manipulation by multielement focused ultrasound phased array

Hiep Xuan Cao[1,2], Van Du Nguyen[1,2], Daewon Jung[2], Han-Sol Lee[1,2], Byungjeon Kang[2,3], Jong-Oh Park[1,2], Chang-Sei Kim[1,2]

[1]School of Mechanical Engineering, Chonnam National University, Gwangju 61186, Korea.
E-mail:hiep.caoxuan@kimiro.re.kr, URL: http://mech.jnu.ac.kr/
[2]Korea Institute of Medical Microrobotics, Gwangju 506813, Korea.
[3]Robotics Engineering Convergence, Chonnam National University, Gwangju 61186, Korea

Introduction

The idea of research aims to develop an acoustic manipulation system as a novel target drug delivery platform in therapeutic. The microrobot is made by lymphocytes T (T cell) and nano particle as drug carrier. The T cells are one of the important white blood cells of the immune system. With the T cells as carrier, the microrobot can stay in the human body without eliminate by human immune system. The research work describes the design and fabrication of the multielement focused ultrasound phased arrays and cell-based microrobot, as well as the proof-of-principle for manipulation in 4 degree of freedom (DoF) – 3 DoF manipulation position and 1 DoF pointing orientation along Z axis, in *in-vitro* experiment.

Experiment

The multielement focused ultrasound phased arrays (UT) is designed with 32 ultrasonic transducers (JAPAN PROBE, Yokohama, JP) with single side arrangement and placed in an acrylic box (300x300x300 mm^3) filled with water[1]. Each transducer of the UT is driven at bipolar voltage amplitude of 60 Vpp and resonant frequency at 1 MHz continuous square wave created by a custom-made amplifier. The control system is designed for controlling the phase delay of 32 ultrasonic transducers independently. Thus, using the phase modulation function of each transducer, the twin trap signal is a combination of position signal and twin signal which will be formed in the water tank. The position of twin-trap will be generated at desired position in three dimensional. To control pointing orientation along the Z axis, the twin signal is rotated along clockwise or counterclockwise follow the transducer order in the array's arrangements. The twin trap is formed with the same orientation of twin signal.

The microrobot is developed based on T cells. These cell-based microrobots were fabricated by assembling nano particles as drug carriers in difference ratio. Therefore, the biocompatibility and biodegradation issues with respect to other microrobots were observed to be minimal [2][3]. Figure 1 shows the microscopy photo of these cell-based microrobot with ratio of T cells and nano particle is 2:1 1(a) and ratio 1:1 in 1(b).

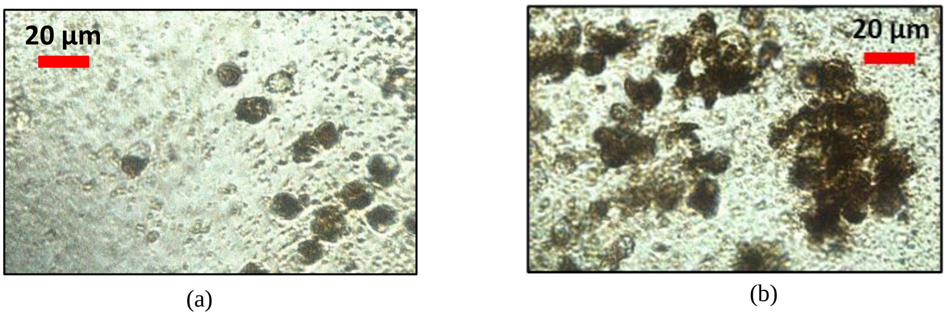

(a) (b)

Figure 1: the microscopy photo of T cells with difference combination with nano particles. (a) The combination with ratio 2:1. (b) the combination with ratio 1:1

Result and discussion

Figure 2 shows the position photo of microrobot with 3 DoF manipulation control. 30 UTs is driven at the same voltage 60 Vpp and with independently phase modulation control. These microrobot is trapped at trapping point as a cluster with the size (0.8x0.4x0.2 mm). It can be manipulated to any point in three dimension working space (3x3x2.5 mm) with the position errors less than 1 times of body length.

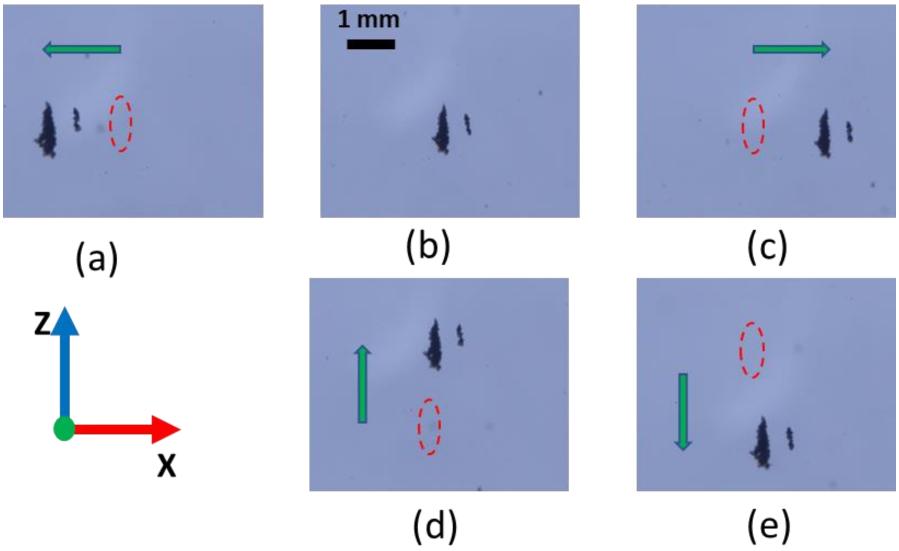

Figure 2: 3 DoF of position manipulation. (a) the microrobot moving to the -3 mm in X direction. (b) the microrobot is trapped at physical focus point (0, 0, 0). (c) the microrobot moving to the +3 mm in X direction. (d) the microrobot moving to the +2.5 mm in Z direction. (e) the microrobot moving to the -3 mm in Z direction.

Figure 3 shows the result of pointing orientation control along the Z axis. The microrobot cluster rotated along the z axis with the 45-degree resolution angles. This resolution is decided by the number of transducers in the UTs. In this study, the UT is designed with 30 transducers, it is divided to 8 pair group in twin signal. Each pair is switched power according to the phase of twin signal.

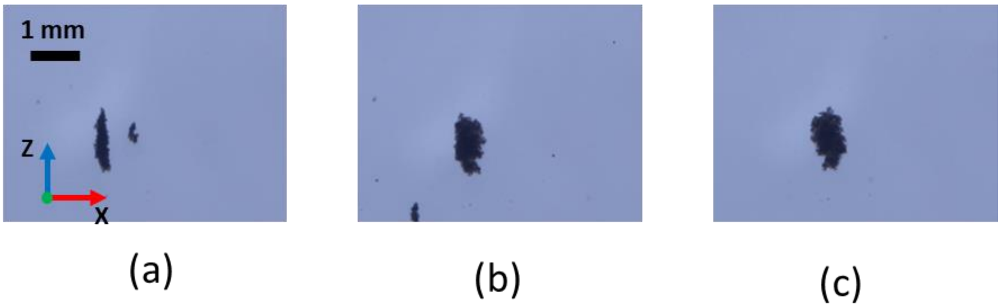

Figure 3: rotation control along the Z-axis. (a) the microrobot is trapped at physical focus point in 0 degree. (b) the microrobot is trapped at physical focus point in 45 degrees. (c) the microrobot is trapped at physical focus point in 90 degrees.

Conclusion

In summary, we have successfully developed an acoustic manipulation system for manipulating the cell-based microrobot with 3 DoF manipulation positions and 1 DoF pointing orientation along the Z-axis. Ongoing work involves expanding the capability of the system with the target manipulate of microrobot in 6 DoF. Finally, upon completion of the research, we aim to manipulate the cell-based microrobot load with the drug in 6 DoF in the *in-vivo* experiment.

Funding: This research was supported by the grant of the Korea Health Technology R&D Project through the Korea Health Industry Development Institute (KHIDI), funded by the Ministry of Health & Welfare, Korea (grant number: HI19C0642).

References

[1] H. X. Cao *et al.*, “Micromotor manipulation using ultrasonic active traveling waves,” *Micromachines*, vol. 12, no. 2, Feb. 2021.

[2] V. Du Nguyen *et al.*, “Active tumor-therapeutic liposomal bacteriobot combining a drug (paclitaxel)-encapsulated liposome with targeting bacteria (Salmonella Typhimurium),” *Sensors Actuators, B Chem.*, vol. 224, pp. 217–224, Mar. 2016.

[3] Y. Feng et al., "A novel and controllable cell-based microrobot in real vascular network for target tumor therapy," 2020. *IEEE/RSJ International Conference on Intelligent Robots and Systems (IROS).*

Acoustofluidics 2021
26-27 August 2021
Virtual Conference

Fourier Acoustical Tweezers: Synthesizing Arbitrary Radiation Force Using Non-Monochromatic Waves on Discrete-Frequency Basis

Yu Zhang, Xiasheng Guo

Key Laboratory of Modern Acoustics (MOE), Department of Physics, Collaborative Innovation Center of Advanced Microstructure, Nanjing University, Nanjing 210093, China
Email: 956601045@qq.com

Introduction

Existing acoustical tweezers (ATs) modulate source geometries to achieve monochromatic focusing, the wide frequency space allowed by sources is neglected. Here an analogous approach is proposed to synthesize AT fields in temporal frequency instead of wave vector. The base element is a standing wave, its counterpart in beam ATs is the field of a pitch. After field periodization, radiation force theory is extended to non-monochromatic waves having arbitrary in-period force based on discrete-frequency Fourier analysis. The Fourier acoustical tweezers (FATs) achieve unprecedented minimal spacing of λ/4 for independent trapping. System complexity is reduced to two sources per dimension.

Methods

We synthesize non-monochromatic ATs through Fourier series, named as Fourier acoustical tweezers (FATs). The idea is straightforward: given a target function of arbitrary acoustic radiation force (ARF), it is decomposed into multiple components in the frequency (ω) space, the acoustic fields required to generate each are summed up and emitted by the sources.

The principle is explained on 1-D basis along the x axis, where positive and negative forces point toward $+x$ and $-x$, respectively. Consider several particles having radius a and acoustic contrast factor Φ in a tweezing area $(-l, l)$, the qth at x_q. The medium has density ρ_0 and speed of sound c_0. The ARF field is designed such that, at each x_q there is a force trap $F_\mathrm{b}(x - x_q)$. The ARF field is then extended to the entire space by repeating the $(-l, l)$ pattern at $2l$ intervals. The target force field becomes

$$F_\mathrm{tar}(x) = \sum_{p=-\infty}^{\infty} \sum_{q} F_\mathrm{b}\left(x - x_q - 2pl\right) \tag{1}$$

As p is an integer, the first summation makes the field periodic, and the second builds the pth period.
In terms of Fourier series [2], the periodic $F_\mathrm{tar}(x)$ is interpreted as the summation of Sine functions of x,

$$F_\mathrm{tar}(x) = \sum_{n=n_L}^{n_H} F_n(x) = \sum_{n=n_L}^{n_H} \Psi_n \sin\left(2k_n x + \varphi_n + \frac{\pi}{2}\right) \tag{2}$$

where $n_\mathrm{L} = 0$, $n_\mathrm{H} = \infty$, n is an integer. The nth component $F_n(x)$ has a spatial frequency $2k_n$ with $k_n = n\pi/2l$, its amplitude Ψ_n and phase φ_n + p/2 are determined by the Fourier coefficients.

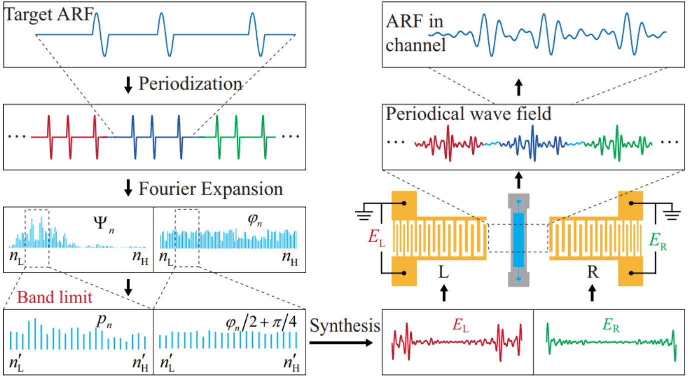

Figure 1: Working mechanism of 1-D FATs. FFT of a target ARF profile gives the amplitudes and phases of monochromatic components, which within a limited band help to synthesize the driving voltage for two opposing sources. An ARF pattern as required is generated in the tweezing area. The prototype is a SAW-driven microfluidic channel.

As the waves travel at a speed c_S(can be different from c_0), decomposition in spatial frequency is then converted to temporal frequency via $\omega_n = k_n c_\mathrm{S}$, and each $F_n(x)$ can be generated by a monochromatic standing wave

$$p_n(x) = p_n \cos\left(\frac{\omega_n}{c_S x} + \frac{\varphi_n}{2} + \frac{\pi}{4}\right) \sin \omega_n t,\ p_n = \left[\frac{\Psi_n \rho_0 c_0^2}{\pi \Phi k_n a^3}\right]^{\frac{1}{2}} \tag{3}$$

We assume the timescale of particle translation as T_p, see Refs. [1]. When the frequency interval in Eq. (2), which is $\pi c_S/2l$, far overweighs $2\pi/T_p$, the pressure field to be synthesized is,

$$p_{\text{syn}}(x) = \sum_{n=n_L}^{n_H} p_n(x) \tag{4}$$

The principle is demonstrated using a surface acoustic wave (SAW) device, and other source types can also be implemented for different applications. The working mechanism of 1-D FATs is in Fig. 1. With a target ARF profile F_{tar} (x) designed through Eq. (1), Fourier expansion in Eq. (2) gives Ψ_n (and in turn p_n) and φ_n. By assuming linear electroacoustic scalings, driving voltages (E_L and E_R) for two opposing sources, L and R, are determined from Eq. (4).

Results

After building a single trap at x=0, ARF represented by x-dependent particle velocity is measured through microparticle image velocimetry (µPIV) [3,4]. In Fig. 2(a), ARF averaged from three repetitive measurements agrees well with the expected F_b(x). The trap width is $\lambda/2$ (measured as the distance between the two zero-crossings surrounding x = 0), where the wavelength $\lambda = 2\pi c_S/\omega_c = 265.3\ \mu$m. Two potential barriers are observed outside the trap, contributing repelling forces pointing outwards. Snapshots of particle acoustophoresis are given in Fig. 2(b), where a single particle line is formed as expected in 6 seconds. Particles ouside the trap are pushed to the secondary traps at x ≈ ±135 μm, i.e., ~ $\lambda/2$ away.

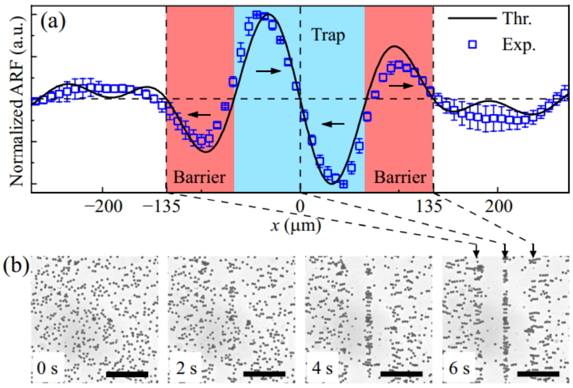

Figure 2: Synthesized single trap in 1-D tweezing. (a) Comparison between the measured ARF, represented by the velocity of 5-µm-radius particles, and the expected ARF as functions of x. (b) Snapshots of particle trapping. Scale bars, 100 *m*m.

Benefiting from reduced trap width, the minimal spacing for independent trapping by FATs is an unprecedented λ/4. The explanation is in Fig. 3(a), where two single-traps, whether band-unlimited or band-limited, merge together when spaced by d = λ/4. In Fig. 3(b), we examine the x-dependent potential field U^r by varing d through numerical analysis. Obviously, the two traps centered at the blue dots coalesce as $d \leq 64$ µm. In Fig. 3(c), two weak traps are identified when d = 66 µm ≈ λ/4. Finally, 1-D particle trappings in Fig. 3(d) show two trapped particle lines as d= 66 µm, while only one can be observed at smaller d.

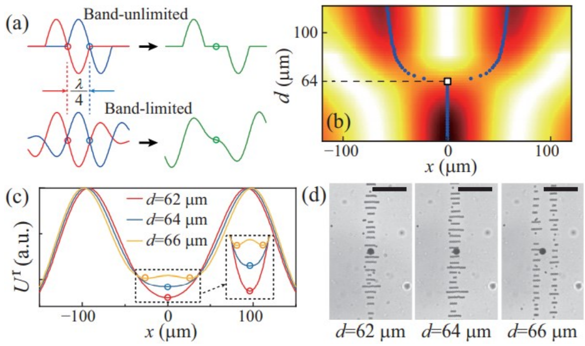

Figure 3: Spacing limit for two traps. (a) Two traps merge as their separated distance is d < λ/2. (b) 1-D potential profiles as functions of d, black: 0, white: 1. (c) Three profiles extracted from (b), corresponding to d = 62, 64, and 66 µm. (d) 1-D trapping, where only d = 66µm (~ λ/4) allows two independent particle lines being trapped. Scale bars, 100 µm.

Conclusion

This work reports a novel way to generate arbitrary ARF by synthesizing non-monochromatic ATs through Fourier series. Multi-objective trappings can be carried out with each trap moving independently. Two or three orthorgonal 1-D fields are decoupled to form 2-D or 3-D FATs. Unprecedented minimal spacing of λ/4 is achieved for independent trapping. *Acoustofluidics 2021 Virtual Conference* on 26 - 27 August 2021.

References

[1] J. W. Ng, C. Devendran, and A. Neild. Lab Chip **17**, 3489 (2017).
[2] J. Wu. *Acoustical tweezers*, J. Acoust. Soc. Am. **89**, 2140 (1991).
[3] S. Liu, G. Xu, Z. Ni, X. Guo, L. Luo, J. Tu, and D. Zhang. Appl. Phys. Lett. **111**, 043508 (2017)
[4] S. Liu, Z. Ni, G. Xu, X. Guo, J. Tu, H. Bruus, and D. Zhang. Phys. Rev. Appl. **11**, 044031 (2019).

Acoustofluidics 2021
26-27 August 2021
Virtual Conference

Generation and transfer of polydisperse droplets using low power surface acoustic waves

Krishnadas Narayanan Nampoothiri[1], Niladri Sekhar Satpathi[1], and Ashis Kumar Sen[1]

[1]Department of Mechanical Engineering, Indian Institute of Technology Madras, Chennai, India
E-mail: 011657@imail.iitm.ac.in, URL: http://www.ashislab.in

Introduction

Generation, transfer, and maneuver of micron-sized droplets is of critical importance in the field of microfluidics for a plethora of applications including electronics cooling [1] and aerosol formation [2]. Even though several microfluidic techniques have been developed for droplet manipulation, precise control of densely packed sub-micron droplets remain a challenge. Hence, it is imperative to develop a platform which can overcome these challenges and perform droplet functionalities efficiently.

Surface acoustic waves (SAWs) can be defined as mechanical vibrations of nanometer amplitudes that propagates on the surface of a piezoelectric substrate [3]. Upon applying an AC electrical signal to interdigitated electrodes (IDTs), at the SAW resonance frequency, waves are formed due to the inverse piezoelectric effect. When SAW encounters a liquid along its path, leaky SAW is introduced into the bulk liquid [3,4]. Through sufficient power, strong capillary waves at the droplet surface overcome capillary stress and result in the mist formation of micron-sized droplets [4–6]. SAW-based nebulization has been reported as an effective technique for extraction of proteins [5] as well as transfer of analytes into a mass spectrometry for peptide detection [6]. Even though wide range of droplet sizes during mist (1-100 μm) have been reported, a systematic and repetitive approach for transfer of these polydisperse droplets onto a substrate has not been demonstrated efficiently. We aim to develop a low power-based SAW device which could transfer polydisperse droplets (1-10 μm) onto a cover slip through tweaking various parameters such as power and time.

Experimental setup

Cr/Au IDTs, of width and interelectrode spacing equal to 25 μm corresponding to the resonance frequency of 39.65 MHz, were patterned on the surface of a 128° rotated Y-cut X propagating lithium niobate ($LiNbO_3$) substrate using standard photolithography and metal etching techniques. Polyester cellulose lint free paper was used as a wick in syphoning liquid from the reservoir to provide a continuous supply of the fluid sample through capillary pressure as depicted in Figure 1. The substrate was inverted, and the generated droplets were transferred onto a cover slip. The contact angle of the drop with the cover slip was measured to be ~ 60° indicating the surface to be hydrophilic. The analysis of the transferred droplets was carried out using 60x objective lens which is connected to an inverted optical microscope as seen in Fig. 1.

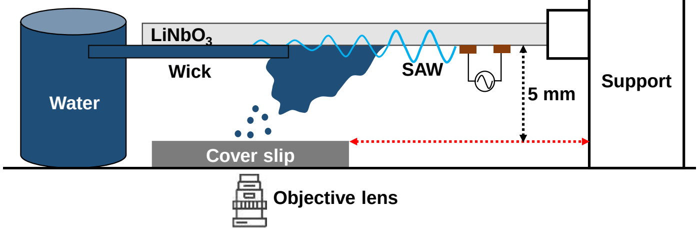

Figure 1: Schematic diagram of the experimental setup.

Results and Discussion

On actuating SAW with a power of 0.2 W (the critical power range [7] for mist generation), using a signal generator and subsequent amplification with a power amplifier, mist was generated within microseconds. When large dense micron-sized droplets got transferred onto the cover slip, due to coalescence, the droplets merged to form larger sized droplets thereby hindering the measurement of minimum droplet size. Therefore, a timer circuit was designed to regulate the power supply for the generation of controlled droplet density for the ease in measurement of the minimum stable droplet size.

The circuit was set at three different timers (30, 50 and 100 ms) and the experiments were conducted for 1.6 s at 0.45 W. Depending on the power on/off cycle for different timers, the frequency for mist generation varied and the distribution of the droplets transferred onto the cover slip differed. Droplet distribution was measured using ImageJ software and Fig. 2 represents the droplet distribution at 0.45 W for various timer circuits. We could observe polydispersity in the droplet size at various cycles for different timer circuits. The mean droplet diameter for various cycles were also tabulated and the mean droplet size ranges from 1-2 μm depending upon droplet count. The modified Kelvin equation [4] for estimating the droplet diameter D can be represented as $D \sim \gamma H^2 We^{0.66}/\mu L^2\, f_c$ where $\gamma = 10^{-2}$ N/m and $\mu = 10^{-3}$ kg/ms are the surface tension and viscosity of the liquid respectively. H and L represents the characteristic height and length of the generated thin film from the wick during SAW and H/L is considered as ~ 0.1 for thin film [4]. We is the acoustic Weber number and is typically taken in the range1-10. By considering inertia forcing of the thin film, capillary wave frequency f_c was calculated as $f_c \sim (\gamma/\rho H^3)^{0.5}$ where $\rho = 10^3$ kg/m^3 and H~1 μm and was observed to be in the order of 1 MHz. The calculated droplet diameter D was observed to agree with experimental range of the droplet sizes (Fig. 2).

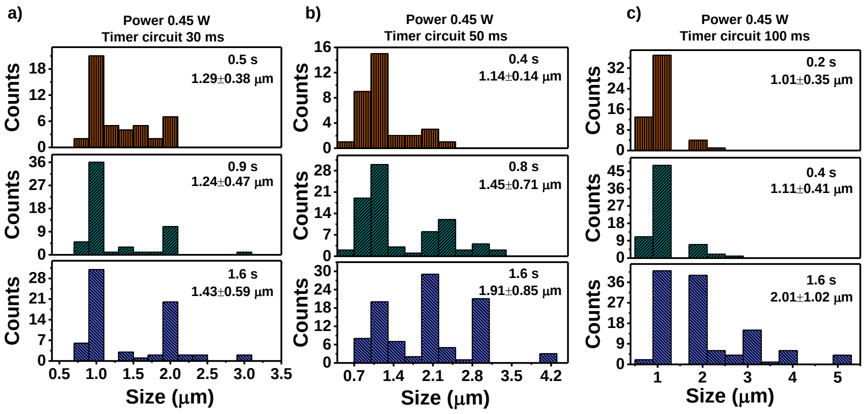

Figure 2: Droplet distribution at various timer circuits a) 30 ms b) 50 ms and c) 100 ms. Droplet mean diameters for different time cycles are also mentioned in each box.

To investigate the effect of actuation power in generating polydisperse droplets, along with 0.45 W, the system was also subjected to 0.2 and 0.3 W. Fig. 3 (a) shows the droplet distribution at 1.6 s for timer circuit of 100 ms. We could observe variation in polydispersity with an increase in power. At high powers, more droplets were transferred as indicated in Fig. 3 (b). Even though the probability of coalescence increases with power (as shown with data representing average droplet interdistance in Fig. 3 (b)), generation and transfer of droplet sizes of the range 5-6 μm will be of interest for cell transfer applications.

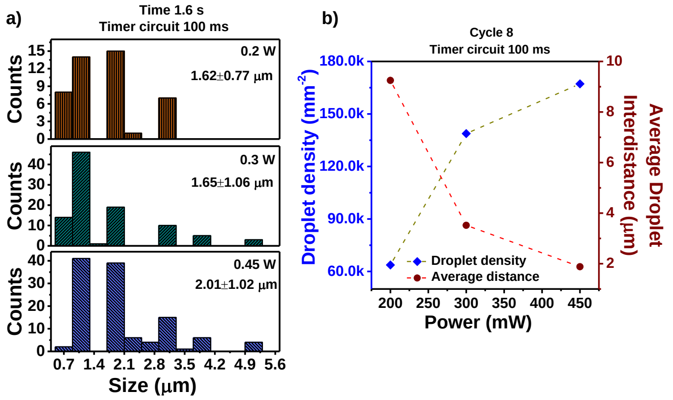

Figure 3: (a) Droplet distribution at various powers for timer circuit 100 ms. (b) Graph representing droplet density and average droplet distance with power.

Conclusion

In summary, we have developed SAW-based microfluidic platform for the generation and transfer of droplets onto a hydrophilic cover slip. By tuning the parameters like power and time, we could achieve polydisperse droplets in the range 1-6 μm which is of significant interest in the transfer of bioreagents for various applications.

References

[1] W. Deng and A. Gomez, Int. J. Heat Mass Transf. **54**, 2270 (2011).

[2] A. R. Metcalf, S. Narayan, and C. S. Dutcher, Aerosol Sci. Technol. **52**, 310 (2018).

[3] A. Sudeepthi, A. Nath, L. Y. Yeo, and A. K. Sen, Langmuir **37**, 1578 (2021).

[4] D. J. Collins, O. Manor, A. Winkler, H. Schmidt, J. R. Friend, and L. Y. Yeo, Phys. Rev. E - Stat. Nonlinear, Soft Matter Phys. **86**, 1 (2012).

[5] A. Qi, L. Yeo, J. Friend, and J. Ho, Lab Chip **10**, 470 (2010).

[6] D. Sun, K. F. Böhringer, M. Sorensen, E. Nilsson, J. S. Edgar, and D. R. Goodlett, Lab Chip **20**, 3269 (2020).

[7] M. Alvarez, J. Friend, and L. Y. Yeo, Nanotechnology **19**, (2008).

Acoustofluidics 2021
26-27 August 2021
Virtual Conference

Droplet impact dynamics on hydrophobic and slippery liquid-infused porous surfaces controlled by propagating surface acoustic waves

Luke Haworth[1]*, Mehdi H. Biroun[1,2*], Prashant Agrawal[1], Bethany Orme[1], Glen McHale[3], Mohammad Rahmati[1], Hamdi Torun[1], Richard YongQing Fu[1]

[1] Faculty of Engineering and Environment, Northumbria University, Newcastle upon Tyne, NE1 8ST, UK
E-mail: luke.haworth@northumbria.ac.uk
[2] Department of Chemical Engineering, University College London, Torrington Place, London WC1E 7JE, UK
[3] Institute for Multiscale Thermofluids, School of Engineering, University of Edinburgh, Kings Buildings, Edinburgh EH9 3FB, UK
[*] These authors have equal contributions.

Introduction

Controlling droplet impact on different solid surfaces is an essential topic in developing diverse types of engineering surfaces. Slippery liquid infused porous surfaces (SLIPs) has recently been used in self-cleaning and anti-icing surfaces[1–3]. This paper introduces a new method to actively control the droplet impact on SLIPs surfaces using surface acoustic wave (SAW) technology. To do that, we designed and fabricated SLIPs on ZnO/Al thin film SAW devices. Our experimental results showed that by applying a SAW wave, the droplets' spreading, and retractions are altered, leading to a change in droplet impact regime.

Experimental Methods

ZnO films deposited onto aluminium plates followed by interdigital transducers (IDTs) fabricated onto the substrate using a standard photolithography and lift-off process. To render the device's surface superhydrophobic, chemically functionalized silica nanoparticles were coated onto the surface of the SAW devices, using a process reported in Ref [4]. The porous nanoparticle structure was then infused with a liquid lubricant to convert the superhydrophobic surfaces into SLIPS.

Droplets of deionized water were generated from a hypodermic needle mounted on a 2D positioner using a syringe pump. The droplets were released from a set height to reach the desired velocity before impacting onto the surface of the device. The capillary regimes which are investigated in this study are in a range that the maximum spreading diameter scales with $We^{0.25}$ [5].The impact sequences and their outcomes were captured from a side view using a high-speed camera. A set of systematic experiments were performed to understand the effects of SAW propagation on the SLIPS and superhydrophobic surfaces on droplet impact dynamics.

Droplet Impact Dynamics without SAW

Figure 1(a) illustrates the droplet impact on the ZnO/Al device's surface without any surface treatment (e.g., non-treated surface, NTS). In this figure, on impact the droplet spreads and then preferentially wets the surface without rebounding. The temporal evolution of the droplet impact on the superhydrophobic surface (e.g., Glaco-treated surface, GTS) is illustrated in Figure 1(b). Here it can be seen that on impact as the droplet spreads to a maximum radius it then uniformly retracts on the surface to forma a jet promoting rebound off the surface. Droplet impact on SLIPS1 (e.g., conformal SLIPS with a minimum lubricant layer thickness in this study) is shown in Figure 1(c). Figure 1(c) clearly shows that for the SLIPS, a capillary neck forms and breaks, leaving behind a smaller droplet on the surface, whereas on the surface of GTS, it appears to be a full rebound.

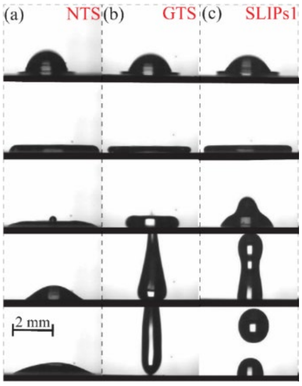

Figure 1. Snapshots of water droplet free impact on the solid surface of ZnO/Al SAW device with (a) no treatment, (b) superhydrophobic surface, (c) SLIPS with lubricant thickness of 2 µm, surface treatment. In all experiments, a droplet with a volume of 3.56 µl is impacting the solid surface with a velocity of 1.4 m/s.

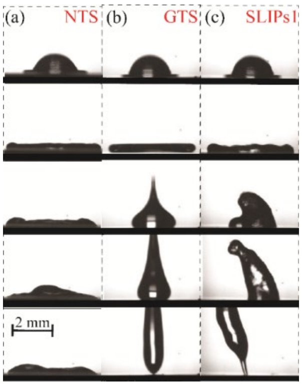

Figure 2. Snapshots of water droplet impact on the solid surface of ZnO/Al SAW device with (a) no treatment (NTS), (b) superhydrophobic and porous surface (GTS), (c) SLIPS with lubricant thickness of 2 µm. In all the experiments, a droplet with a volume of 3.56 µl is impacting the solid surface with a velocity of 1.4 m/s. During the impact, SAW with the power of 8.5 dB (~20 W) is propagating from right to left.

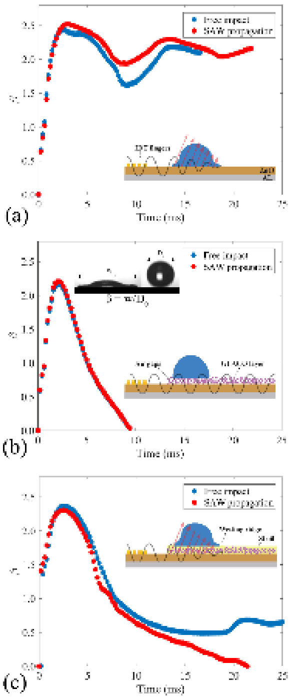

Figure 3: Temporal evolution of contact width for droplet impact on (a) surface without treatment (e.g., NTS), (b) Surface covered with superhydrophobic nanoparticles (e.g., GTS), and (c) conformal SLIPS (SLIPS1). For all the experiments, a droplet with a volume of 3.56 µl is impacting onto the solid surface with a velocity of 1.4 m/s. SAW with a power of 20 W is propagating on the surfaces.

Droplet Impact Dynamics with SAW

Figure 2 shows the recorded droplet impact images onto different substrates while SAWs propagate on the solid surface. Our observations showed that after droplet impact on the untreated ZnO/Al SAW device surface, the applied SAW energy did not change the impact regime. Interestingly, for the porous and superhydrophobic (GTS) surface, no apparent differences were observed in the droplet impact dynamics (compare Figures 1(b) and 2(b)) after applying SAWs. Figure 2(c) shows that after the lubricant has been infused into the superhydrophobic layer (in which a conformal SLIPS is formed and the air gaps in the porous medium are filled), the SAW energy can be effectively transmitted to the droplet during the impact.

For the droplet impact on the NTS (See Figure 3(a)), the experimental results revealed that the SAW energy during the impact is not large enough to overcome the adhesion forces during the impingement, and therefore even by applying a SAW power, the droplet could not be separated from the surface. A comparison between the droplet's normalized contact widths in the impact scenarios on the surface with superhydrophobic (GTS) treatment (See Figure 3(b)) shows that impact dynamics remain unchanged by applying the SAWs. As illustrated in Figure 3(c), for the droplet impact on the SLIPS with a lubricant thickness of 2 µm, SAWs change the impact regime from the partial rebound to complete rebound.

Conclusion

This paper introduced a methodology to control the droplet impact on surfaces using ZnO/Al SAW devices, which were coated with various surface treatments. Our results showed that when the surface was coated with nanoparticles, SAWs did not apparently alter the droplet impact dynamics. However, when a lubricant layer was infused into the nanopores, SAWs can transmit from the device surface through the liquid medium during the droplet impact, thus changing the impact regime, contact time, and rebounding angle. We have found some amazing results, which we are looking forward to presenting for the international acoustofluidics community at *Acoustofluidics 2021 Virtual Conference* on 26 - 27 August 2021.

References

1. Wong, T. S. *et al.* Bioinspired self-repairing slippery surfaces with pressure-stable omniphobicity. *Nature* **477**, 443–447 (2011).
2. Smith, J. D. *et al.* Droplet mobility on lubricant-impregnated surfaces. *Soft Matter* **9**, 1772–1780 (2013).
3. Lafuma, A. & Quéré, D. Slippery pre-suffused surfaces. *Epl* **96**, 1–5 (2011).
4. Geraldi, N. R. *et al.* Double-sided slippery liquid-infused porous materials using conformable mesh. *Sci. Rep.* **9**, 1–8 (2019).
5. Bird, J. C., Dhiman, R., Kwon, H. M. & Varanasi, K. K. Reducing the contact time of a bouncing drop. *Nature* **503**, 385–388 (2013).

Abstract-Only Presentations

Acoustic Devices

AN EASY AND ACCESSIBLE MANUFACTURING METHOD FOR RECONFIGURABLE SAW DEVICES

Roman Mikhaylov[1], Mercedes S. Martin[1], Povilas Dumcius[1], Hanlin Wang[1], Fangda Wu[1], Xiaoyan Zhang[2], Fahad Alghamdi[1], Victory Akhimien[1], Chao Sun[3], Aled Clayton[1], Yongqing Fu[4], Lin Ye[5], Zhiqiang Dong[6], and Xin Yang[1]
[1]Cardiff University, UK, [2]Huazhong Agricultural University, CHINA,
[3]Northwestern Polytechnical University, CHINA,
[4]Northumbria University, UK, [5]Cardiff University School of Medicine, and
[6]Huazhong Agricultural University, CHINA

LAMB WAVE COUPLED RESONANCE FOR SAW ACOUSTOFLUIDICS

Junjie Huang and Xiasheng Guo
Nanjing University, CHINA

A NUMERICAL INVESTIGATION OF THE MIXING ENHANCEMENT IN A Y-JUNCTION MICROCHANNEL INDUCED BY ACOUSTIC STREAMING

Sintayehu Assefa Endaylalu, and Wei-Hsin Tien
National Taiwan Science and Technology University, TAIWAN

Bio-Acoustic Systems

ACOUSTIC DROPLET PRINTING TUMOR ORGANOIDS FOR MODELING BLADDER TUMOR IMMUNE MICROENVIRONMENT

Zhiyi Gong, Yongchang Wei, Fubing Wang, and Shishang Guo
Wuhan University, CHINA

ACOUSTIC FIBROBLAST CELL PATTERNING IN HYDROGEL FOR THREE-DIMENSIONAL CELL NETWORK FORMATION

Le Thi Huong[1], Andreas Lenshof[2], Thomas Laurell[2], and Kyo-in Koo[1]
[1]University of Ulsan, KOREA (ROK) and [2]Lund University, SWEDEN

STUDY OF THE RAYLEIGH LIMIT BY ACOUSTIC FORCE IN MICROGRAVITY

Chloé Dupuis, Xavier Mousset, Lucile Rabiet, Xavier Benoit-Gonin, Mauricio Hoyos, and Jean-Luc Aider
ESPCI, Université de Paris, FRANCE

ACOUSTO-PI: AN INTEGRATED OPTO-ACOUSTOFLUIDIC SYSTEM WITH OPEN-SOURCE ELECTRONICS FOR IN-FIELD DIAGNOSTICS

Jethro Vernon[1], Pep Canyelles-Pericas[2], Hamdi Torun[1], and Richard Yong-Qing[1]
[1]University of Northumbria, UK and [2]University of Twente, NETHERLANDS

Physical Acoustics

PARTICLE CHAIN FORMATION IN ACOUSTOPHORESIS

Thierry Baasch, Wei Qiu, and Thomas Laurell
Lund University, SWEDEN

NUMERICAL SIMULATIONS OF RELOCATION MECHANISM OF COFLOWING IMMISCIBLE FLUIDS EXPOSED TO BULK ACOUSTIC WAVE

Sazid Z. Hoque and Ashis K. Sen
Indian Institute of Technology (IIT), Madras, INDIA

TRAPPING AND “BOUNCING” OF WATER DROPLETS IN OIL-FILLED MICROWELLS UNDER SAW-INDUCED STREAMING

Amal Nath and Ashis K. Sen
Indian Institute of Technology, Madras, INDIA

MODULATED ACOUSTIC RADIATION FORCE IN A CARRIER STANDING WAVE

Mehdi Akbarzadeh, Sebastian Oberst, Shahrokh Sepehrirahnama, and Ben Halkon
University of Technology Sydney, AUSTRALIA

EFFECT OF VIBRATION VELOCITY ON LOW-FREQUENCY SHARP-EDGE ACOUSTIC STREAMING PATTERN

Geyu Zhong[1,2], Chuanyu Zhang[1], Philippe Brunet[1], Laurent Royon[1], YingWen Liu[3], and Xiaofeng Guo[1,2]
[1]Université de Paris, FRANCE, [2]Université Gustave Eiffel, FRANCE, and
[3]Xi'an Jiaotong University, CHINA

3D MODEL OF THE PARTICLE ACOUSTOPHORETIC MOTION IN A RECTANGULAR DEVICE

Abelino Vargas[1,2], Marcela Camacho[1,2], J.D. Muñoz[1], and Itziar González[3]
[1]National University of Colombia, COLOMBIA, [2]International Physics Center (CIF), Biophysics Laboratory, COLOMBIA, and [3]CSIC Spanish National Research Council, SPAIN

MULTIPHYSIC MODEL BASED ON SAW-LIQUID INTERACTION FOR THE PREDICTION OF PHYSICAL STRESSES EXERTED ON CELLS AND TISSUES: SIMULATION VERSUS EXPERIMENT

D.S. Bidouba Sanvany, Francis Kosior, Denis Beyssen, Aude Gigodot, Elisabeth Gaudion, and Frederic Sarry
Université de Lorraine, FRANCE

Acoustic Manipulation

BINARY ACOUSTIC PARTICLE TRAPPING IN GLASS CAPILLARIES

Thierry Baasch[1], Anna Fornell[1,2], Carl Johannesson[1], Johan Nilsson[1], and Maria Tenje[2]
[1]Lund University, SWEDEN and [2]Uppsala University, SWEDEN

SINGLE CELL ENCAPSULATION USING SAW

Andreas Link, Raymond Sparrow, Esther Richter, Mustafa Zaimagaoglu, John McGrath, and Thomas Franke
University of Glasgow, UK

SPIRALING WAVEFRONTS AND DETECTION OF PHASE SINGULARITIES IN OBJECTS IMMERSED IN INHOMOGENEOUS ACOUSTIC FIELDS

Ludovic Alhaïtz, Diego Baresch, Thomas Brunet, Christophe Aristégui, and Olivier Poncelet
University of Bordeaux, FRANCE

CELL PHENOTYPING VIA ACOUSTIC CONTRAST FACTOR BY USING A FILLED TILTED-ANGLE ACOUSTOFLUIDIC DEVICE

Hanlin Wang[1], Joe Boardman[1], Xiaoyan Zhang[1], Chao Sun[2], Meng Cai[3], Jun Wei[3], Zhenlin Wu[4], Yongqing Fu[5], and Xin Yang[1]
[1]Cardiff University, UK, [2]Northwestern Polytechnical University, CHINA, [3]iRegene Pharmaceutical Technology Co., Ltd., CHINA, [4]Dalian University of Technology, CHINA, and [5]Northumbria University, UK

KINETIC AND THERMAL CHARACTERISTICS OF MICRO-DROPLET DRIVEN BY RAYLEIGH SURFACE ACOUSTIC WAVE

Mubbashar Mehmood, Baixin Chen, and Richard Yongqing Fu
Heriot-Watt University, UK

LYOPHILISED MONODISPERSE MICROBUBBLES AS ULTRASOUND CONTRAST AGENT

Ugur Soysal[1], Pedro N. Azevedo[1,2,3], Flavien Bureau[2], Alexandre Aubry[2], Marcio S. Carvalho[3], Amanda C.S.N. Pessoa[4], Lucimara G. de la Torre[4], Olivier Couture[5], Arnaud Tourin[2], Mathias Fink[2], and Patrick Tabeling[1]
[1]ESPCI Paris, FRANCE, [2]Université PSL, CNRS, FRANCE, [3]Pontifical Catholic University of Rio de Janeiro, BRAZIL, [4]University of Campinas, BRAZIL, and [5]Sorbonne Université, CNRS, INSERM, FRANCE

MICROPARTICLE PATTERNING INSIDE CAPILLARY TUBES ON BENDABLE THIN FILM SAW DEVICES

Sadaf MaramiZonouz[1], Mohammad Rahmati[1], Changfeng Jia[2], Tengfei Zheng[2], and Richard Yongqing Fu[1]
[1]Northumbria University, UK and [2]Xian Jiaotong University, CHINA

THREE-DIMENSIONAL STANDING SURFACE ACOUSTIC WAVE SIMULATION MODEL FOR EFFICIENT PARTICLE SEPARATION

Lizhu Liu, Jian Zhou, Dinghong Zhang, and Zhengjia Zhan
Hunan University, CHINA

Acoustofluidics 2021
26-27 August 2021
Virtual Conference

An Easy and Accessible Manufacturing Method for Reconfigurable SAW Devices

Roman Mikhaylov[1], Mercedes Stringer Martin[1], Povilas Dumcius[1], Hanlin Wang[1], Fangda Wu[1], Xiaoyan Zhang[2], Fahad Alghamdi[1], Victory Akhimien[1], Chao Sun[3], Aled Clayton[4], Yongqing Fu[5], Lin Ye[6], Zhiqiang Dong[7], and Xin Yang[1]

[1] Department of Electrical and Electronic Engineering, School of Engineering, Cardiff University, Cardiff CF24 3AA, UK
[2] International Joint Laboratory of Biomedicine and Engineering, Huazhong Agricultural University and Cardiff University, Wuhan, Hubei, 430070, China
[3] School of Life Sciences, Northwestern Polytechnical University, 710072, P.R. China
[4] Tissue Micro-Environment Group, Division of Cancer & Genetics, School of Medicine, Cardiff University, Cardiff CF14 4XN, UK
[5] Faculty of Engineering and Environment, Northumbria University, Newcastle Upon Tyne, Newcastle NE1 8ST, UK
[6] Cardiff China Medical Research Collaborative, Division of Cancer & Genetics, Cardiff University School of Medicine, Cardiff, CF14 4XN, UK
[7] College of Biomedicine and Health, College of Life Science and Technology, Huazhong Agricultural University, Wuhan, Hubei, 430070, China

Email: YangX26@cardiff.ac.uk

Introduction

A development process with easily accessible facilities that can also permit the reconfiguration of a SAW device for different applications could be highly desirable in the acoustofluidic field, since it could facilitate a lower entry point and the ability to test different SAW applications using fewer SAW devices. We present a novel development technique, for both the interdigital transducers (IDTs) and the polydimethylsiloxane (PDMS) microchannel, to create a versatile acoustofluidic device (VAD). The VAD demonstrates precise manipulation of micro-objects at different IDT configurations, that is achieved through a quick assembly and re-assembly of the device using only a vector network analyser (VNA) and no clean room facilities.

Device

The IDTs are manufactured using a flexible printed circuit board (FPCB) pre-patterned with interdigital electrodes (IDEs) and are mechanically coupled with a 128° Y-cut 3-inch lithium niobate ($LiNbO_3$) piezoelectric substrate suing a mostly 3D printed mechanical jig, as shown in Fig. 1. The main components of the assembled VAD can be summarised as follows: heatsink (supports the entire device and dissipates heat), temperature sensors (measure the IDT temperature), $LiNbO_3$ (produces SAWs), FPCB IDEs (convert RF to SAWs), silicon pads (evenly distribute the clamping force), localised pressers (apply the clamping force), force sensitive resistors (FSRs) (measure the clamping force), FSR roofs (hold and press the FSRs), M5 screws (generate the clamping force) and main holders (hold the whole structure onto the heatsink). The PDMS microchannels were manufactured using a 3D printing mould avoid the use of clean room and were bonded to the to the device using an acrylic top and a mechanical presser.

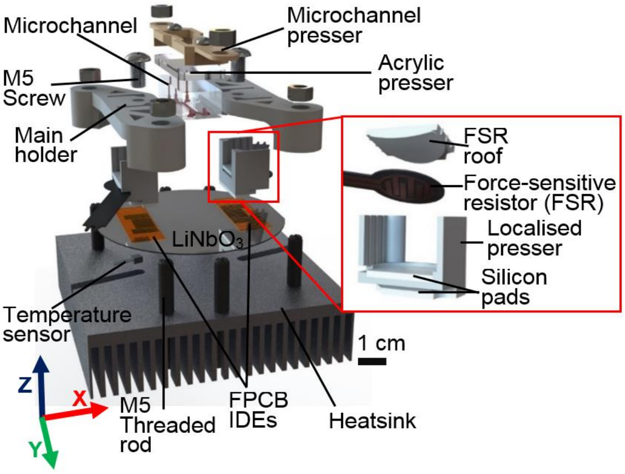

Figure 1. 3D exploded view of the VAD with an inset presenting the assembly and components at the localised pressers.

Results

The VAD could easily generate traveling SAWs, but to create a strong standing SAW precise manual alignment of the two IDTs was required. This was achieved by monitoring the *S* parameters of the device, that were measured using a VNA. The insertion loss (S_{21}) peak was correlated with the angle between the IDTs. The highest S_{21} peak was always observed when the IDTs were parallel and thus acted to monitor the quality of the alignment. While the reflection coefficient (S_{11}) monitored the contact quality between the substrate and the IDTs, with a dip of -28 dB being achieved. But alternatively, the contact quality could also be monitored using the FSRs, which can also indicate the optimal contact quality. A 500 µm PDMS microchannel was developed using our 3D printed mould and used for the microsphere alignment tests. It is demonstrated that the IDTs when parallel create parallel PN lines, Fig. 2A, while by rotating one of the IDTs resulted with the rotation of the PN lines, Fig. 2B. The VAD is also capable of being reconfigured to accommodate tilt angle operation, by designing and 3D printing custom microchannel pressers. These presser with a wider channel demonstrated the ability to tilt the channel and create PN lines at 15°, Fig. 2D, and -5°, Fig. 2E, being observed withing the channel.

Finally, the device, parallelly aligned, is actuated at different power inputs of 15, 20, and 27 dBm and the acoustic energy density is calculated after 99% of the microspheres have aggregated at a PN line, Fig. 3. The power inputs of 15, 20 and 27 dBm have a respective acoustic energy density of 4.6, 9.9, and 36 J/m^3, which also corresponded to an aggregation time lapse of is ~1.9, ~0.6, and ~0.3 sec. This demonstrated that the acoustic radiation force exerted, or the velocity, of microsphere aggregation in the device can be accurately controlled by the input power.

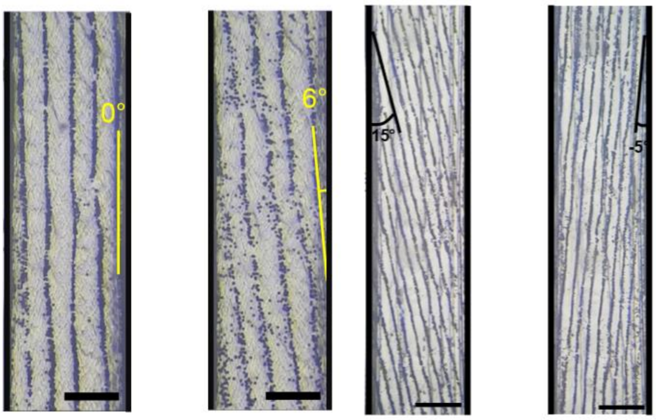

(A) (B) (C) (D)

Figure 2. Image of PN lines when IDTs (A) are parallel or (B) one IDT is rotated (200 µm scale bar). Aggregated microspheres on the PN lines of (D) 15° and (E) −5° angles, in regard to the microchannel wall (450 µm scale bar).

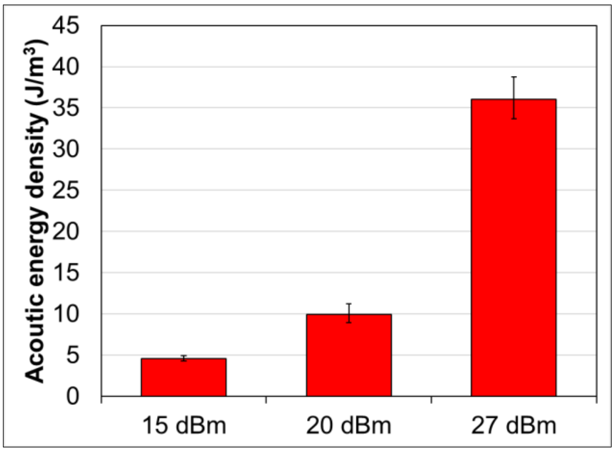

Figure 3. The VAD being driven at 15, 20 and 27 dBm power input and generating the average acoustic energy densities for the three input powers are 4.6, 9.9, and 36 J/m^3, respectively (n = 3).

Conclusion

The manufacturing of VAD demonstrates that a SAW device can be manufactured using accessible means, that is capable of different configuration for testing/ prototyping applications. The VAD components were developed using mostly a 3D printer and assembled using simple mechanical means and with a use of a VNA demonstrated its capability to precisely align microspheres at parallel and tilt angle configurations, with the microsphere aggregation velocity being controlled with different power inputs.

References

[1] R. Mikhaylov, M. S. Martin, P. Dumcius, H. Wang, F. Wu, X. Zhang, F. Alghamndi, V. Akhimien, C. Sun, A. Clayton, Y. Fu, L. Ye, Z. Dong and X. Yang, A Reconfigurable and Portable Acoustofluidic System Based on Flexible Printed Circuit Board for the Manipulation of Microspheres, Journal of Micromechanics and Microengineering, 2021, 31, 074003

Acoustofluidics 2021
26-27 August 2021
Virtual Conference

Lamb wave coupled resonance for SAW acoustofluidics

Junjie Huang, Xiasheng Guo

Key Laboratory of Modern Acoustics (MOE), Department of Physics, Collaborative Innovation Center of Advanced Microstructure, Nanjing University, Nanjing 210093, China
Email: 1747589259@qq.com

Introduction

High in-fluid energy densities are expected to promote the acoustic radiation force (ARF) or acoustic streaming in the acoustofluidic chips. However, SAW acoustofluidics convert electrical energy into acoustic energy at low efficiency, and waves in the sidewalls and the lid are usually neglected but actually play important roles.[1, 2] Here, a surface acoustic wave (SAW)-driven acoustofluidic chip of high energy efficiency is proposed through model analysis. The chip supports propagation of Lamb waves in the lid above a fluid-filled channel. Compared to resonant SAW acoustofluidics (RSA), Lamb wave coupled RSA can make the energy tripled or higher.

Methods

By assuming translational invariance along the y direction, the *x-z* cross section of an LC-RSA chip is sketched in Fig. 1(a). It includes a piezoelectric substrate and two identical IDTs on its upper surface, sidewalls, a lid, and a fluid-filled cavity. The density and longitudinal and transverse wave speeds in the sidewalls and the lid are ρ_w, $c_\mathrm{L,w}$, $c_\mathrm{T,w}$, and ρ_l, $c_\mathrm{L,l}$, $c_\mathrm{T,l}$, respectively. The fluid has density ρ_0, sound velocity c_0, and shear viscosity μ. SAWs of frequency f generated from the IDTs propagate along the upper surface of the substrate at a speed c_SAW and leak into the fluid at the Rayleigh angle $\theta = \sin^{-1}(c_0/c_\mathrm{SAW})$.[3]

As illustrated in Fig. 1(b), Lamb waves propagating in the lid also leak into the fluid. When the in-channel waves impinge on the sidewalls, wave refractions can generate both longitudinal and transverse waves in the walls. To enable improved in-channel resonance, the sidewalls allow total reflections as waves incident at $\alpha = \pi/2 - \theta$.

Dispersion behaviors of the Lamb modes can be obtained using the Rayleigh-Lamb equation:[4]

$$\frac{\tan(sd/2)}{\tan(qd/2)} = -\left[\frac{4k_\mathrm{p}^2 qs}{\left(k_\mathrm{p}^2 - s^2\right)^2}\right]^{\pm 1} \tag{1}$$

where $k_\mathrm{p} = \omega / c_\mathrm{p}$ is the wave number, c_p the phase velocity, $\omega = 2\pi f$ the angular frequency, $q = (k_\mathrm{p}^2 - k_\mathrm{L}^2)^{1/2}$, $s = (k_\mathrm{p}^2 - k_\mathrm{T}^2)^{1/2}$, $k_\mathrm{L} = \omega/c_\mathrm{L,l}$ and $k_\mathrm{T} = \omega/c_\mathrm{T,l}$ are the wave numbers of the longitudinal and transverse waves, Respectively, defines c_p of symmetric and asymmetric Lamb modes as functions of the frequency-thickness-product ($\gamma = f \times d$).

An eigenmode in the *x-z* cross section is described as

$$p(x,z) = p_a \sin(k_x x)\cos(k_z z),\ (-w/2 < x < w/2, 0 < z < h) \tag{2}$$

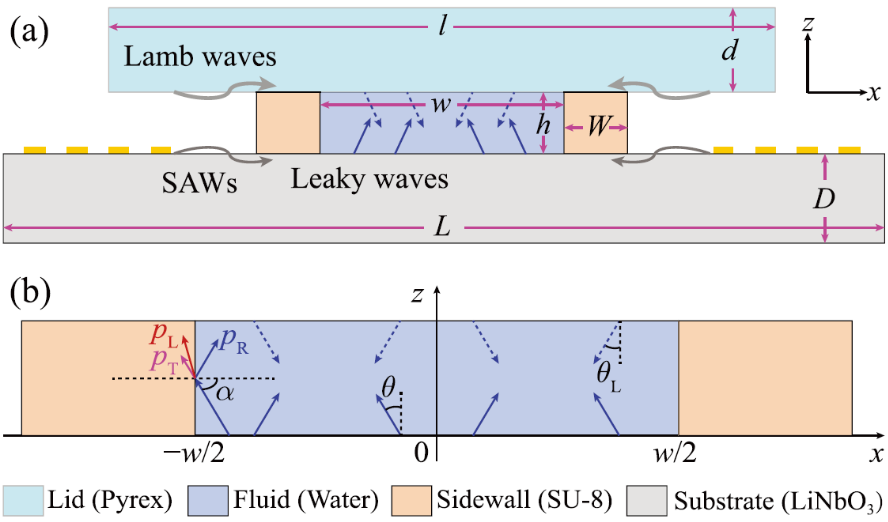

Figure 1:(a) The *x-z* cross section of an LC-RSA chip. (b) Leaky SAWs (solid blue arrows) and Lamb waves (dashed blue arrows) in the fluid and the reflected (P_R) and refracted waves (P_L: longitudinal, P_T: transverse) at the fluid–sidewall interface.

p_a is the pressure amplitude, $k_x = n_x\pi/w$ and $k_z = n_z\pi/h$ are the x- and z-components of the in fluid wave vector k_0, n_x, n_z = (0),1,2,3,… are the numbers of wave nodes in corresponding directions.

The channel sizes is then determined as

$$w = \frac{n_x \lambda_{\mathrm{SAW}}}{2}, \quad h = \frac{n_z \lambda_{\mathrm{SAW}}}{2\cot\theta}. \tag{3}$$

$\lambda_{\mathrm{SAW}} = c_{\mathrm{SAW}}/f$ is the SAW wavelength. An LC-RSA chip further requires $\theta = \theta_L$, such that both the SAWs and Lamb waves are coupled into the resonance. This gives $c_p = c_{\mathrm{SAW}}$, which helps to select γ and determine the working frequency. An example of the protocol is demonstrated here. we choose 128° Y-X lithium niobate ($LiNbO_3$) as the substrate, θ = 22.07°, $c_{T,w}$ = 1800 m/s, γ = 2780.7 MHz/μm, d = 200 μm，f_d =13.9035 MHz, ω = 143.1 μm and h = 58.0 μm, D = 500 μm, L = 1.5 cm, l = 5725.2 μm， W = 29.0 μm .The chip is examined through FE modeling using COMSOL Multiphysics (v5.4, COMSOL, Sweden), and the modeling method is similar to “Model S” in Ref. 2; only that material damping and viscosity are ignored. Specifically, the “Piezoelectric Devices,” “Solid Mechanics,” and “Pressure Acoustic, Frequency Domain” interfaces are, respectively, used for modeling the substrate, the sidewalls and the lid, and the fluid.

Result

With the obtained pressure fields, the device performance is measured through the in-fluid acoustic energy W_{ac}

$$W_{ac} = \int \left(\frac{1}{2}\rho_0 \left\langle \boldsymbol{v}^2 \right\rangle + \frac{1}{2}\frac{1}{\rho_0 c_0^2}\left\langle p^2 \right\rangle \right) dxdz \tag{4}$$

At each frequency, similarity between the obtained field and the theoretical (1, 1) mode (calculated at $f = f_d$) is examined using the matching parameter,

$$S = 1 - \int \left| \frac{\tilde{p} - \tilde{p}_{ref}}{\tilde{p}_{\mathrm{ref}}} \right| dxdz \tag{5}$$

$$\tilde{p} = \left| p / p_{\max} \right|, \; \tilde{p}_{\mathrm{ref}} = \left| p_{\mathrm{ref}} / p_{\mathrm{ref,max}} \right|$$

p_{ref} is the reference pressure field obtained from Eq. (2), and $p_{\max}$ and $p_{\mathrm{ref,max}}$ are the maximum amplitudes in p and p_{ref} .

W_{ac} and S as functions of f are plotted in Fig. 2(a). In the W_{ac} curve, the highest peak $W_{ac,R} = 1.33 \times 10^{-4}$ J/m is found at $f = f_A$ = 13.9077 MHz. f_A is then confirmed as the actual resonant frequency (f_R), giving a frequency deviation $\varepsilon_f = |(f_R - f_d)/f_d| \approx 0.3$. At $f = f_R$, the matching parameter is S = 0.76. Comparison between the theoretical mode in Fig. 2(b) and the simulated pattern(at $f = f_R$) in Fig. 2(c) shows that the LC-RSA chip exhibits similar field distributions to the expected one. Therefore, the target eigenmode (1, 1) is produced at high fidelity.

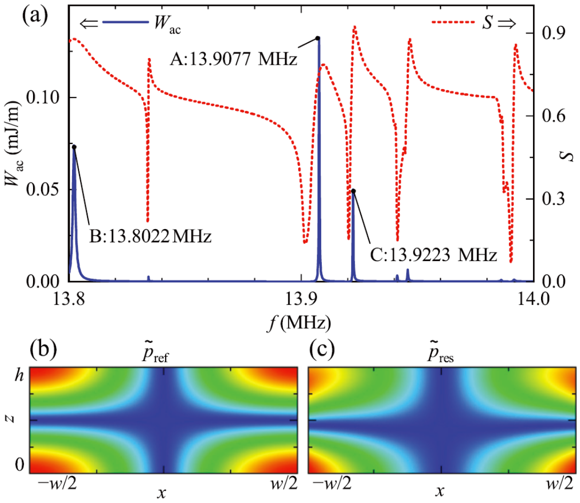

Figure 2: (a) The acoustic energy W_{ac} (solid line) and matching parameter S (dashed line) as functions of f for the (1, 1) LC-RSA chip and the in-channel normalized pressure pattern of (b) theoretical results at f_d = 13.9035 MHz and (c) simulated results at f_R = 13.9077 MHz.

Conclusion

In summary, LC-RSAs benefit from coupling both SAWs and Lamb waves into the eigenmode resonances of acoustofluidic channels. This kind of SAW chip can work at high energy efficiencies with the temperature being effectively controlled. Meanwhile, resonance frequencies can be located easily as the deviation is very small.

References

[1] N. R. Skov and H. Bruus, and A. Neild. Micromachines 7, 182 (2016).
[2] Z. Ni, C. Yin, G. Xu, L. Xie, J. Huang, S. Liu, J. Tu, X. Guo, and D. Zhang, Lab Chip 19,2728–2740 (2019).
[3] M. Gedge and M. Hill, Lab Chip 12, 2998–3007(2012).
[4] J. L. Rose, Ultrasonic Guided Waves in Solid Media (Cambridge University Press, Cambridge, 2014).

Acoustofluidics 2021
26-27 August 2021
Virtual Conference

A numerical investigation of the mixing enhancement in a Y-junction microchannel induced by acoustic streaming

Sintayehu Assefa Endaylalu[1] and Wei-Hsin Tien[1]

[1]Department of Mechanical Engineering, National Taiwan Science and Technology University, Taipei City, Taiwan
E-mail: sintaman2001@gmail.com

Introduction

Acoustofluidics is the combination of acoustics and microfluidics that is used to move and manipulate microparticles in microchannels, which has been implemented for many applications such as microfluidic pump [1], bimodal signal amplification [2], mixing and migration of micro-size particles [3]. Acoustic streaming is caused by the time-averaged nonlinear dynamics of the fluid-solid interaction in a viscous flow [4] and can be used to drive flows inside the microchannel. The mixing of two or more fluids is a critical problem process in many microfluidic devices because the flow is very laminar due to the small contact area. Y-junction microchannel is one of the microchannel geometrical configurations often used in mixing applications, its configuration is generally defined by their two inlets and with the single outlet. The purpose of this study is to use acoustic streaming around the Y-microchannel junction region to generate two counter vortices to assist mixing of the fluids. A numerical study was conducted for this acoustofluidic device and different parameters such as oscillation amplitude, frequency, geometrical design and their effects to vorticity generation were tested. The simulation results show that sharper 30^o top edge angle is 48.02% more effective than other angles i.e. 60^o and 82.37^o. It is also found that higher oscillation amplitude is 88.2% more effective to vortices generation compared to low oscillation amplitude in this simulation result.

Materials and Methods

The CAD design of the microchannel in the current study is shown in figure 1(a). A triangle structure is put at the junction region of Y-shaped channel which separated by a 120^o gap. Different fillet dimensions were tested in order to reduce the channel edge effect and increase the junction volume. The triangular structures added have 30^o, 60^o, 82.37^o tip angles and were compared with the baseline case with simply the Y-junction. The numerical scheme is modeled using COMSOL Multiphysics 5.6 software[5], in which the Thermoacoustics and Laminar Flow Physics modules were included to solve both the acoustic field and acoustic stream flow inside the Y-microchannel. Oscillation boundary condition at 13kHz frequency was implemented at the tip of the triangular structure with a 1µm fillet radius. The trajectories of microspheres with 1µm diameter released from both inlets to the single outlet of the microchannel, which are driven by the streaming flow and radiation force, was further modeled using the Particle Tracing for Fluid Flow module.

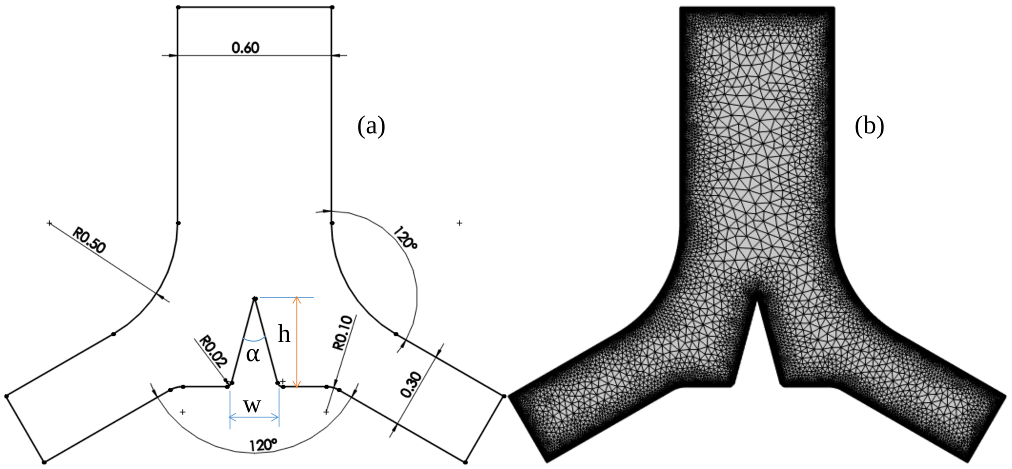

Figure 1: (a) Concept of Y-microchannel configuration: dimensions in mm, (b) Computational mesh

The water domain is surrounded by solid walls that cannot be moved. Therefore, the maximum element computational mesh is generated from the boundaries 0.75δ and 12δ in the bulk of fluid region as shown in figure 1(b). δ is the viscous boundary layer thickness.

Result and Discussion

Figure 2 illustrates the acoustic streaming generation and particle tracing in the y-microchannel in the junction area at 30^{o} top edge triangle geometry with 0.016μL/min and 13kHz operation frequency. The acoustic streaming velocity is greatest near the triangle structure sharp top edge. It originates from this sharp edge and generates two counter-rotating equal vortices from each side inlets of the junction region as shown in figure 2(a). The 1μm diameter suspended particles then move and follow its trajectories, as shown in figure 2(b), (c) and (d) at the t = 1second, 4second, and 10second, respectively.

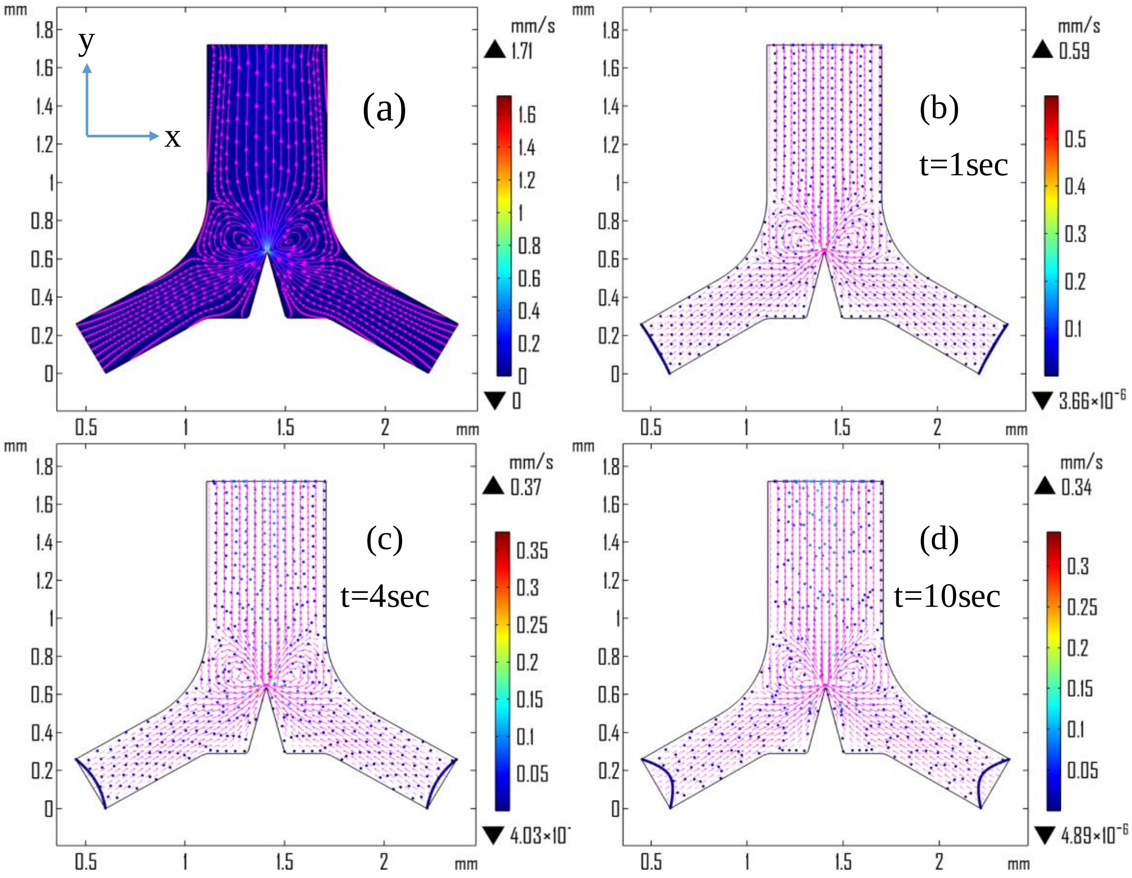

Figure 2: (a) acoustic stream velocity profile, (b), (c) and (d) particle trajectory velocity vector field at a time of 1 sec, 4 sec and 10 sec, respectively.

The streaming strength of vortices depends on top geometry angle, and vibration amplitude. It is more powerful when the angle is small, and the vibration amplitude is high.

Conclusion

In this study, a numerical simulation was conducted to model the generation of acoustic streaming and the motion of 1μm diameter microsphere inside a novel Y-junction microchannel mixer configuration. The results indicate that a 99.7% of vorticity generation improvement using acoustic streaming around 120^{o} Y-microchannel junction region. The vorticity strength generation is stronger at 30^{o} geometry, and weaker at high 82.37^{o} top edge angle, which are all much very stronger than the simple Y-junction configuration to enhance mixing. The 1μm particle motion due to Stoke's drag and acoustic radiation forces can be used to compare with future experimental results.

References

1. Ozcelik, A. and Z. Aslan, *A practical microfluidic pump enabled by acoustofluidics and 3D printing.* Microfluidics and Nanofluidics, 2021. **25**(1): p. 10.
2. Hao, N.J., et al., *Acoustofluidics-Assisted Fluorescence-SERS Bimodal Biosensors.* Small, 2020. **16**(48): p. 11.
3. Gelin, P., et al., *Study on the mixing and migration behavior of micron-size particles in acoustofluidics.* Chemical Engineering Journal, 2019. **369**: p. 370-375.
4. Bach, J.S. and H.J.P.R.L. Bruus, *Suppression of acoustic streaming in shape-optimized channels.* 2020. **124**(21): p. 214501.
5. *COMSOL Multiphysics 5.6*. 2021; Available from: www.comsol.com.

Acoustofluidics 2021
26-27 August 2021
Virtual Conference

Acoustic droplet printing tumor organoids for modeling bladder tumor immune microenvironment

Zhiyi Gong [1], Yongchang Wei[2], Fubing Wang[3] and Shishang Guo[1]

[1] Key Laboratory of Artificial Micro- and Nano-structures of Ministry of Education, School of Physics and Technology, Wuhan University, Wuhan 430072, China (Times New Roman 11 pt)
E-mail: 1158296527@qq.com
[2] Department of Laboratory Medicine and Center for Single-Cell Omics and Tumor Liquid Biopsy, Zhongnan Hospital of Wuhan University, Wuhan 430071, China
[3] Department of radiation & medical oncology, Zhongnan Hospital of Wuhan University, Wuhan 430071, China

Introduction

As the second most common malignant tumor of the genitourinary system, bladder cancer has a poor prognosis and the conventional treatment is highly toxic. Therefore, an in vitro tumor model is urgently needed as a preclinical tool to guide personalized patient treatment. The traditional two-dimensional culture model is difficult to simulate three-dimensional solid tumors, and the PDX model is limited by the physiological differences between humans and animals. In contrast, organoid is derived from the patient, can reconstruct the complexity within the tissue, and can be used as a novel in vitro tumor 3D model. However, most of the currently prepared organoids have the challenges of not being able to preserve the tumor immune microenvironment, not being able to control the size of the organoids, being time-consuming and troublesome to recover[1]. Therefore, using the characteristics of low damage to cells and non-invasive operation of acoustic waves, we have rapidly prepared bladder tumor organoids that can preserve the tumor microenvironment and have controllable size by using open-cavity acoustic droplet printing device, which has no introduction of oil phase, low energy application, and can excite picoliter droplets[2]. Then the organoid was co-cultured with autologous-derived immune cells for two days to expand a large number of tumor-reactive T cells in vitro, providing a novel therapeutic option for rapid immunotherapy[3].

Results and discussion

The nozzle free acoustic droplet printer was based on surface acoustic waves (SAW) to fabricate tumor organoids. The acoustic droplet bioprinter consists of an open chamber and a pair of focused interdigital transducers (FIDTs) deposited on lithium niobate ($LiNbO_3$) substrate, allowing control of droplet volume (31±5.7~200±16.57nL) and droplet position (defined on x, y axes), respectively. The open chamber is used to store various bio-inks. High concertation (30 million·mL-1) of mouse derived bladder tumor cells mixed with bladder organoid culture medium and Matrigel were loaded into open cavity for automated droplet ejection. When a sinusoidal radiofrequency (RF) signals at the resonant frequency is applied to IDTs, the surface of the $LiNbO_3$ will generate symmetrically propagating surface acoustic waves (SAWs). These SAWs diffracted into the liquid at Rayleigh angles, resulting in disturbances at the air-liquid interface and generating an intense acoustic radiation force at the geometric focus point beneath the liquid interface. The acoustic radiation force and the viscous normal stress generated by the acoustic flow act together at the focal point to cause the liquid surface to bulge upward, forming an elongated jet that overcomes the surface tension of the liquid to pinch off one droplet at the end of jet. Tumor cell mixture was encapsulated in the ejected droplets and deposited on the hydrophobic substrate above, as shown in Figure 1A.

The polydimethylsiloxane (PDMS) hydrophobic substrate, with well-defined nanoembossed structure was obtained by replicating the surface of the rose petals. The use of this bionic structure does not require additional chemical processing and the introduction of chemical reagents to achieve hydrophobic effects, and the operation is simple, reproducible and biocompatible. Acoustic droplet printer excites droplets upward to the hydrophobic layer, forming inverted droplets. The hydrophobic interface reducing the contact area between the cells and the substrate surface, allows the cell-laden droplets to be more spherical rather than dispersed on the surface, thereby so that reducing the loss of cells due to adhesion to the surface. The volume of droplets ejected by the acoustic printer is in the picolitre-microliter level, which is much smaller than the volume of droplets deposited by inkjet printers or pipette. We can easily release the organoids for subsequent culture due to the hydrophobicity of the biomimetic PDMS substrate. Cells in the micro inverted droplets aggregated on the basis of gravity, which is further enhanced by Matrigel in the process of temperature control. At 4°C, Matrigel is in a liquid state, and the liquid state facilitates the settling of cells. It allows and high concentration of cells to settle freely in tiny droplets (31 to 200 nL), accelerating spheroid formation, compared to the large volume of droplets (3 μL to 50 μL) in the conventional method.

The experimental results demonstrate that organoids fabricated with acoustic droplets can still retain immune components analogous to the original tissue over a period of 2 weeks. The mouse derived bladder tumor organoid generated by acoustic printer preserved integrated immune component without artificial reconstitution.

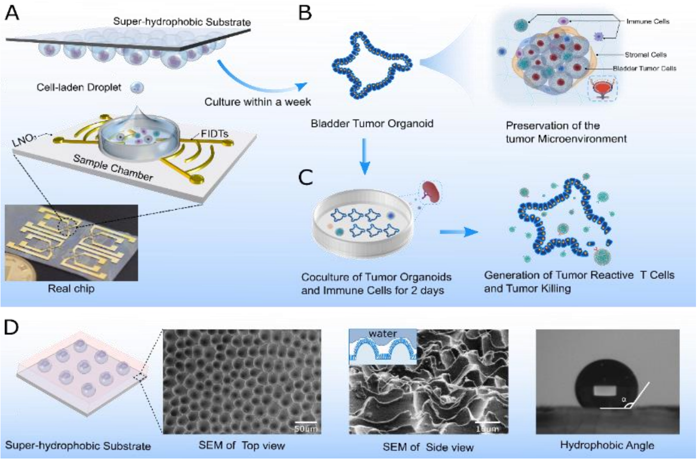

Figure 1: Working principle of acoustic droplet-based organoid printing platform (A) Schematic figures of bladder tumor organoid formation. (not to scale). (B) Schematic of organoid preserved the immune microenvironment of bladder tumor. (C) Schematic of bladder tumor organoid co-cultured with autologous immune cells derived from spleen to generate tumor reactive T cells. (D) The SEM image and contact angle of hydrophobic substrate.

Co-culture organoids and immune cells

We reported a methodology of co-culture autologous immune cells and mouse derived bladder tumor organoid, that preserved the immune microenvironment, to study their interactions at a personalized level. Tumor recognition by cytotoxic T cell was evaluated by staining IFNγ, perforin and Granzyme B. Secretion of perforin, IFNγ and granzyme B in CD8+ T cells was induced by autologous organoid stimulation after 48 hours of co-culture. In addition, to assess whether T cells entered in the organoids or just remained in the culture medium during the co-culture process, we performed immunostaining on the bladder tumor organoids and immune cells in advance. we observed a homogeneous and deep infiltration of immune cells into the bladder tumor organoids in this co-culture system. Thus, bladder tumor organoids with an immune microenvironment could be rapidly produced with acoustic droplets within a week after isolation, and tumor-killing T cells were generated after two days of co-culture with autologous lymphocytes. Overcoming the time difficulty of immunotherapy and providing a novel immunotherapeutic alternative.

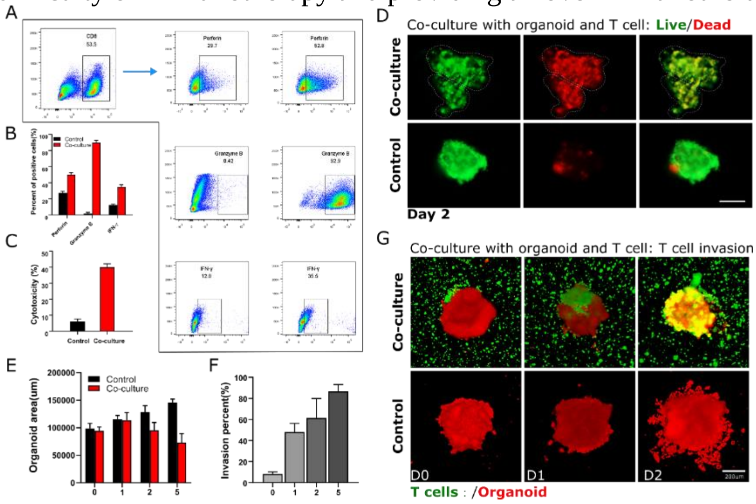

Figure 2: Co-culture with autologous bladder tumor organoids induced tumor reactivity of autologous T cells (A) and (B) Generation of tumor reactive T cells by co-culture tumor organoid and immune cells (C) Cytotoxicity of T cells after co-culture (D) Live/dead staining of organoids after co-culture at day 2 of co-culture (E) Variation of organoids size after co-culture (F) The invasion percent increased over the co-culture days. (G)T cell invasion in organoids during co-culture. Scale bar: 200μm.

Conclusion

We proposed a novel acoustic droplet based platform in improving the tumor organoid formation time using, homogeneity, throughput and viability. The acoustic droplet printer is nozzle-free, will not cause nozzle clogging during organoid preparation, and the device is reusable and also suitable for variety of cell types. As a proof of concept, the platform can prepare tumor spheroids within one day and quickly cultivate them into organoids (within a week), and the organoids prepared by this method can still retain the immune microenvironment similar to the primary tissue within two weeks. It overcomes the limitation that existing organoid models cannot realistically mimic the tumor microenvironment.

References

[1] J. A. Brassard, M. Nikolaev, T. Hubscher, M. Hofer, M. P. Lutolf. Nat Mater (2021), **20**, 22.
[2] K. Chen, E. Jiang, X. Wei, Y. Xia, Z. Wu, Z. Gong, Z. Shang, S. Guo. Lab Chip (2021), **21**, 1604.
[3] K. K. Dijkstra, et al. Cell. (2018), **174**, 1586.

Acoustic fibroblast cell patterning in hydrogel for three-dimensional cell network formation*

Le Thi Huong[1], Andreas Lenshof[2], Thomas Laurell[2, #] , and Kyo-in Koo[1, #]

[1]Department of Biomedical Engineering, School of Electrical Engineering, University of Ulsan, Ulsan, Republic of Korea
E-mail: lehuong94alhp@gmail.com, URL: http://mdl.ulsan.ac.kr
[2]Department of Biomedical Engineering, Lund University, Lund, Sweden

* This abstract is a summary of authors' publication in *Micromachines* at 2021[1].

# These authors equally contribute as corresponding authors.

Introduction

In the field of engineered organ, three-dimensional network-structured tissue has been long-sought goal. Within engineered tissue, cells should be sufficiently close (within 200 µm) to uniformly distributed blood capillaries in order to prevent necrotic core formation [2], induced by diffusion-limited oxygen and nutrient supply [3-5]. Hence, development of engineered 3D microvascular networks are critical in therapeutic applications of engineered tissue [6, 7]. This abstract presents a direct extrusion method combined with ultrasound standing waves to manipulate fibroblast cells into a network structure with junctions and branches. A square-shaped glass capillary was continuously perfused by fibroblast cells suspended in sodium alginate generated a hydrogel string. In the transition from one stream to four streams where the standing wave frequency was shifted from 2 MHz to 4 MHz the aligned fibroblast cells were continuously rearranged into branched structures.

Materials and Methods

A 400 µm square-shaped glass capillary (VitroCom, NJ, USA) was glued to one 2 MHz and one 4 MHz ultrasound transducer (MEGITT A/S, Kvistgaard, Denmark) for actuation (Fig. 1a). The alginate hydrogel was mixed with 200 µL, 10-micrometer (diameter) polystyrene microparticles, with 1.1×10^8 microparticles/mL (MERCK, Madison, USA) and 3 mL of 0.3% (w/v) sodium alginate (MERCK, Madison, USA). For the cell manipulation experiment, 200 µL of 1×10^7 cells/mL fibroblast cell (NIH/3T3) was suspended in 3 mL of autoclaved 0.3% (w/v) sodium alginate. The solution was injected into a beaker of 300 mM $CaCl_2$ (MERCK, Madison, USA) for immediate cross-linking. The fabricated cell scaffolds were cultured at 37 °C, 5% CO_2 and the culture medium was replaced every 2 days. During culturing, on day 1, day 3, day 5 and day 10, the cell scaffolds were stained with LIVE/DEAD staining solution (Molecular Probes, USA) for cell viability monitor.

Acoustic microparticles patterning in the sodium alginate hydrogel

When applying 2 MHz ultrasound in a 400 µm square-shaped glass capillary, the acoustic radiation force focused the microparticles into one stream at the center of the capillary (Fig. 1b) and four parallel lines of microparticles were generated in the case of 4 MHz (Fig. 1c, d). When 2 MHz and 4 MHz of frequency was applied alternating, the microparticles were aligned to one stream or four streams according to the selected actuation frequency. That resulted in the manipulated microparticles continuously and repeatedly branching out into to four streams and converging into one stream inside the alginate hydrogel (Fig. 1e -g).

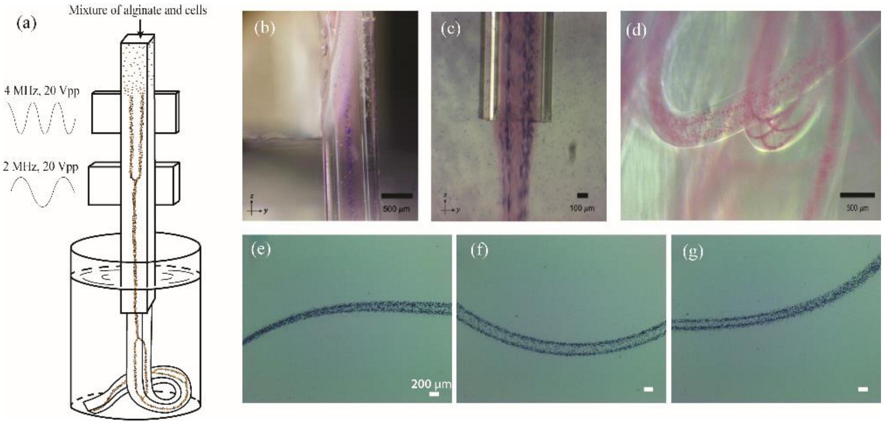

Figure 1. (a) The conceptual sketch of the network generator. (b), (c) The view of the focused particles in the x-direction at 2MHz and 4MHz, respectively. (d) The generated microparticle network in calcium alginate hydrogel. (e-g) The manipulated microparticles in transition between one and four streams or vice versa.

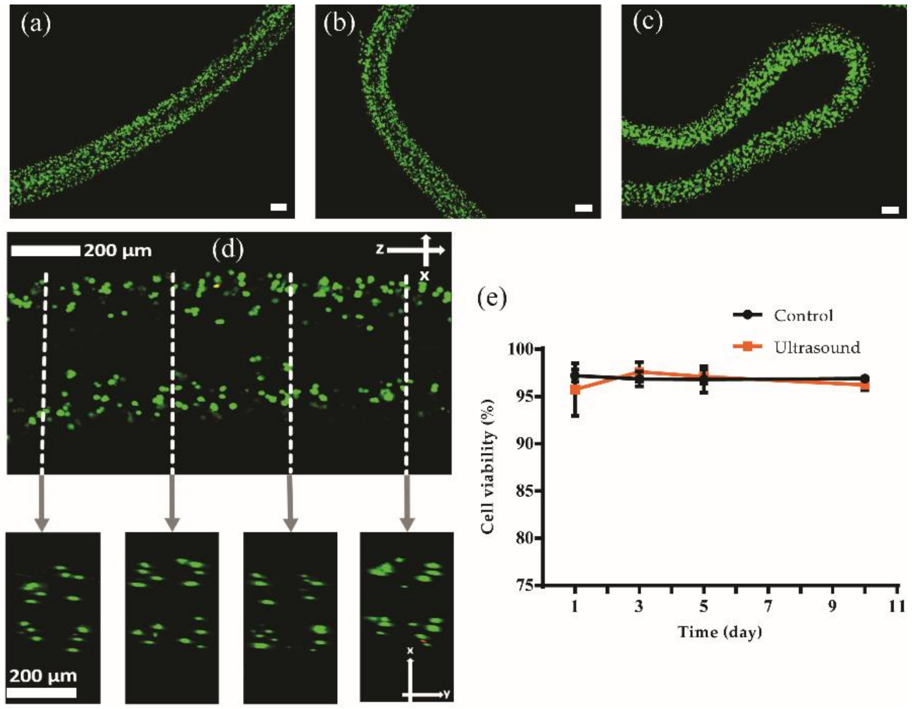

Figure 2. (a), (b)The manipulated fibroblast cells in the transition from one stream to four streams or vice versa on day 3, respectively. (c) The fibroblast cells unexposed to ultrasound on day 3. (d) Confocal microscope image of the aligned fibroblast cells as four streams on day 3. (e) Viability comparison of the ultrasound-exposed fibroblast cells vs. the unexposed control sample. Live and dead cells were stained green and red, respectively.

Acoustic NIH/3T3 cells pattering in the sodium alginate hydrogel

Figure 2a-b shows fibroblast cells transitioning from a single stream of cells to four streams and, again, switching back to 2 MHz actuation, forming a branch structure inside the alginate hydrogel scaffold. Figure 2c shows the non-ultrasound-exposed distribution of the fibroblast cells in scaffold. By confocal imaging, the cross-section of the aligned part was collected as shown in Figure 2d. Four regions of enriched cells were clearly distinguishable allowing us to infer that the four streams of fibroblast cells were aligned. The result of the cell viability comparing the ultrasound-exposed and unexposed fibroblast cells, is shown in Figure 2e, indicating that cell viabilities between the two groups are not significantly different. The viability of the ultrasound-aligned fibroblasts was found to range between 95 and 98% from day 1 to day 10.

Conclusion

Using acoustically controlled 3D fibroblast cell patterning, this study demonstrated the potential to arrange live cells into 3D networks within extruded hydrogels. Currently we are focusing on manipulation of other cells, such as endothelial cells, smooth muscle cells, and neuronal cells, in Type I collagen for artificial blood vessel network and artificial neuronal network formation.

Acknowledgement

This work was supported by the Ministry of Science and ICT, Republic of Korea (2020R1F1A1075779).

References

[1] K.-i. Koo, A. Lenshof, L.T. Huong, T. Laurell, Micromachines **12**, 1-12 (2021).

[2] M. Radisic, L. Yang, J. Boublik, R.J. Cohen, R. Langer, L.E. Freed, G. Vunjak-Novakovic, Am J Physiol Heart Circ Physiol **286**, H507-H516 (2004).

[3] N. Asakawa, T. Shimizu, Y. Tsuda, S. Sekiya, T. Sasagawa, M. Yamato, F. Fukai, T. Okano, Biomaterials **31**, 3903-3909 (2010).

[4] R.K. Jain, P. Au, J. Tam, D.G. Duda, D. Fukumura, Nature Biotechnology **23**, 821-823 (2005).

[5] M.W. Laschke, B. Vollmar, M.D. Menger, Tissue Engineering Part B: Reviews **15**, 455-465 (2009).

[6] T. Hitchcock, L. Niklason, Annals of the New York Academy of Sciences **1131**, 44-9 (2008).

[7] E.S. Comeau, D.C. Hocking, D. Dalecki, Journal of Cell Science **130**, 232-242 (2017).

Acoustofluidics 2021
26-27 August 2021
Virtual Conference

Study of the Rayleigh limit by Acoustic Force in Microgravity

Chloé Dupuis[1], Xavier Mousset[1], Lucile Rabiet[1], Xavier Benoit-Gonin[1], Mauricio Hoyos[1], and Jean-Luc Aider[1]

[1]Laboratory of Physics and Mechanics in Heterogeneous Medium (PMMH), UMR 7636 CNRS, ESPCI Paris-PSL, Sorbonne Université, Université de Paris, 1 rue Jussieu, 75005 Paris, France
E-mail: chloe.dupuis@espci.fr, jean-luc.aider@espci.fr

Introduction

In a Bulk Acoustic Wave (BAW) resonator, spherical objects, such as particles, can be maintained in an equilibrium position, between the walls of the resonant cavity. In the so-called acoustic levitation plane the gravity is counterbalanced by the Acoustic Radiation Force (ARF) created when the resonance condition is respected (height of the cavity h equal to the half of the acoustic wavelength λ_{ac}). The analytical expression commonly used to describe the ARF applied to a spherical particle is obtained by assuming that the acoustic wavelength is large compared to the diameter of the irradiated particle, an assumption called "Rayleigh's approximation" or Rayleigh's limit [1,2]. It is therefore perfectly applicable to objects of microscopic sizes (d_p = 1 to 20 μm) and an ultrasonic source of the order of a few MHz (λ_{ac} of the order of a few hundred μm). In this context, particles or cells can be moved toward the acoustic levitation plane where they can form large aggregates.

It was shown recently that it is possible to maintain in acoustic levitation large objects (cells spheroids) whose diameter is close to the acoustic wavelength [3], in contradiction with the Rayleigh's hypothesis. In order to study more precisely the limits of this hypothesis it is interesting to run experiments in microgravity. In this case, the gravity will not limit the ARF and it will be possible to handle large and / or dense objects, which would sediment quickly in standard laboratory conditions on Earth. We present in this talk the first experimental results showing that indeed ARF can move and levitate large objects far beyond the Rayleigh's limit.

Theoretical background

As previously described [4], the ARF can be considered as "artificial gravity" in a Zero-G environment allowing the self-assembly of a large number of microparticles which would have stayed in suspension otherwise. When levitating a large number of cells, we can form aggregates as large as the acoustic wavelength, meaning we overcome the Rayleigh limit. Indeed, being able to levitate large objects (500 µm diameter vs $\lambda_{ac} = 700$ µm) shows that either the ARF expression is still valid or that it should be corrected for large objects. Numerical simulations were developed to extract the trajectories of several acoustically and hydrodynamically interacting particles beyond the Rayleigh regime to replicate experimental results obtained with large concentration of particles clumping at pressure nodes [5]. However, to our knowledge, this phenomenon was never investigated experimentally, especially in the context of microgravity.

Therefore, to shed light on this peculiar behavior, we chose to study, during the parabolic flight campaign of Novespace in March 2021, large and dense particles in microgravity which could not be moved by the ARF on Earth.

Experiment design for microgravity

In our conventional lab set-up, the acoustic levitation is studied in home-made sub-millimetric cavities. We observe aggregates with an inversed microscope and a camera. The ARF is generated by an ultrasonic transducer powered by a sinusoidal electric signal and controlled by a computer. The working frequencies we uses are around 2 MHz so that the ultrasound can resonate in our home-made cavities. The generator can provide an electrical power between 1 and 12V allowing to modulate the acoustic energy inside the chamber and thus the ARF.

To run these experiments in the Airbus Zero-G of Novespace, we designed two racks. The monitoring rack was conceived to allow for quick data acquisition while the experimental setup was designed to fit into a sealed Zarges box for security reasons. The particles in acoustic levitation were studied using an inverted Zeiss microscope and a PCO Panda Bi camera. A piezoelectric stage from ASI imaging was used in order to follow closely the beads during the parabolas and extract their precise position. The variety of samples were composed of polystyrene beads of 1.00 g/cc and 5 µm in diameter, polyethylene fluorescent beads with a density of 1.00 g/cc and sizes ranging from 150 to 700 µm as well as Titanium beads with a density of 4,5 g/cc and 150 µm in diameter.

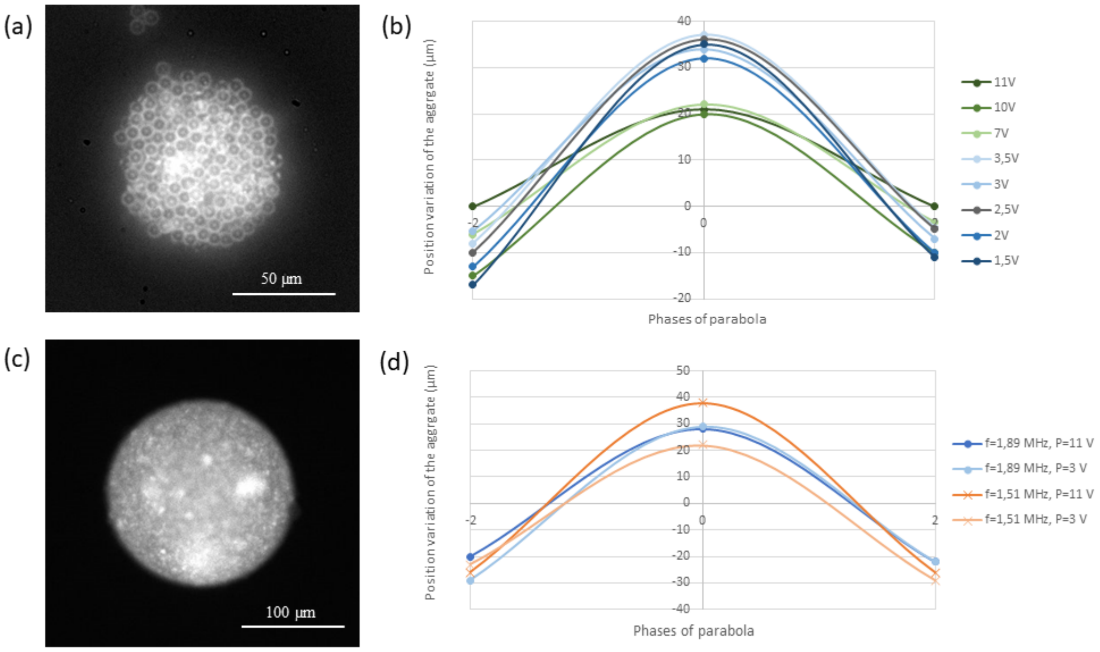

Figure 2: (a) Picture of the aggregate of small polystyrene beads (5 µm in diameter) and (b) its position variation during the parabola phases. Each lines represents a different experiment and thus a different parabola. The parameter which varied between experiments was the acoustic power delivered. The low and high regimes are shown in blue and green shades respectively. (c) Picture of the big fluorescent bead (150 µm in diameter) and (d) its position variation during the parabola phases. The low and high regime are defined as light and dark color respectively and the two different resonant frequencies are represented by orange shades and crosses for 1.51 MHz and blue shades and dots for 1.89 MHz

Results

We first created an aggregate of small beads (Fig 2.a) to measure the evolution of the position of the acoustic levitation plane for different gravities phases during one parabola, starting with a 2g phase followed by a microgravity period of about 20 s and ending with another 2g phase. The position of reference was taken at standard gravity conditions (1g), before the parabola. All values are then variations compared to the 1g case. In all cases, we used a 2,04 MHz source which is the resonant frequency of our cavity. In Fig 2.b, the position variation of the aggregate is plotted against the different phases of the parabola. We first distinguish two regimes at low (P = [1.5 ; 3,5] V) and high (P = [7 ; 11] V) power. At high power, the levitation plane position varied less than at low power. In particular, the aggregate position during the microgravity phase was almost two times higher at low power compared to high power.

We then studied bigger particles (Fig 2.c and d) under those two regimes and at different resonant frequencies. As expected, the highest relative position of the bead in microgravity was at the lowest frequency (1.51 MHz). However, it is relevant to notice that the position variation at low regime in microgravity was two times smaller than at high regime and even smaller than for the higher frequency at the same acoustic power. These results contradict the results obtained with the aggregate of small beads. This could be explained by the cohesive forces between particles playing a role in the way the aggregate respond to ARF compared to an independent large particle. We were not able to levitate bigger polyethylene beads (diameter > 500 µm) but the dense Titanium beads showed a response when submitted to ARF and even formed plane aggregates.

Conclusion

Thanks to experiments in parabolic flights, we were able to handle large and dense particles that could not be moved in standard gravity conditions. We carried out parametric studies and demonstrated that it is indeed possible to handle large particles or large aggregates of particles using ARF beyond the Rayleigh limit.

References

[1] Doinikov, A. (1994). *Acoustic radiation pressure on a compressible sphere in a viscous fluid.* Journal of Fluid Mechanics, 267, 1-22.

[2] G. T. Silva, H. Bruus (2014). *Acoustic interaction forces between small particles in an ideal fluid*, Phys. Rev. E 90, 063007.

[3] Jeger-Madiot, N., Arakelian, L., Setterblad, N. et al. (2021) *Self-organization and culture of Mesenchymal Stem Cell spheroids in acoustic levitation*. Sci Rep 11, 8355.

[4] Dumy, G., Jeger-Madiot, N., Benoit-Gonin, X., Mallouk, T. E., Hoyos, M., & Aider, J.-L. (2020). *Acoustic manipulation of dense nanorods in microgravity*. Microgravity Science and Technology, 32(6), 1159-1174.

[5] Baasch T., Dual J. (2018) *Acoustofluidic particle dynamics: Beyond the Rayleigh limit.* The Journal of the Acoustical Society of America 143, 509

Acoustofluidics 2021
26-27 August 2021
Virtual Conference

Acousto-Pi: An Integrated Opto-Acoustofluidic System with Open-Source Electronics for In-Field Diagnostics

Jethro Vernon[a], Pep Canyelles-Pericas[b], Hamdi Torun[a], Richard Yong-Qing [a]

[a] Faculty of Engineering & Environment, University of Northumbria, New1castle upon Tyne, NE1 8ST, United Kingdom

[b] Department of Integrated Devices and Systems, MESA+ Institute for Nanotechnology, University of Twente, Enschede, 7522 NB, the Netherlands

*Presenting author: Jethro Vernon, e-mail: jethro.vernon@northumbria.ac.uk

Introduction: Surface acoustic wave (SAW) devices are increasingly applied in life science, biology, and point-of-care applications due to their combined acoustofluidic sensing and actuating properties [1]. Despite the advances in this field with open-source electronic setups [2], there remain significant gaps in interfacing hardware and control strategies to facilitate system integration with high performance and low cost. In this work, we present an integrated, versatile and digitally controlled acoustofluidic platform using Raspberry Pi by demonstrating key functions for biological assays such as droplet transportation, mixing and heating using closed-loop feedback control with image recognition. We integrate optical detection by demonstrating in-situ fluorescence sensing capabilities with a standard camera with digital filters, bypassing the need for expensive and complex optical setups.

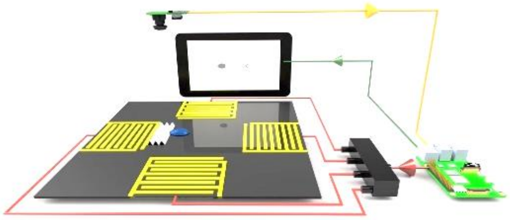

Figure 1 An illustration of SAW platform integrated with a Raspberry Pi

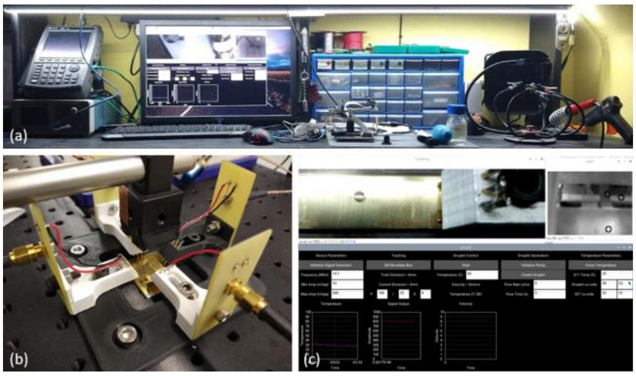

Figure 2 (a) overall Raspberry pi setup (b) SAW device and 3d mountings (c) GUI as seen on screen

Background: To manage disease outbreaks and reduce rapid spreading; fast, accurate and affordable diagnostics techniques are needed. The most established techniques for medical diagnostics based on nucleic acid (DNA and RNA) detection are polymerase chain reaction (PCR) and loop-mediated isothermal amplification (LAMP). Both PCR and LAMP facilitate biological reactions that result in exponential amplification of targeted DNA for a subsequent detection step. In these methods, the biological sample from the test subject is processed with a series of reagents in regulated protocols for DNA extraction, amplification and detection, which require microfluidic functions such as mixing, dispensing and heating. For DNA detection, the reagents produce a bound marker that is typically fluorescent to be optically measured in real time during the amplification reaction. All these functions can be realised and have been demonstrated using ultrasonic technology [3][4]. However, there is a need for interfacing hardware and control strategies to facilitate system integration with high performance and low cost. The platform presented here is integrated with two cameras, e.g., a Raspberry Pi camera and an infrared camera, which can be monitored simultaneously. The visible light camera is used for droplet position control and fluorescent measurements. The infrared camera is used for contactless temperature measurements (see Figure 1). Taking advantage of Raspberry Pi and Python programming language, the system can be adaptive and interface with a large range of components and equipment needed for SAW biomicrofluidics.

Results: We demonstrate the remote-control functions of generation, pumping, moving, and mixing of single and multiple droplets using thin film SAW devices. we test transport droplet in multiple directions to any location on a surface using multiple PID controllers in the lateral plane. During these movements, a target speed is set. Fluorescent measurements are investigated using various concentrations and droplet sizes. We measure the input grayscale brightness (Relative Intensity) using the Raspberry Pi camera on our developed platform. When a 5 µl of Quinine solution is mixed with the water driven by the SAW, the brightness increases. The growth of intensity is more significant for the first mixing of solution, and further introduction of solutions results in stagnated increase of intensity (because of the increase of total volume of the droplet).

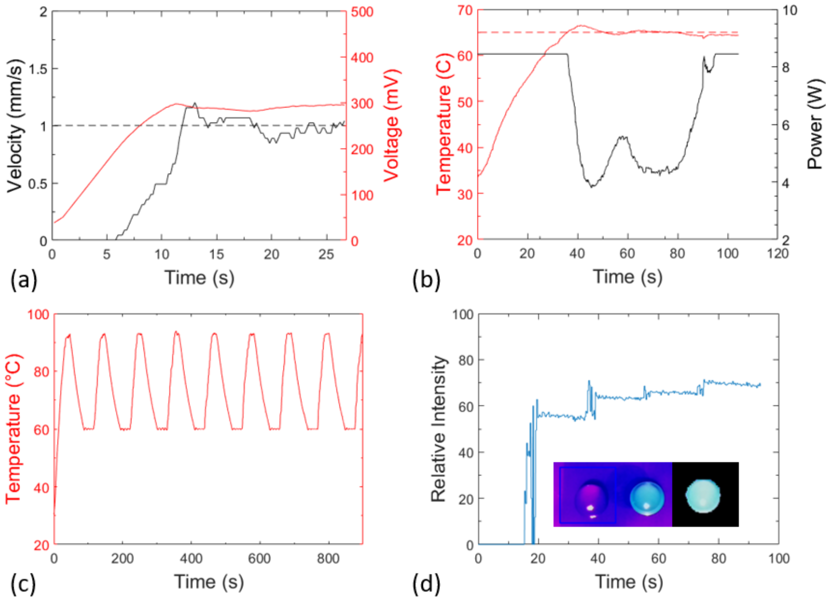

Figure 2 (a) example of 10ul droplet movement (b) example of droplet temperature control for LAMP reactions (c) example of thermal cycling for PCR (d) example of mixing and increasing fluorescence over time, with view of a digitally filtered droplet using Raspberry Pi camera.

Conclusion: In this work we have presented the Acousto-Pi: a versatile and adaptable opto-acoustofluidic platform with embedded open-source electronics for biological assay applications. The platform can be used to interface and control any SAW device. Using thin film SAW devices, we simulate a biological reaction for DNA amplification by showing all the specific steps that an opto-acoustofluidic system needs to achieve. The setup is an adaptable system that can be adjusted to be used on different assays, including variations in target temperature, volume or type of reagents and samples used. Using open-sources technology additional functions can be included, allowing for a large amount of modularity without a large increase in complexity. Moreover, the Raspberry Pi can be used for embedded computation with machine learning algorithms and to store and transmit data to the cloud.

References

[1] L. Y. Yeo and J. R. Friend, “Surface Acoustic Wave Microfluidics,” *Annu. Rev. Fluid Mech.*, vol. 46, no. 1, pp. 379–406, Jan. 2014.

[2] A. Marzo, T. Corkett, and B. W. Drinkwater, “Ultraino: An Open Phased-Array System for Narrowband Airborne Ultrasound Transmission,” *IEEE Trans. Ultrason. Ferroelectr. Freq. Control*, vol. 65, no. 1, pp. 102–111, Jan. 2018.

[3] J. Reboud *et al.*, “Shaping acoustic fields as a toolset for microfluidic manipulations in diagnostic technologies,” *Proc. Natl. Acad. Sci. U. S. A.*, vol. 109, no. 38, pp. 15162–15167, Sep. 2012.

[4] G. Xu, R. N. Gunson, J. M. Cooper, and J. Reboud, “Rapid ultrasonic isothermal amplification of DNA with multiplexed melting analysis-applications in the clinical diagnosis of sexually transmitted diseases,” *Chem. Commun.*, vol. 51, no. 13, pp. 2589–2592, 2015.

Acoustofluidics
2021
26-27 August 2021
Virtual Conference

Particle chain formation in acoustophoresis

Thierry Baasch[1], Wei Qiu[1] and Thomas Laurell[1]

[1]Department of Biomedical Engineering, Lund University, Lund, Sweden
E-mail: thierry.baasch@bme.lth.se

Introduction

We investigate the acoustic particle-chain formation experimentally and theoretically. During acoustic manipulation, the competition between primary and secondary (i.e. interparticle) acoustic radiation force leads to an interesting phenomena: the particles collect in chains along the pressure node, while repelling each other in the direction of the pressure gradient. Ultimately, at a specific gap distance, the particle chains reach an equilibrium position. We present a theory for the equilibrium gap-distance between the particle chains. The theory is validated experimentally for full glass beads (4 µm diameter, shown in Fig. 2a and 10 µm diameter shown in Fig. 2b) and three types of hollow glass beads (Figs. 2c – 2e). The gap distance scales with the square of the density scattering coefficient, and thus the effect can also be observed for particles lighter than the surrounding medium (PBGH 18, shown in Fig. 2c).

Methods and results

The experiments were carried out in a standard bulk acoustic-wave device [1] that was excited at the $\lambda/2$ mode at 1.97 MHz. For the experiments, the particle-water-surfactant mixture was flushed into the channel and then the flow was stopped. The acoustics was turned on after the particles either sedimented or reached the top of the channel (PBGH 18 particles). All the used particles have positive acoustic contrast, thus after turning on the acoustics, the particles migrated towards the center of the channel. The snapshots were taken at the pressure node as soon as the particle center-to-center gap distance for the particle chains was stable. Based on the theory by Silva et al. [2], we derived the gap distance d_{IP} between a pair of particles as

$$d_{\mathrm{IP}} = \left(\frac{3 f_2^2 a^3}{\phi k^2} \right)^{1/5}, \qquad (1)$$

with the dipole scattering coefficient f_2, the acoustic contrast factor ϕ, the wavenumber k, and the particle radius a. The gap distances were measured in at least 3 positions per panel for each of the 30 panels from Fig. 2 and then averaged for the respective particle types. The theoretical gap distance (Fig. 1 left) of 22 µm for the Kisker 10 µm and 13 µm for the Kisker 4 µm are in line with the measured gap distances of 18 ± 3 µm and 13 ± 2 µm shown in Figs. 2a and 2b, respectively. Hollow particles can be characterised by the ratio between inner and outer diameter α. According to Leibacher et al. [3] the PBGH 18 particles shown in Fig. 2c are well described by $\alpha = 0.9$ and a positive ϕ even though they are lighter than water. Our theory then predicts a gap distance of 44 µm that matches the measured gap distance of 41 ± 6 µm well (right panel of Fig. 1 and Fig. 2c). The $\alpha = 0.8$ of the PBGH 11 particles was determined based on their density, while using the same material properties as for the PBGH 18 particles. The theoretical gap distance of 9.6 µm underestimates the meaured gap distance of 18 ± 4 µm from the experiments (right panel Fig. 1 and Fig. 2d). This discrepancy could be due to the large variability in the material properties and size of the PBGH 11 particles. Due to a lack of data we were not able to calculate the gap distance for PBGH 10 particles. In the experiments, the gap distance measured 17 ± 3 µm, see Fig. 2e.

Conclusion

We have presented a theoretical and experimental investigation of the particle chain formation that appears in acoustic particle manipulation. The theory matches well for the particles with known material properties. As a next step, we will validate and complement the analytical theory with finite-element modeling and multibody dynamic simulations [4].

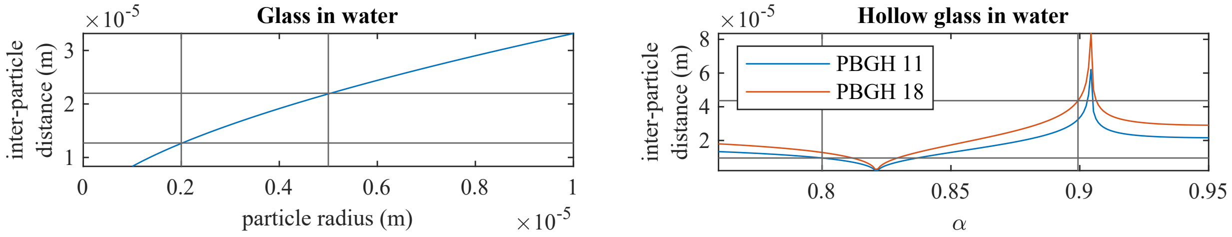

Figure 1: Theoretical predictions of the particle center to particle center to center gap-distance between particle chains.

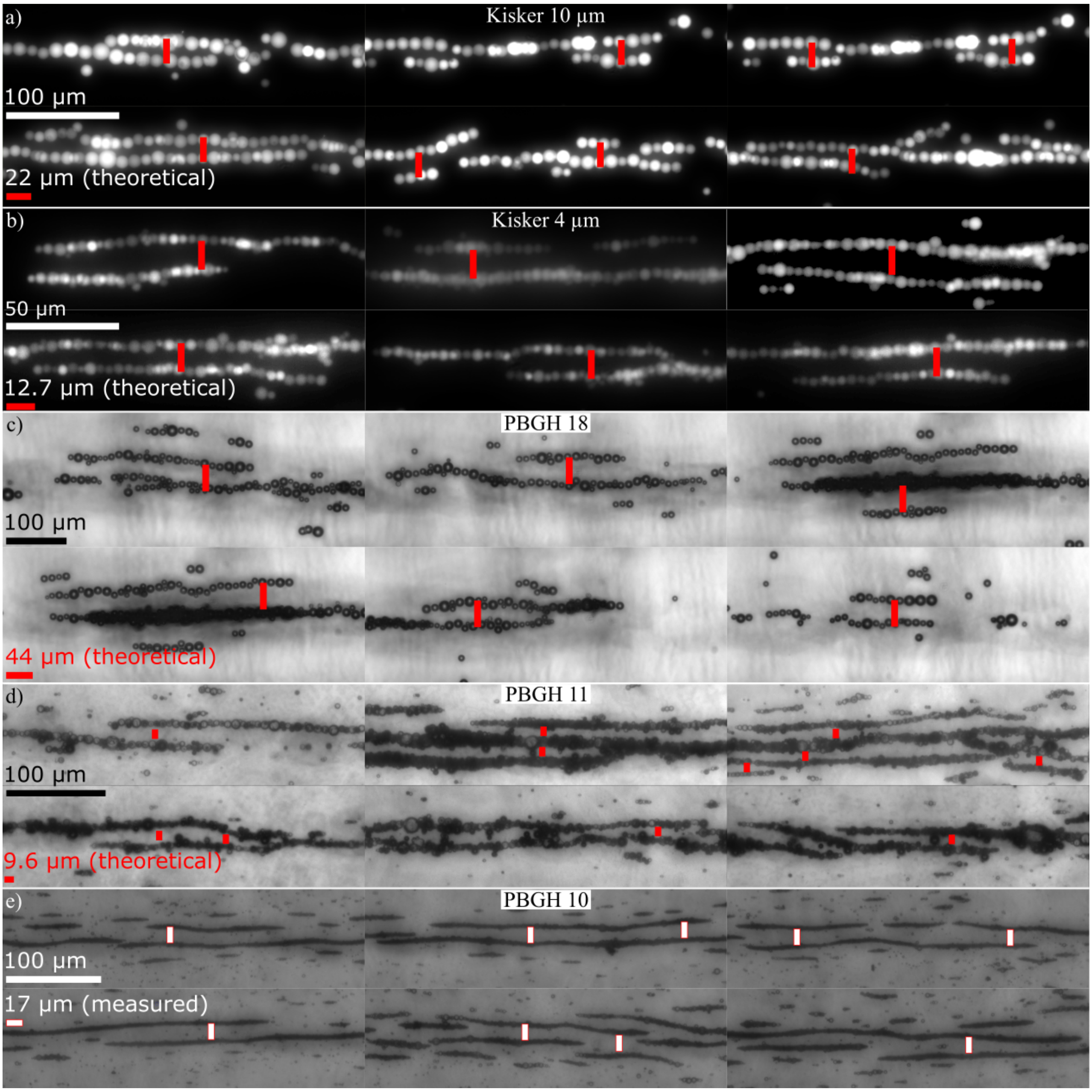

Figure 2: Particle chain formation and the theoretical distances for full glass particles of 10 µm (a) and 4 µm (b) diameter. The results for different types of hollow glas beads are shown in c), d) and e).

References

[1] W. Qiu, H. Bruus, and P. Augustsson. Physical Review E **102**, 013108 (2020).
[2] G. T. Silva, and H. Bruus. Physical Review E **90**, 063007 (2014).
[3] I. Leibacher, W. Dietze, P. Hahn, J. Wang S. Schmitt and J. Dual. Microfluidics and nanofluidics **16**, 513–524 (2014).
[4] T. Baasch, I. Leibacher and J. Dual. JASA **141**, 1664–1674 (2017).

Acoustofluidics
2021
26-27 August 2021
Virtual Conference

Numerical simulations of relocation mechanism of coflowing immiscible fluids exposed to bulk acoustic wave

Sazid Z. Hoque[1], and Ashis K. Sen[1]

[1]Department of Mechanical Engineering, IIT Madras, Chennai, India
E-mail: ashis@iitm.ac.in, URL: http://www.ashislab.in

Introduction

Hertz and Mende, in 1939, experimentally showed that fluid interfaces deformed when exposed to acoustics beam [1]. This noticeable result leads to the acoustic radiation pressure on a fluid-fluid interface that is further exploited in biomedical applications [2]. Hemachandran et al. recently demonstrated the relocation dynamics of coflowing liquid streams due to a bulk acoustic wave [3]. It is observed that the higher-order impedance liquid relocates towards the center of the microchannel. Lee and Wang developed an expression for acoustic radiation pressure due to a sound beam incident on a partially reflecting interface [4]. Here, we report the dynamic relocation mechanism of the immiscible liquid interfaces by developing an expression for acoustic radiation pressure force due to bulk acoustic wave. We show using numerical simulations that the relocation of the interface depends on the competition between the acoustic radiation force (ARF) and the interfacial tension force (IFT) as observed in the experiments [3].

Theoretical modelling

Classically, the acoustic radiation pressure acting on a fluid interface is defined by the difference in the mean Lagrangian pressure across the interface [5]. Considering a straight interface at $x = 0$ between two fluids a and b, we obtained the Lagrangian pressure difference when the fluids are exposed to bulk acoustic wave as,

$$\langle \Delta p_2^L \rangle = -\langle E_{ac} \rangle \left[(e^{+i2k_a x} + (\Delta \overline{Z})^2 e^{-i2k_a x}) - \frac{\rho_b}{\rho_a}(1 - (\Delta \overline{Z})^2) e^{+i2k_b x} \right] \tag{1}$$

where, $\langle E_{ac} \rangle$ is the average acoustic energy density defined as, $\langle E_{ac} \rangle = \frac{1}{2}\rho_a k_a^2 A_a^2$, and $\Delta \overline{Z} = \frac{z_b - z_a}{z_b + z_a}$. Here, $z_a = \rho_a c_a$ and $z_b = \rho_b c_b$ are the acoustic impedances of the fluid a and fluid b having density ρ_a and ρ_b and c_a, c_b represents the speed of sound in fluid a and fluid b respectively. Further, k_a and k_b are the wave number of the acoustic wave in fluid a and fluid b. The amplitude of the incident wave in fluid a is denoted as A_a.

The acoustic radiation force per the interface area, A is given by [5],

$$F_{ac}/A = \langle \Delta p_2^L \rangle \mathbf{n} \tag{2}$$

where, $\mathbf{n}$ is the normal vector pointing from fluid to fluid b. The eqn.[2] is modeled as a body force term in Navier-Stokes equation to incorporate the effect of the bulk acoustic wave in case of immiscible fluids. Further, the interface between the two fluids are captured using the phase field method. Sufficiently fine uniform mesh is created to capture the interface deformation through out the fluid domain.

Results and discussion

We numerically simulated the transient evolution of the immiscible fluid interface in a microchannel of cross-section 370 $\mu m \times 150$ μm due to combined effect of ARF and IFT forces. The average acoustic energy density $\langle E_{ac} \rangle$ is varied to show that the immiscible fluids may not relocate when the ARF is small compared to the IFT force, i.e., $F_{ac} << F_{st}$. Fig. 1 shows that the transient variation of the interface considering water and mineral oil (5% span) as the two immiscible fluids. The relocation is observed for $\langle E_{ac} \rangle = 50 J/m^3$, as shown in Fig 1(a). However, for a lower value of average acoustic energy density $\langle E_{ac} \rangle = 30 J/m^3$, there is no relocation of the interface. The phenomenon is characterised by the acousto-capillary number Ca_{ac} defined as, $Ca_{ac} = F_{ac}/F_{int}$ [3]. Simulations are carried out considering different immiscible fluid combinations to showcase the relocation and non-relocation regimes in terms of ARF and IFT forces and the result is presented in

Fig. 2. We have seen that, when the ARF force dominates over the IFT force, i.e., $Ca_{ac} >> 1$, the relocation of the high imedance fluid towards the center of the microchannel is observed. On the other hand, when the ARF force is negligible compared to IFT (i.e., $Ca_{ac} << 1$), we observed no relocation of the interface. Further, the critical acoustocapillary number from simulations for various fluid combinations is found to be, $Ca_{ac_0} = 0.97$.

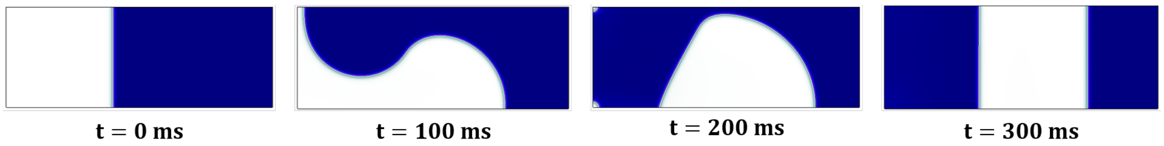

(a) Relocation of immiscible fluids at $\langle E_{ac} \rangle = 50\, J/m^3$

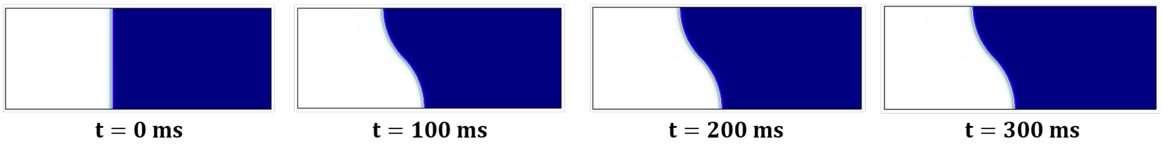

(b) Non-relocation of immiscible fluids at $\langle E_{ac} \rangle = 30\, J/m^3$

Figure 1: The transient dynamical motion of the immiscible fluid interface (Blue, mineral oil(5% span);White, water)), (a) Relocation of the fluid interface at $\langle E_{ac} \rangle = 50J/m^3$, (b) Non-relocation of the fluid interface at $\langle E_{ac} \rangle = 30J/m^3$. The height and width of the microchannel is $150\mu m$ and $370\mu m$.

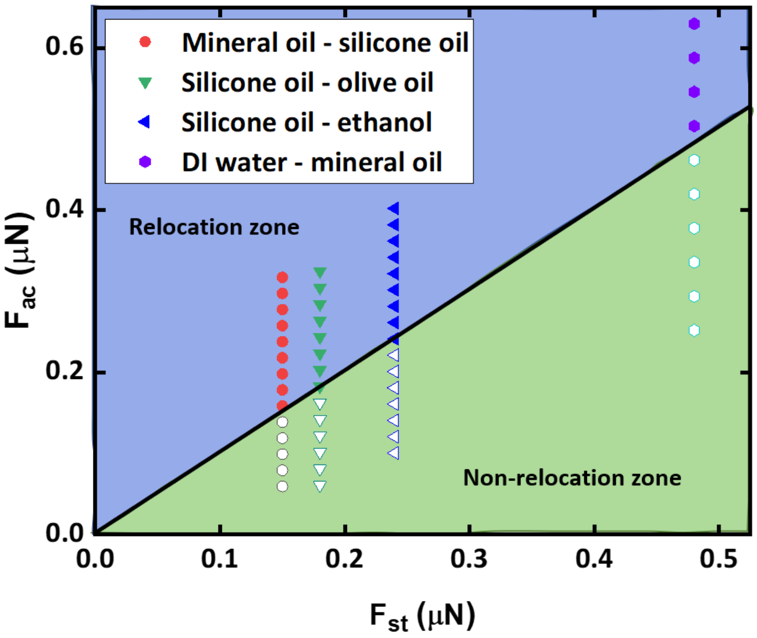

Figure 2: Relocation and non-relocation regimes described in terms of the acoustic radiation pressure force (F_{ac}) and interfacial tension force (F_{st}). The relocation phenomenon is observed for $Ca_{ac} >> 1$ and the critical capillary number is found to be $Ca_{ac_0} = 0.97$.

Conclusion

We provided a better understanding of the relocation phenomena in coflowing immiscible fluids by developing a theoretical formulation and numerical simulations. We observed that the high impedance liquid relocates from the below towards the center on the microchannel. We found that, the relocation dynamics is governed by the competition between the F_{ac} and F_{st} force in terms of Ca_{ac}.

References

[1] G. Hertz and H. Mende, Z. Phys. 114, 354 (1939).
[2] M. Fatemi and J. F. Greenleaf, Science 280, 82 (1998).
[3] E. Hemachandran, S. Karthick, T. Laurell, A. K. Sen, Europhys. Lett. 125, 54002 (2019).
[4] C. P. Lee and T. G. Wang, J. Acoust. Soc. Am. 94, 1099 (1993).
[5] J. T. Karlsen, P. Augustsson, and H. Bruus, Phys. Rev. Lett. 117, 114504 (2016).

Acoustofluidics 2021
26-27 August 2021
Virtual Conference

Trapping and ‘bouncing’ of water droplets in oil-filled microwells under SAW-induced streaming

Amal Nath[1], and Ashis K. Sen[1]

[1]Fluid Systems Laboratory, Department of Mechanical Engineering, Indian Institute of Technology Madras, Chennai, India
E-mail: me17d008@smail.iitm.ac.in, URL: http://www.ashislab.in

Introduction

Manipulation in microwell systems using acoustic waves has potential applications in microwell titre plate arrays, widely used in biochemical assays in combinatorial drug discovery workflow. In this study, we explore the possibility of trapping large water droplets (with radius $R \sim 1$ mm) inside microwells containing lighter oils. To achieve this, we use surface acoustic waves (SAW) to create a *single acoustic streaming vortex* in the microwell by a careful choice of well dimensions and actuation frequency. We observed that while large streaming velocities (or actuation powers) facilitate the trapping of water droplets in olive oil, trapping did not occur when the microwell was filled instead with mineral oil, and settling of the droplet to the bottom was observed. Interestingly, when a small volume of olive oil was added to the mineral oil-filled microwell, the droplet dynamics was significantly altered and the dispensed droplet was seen to bounce off the bottom of the microwell.

Experimental methods

Polydimethylsiloxane (PDMS) microwell (Sylgard 184, Dow Corning) with dimensions of width $W = 3$ mm, height $H = 3$ mm, length 6 mm and wall thickness 2 mm was first fabricated by pouring uncured PDMS in a PMMA based mould. After curing, the microwell is bonded to a LN substrate (128^0 rotated Y-cut X propagating $\mathrm{LiNbO_3}$) by oxygen plasma treatment. The LN substrate has a pair of comb-shaped gold electrodes deposited on it using standard photolithography process. The gaps between electrodes are the same as the finger width ($= \lambda/4$) and the SAW wavelength $\lambda = 200$ µm corresponds to resonant frequency $f = 19.84$ MHz. The SAW device is actuated with a sinusoidal signal from an RF signal generator after amplification. Adjusted for the losses in electromechanical coupling of the substrate, the operated actuation powers lie within the range 3 mW to 200 mW. The continuous phase used in the experiments are olive oil and/or mineral oil and the dispersed phase is deionized water.

Results and Discussion

The dissipation of leaky Rayleigh wave in the viscous fluid inside the microwell results in steady state swirling motion termed *Eckart streaming* (Fig. 1). Acoustic attenuation lengths [1] in the fluid (f) and the substrate (s) can be computed as $l_\mathrm{f} = 3/16\rho_\mathrm{f}c_\mathrm{f}^3/\pi^2\mu_\mathrm{f}f^2$ and $l_\mathrm{s} = \rho_\mathrm{s}c_\mathrm{s}^2/\rho_\mathrm{f}c_\mathrm{f}f$, where ρ, c and μ correspond to density, speed of sound and viscosity respectively. With olive oil as the continuous phase, we get $l_\mathrm{s} = 2.89$ mm < well width, W and $l_\mathrm{f} = 1.76$ mm < well height, H. Therefore, the motion of a water droplet dispensed into the microwell at steady state streaming flow is dominated by streaming-

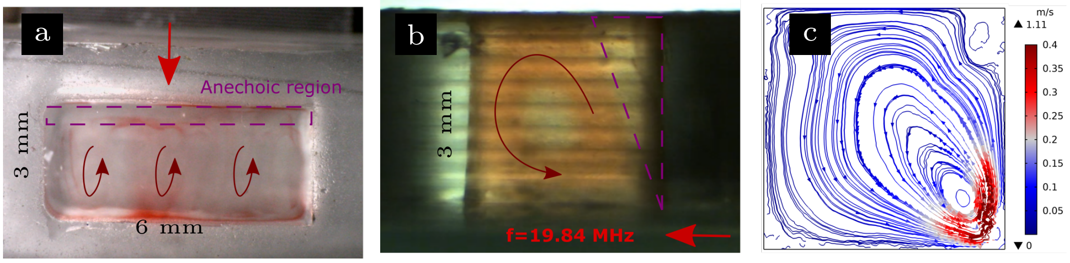

Figure 1: The streaming flow generated in an olive oil (dyed with Oil Red O) filled microwell by actuating the IDT at frequency $f = 19.84$ MHz is shown. (a) Top view of the microwell which is 3 mm along and 6 mm perpendicular to the SAW propagation direction, shown by a red line. The direction of bulk streaming flow is marked as dark red curves. (b) The large microwell depth of 3 mm results in a clear formation of an anechoic region (marked as dashed pink lines) having a weak counter-rotating vortex. (c) The numerical model helps qualitatively in determining optimum dimensions to generate a single streaming vortex.

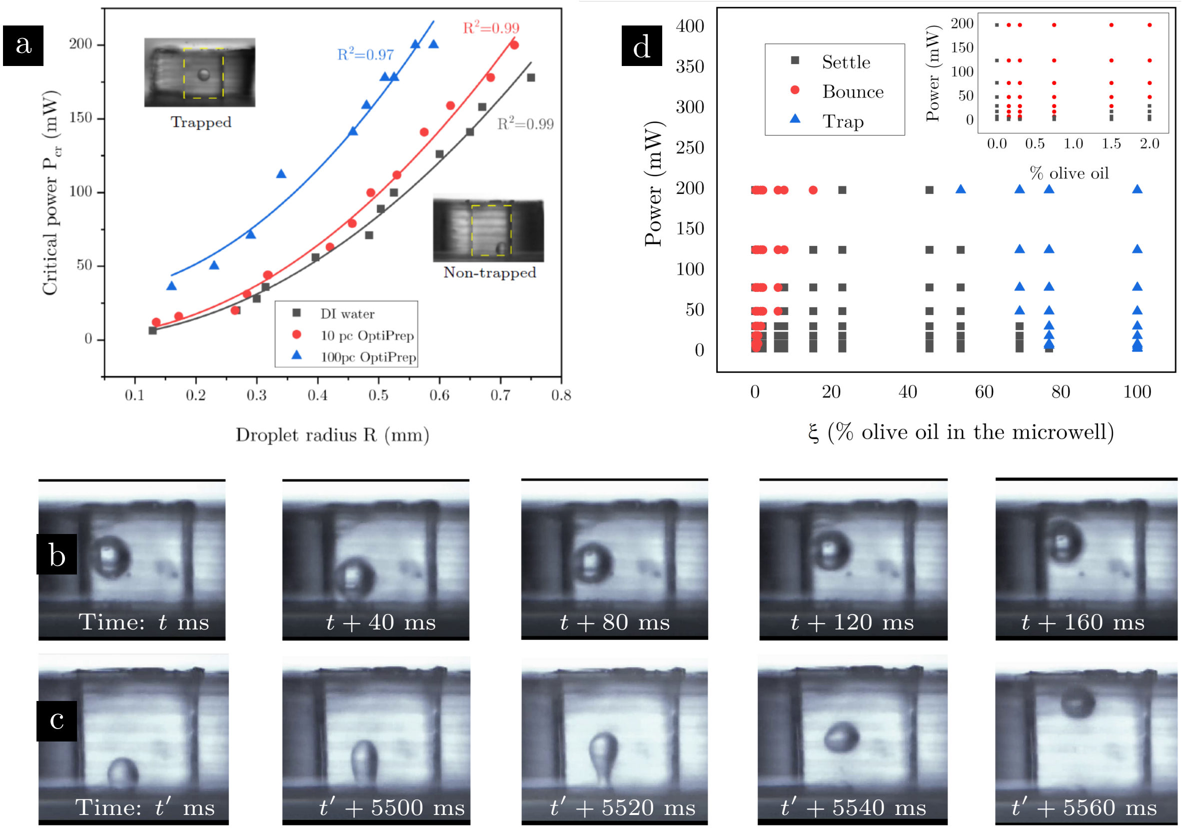

Figure 2: (a) The minimum power required to trap the water droplet (of volume 0.5 µ*l*) in the streaming vortex in olive oil is quantified for different droplet densities, (b) at $\xi < 5$, bouncing of the dispensed 0.5 µ*l* volume droplet from the substrate is shown, (c) at $5\% < \xi < 10\%$, jetting of the droplet initiates after $t = 5.5$ s leaving a much smaller droplet at the bottom , (d) the different regimes observed when the oil composition (mineral oil: olive oil) inside the microwell was changed.

induced drag force. The upward component of the streaming drag force $F_{\mathrm{str}} = 6\pi\mu v_{\mathrm{str}} R$ balances the effective weight of the water droplet $F_{\mathrm{w}} = 4/3\pi\,(\rho_{\mathrm{w}} - \rho_{\mathrm{oil}})\,R^3$ and the droplet gets trapped at the center of the vortex. For fixed operational parameters, the critical power needed to trap the droplet is seen to vary quadratically (Fig. 2a), which also follows from a balance of the forces, $F_{\mathrm{str}}/F_{\mathrm{w}} \sim P/R^2$, since the streaming velocity scales with actuation power $u_{\mathrm{str}} \sim P$.

Interestingly, when the microwell is filled with a combination of olive oil and mineral oil at different percentages, the dynamics of the dispensed water droplet is significantly altered. The two immiscible oils, initially layered with the denser olive oil at the bottom of the well, circulate with respect to each other in a single streaming vortex at steady state. The behavior of a droplet dispensed at steady state depends on the percentage of olive oil (ξ) in the microwell and the actuation power (Fig. 2d). At low powers, the following regimes are observed: (a) at ($\xi < 5\%$), the droplet dispensed at steady state *bounces* off the bottom of the microwell without any breakup (Fig. 2b), (b) at $5\% < \xi < 10\%$, the settled droplet *jets* towards the top (Fig. 2c) leaving a residue droplet at the bottom, (c) at $10 < \xi < 80$, the droplet is seen to settle to bottom without any bouncing/jetting, and (d) at $\xi > 80\%$, droplet traps at the vortex center, similar to the inset in Fig. 2a shown for a case where the microwell contains olive oil alone ($\xi = 100\%$). The bouncing of the droplet at low but nonzero values of ξ can be attributed to the possible formation of a very thin layer (of thickness $\sim \lambda_{\mathrm{f}}$) of the denser olive oil at the bottom of microwell at steady state. The mismatch in acoustic impedance [2] between this olive oil layer and the water droplet and the resulting acoustic radiation pressure at the interface may impart an upward force that leads to bouncing of the droplet.

Conclusion

The dynamics of a water droplet dispensed in an oil-filled microwell under SAW-induced streaming is studied. The droplet is seen to either settle to the bottom, get trapped in the streaming vortex or 'bounce' off the bottom depending on composition of the oil in the microwell and the actuation power.

References

[1] C. Chen, S.P. Zhang, Z. Mao, N. Nama, Y. Gu, P.H. Huang, Y. Jing, X. Guo, F. Costanzo and T.J. Huang Lab Chip **18**, 3645-3654 (2018).
[2] G. Altshuler and O. Manor Phys. Fluids **27**, 102103 (2015).

Acoustofluidics 2021
26-27 August 2021
Virtual Conference

Modulated acoustic radiation force in a carrier standing wave

Mehdi Akbarzadeh[1], Sebastian Oberst, Shahrokh Sepehrirahnama, and Ben Halkon

[1] Centre for Audio, Acoustics and Vibration, University of Technology Sydney, Sydney, Australia. E-mail: Mehdi.Akbarzadeh@student.uts.edu.au

Introduction

For many applications, such as sorting, separation, and manipulation of differently shaped particles [1-3], it is desirable to be able to control the direction of the acoustic radiation force (F_{rad}) and produce e.g., alternating pushing and pulling forces [4]. Using progressive acoustic plane waves, it has been demonstrated that pulsating spherical carriers experience a force direction reversal owing to radiation energy originating from the pulsating surface [5] with the limitation that the oscillation of the particle is limited to its boundaries. Here, and by using an acoustic standing plane wave, oscillating positive and negative radiation forces studied theoretically and numerically. By using Gor'kov's formulation, the acoustic contrast factor [6], is calculated for modulated acoustic field quantities. The ability of producing both positive and negative forces leads to the ability to control the vibration of an object. Fushimi et al. suggested an experimental model of a nonlinear stiffness model of the trapping of a solid particle in a single-axis acoustic levitator [7]. Here, by using their experimental data the presented analytical and numerical model are validated and discussed.

Nonlinear dynamic model of a spherical object inside a single-axis acoustic levitator

Let's consider a naturally buoyant spherical object (particle) with rigid body oscillations in form of $Z_p(t) = A\sin(\omega_o t)$ within an ideal fluid and subjected to an incident pressure standing wave $P_{in} = P_a\cos\left(kz(t)\right)\cos\left(\omega t\right)$, as schematised in Figure 1. The particle can be assumed to be a harmonic oscillator with mass of M_p and nonlinear stiffness k_s which oscillates about its equilibrium position e at distance z from the pressure anti-node.

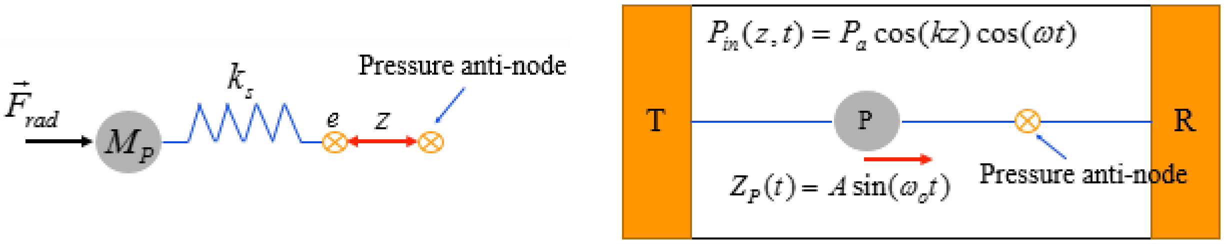

Figure 1: A schematic of an oscillatory particle suspended between a transducer and a reflector with its mechanical model.

Using this mathematical model, the incident pressure field can therefore be re-written as

$$P_{in}(z,t) = \left(P_a C_1(t)\cos(kz) + P_a C_2(t)\sin(kz)\right) \tag{1}$$

with $C_1(t) = \cos\left(\omega t\right)\cos\left(\left(Ak\right)\sin\left(\omega_o t\right)\right)$ and $C_2(t) = \cos\left(\omega t\right)\sin\left(\left(Ak\right)\sin\left(\omega_o t\right)\right)$.

According to Gor'kov's theory [7], F_{rad} is calculated as

$$F_{rad} = 4k\pi r^3 E_{ac}\Phi(\tilde{\kappa},\tilde{\rho})\sin\left(2kz\right) \tag{2}$$

where k is the wave number, r is the particle radius, E_{ac} is the acoustic energy density [7], Φ is the acoustic contrast factor, and $\tilde{\kappa}$ and $\tilde{\rho}$ represent the relative compressibility and density between, particle and host fluid, respectively. To verify the equations, we study F_{rad} as exerted by a standing wave in form of a background pressure field, Eq. (1), and its effect on a particle immersed in water using a 2D axisymmetric geometry (COMSOL Multiphysics 5.5). Radiation boundary conditions are used to mimic the particle's free space scattering by conducting a finite element simulation.

Analytical and numerical examples

We conduct a parametric analysis to calculate F_{rad} on an oscillatory particle comparing analytical and numerical simulations. The parameters used for the calculations are: $c_1 = 6559\ \left[\mathrm{m/s}\right]$, $\rho_1 = 2000\ \left\lfloor \mathrm{kg/m^3} \right\rfloor$,

$\lambda = 1.48\ [\mathrm{mm}]$, $z = \lambda/8\ [\mathrm{mm}]$, $c_0 = 1480\ [\mathrm{m/s}]$, $\rho_0 = 1000\ \left[\mathrm{kg/m^3}\right]$, $\omega = 1\ [\mathrm{MHz}]$, and $\omega_o = 10\ [\mathrm{KHz}]$. When, c being the speed of sound and ρ is the density with indices 0 and 1 denoting the fluid and the particle, respectively, z is the distance between the pressure anti-node and the center of the particle in the wave direction, and λ is the wavelength. Figure 2 shows the mean value of time functions of Eq. (1) and an acoustic contrast factor Φ for different normalized amplitude, Ak. F_{rad} changes its sign, indicating direction reversal.

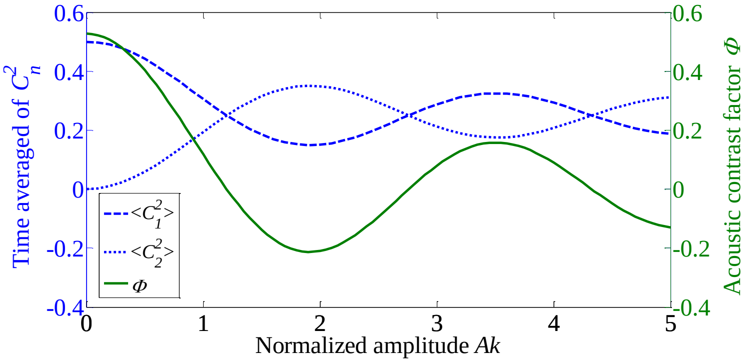

Figure 2: The acoustic contrast factor and $\left\langle C_n(t)^2 \right\rangle$, $n = 1, 2$ for different value of the Ak.

Figure 3 depicts the acoustic radiation force function (Y_{st}) [2] as dimensionless value of F_{rad}, against the dimensionless particle radius kr for two different values of Ak. Y_{st} shows that the different values of the positive and negative of F_{rad} can be achieved.

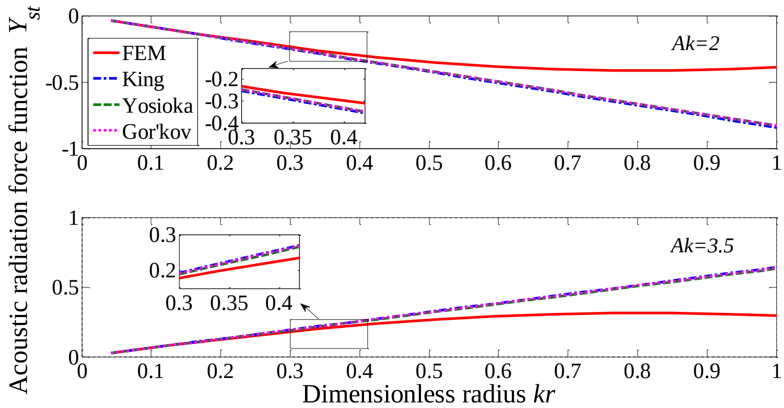

Figure 3: A comparison of the Y_{st} between numerical and analytical results for an oscillatory particle in a standing acoustic wave field over.

A single degree-of-freedom nonlinear dynamical equation of motion can be written as

$$\ddot{\theta} + \alpha\left|\dot{\theta}\right|\dot{\theta} + \beta\sin(\theta) = \gamma\cos(\theta)\sin(\omega_o t) \qquad (3)$$

when $\theta(t) = \sigma z(t)$ and α, β, γ, and σ are constant coefficients.

Conclusion

Due to the vibrating particle, the modulated incident acoustic pressure produces positive, zero and negative F_{rad}.. This suggests that the exposure of the particle to e.g., externally applied vibrations can provide an alternative means of controlling F_{rad}. A single degree-of-freedom nonlinear model of a solid particle trapped inside a mid-air single-axis levitator has been presented and will be compared to validate experimental findings of Fushimi [7].

References

[1] P. L. Marston, T. D. Daniel, A. R. Fortuner, I. P. Kirsteins, A. T. Abawi, Specular-reflection contributions to static and dynamic radiation forces on circular cylinders. The Journal of the Acoustical Society of America, 149(5), 3042–3051 (2021).

[2] F. B. Wijaya, S. Sepehrirahnama, K. M. Lim, Interparticle force and torque on rigid spheroidal particles in acoustophoresis. Wave Motion, 81, 28–45, (2018).

[3] H. Bruus, Acoustofluidics 7: The acoustic radiation force on small particles. Lab on a Chip, 12(6), 114–121, (2012).

[4] M. Rajabi, A. Mojahed, Acoustic radiation force control: Pulsating spherical carriers. Ultrasonics, 83, 146–156, (2018).

[5] M. Azarpeyvand, M. Azarpeyvand, Acoustic radiation force on a rigid cylinder in a focused Gaussian beam. Journal of Sound and Vibration, 332(9), 2338–2349, (2013).

[6] L. P. Gor'kov, On the forces acting on a small particle in an acoustical field in an ideal fluid, Soviet Physics-Doklady, (6), 773-775, (1962).

[7] T. Fushimi, T. L. Hill, A. Marzo, B. W. Drinkwater, Nonlinear trapping stiffness of mid-air single-axis acoustic levitators. Applied Physics Letters, 113(3), 34102-341205, (2018).

Acoustofluidics 2021
26-27 August 2021
Virtual Conference

Effect of Vibration Velocity on Low-Frequency Sharp-Edge Acoustic Streaming Pattern

Geyu Zhong[1,2,4], Chuanyu Zhang[1], Philippe Brunet[2], Laurent Royon[1], YingWen Liu[4], Xiaofeng Guo[1,3]

[1] Université de Paris, CNRS, LIED, UMR 8236, F-75013, Paris, France
[2] Université de Paris, CNRS, MSC, UMR 7057, F-75013, Paris, France
[3] Université Gustave Eiffel, ESIEE Paris, F-93162, Noisy le Grand, France
E-mail: Xiaofeng.Guo@esiee.fr, URL: https://perso.esiee.fr/~guox/
[4] Key Laboratory of Thermo-Fluid Science and Engineering of MOE, School of Energy and Power Engineering, Xi'an Jiaotong University, Xi'an, 710049, P. R. China

Introduction

Low-frequency vibrations are omnipresent in environment and can be harvested for process intensification purposes. To understand Sharp-Edge Acoustic Streaming (SEAS) at such low frequency, a numerical model is established for a sharp-edged mili-channel (Fig.1). Structured meshing is employed to optimize calculation accuracy. Different acoustic velocities (V_a) under a frequency of 10Hz are prescribed. Averaged-velocity field, velocity streaming and maximum streaming velocity ($V_{s,max}$) are extracted to characterize SEAS.

Description of Numerical model

The numerical method is based on the direct solving of the Navier-Stokes equation (DNS) with a laminar flow model. The numerical results are carefully validated by comparing with our previous experiments in a micro-channel [1]. Periodic velocity boundary conditions are employed in this study, as shown in Fig.1.

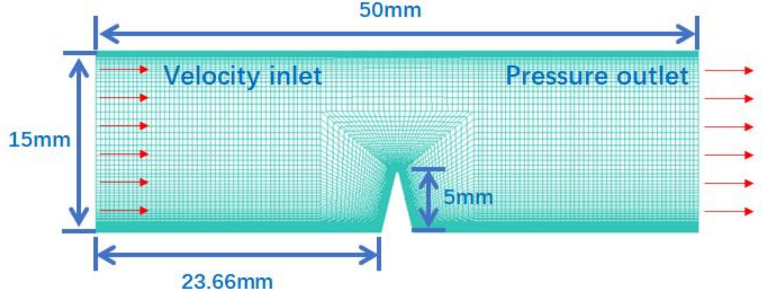

Figure 1: Scale, mesh and boundary conditions of numerical model. The inlet velocity is provided as periodically with frequency of 10Hz.

Results and Discussions

At low frequency, the position, size and shape of streaming vortices depend on vibration velocity, as shown in Fig.2. When the amplitude of vibration displacement is smaller than the curvature diameter of the sharp-edge, streaming vortices are symmetrical and in agreement with previous research [1]. However, this flow pattern undergoes a transition after the amplitude exceeds the mentioned threshold. From a symmetrical structure, the vortices turn into a more complex compressed shape, then to a single vortex. It implies that at low frequency, the vortices feature may change at higher acoustic velocity.

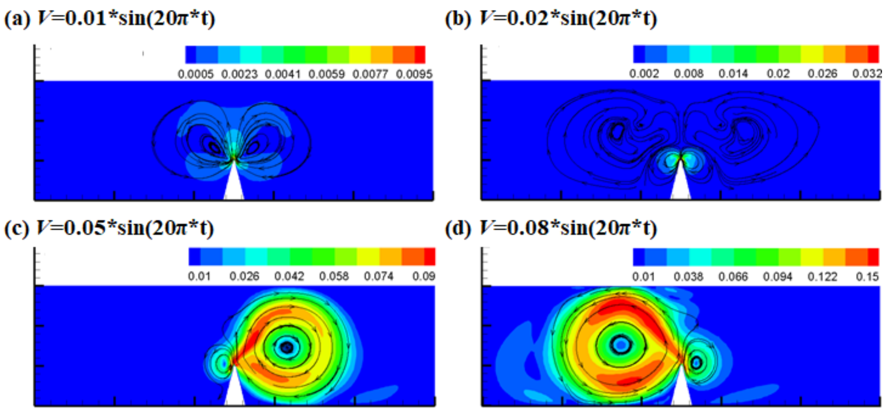
(a) V=0.01*sin(20π*t)
(b) V=0.02*sin(20π*t)
(c) V=0.05*sin(20π*t)
(d) V=0.08*sin(20π*t)

Figure 2: Changes of acoustic streaming pattern with different vibrating velocity in low frequency. (a) V_a=0.01m/s, (b) V_a=0.02m/s, (c) V_a=0.05m/s, and (d) V_a=0.08m/s.

From Fig.3a and b, $V_{s,max}$ increases with vibration velocity, which shows quadratic (V_a^2) and linear relationships (V_a) below and above the threshold, respectively. The formation and transition process of vortex in the first-order flow are supposed to be the key factor influencing SEAS pattern. The streaming velocity goes up with the increase of vibration velocity. When the quantities $V_{s,max}$ and V_a become comparable, the streaming flow should induce a feedback on the forcing conditions. Therefore, this interaction between first and second order flow contributes to the unstationary dynamics and transition of the streaming flow pattern, as shown in Fig.1.

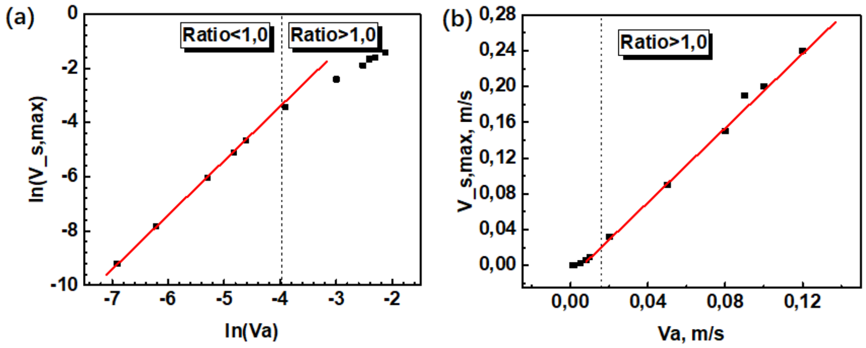

Figure 3: The variations of maximum streaming velocity with vibration velocity, showing (a) quadratic dependence for low V_a, and (b) linear dependence for higher V_a.

Conclusion

This work discussed the phenomenon of transformation in streaming vortex. We attempted to provide an explanation from a coupling between streaming velocity and vibration velocity. It pushes forward the understanding of SEAS flow pattern at low frequency in relation with the vibration amplitude when the latter becomes larger than the edge tip curvature diameter. Further investigations will be focused on the validation by a new experimentation platform.

References

[1] Zhang C, Guo X, Royon L, et al. Unveiling of the mechanisms of acoustic streaming induced by sharp edges. Physical Review E, 2020, 102(4): 043110.

Acoustofluidics 2021
26-27 August 2021
Virtual Conference

3D model of the particle acoustophoretic motion in a rectangular device

Abelino Vargas[1,2], Marcela Camacho[1,2], J.D. Muñoz[1] and Itziar González[3]

[1]National university of Colombia, Bogotá, Colombia, E-mail: avargasj@unal.edu.co
[2]International Physics Center (CIF), Biophysics Laboratory, Bogotá, Colombia.
[3]Department of Ultrasounds, ITEFI, CSIC Spanish National Research Council, Madrid (Spain), iciar.gonzalez@csic.es URL: http://www.itefi.csic.es/en/research-departments/

Introduction

In this work, we present a three-dimensional model of the particle motions within the acoustic field generated by ultrasonic standing waves. This model allows a theoretical study of the three-dimensional **F**$_R$ induced by a standing acoustic wave in a microfluidic chamber with rectangular geometry on N spherical particles and the simulation of the aggregation process. To achieve this, expressions for the 3D **F**$_R$ were obtained with two different sets of boundary conditions, and the optimized Forest–Ruth algorithm was employed in a numerical simulation in C++ to derive the dynamics of N spherical particles. The theoretical results were compared with the formation of pearl-chain aggregates within rectangular glass capillary.

3D Model

The acoustic pressure of a 3D standing wave established with in a resonating chamber with rigid or free x-walls as boundary conditions can be described by :

$$p_1(\vec{r}) = p_0 \cos(k_x x)\cos(k_y y)\cos(k_z z) \tag{1}$$

$$p_1(\vec{r}) = p_0 \sin(k_x x)\cos(k_y y)\cos(k_z z) \tag{2}$$

With a pressure amplitude of the incident wave, p_0, and acoustic wave numbers $k_i = n_i\pi/l_i$ for $i=x,y,z$ along the three ortogonal directions in a chamber of rectangular geometry with dimensions l_x, l_y and l_z , $k^2=k_x^2+k_y^2+k_z^2$.The radiation force **F**$_R$ acoustically induced is derived as a gradient of the acoustic potential and acquires the expressions for x-rigid walls [1]:

$$\begin{aligned}\boldsymbol{F}_R = {}& 2k_x\phi U_o \sin(2k_x x)\left[\frac{1}{4}+\frac{1}{4}\cos(2k_y y)\cos(2k_z z)+\left\{\frac{1}{4}-\frac{\phi' k_z^2}{2k^2}\right\}\cos(2k_y y)+\left\{\frac{1}{4}-\frac{\phi' k_y^2}{2k^2}\right\}\cos(2k_z z)-\frac{\phi'}{2k^2}\left\{k_y^2+k_z^2\right\}\right]\hat{\boldsymbol{i}}\\ &+2k_y\phi U_o \sin(2k_y y)\left[\frac{1}{4}+\frac{1}{4}\cos(2k_x x)\cos(2k_z z)+\left\{\frac{1}{4}-\frac{\phi' k_z^2}{2k^2}\right\}\cos(2k_x x)+\left\{\frac{1}{4}-\frac{\phi' k_x^2}{2k^2}\right\}\cos(2k_z z)-\frac{\phi'}{2k^2}\left\{k_x^2+k_z^2\right\}\right]\hat{\boldsymbol{j}}\\ &+2k_z\phi U_o \sin(2k_z z)\left[\frac{1}{4}+\frac{1}{4}\cos(2k_x x)\cos(2k_y y)+\left\{\frac{1}{4}-\frac{\phi' k_y^2}{2k^2}\right\}\cos(2k_x x)+\left\{\frac{1}{4}-\frac{\phi' k_x^2}{2k^2}\right\}\cos(2k_y y)-\frac{\phi'}{2k^2}\left\{k_x^2+k_y^2\right\}\right]\hat{\boldsymbol{k}},\end{aligned} \tag{3.a}$$

And x-free walls [1]:

$$\begin{aligned}\boldsymbol{F}_R = {}& -2k_x\phi U_o \sin(2k_x x)\left[\frac{1}{4}+\frac{1}{4}\cos(2k_y y)\cos(2k_z z)+\left\{\frac{1}{4}-\frac{\phi' k_z^2}{2k^2}\right\}\cos(2k_y y)+\left\{\frac{1}{4}-\frac{\phi' k_y^2}{2k^2}\right\}\cos(2k_z z)-\frac{\phi'}{2k^2}\left\{k_y^2+k_z^2\right\}\right]\hat{\boldsymbol{i}}\\ &+2k_y\phi U_o \sin(2k_y y)\left[\frac{1}{4}-\frac{1}{4}\cos(2k_x x)\cos(2k_z z)-\left\{\frac{1}{4}-\frac{\phi' k_z^2}{2k^2}\right\}\cos(2k_x x)+\left\{\frac{1}{4}-\frac{\phi' k_x^2}{2k^2}\right\}\cos(2k_z z)-\frac{\phi'}{2k^2}\left\{k_x^2+k_z^2\right\}\right]\hat{\boldsymbol{j}}\\ &+2k_z\phi U_o \sin(2k_z z)\left[\frac{1}{4}-\frac{1}{4}\cos(2k_x x)\cos(2k_y y)-\left\{\frac{1}{4}-\frac{\phi' k_y^2}{2k^2}\right\}\cos(2k_x x)+\left\{\frac{1}{4}-\frac{\phi' k_x^2}{2k^2}\right\}\cos(2k_y y)-\frac{\phi'}{2k^2}\left\{k_x^2+k_y^2\right\}\right]\hat{\boldsymbol{k}},\end{aligned} \tag{3.b}$$

In addition to this 3D force, $\mathbf{F}_R$, other forces that affect particle motions must be considered, such as, the viscous drag force $\mathbf{F}_d$, the buoyancy force $\mathbf{F}_b$ and the Hertzian contact stress $\mathbf{F}_{ij}$ that is established between particles by their contact in the pressure node. The 3D equation of motion for particle $\boldsymbol{i}$ with mass $\boldsymbol{m_i}$ exposed to these forces is:

$$m\vec{\boldsymbol{a}} = \boldsymbol{F_R} + \boldsymbol{F_d} + \boldsymbol{F_b} + \boldsymbol{F_{ij}} \tag{4}$$

where $\boldsymbol{a}$ is the acceleration and $\boldsymbol{f}$ is the net force exerted on particle $\boldsymbol{i}$.

The 3D motion equation, Eq. (4), was solved for N particles using an optimized Forest–Ruth algorithm [2] with a C++ code developed by us [1]. Figures 1 and 2 show results numerically obtained for N=144 spherical polystyrene particles of 15 μm diameter immersed in water in the chamber of rectangular geometry during the application of the ultrasonic wave assuming rigid and free *x*-walls respectively, for the rectangular vibration mode (2,1,1). The particles collect at different positions within the chamber to form clusters that become relocated over time.

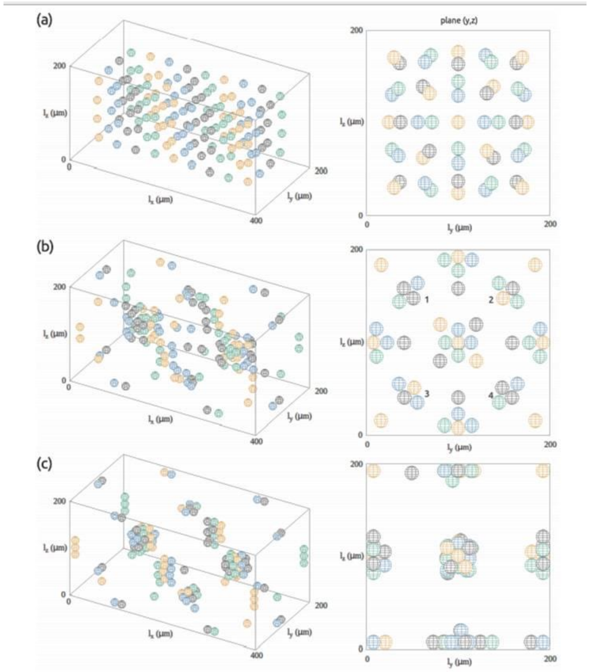

Figure 1: Particle movements generated by the 3D $\mathbf{F}_R$ in a rectangular chamber with rigid walls. (a) Initial motions due to the acoustic force; (b) cluster formation in the chamber center; (c) final particle positions [1].

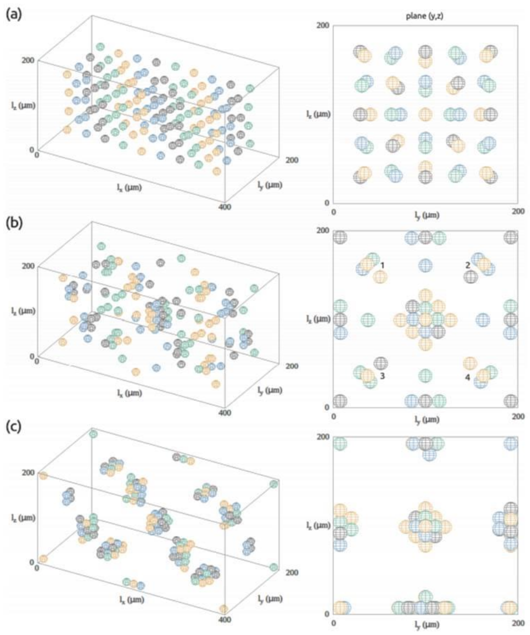

Figure 2: Particle movements generated by the 3D $\mathbf{F}_R$ in a rectangular chamber with free walls. (a) Initial motions due to the acoustic force; (b) cluster formation in the chamber center; (c) final particle positions [1].

Conclusion

This work presents a 3D model of the effects of a three-dimensional radiation force generated by an acoustic standing wave in resonant cavities of rectangular and square geometry. A numerical simulation in C++ was developed to predict the simultaneous dynamics of N particles in microfluidic channels using an optimized Forest–Ruth algorithm. This model allows the study of aggregation processes in rectangular channels.

References

[1] A. Vargas-Jiménez, M. Camacho, J.D. Muñoz, I. González, A 3D analysis of the acoustic radiation force in microfluidic channel with rectangular geometry, Wave Motion, Volume 101, 2021, 102701.

[2] I. Omelyan, I. Mryglod, R. Folk, Optimized forest–ruth- and suzuki-like algorithms for integration of motion in many-body systems, Comput. Phys. Comm. 146 (2) (2002) 188–202.

Acoustofluidics
2021
26-27 August 2021
Virtual Conference

Multiphysic model based on SAW-Liquid interaction for the prediction of physical stresses exerted on cells and tissues: simulation versus experiment

D.S. Bidouba Sanvany[1], F.Kosior[1], D.Beyssen[1], A.Gigodot[1], E.Gaudion[1] and F.Sarry[1]

[1] Université de Lorraine, CNRS, IJL, F-54000 Nancy, France
E-mail: doll-spencerh.bidouba-sanvany@univ-lorraine.fr

I. Introduction

With the development of lab-on-chip (LOC), microfluidics has emerged as an ideal candidate in the field of chemistry, biology and medicine due to its many advantages, namely: system miniaturization, low cost, reduced reagent consumption, automation, precise control of the microenvironment and speed [1].

In recent years, many studies have shown the benefits of using Surface Acoustic Waves (SAWs) for actuation, detection and analysis of biological substances (bacteria, DNA, viruses, cells, etc.) [2]. SAW devices reply to the advantages of LOC and they can be totally biocompatible.

Our study consists in investigating the effect of SAWs on adherent (SaOs-2 osteoblasts) and circulating (THP-1 monocytes) biological cells to determine the physical stresses on the latter (acoustic radiation pressure and shear stresses), which are important in biomedicine for cell stimulation. The frequency, the power applied to the electrodes and the energy dose applied to the cells or tissues are important parameters for this study. However, acoustic radiation pressure and shear stresses are not yet experimentally accessible. So it is important to perform simulations to quantify them in order to optimize our SAW actuators. We will first of validate our simulations carried out on Comsol Multiphysics by comparing the response with our 20 MHz probe. The biological medium is assimilated to a fluid whose viscosity is close to PBS (Phosphate Buffered Saline) and to the cell culture medium used for biological experiments (RPMI for THP-1 monocytes and McCoy for SaOs-2 osteoblasts). This biological medium allows to keep the osmotic equilibrium between the biological medium and the cells and thus avoids the explosion of the cells.

II. Theorical simulation approach

By exploiting perturbation theory in the equations for conservation of mass and angular momentum, we obtain the equations that account for the ultrasonic field and the streaming.

$$p - p_0 = \varepsilon p_1 + \varepsilon^2 p_2 + \cdots \tag{1.a}$$

$$\rho - \rho_0 = \varepsilon \rho_1 + \varepsilon^2 \rho_2 + \cdots \tag{1.b}$$

$$u - u_0 = \varepsilon u_1 + \varepsilon^2 u_2 + \cdots \tag{1.c}$$

We are able to rewrite the sound equation (first order):

$$\frac{\partial \rho_1}{\partial t} + \rho_0(\nabla . u_1) = 0 \tag{2.a}$$

$$\rho_0 \frac{\partial u_1}{\partial t} = -\nabla p_1 + \left[\mu_B + \frac{\mu}{3}\right] \nabla(\nabla . u_1) - \mu \nabla^2 u_1 \tag{2.b}$$

and also the streaming equation (second order):

$$\rho_0 \nabla . \langle u_2 \rangle = -\nabla . \langle \rho_1 u_1 \rangle \tag{3.a}$$

$$-\langle \nabla p_2 \rangle + \left[\mu_B + \frac{\mu}{3}\right] \langle \nabla(\nabla . u_2) \rangle - \langle \mu \nabla^2 u_2 \rangle = \langle \rho_1 \frac{\partial u_1}{\partial t} \rangle + \rho_0 \langle (u_1 . \nabla) u_1 \rangle \tag{3.b}$$

where μ is the dynamic viscosity, μ_B is the volumic viscosity, u_1 is the first order velocity of the fluid particle ρ_1 is the first order density and ρ_0 is the fluid density at equilibrium. ε is the Mach number and

$\langle A \rangle$ the time average of the quantity A over an oscillation period. From this theorical approach we proposed a simulation model with Comsol Multiphysics.

III. Experimental device

We performed our experiments using $LiNbO_3$ 128Y-X as piezoelectric substrate, arranged vertically and immersed in water contained in a small plexiglass container with a diameter of 10 mm (Figure 1.a).

The acoustic probe consists of 50 pairs of interdigital transducers (IdTs) designed on a 3 cm long $LiNbO_3$ 128Y-X substrate (Figure 1.b). By applying a radio frequency signal to the IdT, the substrate starts to vibrate and generates Rayleigh waves through the inverse piezoelectric effect. The Rayleigh wave in contact with the liquid becomes an evanescent Rayleigh wave (Leaky SAW) and propagates in the liquid as a compressional wave (represented by the 1st order equation) and generates the flow within the liquid (streaming represented by the 2nd order equation).

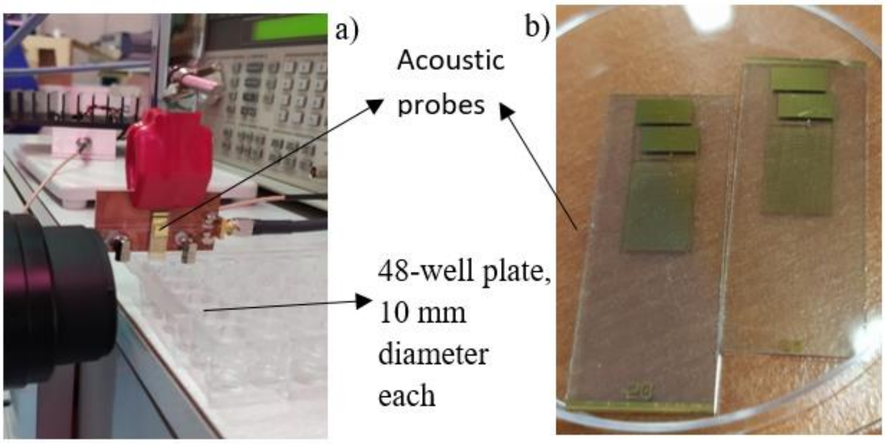

Figure 1: Set-up of the experimental device, a) Probe immersed in a 10 mm diameter well containing 800 µl of water. b) Acoustic probe manufactured in a clean room.

IV. Discussion

2D simulations were first performed due to the complexity of building a 3D model and the time consumption. Figure 2.a) shows the comparison of the evolution of the amplitude of the SAW between the experiment and the simulation for different RF power. We observe a perfect agreement between the profile of the curves and a maximum difference of 4.5% at 19 dBm. Figure 2.b) presents the two vortices, a large one rotating clockwise and a small one rotating counterclockwise. They are also present on the experimental part. Figure 2.c) shows the evolution of the particle velocities in the well, measured by Particle Image Velocimetry (PIV) method.

We observe a good agreement up to 17 dBm and a divergence starting from 20 dBm with a maximum divergence of a coefficient 4 at 30 dBm. This difference should be explained by the different velocities in simulation and experiment (maximum vs average) and the fact that we consider a characteristic impedance of 50 ohms in the simulation. Moreover the simulations are obtained with only 5 pairs of IdTs.

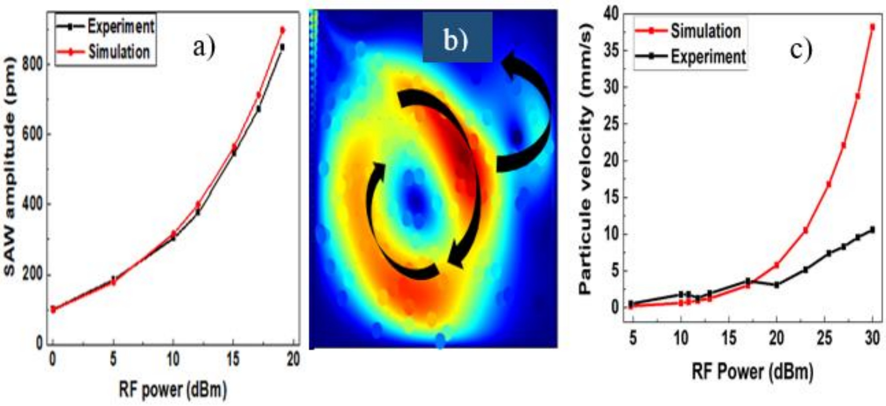

Figure 2: Comparison between simulation and experiment a) Amplitude of SAW, the experimental data are taken from the article by Greco et al.[4]. b) Result of the simulation of the shape of the vortex. c) Velocity of the particles in mm/s, in the simulation the maximum velocities and experimentally (PIV method) the average velocities are presented.

V. Conclusion

The simulation model presented gives us very satisfactory results in terms of electrical and mechanical characterization of piezoelectric probe, and representation of the phenomenon observed in the experiment, namely the generation of two vortices (one large clockwise and one small counterclockwise). In order to compare the same velocities, we have to make adjustment to determine the instantaneous velocities for PIV experiment and simulation.

In conclusion, the presented model will be used to determine the mechanical stresses exerted on the cells and tissues in the framework of studies on mechanobiology.

References

[1] X. Ding *et al.*, *Lab Chip*, vol. 13, nº 18, p. 3626, (2013)

[2] Y. Huang, P. Kr. Das, et V. R. Bhethanabotla, *Sensors and Actuators Reports*, vol. 3, p. 100041 (2021).

[3] WLM Nyborg, *11 - Acoustic Streaming*, Physical Acoustics, Academic Press, Volume 2, Part B, 1965, pp 265-331, ISBN 9780123956620.

[4] G. Greco, M. Agostini, I. Tonazzini et al. Cecchini,*Anal. Chem.*, vol. 90, nº 12, p. 7450-7457, (2018).

Acoustofluidics 2021
26-27 August 2021
Virtual Conference

Binary acoustic particle trapping in glass capillaries

Thierry Baasch[1], Anna Fornell[2,3], Carl Johannesson[1], Johan Nilsson[1] and Maria Tenje[2]

[1]Department of Biomedical Engineering, Lund University, Lund, Sweden
E-mail: Thierry.Baasch@bme.lth.se
[2]Department of Materials Science and Engineering, Uppsala University, Uppsala, Sweden
[3]MAX IV Laboratory, Lund University, Lund, Sweden

Introduction

We show that melamine particles can be selectively trapped out of a polystyrene and melamine particle mixture in an acoustically activated capillary by tuning the density of the buffer. It has been shown that acoustically excited capillaries (Fig. 1a1) can be used for both focusing particles in the capillary height (Fig. 1a3) and trapping the particles against the flow (Fig. 1a2) [1]. In this experimental, numerical and theoretical study, we show that the density contrast is mainly responsible for the acoustic trapping force while the focusing is driven by both the density and compressibility contrast of the particles with the surrounding medium. Only particles with density higher than the surrounding medium can be trapped in the capillary. This effect can be exploited by tuning the density of the buffer such that melamine particles (density $1500\,\mathrm{kg\,m^{-3}}$) are trapped while polystyrene particles (density $1050\,\mathrm{kg\,m^{-3}}$) are not trapped.

Methods, theory and results

The experiments were carried out in a standard capillary (Fig. 1a1) that was excited at its $\lambda/2$ mode in y direction by a kerfed transducer with strong resonance at 4 MHz. Water was mixed with Ficoll to tune the density of the media. The density of water, 14% Ficoll and 28% Ficoll are approximately $1000\,\mathrm{kg\,m^{-3}}$, $1050\,\mathrm{kg\,m^{-3}}$, and $1100\,\mathrm{kg\,m^{-3}}$, respectively. In experiments, polystyrene particles could be trapped against flow in water (Fig. 1b1) but not in Ficoll solutions of 14% or more (Fig. 1b2 and 1b3). The heavier melamine particles, however, could be trapped in a 14% Ficoll solution (Fig. 1b4). In all the used solutions (water, 14% Ficoll, 28% Ficoll), the both the melamine and polystyrene particles could be focused in the y direction (Figs. 1c1 to 1d2).

We built a two-dimensional finite-element model of the capillary (Fig. 1f1) to compute the squared time-averaged pressure (Fig. 1f2) and velocity fields (Fig. 1f3). Assuming the particles are heavier (positive dipole scattering coefficient) and less compressible (positive monopole scattering coefficient) than the surrounding medium, then, according to Gorkov's theory [2], the acoustic radiation force on the particles is composed of two contributions: one contribution proportional to the monopole scattering coefficient f_1 that acts towards the minimum of the average squared pressure field $\langle p^2\rangle$ and a second contribution proportional to the dipole scattering coefficient f_2 acting towards the maximum of the average squared velocity field $\langle v^2\rangle$. Please note that the monopole scattering coefficient f_1 is a function of the particle and fluid compressibility, while the dipole scattering coefficient f_2 is a function of the particle and fluid density. The shapes of the $\langle p^2\rangle$ and $\langle v^2\rangle$ fields (Figs. 1f2 and 1f3) suggest that both the monopole f_1 and dipole f_2 scattering coefficients contribute to the focusing force, while only the dipole coefficient contributes to the trapping force.

We analytically modeled the retention force F_r, i.e. the acoustic force acting in the x direction that holds the particles against the flow. To this end, we assumed a two-dimensional background wave and applied Gorkov's theory to derive

$$F_r = -V_p \frac{3 f_2 p_0^2}{4\omega^2 \rho_0} k_x k_y^2 \cos(k_x x)\sin(k_x x). \tag{1}$$

Where we used the volume of the particle V_p, the dipole scattering coefficient f_2, the pressure amplitude p_0, the angular frequency ω, the fluid density ρ_0, the wavenumber in the x and y direction k_x and k_y, respectively. The analytical result shows that the retention force is independent of the monopole f_1 scattering coefficient and only particles with positive dipole scattering coefficient f_2 can be trapped, which is confirmed by our experimental findings.

Finally, we performed binary trapping experiments: a mixture of fluorescent polystyrene and non-fluorescent melamine particles in 16% Ficoll solution was flowed through the trapping capillary. The

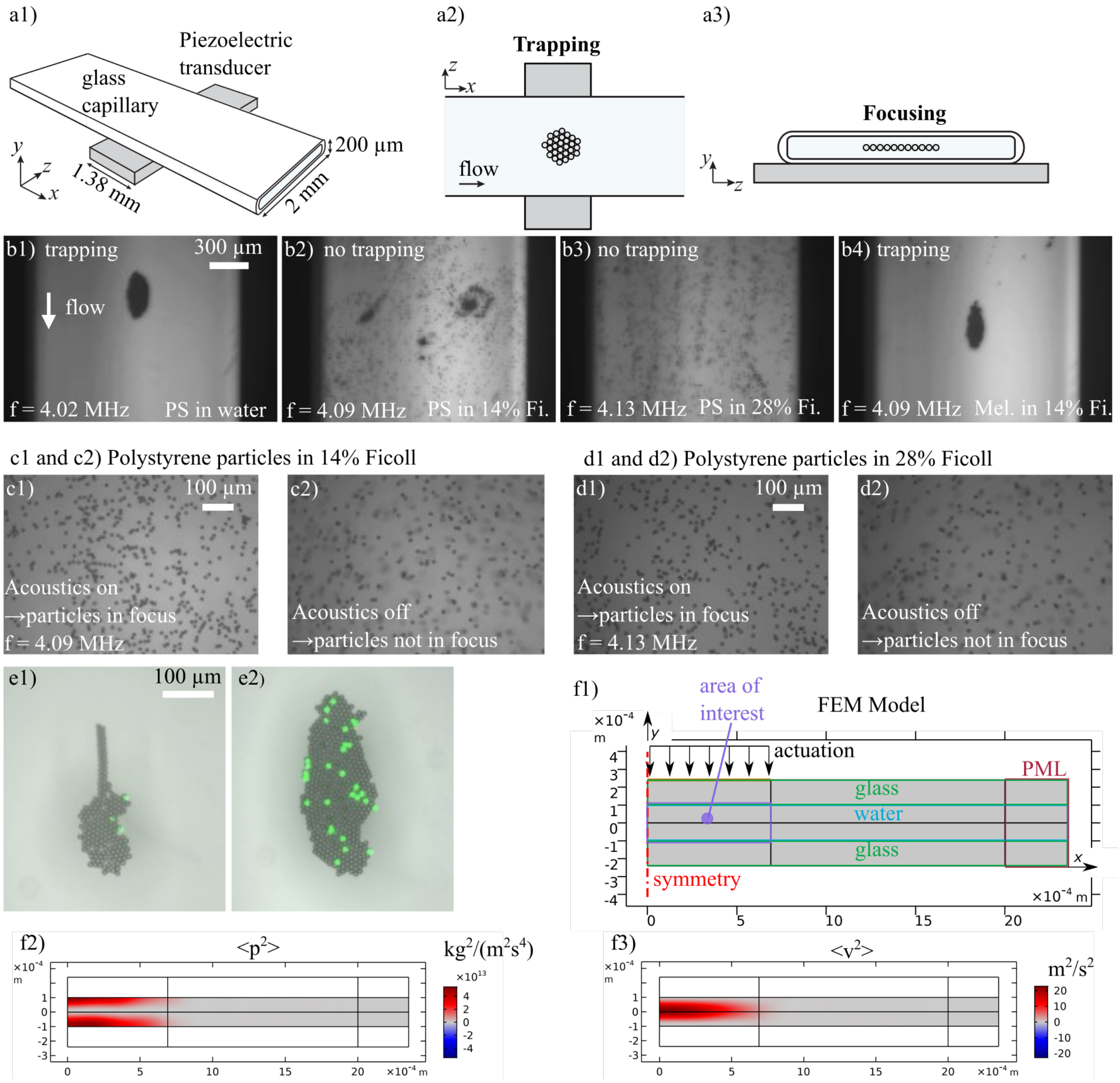

Figure 1: Sketch of the experimental setup (a1), the trapping (a2) and focusing (a3) of particles. Polystyrene particles could be trapped in water (b1) but not in Ficoll solutions higher than 14% due its higher density (b2 and b3). Melamine particles could be trapped in a 14% Ficoll solution (b4). Polystyrene particles could be focused in 14% (c1) and 28% (d1) Ficoll. Nonfluorescent melamin and a few fluorescent polystyrene particles in the trap (e1 and e2). The Comsol model (f1) and the resulting $\langle p^2 \rangle$ and $\langle v^2 \rangle$ fields.

melamine particles were trapped, while only very few polystyrene particles were found in the trapped cluster. This experiment was carried out both at low (Fig. 1e1) and high (Fig. 1e2) total particle concentration.

Conclusion

We have shown experimentally and theoretically that the acoustic trapping force only acts on particles of higher density than the surrounding medium. We exploited this effect to selectively trap melamine particles out of a mixture of polystyrene and melamine particles inside an acoustically activated glass capillary.

References

[1] A. Fornell, T. Baasch, C. Johannesson, J. Nilsson, and M. Tenje. Journal of Physics D: Applied Physics **54**, (2021).
[2] L. P. Gorkov. Doklady Akademii Nauk. **140**, (1961).

Acoustofluidics 2021
26-27 August 2021
Virtual Conference

Single cell encapsulation using SAW

Andreas Link[1], Raymond Sparrow[1], Esther Richter[1], Mustafa Zaimagaoglu[1], John McGrath[1] and Thomas Franke[1]

[1]Division of Biomedical Engineering, School of Engineering, University of Glasgow, Oakfield Avenue, G12 8LT Glasgow, UK
E-mail: Thomas.Franke@glasgow.ac.uk, https://www.gla.ac.uk/schools/engineering/staff/thomasfranke/

Introduction

The majority of published microfluidic single-cell cell encapsulation work has focused on the development and use of non-deterministic, passive encapsulation methods.[1] We: i) demonstrate the use of an acoustic device to actively encapsulate single red blood cells into individual droplets in a T-junction, ii) compare the active encapsulation with the passive encapsulation depending on the number of loaded cells as well as the created droplet volumes. This method overcomes the limitation of Poisson statistic loading of cells for the passive encapsulation. In our experiments we reach a single cell encapsulation efficiency of 97.9 ± 2.1 % at droplet formation rates exceeding 15 Hz.

Methods

Design and fabrication of hybrid chip consists of a single layer of Polydimethylsiloxane (PDMS) assembled between a piezoelectric substrate and a plastic cover using screws to control the pressure manually. A tapered interdigital transducer (TIDT) was produced by depositing 60 finger pairs of gold electrodes on top of a piezoelectric substrate (polished, 128° rot, Y-cut LiNbO3), coated with a 200 nm SiO2 layer, to generate travelling surface acoustic waves (T-SAWs). The distance between the electrode fingers varies such that, the transducer wavelength is 23.0 to 24.2 microns and has an aperture width of 500 microns. The resonance frequency of the T-IDT ranges from 160 to 167 MHz. PDMS channels are manually aligned on the T-IDT chip and flushed with Aquapel before use.

Red blood cells were prepared from whole blood obtained from a healthy donor and washed three times in phosphate buffered saline solution (PBS 1x, pH 7.4, 330 mOsm/L, Gibco life technologies). After each washing step, we centrifuge the sample for 5 min at 2500 RPM (mini spin plus centrifuge, Eppendorf) and remove the white buffy coat and supernatant. After the last centrifugation step, we take 80 µl of concentrated RBC from the bottom of the reaction tube and incubate in 1 ml green-fluorescent Calcein-AM solution (5 µM) for 30 min at 37°C, followed by three times washing with PBS. To avoid sedimentation of cells during the experiment we suspend the cells in a density matched solution using a density gradient solution (OptiPrep Density Gradient Medium, Sigma Life Science). 533 µL OptiPrep solution was mix with 1407 µL PBS/BSA (14 mg/ml) and suspend 60 µL of concentrated fluorescent-labelled RBC solution. The final density of this solution is $\rho = 1.080$ g/mL. The cell solution is stored at room temperature and is degassed for at least 15 min in the desiccator before use. The hematocrit (Ht.) of this solution is 1 %.

Results

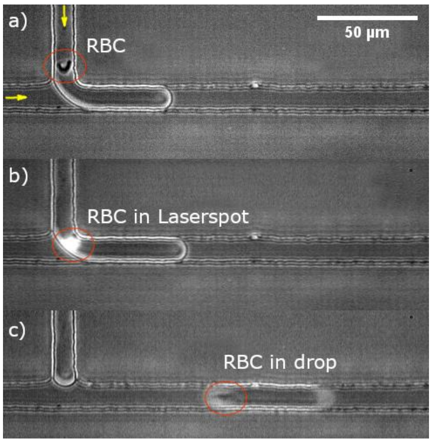

Figure 1: Active RBC encapsulation in droplet: Series of micrographs showing the encapsulation mechanism and the pinch-off of a droplet actuated by a pressure increase in the continuous phase which is induced via surface acoustic waves. A cell flowing in the aqueous discontinuous phase approaching the T-junction (red circle) (a). The cell is detected by the laser focused at the T-junction and the fluorescence is detected by a photomultiplier. The fluorescence level is analysed in custom-made software. If the signal is above a fluorescence threshold, the SAW is triggered and the drop is cut-off (c). For this encapsulation experiment, we use a power of $P = 29$ dBm and a pulse of $t_{pulse} = 0.6$ ms. The yellow arrows indicate the flow direction of the continuous and dispersed phase. The scale bar in the micrograph is 50 µm.

We actively control the size of drops formed at the T-junction drop-maker one by one. We acoustically trigger the drop pinch-off by actuating a SAW pulse at the TIDT for a short period of time using a power of $P = 29$ dBm and a pulse length of $t_{\text{pulse}} = 0.6$ ms. [2,3] The acoustic pulse creates a temporary pressure increase at the T-junction that causes the drop to form. [3] At this power and a pulse length the pinch-off takes typically $t_{\text{pinch-off}} = 0.7 \pm 0.1$ ms. To synchronize droplet formation with the cell flow, we detect each cell flowing into the T-junction section. A laser spot (488 nm) is focused at the T-junction exciting fluorescence Calcein-AM (Sigma Life Science, USA) labelled red blood cells. The fluorescence is detected with a photomultiplier-tube (PMT) and the fluorescence level is analysed with custom-made software. If a cell is detected by the custom-made software (LabView) it triggers the SAW to pulse and pinch-off the drop as shown in Fig. 1. We evaluate the efficiency of active SAW cell encapsulation by comparing it with passive encapsulation into drops in the same microfluidic channel as shown in Fig. 2. For the passive cell encapsulation, different drop sizes were produced by variation of the pressure for the continuous oil phase p_{oil}, keeping the pressure for sample flow p_{sample} constant.

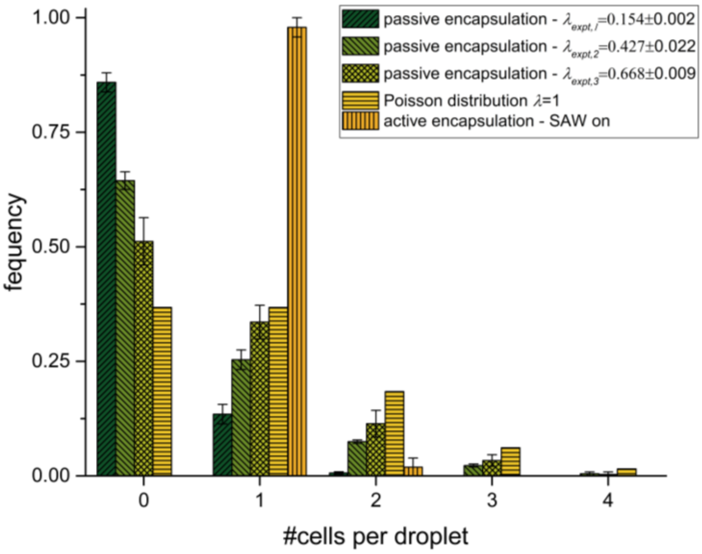

Figure 2: Histogram of frequency of drops (loading efficiency) depending on the number of RBCs per drop. Encapsulation is shown for the passive case for three volumes used (green), the active SAW encapsulation (orange) and for reference the theoretical limit for Poisson encapsulation (yellow). The loading efficiency E for single cell encapsulation for V_1 is $E_1 = 13.5 \pm 2.1$ %, for V_2 is $E_2 = 25.4 \pm 2.1$ % and for V_3 is $E_3 = 33.6 \pm 3.7$ %. The theoretical limit as given by the Poisson distribution is $E_{\text{Poisson}} = P_{\lambda=1}(1) = 36.8$ %. For the active encapsulation droplet loading efficiencies exceed the theoretical limit for passive encapsulation by a factor of 2.7 to be $E_{\text{SAW}} = 97.9 \pm 2.1$ %. Note, that no drop is empty and very few contain two cells in contrast to Poisson distributed loading.

Conclusion

Here, we have described a droplet microfluidic system with integrated SAW, which enables the ~98 % efficient encapsulation of single cells within droplets at rates exceeding 15 Hz. By utilizing laser-based cell detection which triggers rapid SAW-actuated droplet pinch-off, we have overcome the limitations of the Poisson distribution to repeatably encapsulate single cells in individual droplets on demand. This microfluidic chip can perform efficient encapsulation of single cells on a relatively small device footprint (4 mm^2), which offers easy integration into droplet-based microfluidic Lab on a Chip (LoC) devices having low sample availability. Further, this droplet microfluidic device is especially suitable for use with small sample volumes and can be used with heterogenous cell samples. Thus, this system can be of use in a range of biomedical or manufacturing applications that involve rapid, low-cost, continuous single-cell encapsulation.

References

[1] D. J. Collins, A. Neild, A. DeMello, A.-Q. Liu and Y. Ai, *Lab Chip*, **15**, 3439–3459 (2015).
[2] L. Schmid and T. Franke, *Lab Chip*, **13**, 1691 (2013).
[3] L. Schmid and T. Franke, *Appl. Phys. Lett.*, **104**, 133501 (2014).

Acoustofluidics 2021
26-27 August 2021
Virtual Conference

Spiraling wavefronts and detection of phase singularities in objects immersed in inhomogeneous acoustic fields

Ludovic Alhaïtz[1], Diego Baresch[1], Thomas Brunet[1], Christophe Aristégui[1], Olivier Poncelet[1]

[1]Univ. Bordeaux, CNRS, Bordeaux INP, ENSAM, INRAE, UMR 5295 I2M, F-33405 Talence, France
E-mail: ludovic.alhaitz@u-bordeaux.fr

Introduction

We are interested in the scattering of acoustic evanescent plane waves by an isolated particle. Recent studies in optics or acoustics have dealt with their non-classical properties which could be exploited for applications in particle manipulation [1,2] or imaging [3]. In this work, we investigated experimentally the field properties of such a system.

Experimental procedure

We conducted experiments at ultrasonic frequencies on a resonant droplet immersed in a non-miscible host fluid. Evanescent waves were generated by total internal reflection at a two-fluid interface at which the droplet was closely injected. Then field scans were performed inside and outside the droplet using a fibre optic hydrophone. The experimental set-up is presented in Fig. 1. A certain frequency range set by the bandwidth can be explored and the angle of incidence can be tuned so as to choose the evanescence degree.

Spiraling scattered waves and phase singularities

Due to symetry breaking effects occuring in the scattering of an evanescent wave, waves propagating angularly along the particle circonference are selected by increasing the evanescence degree. Interestingly, phase singularities may appear inside the particle as a consequence of destructive interferences (see Fig. 2(b)). The topological charge of the internal singular waves depends on the targeted scattered mode, fixed by the particle size and driving frequency. As a result, multiple spiraling scattered waves propagating away from the scatterer are generated and carry a transverse angular momentum density of orbital nature (Fig. 2(a)).

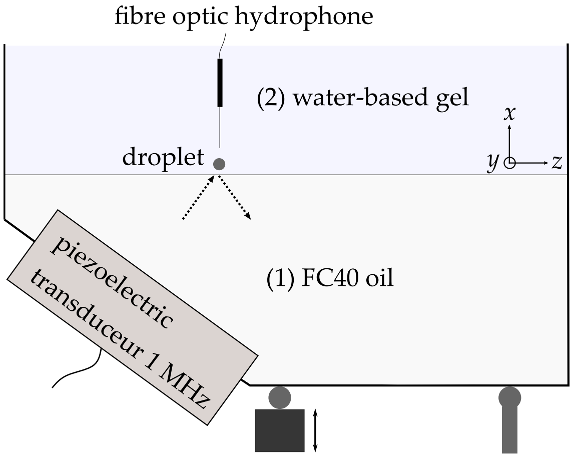

Figure 1: Experimental set-up for the generation of evanescent waves and scattering measurements. The source is placed in liquid (1) and is oriented beyond the critical angle of transmission. FC40 oil (1) is denser and has a lower sound speed than the water-based gel (2) to achieve the critical angle condition. A droplet is injected and stabilized in the gel near the interface.

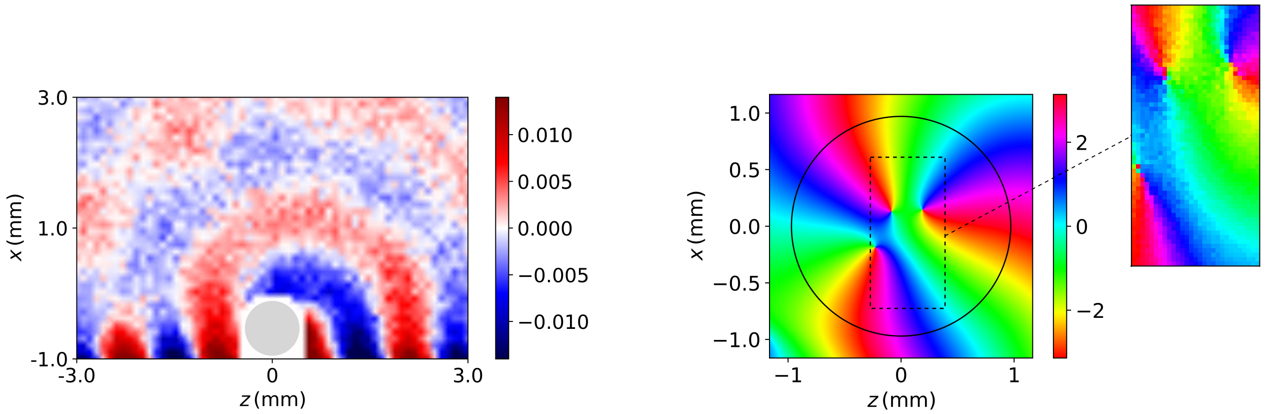

(a)

(b)

Figure 2: (a) Experimental scan of the pressure field outside a droplet. The central frequency corresponds to the dipolar resonance of the droplet. (b) Phase of the pressure field inside a droplet at its hexapolar resonance frequency: theory (left) / experiment (right).

Conclusion

The transversal angular momentum carried by the field in this case offers a different degree of freedom from that of usual vortex beams [4]. In addition, the emergence of topological singularities could be linked to an acoustic spin density, important for applications involving radiation force and torque [5].

References

[1] A. Canaguier-Durand and C. Genet. Phys. Rev. A **89**, 033841 (2014).
[2] V. Aubert, R. Wunenburger, T. Valier-Brasier, D. Rabaud, J-P. Klemandef, and C. Poulain. Lab on a Chip **324**, 2351 - 2542 (2016).
[3] C. Ma, S. Kim, and N. X. Fang. Nature Comm. **10**, 204 (2019).
[4] B. T. Hefner, and P. L. Marston. J. Acoust. Soc. Am. **106**, 3313 (1999).
[5] I. D. Toftul, K. Y. Bliokh, M. I. Petrov, and F. Nori. Phys. Rev. Lett. **123**, 183901 (2019).

Acoustofluidics 2021
26-27 August 2021
Virtual Conference

Cell phenotyping via Acoustic Contrast Factor by Using a Filled Tilted-Angle Acoustofluidic Device

Hanlin Wang[1], Joe Boardman[1], Xiaoyan Zhang[1], Chao Sun[2], Meng Cai[3], Jun Wei[3], Zhenlin Wu[4], Yongqing Fu[5], Xin Yang[1]

1 Department of Electrical and Electronic Engineering, Cardiff University, Cardiff, UK
E-mail: Wangh50@cardiff.ac.uk
2 School of Life Sciences, Northwestern Polytechnical University, Xi An, P.R. China
3 iRegene Pharmaceutical Technology Co., Ltd., Wuhan, P.R. China
4 School of Optoelectronic Engineering and Instrumentation Science, Dalian University of Technology, Dalian, P.R. China
5 Mathematics, Physics and Electrical Engineering, Northumbria University, Newcastle, UK

Introduction

This study developed a novel acoustofluidic device based on a filled tilted-angle (FTA) standing surface acoustic waves (SSAW) configuration, to characterise and phenotype cells. The trajectory of cells within the FTA device was captured to determine their acoustic contract factor. The FTA device produced a higher acoustic energy intensity [1] to effectively deflect cells to form aggregation on pressure nodes (PNs). By tuning the radio frequency (RF) input power of the FTA device, we achieved a threshold input power that laterally deflected and trapped most of the cells to the PN. The threshold input power was then used to determine the acoustic contract factor. The result showed the trajectory of three types of cells including cancer cells and white blood cells (WBCs), whose acoustic contract factors were found to be 0.1202, 0.1582, and 0.1020, respectively.

Background

Cell phenotyping plays an important role in disease diagnosis and prognosis especially for cancer[2], as pathological and physiological behaviours of cancer cells are related to the molecular, biophysical properties of cancer cells[3]. Acoustofluidic techniques have been increasingly applied to manipulate bioparticles such as cells[4], exosomes[5], and organelles[6] using a contactless fashion. Owing to low acoustic power and flexibility in integration with microfluidics, acoustofluidic manipulation has shown high biocompatibility and great versatility[6]. Acoustofluidic phenotyping has also been demonstrated to classify tumour cells in the process of metastasis, resulting in distinct mechanical phenotypes compared with those in the primary tumor [7].

Methods

Inside the FTA device, the trajectory of the cell is determined by,

$$S = \int_0^T A \cdot \varphi \cdot \sin(2kx) + u_f \, dt \ , (1) \quad A = \alpha \frac{\pi R_\mathrm{p}^2 \beta_\mathrm{m} P_\mathrm{I} \rho_\mathrm{s} c_\mathrm{s}}{9 A_w \lambda \mu} \ , (2) \quad \varphi_\mathrm{p} = \frac{9A \ \varphi \lambda \mu \mathrm{A}_w}{\pi R_\mathrm{p}^2 \alpha P_\mathrm{I} \rho_\mathrm{s} C_\mathrm{s} \beta_\mathrm{m}} \ , (3)$$

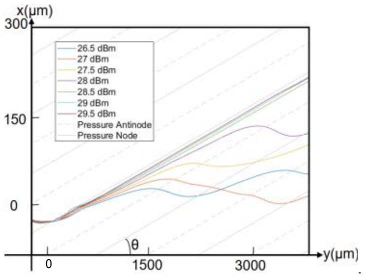

Figure 1 Plot of numerical trajectories for 10 μm polystyrene microspheres in incrementing input power.

here R_P, β_m, P_I, ρ_s, C_s, A_w, λ, μ, φ, k, x, u_f and T are radius of cell, ompressibility of medium, input power, density of substrate, phase velocity f surface wave, work area, wavelength, viscosity of medium, acoustic ontrast factor, wave number, x coordinate, velocity of flow, cells moving me. For a given cell, when the RF input power is greater than the threshold, e cell will be trapped onto the PN soon after entering the acoustic region. Vhile the cell escapes when the input power is smaller than this threshold. ig. 1 shows the numerical simulation[8] of 10 μm polystyrene microsphere trajectory against a range of input powers. In which, the microsphere escapes from the PN when the input power is smaller than the threshold power of 28.5 dBm. One can experimentally obtain the threshold input power by observing the microsphere trajectory inside the FTA device. In practice, when a population of microspheres or cells enter the FTA device, the threshold input power is determined when 80% microspheres or cells are trapped on the PN. The threshold input power is then substituted to Eq. 2 to determine the value for *A*. One can run 10 μm polystyrene microspheres in the FTA device with the known φ to derive a reference trajectory using Eq. 1, which can produce a product of A and φ (0.0018 for 10 μm polystyrene microspheres). Any other microparticles with the trajectory approximating to the reference trajectory should have the same product value, which can be then substituted in Eq. 3 to determine their acoustic contract factor, φ_p.

Polystyrene microspheres with diameters of 5 μm and 15 μm were applied to test the algorithm for measuring the acoustic contrast factor. The measured threshold input powers are 34.5 dBm and 26 dBm, respectively. The calculated acoustic contrast factors are 0.1985 and 0.1966, respectively which are close to the nominated value of 0.1939. The validation indicated the proposed algorithm for determining the acoustic contract factor of microparticles is reliable.

Cell phenotyping

After the validation, A549 (non-small-cell lung carcinoma cell), MDA-MB-231 (human breast cancer cell) and WBCs were commercially sourced and then introduced to the FTA device individually. For each cell type, we increased the input power until 80% of cells are trapped by the PN, which could be reflected by measuring the lateral distribution of the cell inside the acoustic region as shown in Fig. 2. The size distribution of each cell type results in a range of lateral displacement, particularly in the input power lower than the threshold. Once the input power achieves the threshold, most of the cells migrate to the PN located around 270 μm from the baseline with a much smaller distribution in lateral positions.

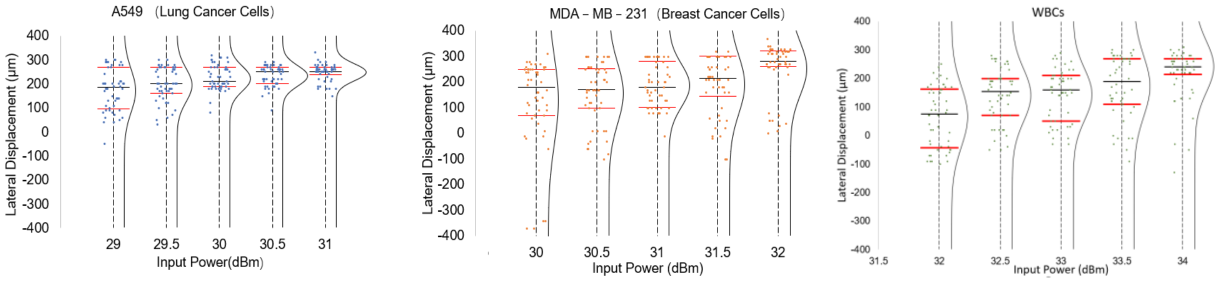

Figure 2: Lateral displacement of A549, MDA-MB-231, and WBCs under different input powers. Red horizontal lines show the 10th and 90th percentiles, black horizontal lines show the median value, black curves show the normal distribution. The threshold input powers for the three types of cells are 31dBm, 32 dBm, and 34 dBm, respectively.

The acoustic contract factor for the three types of cells was then determined accordingly as the result shown in Fig. 3. The MDA-MB-231 cells have largest mean value of 0.1582, while the WBCs have the least mean value of 0.1020. By applying one-way ANOVA analysis, the difference in the acoustic contract factor is found to be statistically significant, which denotes the FTA device is able to effective phenotype and characterise the three types of cells. The result also confirms that the potential use of the acoustic contrast factor as a biomarker for distinguishing cell types in the FTA device.

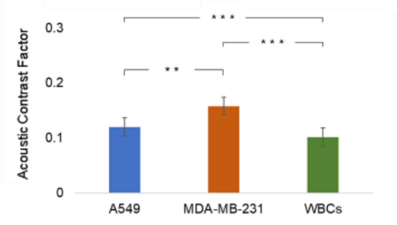

Fig 3: Acoustic contrast factors of three types of cells. Y-axis represent the average acoustic contrast factor. One-way ANOVA was used for significance analysis, stars represent Bonferroni-corrected post hoc tests, 0.001<**P<0.01; ***P<0.001.

Conclusion

In this study, we developed a label-free acoustic phenotyping method using the FTA device. We demonstrated the feasibility of using the acoustic contrast factor as a biomarker for distinguishing cell types. The acoustic contract factor was calculated by the threshold input power obtained in measuring cell’s lateral displacement inside the FTA device. The theoretical estimation of the acoustic contract factor was validated by using polystyrene microspheres. We further applied three types of commonly used cells to demonstrate the phenotyping resulting in the acoustic contract factors of A549, MDA-MB-231, and WBCs of 0.1202, 0.1582, and 0.1020. In future work, the method can be exploited in the phenotyping of cancer cells with different metastatic potential based on their acoustic contrast factor and studying the biophysical change of cells during the pathological process.

References

[1]F. Wu et al, IEEE Electron Device Letters, 42, 577-580 (2021).
[2]M. Bafadhel et al, Chest, 140, 634-642 (2011).
[3]Y. Geng et al, Nanomedicine: Nanotechnology, Biology and Medicine, 14, 1931-1939 (2018).
[4]M. Wu et al, Microsystems & Nanoengineering, 5, 32 (2019).
[5]M. Wu et al, Proceedings of the National Academy of Sciences, 114, 10584 (2017).
[6]K. Norregaard et al, Chemical Reviews, 117, 4342-4375 (2017).
[7]C. Sun et al, Ultrasonics, 108, 106202 (2018).
[8]Y. Wu, A. G. Stewart and P. V. S. Lee, Lab on a Chip, 1473-0197 (2021).
[9]X. Ding et al, Proceedings of the National Academy of Sciences, 111, 12992 (2014).

Acoustofluidics
2021
26-27 August 2021
Virtual Conference

Kinetic and thermal characteristics of micro-droplet driven by Rayleigh surface acoustic wave.

Mubbashar Mehmood[1], Baixin Chen[1], and Richard Yongqing Fu[2]

[1]School of Engineering and Physical Sciences, Heriot-Watt University, Edinburgh, EH14 4AS, UK.
E-mail: m.mehmood@hw.ac.uk
[2]Faculty of Engineering and Environment, Northumbria University, Newcastle upon Tyne, NE1 8ST, UK.

Introduction

Surface acoustic waves (SAW) can be generated using interdigital transducer (IDT). When a water micro-droplet is placed on the path where SAW propagates, waves penetrate inside the droplet at the Rayleigh angle (θ), defined by Snell's law [1]; $\theta = sin^{-1}(V_s/V_f)$, where V_s is the sound velocity in solid and V_f is the sound velocity in the fluid [2]. Due to mismatch of sound velocities between solid and liquid, internal streaming generates inside the droplet [3]–[5]. Furthermore, SAW energy transferred to the droplet increases thermal energy of the droplet [6]–[9].

At low power, droplet remains stationary with some power utilizing in the internal kinetics and some power consumes in increasing the thermal energy but at higher power, droplet may move. It is interesting to know the threshold power where the droplet starts moving away from the IDT in the direction of the waves and the power where the temperature gradient becomes zero.

Experiment Details

An experimental study has been conducted to investigate kinetic and thermal impacts of Rayleigh SAW (R-SAW) on a 25 µl water droplet using zinc oxide (ZnO) fabricated on an aluminum plate. This study has been carried out at an input power of 0.38 W to 4.0 W at the resonant frequency of 26.300 MHz. A charged-couple device (CCD) camera has been used to monitor the kinetics of the droplet, FLIR thermal camera has been used to examine the thermal impact of the waves on the droplet. Furthermore, a MATLAB code has been developed to read the images of temperature distribution inside the droplet.

Results and discussion

Figure 1 shows an image from CCD and FLIR camera to monitor kinetic and thermal impacts of the SAW on the droplet. Figure 1-a showing red polystyrene particles of size 6 µm to visualise streaming of particles. The streaming of particles has been monitored at different positions inside the droplet. Similarly, the temperature of the droplet (T_d) has been measured at different points inside the droplet to get the average temperature (°C). Thermal impacts of the droplet have been investigated in the literature [6], [10], [11] but less understanding of transient response of the R-SAW on droplet.

Thermal and kinetic impacts of the R-SAW for critical power levels (3.2 W and 4.0 W) demonstrated in Figure 2. It is clear from Figure 2-a that the droplet starts moving immediately as soon as SAW enters inside the droplet, but it stops after 4.0 s as the surface tension overcomes the SAW input power. There is more pumping force at an input power 4.0 W with the maximum droplet velocity of 0.60 mm/s. The momentum of the droplet has been presented in Figure 2-b that has been calculated using formula, p= mv, where 'm' is the mass of the droplet and 'v' is the velocity. The temperature gradient of the droplet at an input of 3.2 W and 4.0 W is shown in Figure 2-c. It is understandable that the gradient (°C/s) is higher at the start of input power, and it decreases with time as it approaches to the steady state. At an input power of 3.2 W, the gradient decreases with time and it reaches to ~0.3 °C/s after 45.0 s of the SAW elapsed time. However, gradient becomes zero at an input power of 4.0 W that means saturation occurs at this input power after 45.0 s of the SAW.

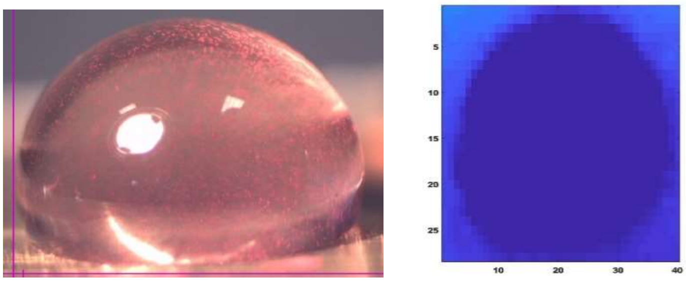

(a) (b)

Figure 1: (a) An image from CCD camera to monitor kinetic impacts, (b) An image from FLIR camera to monitor thermal impacts of the SAW.

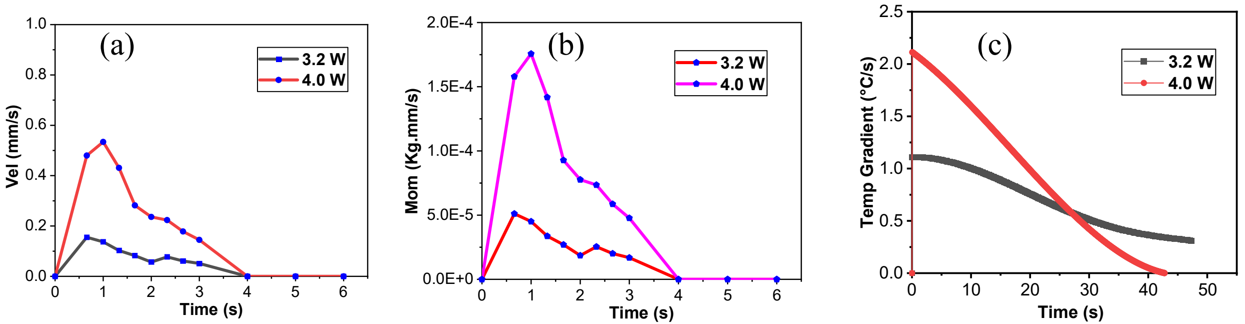

Figure 2: (a) Pumping velocity of the droplet (b) Momentum caused by the movement of the droplet (c) Temperature gradient of the droplet at the input power of 3.2 W and 4.0 W.

The average streaming velocity and an average temperature of the droplet at input power levels of 0.38 W to 3.2 W is shown in Figure 3. Average streaming velocity has been calculated by taking average of streaming velocities at different positions inside the droplet. However, average temperature has been measured using the temperature distribution obtained by the MATLAB code. Figure 3 shows almost linear trend for both streaming and temperature change inside the droplet. It is found from figure 3-a that with the increase in input power level, the streaming velocity increases at a rate of ~5.0 mm/s/W. However, temperature increases at the rate of ~10.0 °C/W as indicated in figure 3-b.

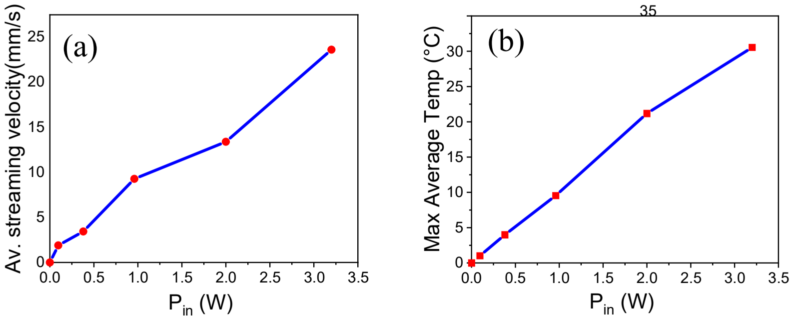

Figure 3: Streaming and thermal impact at an input power levels (0.38 W to 3.2W) (a) Average streaming inside the droplet versus input power (b) Average temperature of the droplet versus input power.

Conclusion

Kinetic and thermal impacts of R-SAW have been experimentally investigated in this study. It has been observed that both streaming and temperature change of the droplet increases linearly with the increase in input power. There is no pumping velocity for the input power < 3.0 W. However, the droplet moves on the surface of the substrate at input power of 3.2 W and 4.0 W and stops within 5.0 s of the SAW input. Thermal steady state achieved at an input power of 4.0 W after 45.0 s the SAW elapsed time.

Acknowledgements

This work was financially supported by the UK Engineering, and Physical Sciences Research Council (EPSRC) grants EP/P018998/1, and Special Interests Group of Acoustofluidics under the EPSRC-funded UK Fluidic Network (EP/N032861/1).

References

[1] K. Sritharan, C. J. Strobl, M. F. Schneider, A. Wixforth, and Z. von Guttenberg, "Acoustic mixing at low Reynold's numbers," *Appl. Phys. Lett.*, vol. 88, no. 5, p. 54102, 2006.

[2] Z. Wang and J. Zhe, "Recent advances in particle and droplet manipulation for lab-on-a-chip devices based on surface acoustic waves," *Lab Chip*, vol. 11, no. 7, pp. 1280–1285, 2011.

[3] C. Chen *et al.*, "Three-dimensional numerical simulation and experimental investigation of boundary-driven streaming in surface acoustic wave microfluidics," *Lab Chip*, vol. 18, no. 23, pp. 3645–3654, 2018.

[4] H. Zec, D. J. Shin, and T.-H. Wang, "Novel droplet platforms for the detection of disease biomarkers," *Expert Rev. Mol. Diagn.*, vol. 14, no. 7, pp. 787–801, 2014.

[5] A. Wixforth, C. Strobl, C. Gauer, A. Toegl, J. Scriba, and Z. v Guttenberg, "Acoustic manipulation of small droplets," *Anal. Bioanal. Chem.*, vol. 379, no. 7–8, pp. 982–991, 2004.

[6] J. Kondoh, N. Shimizu, Y. Matsui, M. Sugimoto, and S. Shiokawa, "Development of temperature-control system for liquid droplet using surface Acoustic wave devices," *Sensors Actuators A Phys.*, vol. 149, no. 2, pp. 292–297, 2009.

[7] S. Ito, M. Sugimoto, Y. Matsui, and J. Kondoh, "Study of surface acoustic wave streaming phenomenon based on temperature measurement and observation of streaming in liquids," *Jpn. J. Appl. Phys.*, vol. 46, no. 7S, p. 4718, 2007.

[8] A. Renaudin, V. Chabot, E. Grondin, V. Aimez, and P. G. Charette, "Integrated active mixing and biosensing using surface acoustic waves (SAW) and surface plasmon resonance (SPR) on a common substrate," *Lab Chip*, vol. 10, no. 1, pp. 111–115, 2010.

[9] G. Greco, M. Agostini, R. Shilton, M. Travagliati, G. Signore, and M. Cecchini, "Surface Acoustic Wave (SAW)-Enhanced Chemical Functionalization of Gold Films," *Sensors*, vol. 17, no. 11, p. 2452, 2017.

[10] R. J. Shilton *et al.*, "Rapid and controllable digital microfluidic heating by surface acoustic waves," *Adv. Funct. Mater.*, vol. 25, no. 37, pp. 5895–5901, 2015.

[11] Y. Wang *et al.*, "A rapid and controllable acoustothermal microheater using thin film surface acoustic waves," *Sensors Actuators A Phys.*, vol. 318, p. 112508, 2021.

Acoustofluidics 2021
26-27 August 2021
Virtual Conference

Lyophilised Monodisperse Microbubbles as Ultrasound Contrast Agent

Ugur Soysal[1], Pedro N. Azevedo[1,2,3], Flavien Bureau[2], Alexandre Aubry[2], Marcio S. Carvalho[3], Amanda C. S. N. Pessoa[4], Lucimara G. de la Torre[4], Olivier Couture[5], Arnaud Tourin[2], Mathias Fink[2], Patrick Tabeling[1]

[1]Laboratoire de Microfluidique, MEMS et Nanostructures, ESPCI Paris, France; [2]Institut Langevin, ESPCI Paris, Université PSL, CNRS, France; [3]Department of Mechanical Engineering, PUC-Rio, Brazil; [4]School of Chemical Engineering, University of Campinas, Brazil; [5]LIB, CNRS, Sorbonne, INSERM, France;

Introduction

Over the last years, the interest of using monodisperse bubbles as ultrasound contrast agents (UCA) has been underlined. The small coefficient of variation (CV), of their size distribution (SD), leads to narrow resonance spectrum[1]. This feature increases the number of bubbles in the UCA population that are excited by ultrasound scanners used in clinics, augmentating the signal-to-noise ratio, and reducing shadowing effects in deep tissue imaging[2]. A CV below 6%, could lead to quantitative local pressure measurements, by exploiting the relation between the bubbles resonance frequency and local pressures[1]. In the Molecular diagnosis field, the higher acoustic sensitivity of the bubbles would aid revealing the presence of the target molecules. Moreover, the high sensitivity of the resonance frequency shift would allow to differentiate freely circulation and bound bubbles[3]. Drugs, genes, or therapeutic gases transport applications can also be optimized owing to the precise control of monodisperse bubbles[4]. However, the existing monodisperse microbubbles in research laboratories are neither storable nor transportable; this is a major bottleneck that hampers their usage in clinical applications. Attempts made in this area required the use of toxic solvents, rising regulatory issues[5]. In this work, thanks to a novel collection method, at the outlet of the microfluidic generation device, we succeeded to directly lyophilize microfluidic-generated monodisperse microbubbles (40 and 5µm in diameter), and resuspend them, without any degradation of their monodispersivity. This paves a road towards a new generation of contrast agents, in the form of a stable lyophylisate, that can be stored for months, transported, and resuspended, and thus can be used directly in clinical applications.

Material and methods

We used polyvinyl-alcohol (PVA) as shell material due to their high echogenicity and stability[7]. The gas phase used was Perfluorohexane (C_6F_{14}) due to its high hydrophobicity, lower solubility, and higher molecular weight in comparison with air. The microbubbles were produced in a flow-focusing and step-emulsification PDMS (PolydiMethyl Siloxane)-based microfluidic device, with an anti-clogging system, to avoid large aggregates, ensuring a long and stable generation. A production of 40µm and 5µm diameter microbubbles was made at a rate up to $\sim 6\times10^5$ bubbles/min, and a CV<5%. The bubbles are spread over a glass plate, so as to suppress coalesence, Ostwald ripening or creaming that degrade monodispersivity. Images of all the steps of the process, from production, collection, freeze-drying and resuspension, were made. In a PDMS chamber (35mm×10mm×1mm), the backscattered acoustic response of the bubbles *in vitro* was measured for the freshly generated and the resuspended microbubbles, with a emitter/receiver focal transducer (bandwidth of ~50%, a 38 mm focal length, with a central frequency of 2.25 MHz). The bubbles were excited with sinusoidal 1 cycle burst signal,with pulse repetition frequency of 1kHz, and 134kPa peak negative acoustic pressure. The acquisition frequency was of 20Hz with a sample rate of 65MSamples/s. A Fast Fourier Transform (FFT) was made for the region of interest, located in the focal zone of the transducer.

Results

Figure1A and 1B show populations of freeze dried bubble dispersed onto glass plates, along with the corresponding size distributions (SD) for 44 and 5 µm diameters, respectively. In both cases, distributions are narrow and thereby monodispersivity is conserved. The larger CV of 10% for 44µm bubbles, resulted from the close packing of bubbles, favoring shape deformations. The SEM image of the insert of Fig 1C, indicates a shell thickness of ~70 nm. The resuspension of the bubbles with DI water resulted in a CV of 6% and 5% for the 44µm and 5µm bubbles, respectively(Figure 1D and 1E). These values were undistinguishable from the freshly generated bubbles, demonstrating that the monodispersity was conserved along the entire process, i.e collection, freeze-drying and resuspension. Figure 1F shows the resonance spectra obtained from the *in vitro* backscatter acoustic measurement for the 5 µm freshly generated and the freeze-dried bubbles. The difference between the two spectra is in the resonance frequencies is of ±2% and ±10% in the maximum amplitudes. Both resonance response had a 10% standard deviation ensuring a narrow bandwidth of monodisperse bubbles. The acoustic measurements confirmed that monodispersity was conserved.

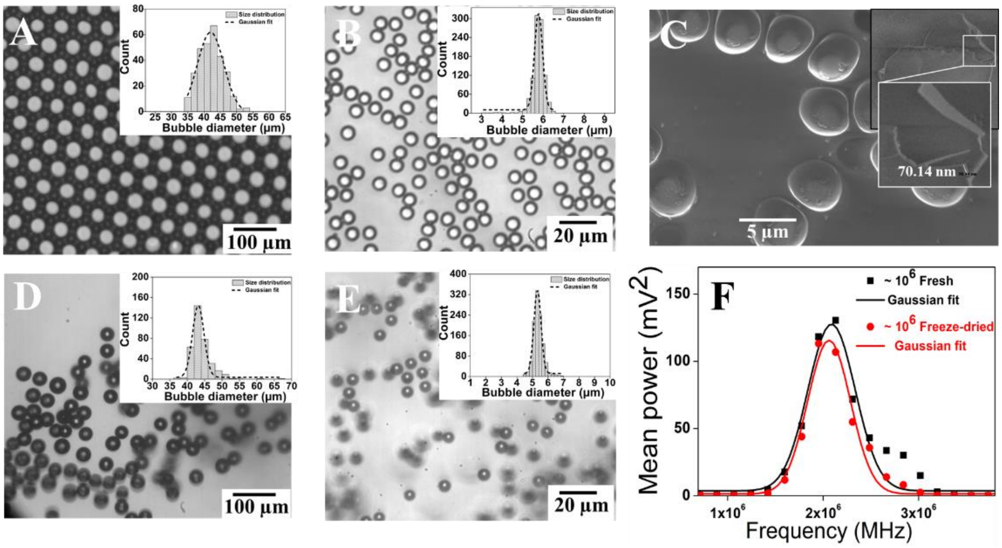

Figure 1: Image and SD of the lyophilisates (A) 42 µm (σ of 4 and CV of 9%), and (B) 5.8 µm (σ of 0.3 and CV of 5%) in average diameters. (C) A SEM image of the 5 µm lyophilisate. The inset shows a broken bubble and the magnified image provides an estimate of the shell thickness (~70 nm). (D and E) Resuspended bubbles and their SD show the average diameters of the bubbles as 44 µm (with 6% CV) and 5.4 µm (5% CV). (F) Backscattered spectra of fresh and freeze-dried PVA bubbles, for the same concentrations, showing almost identical backscattered acoustic responses (the difference of ±2% in the resonance frequency and ±10% in the maximum amplitude).

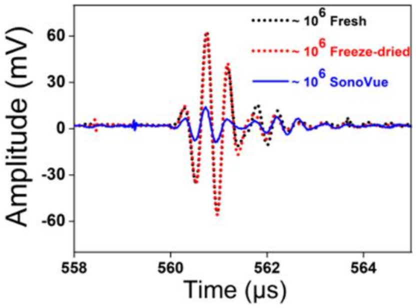

Figure 2: Typical backscattered responses of fresh, freeze-dried PVA monodisperse bubbles, and SonoVue at the same microbubble concentrations.

An important feature we found, consistent with literature [2], was that monodisperse bubbles show a one order of magnitude larger backscattered signal than polydisperse bubbles. This is shown in Figure 2.

Conclusions

The geometrical and acoustical characterization of microbubbles before and after the freeze-drying process, showed that, by using a novel collection process at the outlet of the microfluidic generation device, we can accurately conserve microbubble monodispersity. The technology makes thus feasible to transport and store monodisperse microbubbles, opening up a pathway towards a new generation of ultrasound contrast agents that could be used directly in clinical applications. With the production rate we achieved, by parallelizing devices one thousand times, we can produce 10^{14} bubbles per year. This figure is to be compared to the 10^{17} world production. By optimizing the production conditions, the gap can be drastically reduced. Last but not least, as noted above, when monodisperse bubbles are used, ten times fewer bubbles are required for US imaging, a result that certainly has interesting cost consequences.

References

[1] Tremblay-Darveau C, Williams R, Burns PN. Ultrasound in Medicine and Biology Elsevier, 2014;40:775–78.

[2] Segers T, Kruizinga P, Kok MP, Lajoinie G, de Jong N, Versluis M.Ultrasound in Medicine&Biology 2018b; 44:1482–1492.

[3] Overvelde M, Garbin V, Dollet B, de Jong N, Lohse D, Versluis M. Ultrasound in Medicine&Biology 2011; 37:1500–1508

[4] Dixon AJ, Li J, Rickel J-MR, Klibanov AL, Zuo Z, Hossack JA. Ann Biomed Eng 2019;47:1012–1022

[5] Song R, Peng C, Xu X, Wang J, Yu M, Hou Y, Zou R, Yao S. ACS Appl Mater Interfaces 2018;10:14312–14320.

[6] Grishenkov D, Kari L, Brodin L-Å, Brismar TB, Paradossi G. Ultrasonics 2011;51:40–48.

Acoustofluidics 2021
26-27 August 2021
Virtual Conference

Microparticle Patterning inside Capillary Tubes on Bendable Thin Film SAW Devices

Sadaf MaramiZonouz[1], Mohammad Rahmati[1], Changfeng Jia,[2] Tengfei Zheng,[2] and Richard Yongqing Fu[1]

[1] Faculty of Engineering and Environment, Northumbria University, Newcastle upon Tyne, NE1 8ST, UK
[2] State Key Laboratory for Manufacturing Systems Engineering, Xian Jiaotong University, 710049, Xian, 710048, P.R. China

E-mail: sadaf.maramizonouz@northumbria.ac.uk

Introduction

Capillary tubes can potentially substitute conventional microchannels and become integrated with SAW devices either without fluid flow or in a continuous flow application for manipulating microparticles and cells. They have been used to manipulate, deform, trap, enrich, align, arrange, focus, pattern and separate microparticles and biological cells, for applications such as cell studies [1, 2] to immobilise cells in a cured gel to form a fibre and continuous flow applications to trap [3-6] and to focus [7] microparticles. There have also been a few studies on modelling of acoustofluidics platforms integrated with capillary tubes to investigate the fundamentals of particle manipulation inside capillary tubes [4, 8-10]. However, various patterns generated by using different cross-sections of capillary tubes and positioning the tubes at different directions compared with the electrode directions have not been systematically studied. Moreover, the published work is focused only on rigid and brittle lithium niobate ($LiNbO_3$) SAW devices [1, 11, 12] without addressing flexible thin film SAW devices, which have advantages such as better mechanical qualities and potential applications in flexible microfluidic platforms, body conforming wearable devices, flexible sensors and electronics as well as soft robotics. This study aims to systematically investigate the patterning and alignment of microparticles inside glass capillary tubes using a zinc oxide (ZnO) thin film based flexible SAW device and capillary tubes with rectangular and circular cross-sections and at different tube positioning relative to the direction of the IDTs. The effects of positioning the tubes on the SAW device at different angles in relation to the IDTs were also studied. Additionally, both the rectangular and circular capillary tubes were used in a continuous flow setup to understand the effects of different flow rates on the particle patterning and alignment inside the tube.

Particle Patterning inside Rectangular Glass Capillary Tube

The effects of different angles of the rectangular capillary tube with respect to the alignment of the IDTs on silica microparticle patterning were studied and the microparticle patterning results as well as simulation results of the acoustic pressure field from the top view are presented in Figure 1.

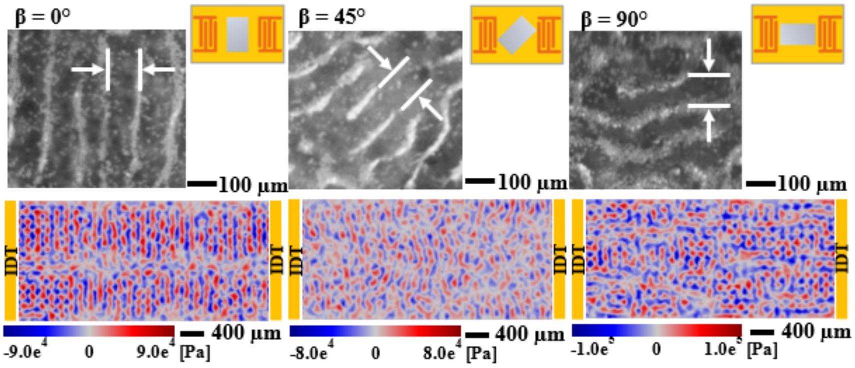

Figure 1: Particle patterning and acoustic pressure field for rectangular capillary tube with 13.12 MHz frequency.

Particle Patterning inside Circular Glass Capillary Tube

Effects of different angles of the circular capillary tube with respect to the alignment of the IDTs on silica microparticle patterning were studied and the microparticle patterning results as well as simulation results of the acoustic pressure field from the top view are presented in Figure 2.

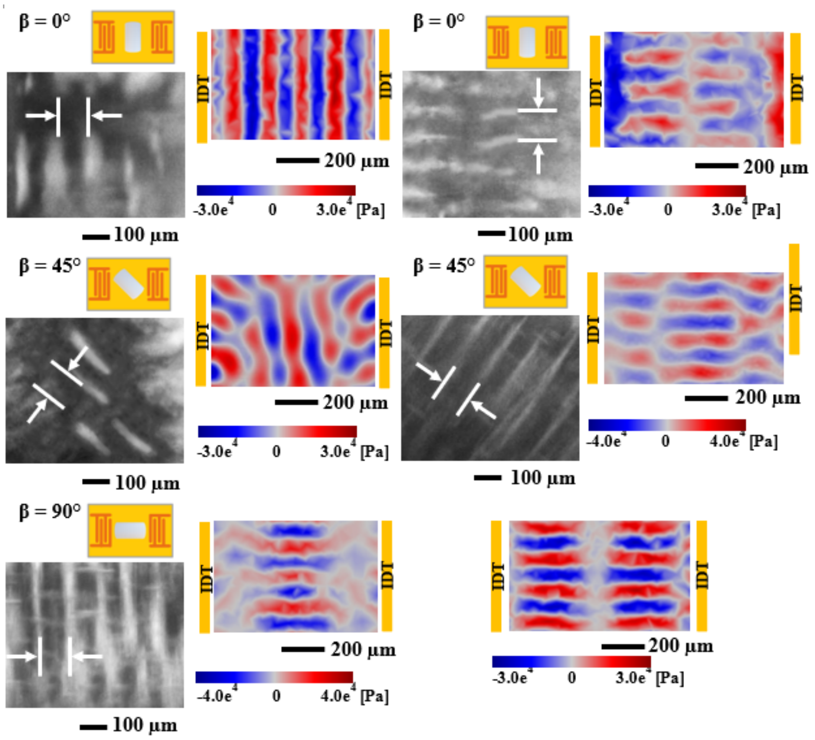

Figure 2: Particle patterning and acoustic pressure field for circular capillary tube with 13.12 MHz frequency.

Discussions and Conclusions

This research investigated the patterning and alignment of microparticles inside glass capillary tubes with and without flow using ZnO/Al thin film SAW device, and studied the effects of different cross-sections of the capillary tubes as well as their positions and relative angles regarding to the directions of the IDTs.

For a rectangular glass capillary tube placed at an angle relative to the IDTs, particle pattern lines are parallel to the tube walls. This is resulted from the standing wave field generation inside the rectangular glass tube. The particles also seem to form some checker-board patterns at the bottom of the tube.

For circular glass capillary tubes, different particles patterns can be observed which depends on their position along the tube's height. In the bottom of the tube, the particle pattern lines are parallel to the tube direction when the tube is placed at an angle in relation to the IDTs. The particle patterns ae in lines parallel to the tube direction at the bottom of the circular glass tube, due to the acoustic wave propagation into the water and formation of a standing wave along the direction of the circular tube. Whereas, near the middle of the glass tube with a circular cross-section, the particle pattern lines are perpendicular to the tube direction with the tube positioned at an angle regarding the IDTs. When the circular glass tube is perpendicular to the IDTs, the pattern lines of the particles are parallel to the IDTs. The standing wave then propagates around the circular cross-section of the tube perpendicular to the tube direction and thus at the middle of the tube, the particles forms pattern perpendicular to the tube walls.

The continuous fluid flow inside the rectangular and circular glass tubes causes the particles to form smooth line patterns parallel to the direction of the flow for all the angles and eliminates the other type of patterns.

Acknowledgements: UK EPSRC (EPSRC EP/P018998/1), UKFN SIG Acoustofluidics (EP/N032861/1), International Exchange Grant through Royal Society and the National Natural Science Foundation of China (IEC/NSFC/201078).

References

[1] J. P. Lata, et al., *Advanced Materials*, **28**, 8632-8638, 2016.
[2] G. Lisa, et al., 2002.
[3] B. Raiton, et al., *Applied Physics Letters*, **101**, 044102, 2012.
[4] I. Gralinski, et al., *Journal of Applied Physics*, **115**, 054505, 2014.
[5] P. O'Mahoney, et al., *Optofluidics, Microfluidics and Nanofluidics*, **1**, 2016.
[6] B. Hammarström, et al., *Lab on a chip*, **10**, 2251-2257, 2010.
[7] G. Goddard, et al., *The Journal of the International Society for Analytical Cytology*, **69**, 66-74, 2006.
[8] I. Gralinski, et al., *The Journal of the Acoustical Society of America*, **132**, 2978-2987, 2012.
[9] M. W. Ley, et al., *Physical Review Applied*, **8**, 024020, 2017.
[10] J. S. Bach, et al., *Physical Review E*, **101**, 023107, 2020.
[11] Z. Mao, et al., *Acs Nano*, **11**, 603-612, 2017.
[12] F. Guo, et al., *small*, **11**, 2733-2737, 2015.

Acoustofluidics 2021
26-27 August 2021
Virtual Conference

Three-dimensional standing surface acoustic wave simulation model for efficient particle separation

Lizhu Liu,[1] Jian Zhou,[1,*] Dinghong Zhang,[1] Zhengjia Zhan[1]

[1] College of Mechanical and Vehicle Engineering, Hunan University, Changsha 410082, China
Corresponding E-mail: jianzhou@hnu.edu.cn

Introduction

Recently, researchers have demonstrated that surface acoustic wave (SAW) [1] is capable of controlling particles within the acoustic field at precise locations [2], such as particle pattern, transportation [3], and separation [4]. The rational setting of the SAW device parameters to control the particle motion is the key to realize high efficient particle separation. However, the design of acoustic devices is very complicated, which introduces the coupling of multiple physical fields such as sound pressure field, flow field and electric field. Using 3D simulation models to guide experiments, we can effectively reduce the errors caused by direct device design. Therefore, we developed a 3D SAW sorting model to show the particle sorting experiments. The model integrates the effects of the pressure field, flow field and electric field distributions on particles in three dimensions. As a result, the model can effectively reproduce the motion of particles in the microfluidic chip in real scenarios. The optimal parameters obtained through the optimization of the model were finally used to guide the sorting experiments of 15μm and 1μm particles, and the effectiveness of the model was successfully verified.

Simulation Methods

We completed the modelling of the simulation on COMSOL Multiphysics software. We divided the simulation into four steps. The first step is to set the basic parameter, including the setting of the basic parameters of the SAW (such as wavelength, frequency, sound speed, piezoelectric substrate, etc.) and the establishment of the 3D model. In the second step, simulating the flow field distribution, we assume that the flow in the channel is laminar and obtain the flow velocity distribution in the 3D model as shown in Figure 1(a) with steady-state calculation. The third step is to calculate (as shown in Fig. 1(b)) the time-domain pressure distribution of the acoustic surface wave on the substrate, which is calculated by setting the acoustic structure boundary extension to obtain the pressure distribution water body. The periodic pressure distribution formed in the water body can generate acoustic radiation force on the particles, which controls the movement of the particles. Then, we analyzed the effects of the three primary forces on the particle motion, namely, acoustic radiation, lift and traction, and calculated the particle trajectory in the time domain by integrating the previously calculated flow field distribution and pressure distribution as shown in Figure 1(c). Finally, we obtained the guiding parameters, which effectively guided the completion of the subsequent experiments.

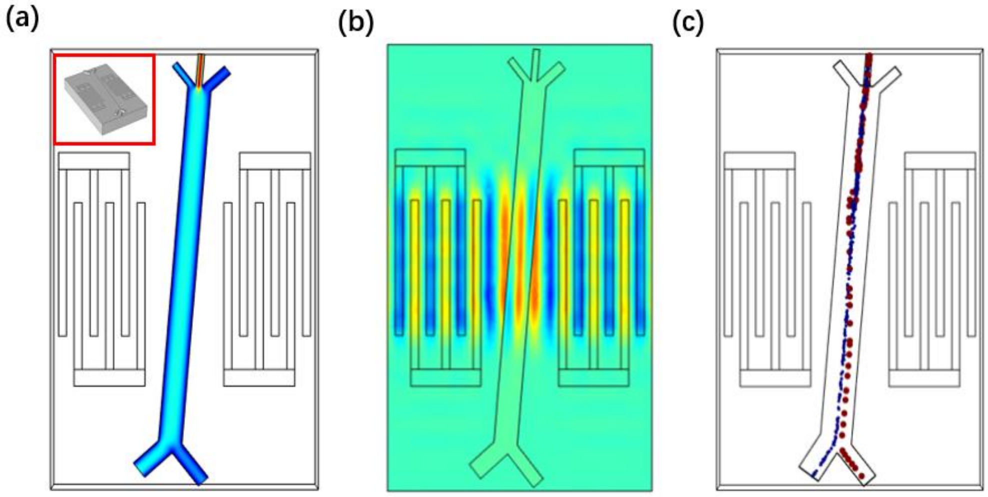

Figure 1: (a) The velocity distribution of the channel; (b) Pressure distribution of the model in the time domain (c) The trajectory of the particle in the time domain

Experiment

We designed a notch in the center area in terms of PDMS channel design so that the IDT does not contact the PDMS, effectively reducing energy loss. PDMS channel height is 100μm, and width is 800μm. We bond the designed PDMS channel to the SSAW device, as shown in Fig. 2(a). The SAW device consists of metallic interdigital electrode (IDTs) that we have fabricated on a piezoelectric lithium niobate substrate (LN). The IDT has a wavelength of 100μm. The particles we choose are 15μm and 1μm polystyrene beads, close to the density of human cells and can effectively guide cell sorting work. We use sheath flow to control the initial distribution of particles in the flow channel for subsequent separation, as shown in Fig. 2(b). For the three tracks, the flow rate control from top to bottom is 5μl/min, 1μl/min and 1μl/min, respectively, to make the flow rate distribution in the channels conform to the simulation model. When the power was used to activate a pair of IDT, the 15μm particles move at an angle toward the lower part of the microchannel, deviating from their original trajectory as shown in Fig. 2(c). Finally, we achieved the separation of 15μm and 1μm particles, and the effect is close to the simulation results, as shown in Fig. 2(d).

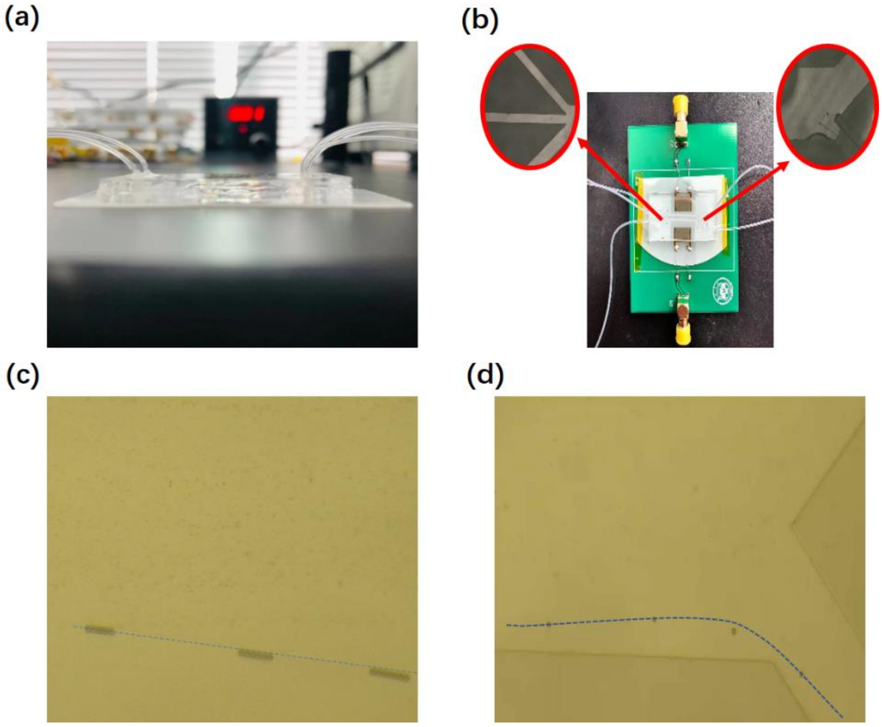

Figure 2: (a) SAW microfluidic chip; (b) Particle deviation from the original trajectory (c) Achieving 15μm particle separation

Conclusion

We have developed a particle analysis-based 3D acoustic surface wave microfluidic model, which integrates the coupling of multiple physical fields during the operation of acoustic surface wave microfluidics. We used the model to obtain the optimal design parameters of the SAW devices and conducted experiments on 15μm and 1μm particles, proving that the model can effectively guide the structural design and particle selection of SAW microfluidic devices. In the future, we will further explore the separation of biological cells.

References

[1] P. Li, Z. Mao, Z. Peng, L. Zhou, Y. Chen, P.-H. Huang, C.I. Truica, J.J. Drabick, W.S. El-Deiry, M. Dao, Acoustic separation of circulating tumor cells, Proc. Natl. Acad. Sci. 112 (16) (2015) 4970–4975.

[2] A. Barani, H. Paktinat, M. Janmaleki, A. Mohammadi, P. Mosaddegh, A. Fadaei-Tehrani, A. Sanati-Nezhad, Microfluidic integrated acoustic waving for manipulation of cells and molecules, Biosens. Bioelectron. 85 (2016) 714–725.

[3] L. Meng, F. Cai, J. Chen, L. Niu, Y. Li, J. Wu, H. Zheng, Precise and programmable manipulation of microbubbles by two-dimensional standing surface acoustic waves, Appl. Phys. Lett. 100 (17) (2012) 173701.

[4] G. Destgeer, B.H. Ha, J.H. Jung, H.J. Sung, Submicron separation of microspheres via travelling surface acoustic waves, Lab Chip 14 (24) (2014) 4665–4672.

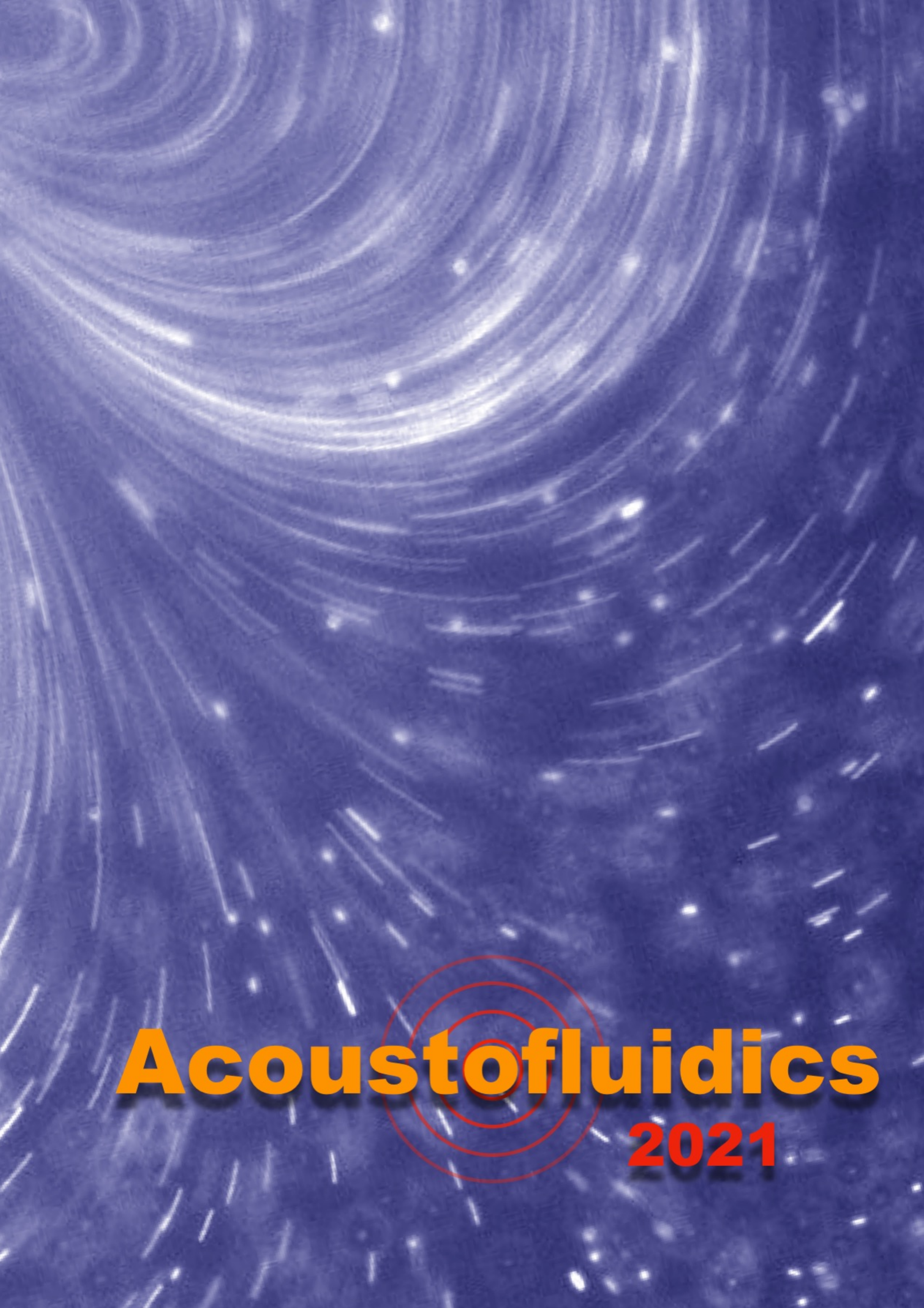

Acoustofluidics

2021